ISSN 1881-7815 Online ISSN 1881-7823

BST BioScience Trends

Volume 14, Number 2
April, 2020

IRCA BSSA

IACMHR

www.biosciencetrends.com

BST
BioScience Trends

ISSN: 1881-7815
Online ISSN: 1881-7823
CODEN: BTIRCZ
Issues/Year: 6
Language: English
Publisher: IACMHR Co., Ltd.

BioScience Trends is one of a series of peer-reviewed journals of the International Research and Cooperation Association for Bio & Socio-Sciences Advancement (IRCA-BSSA) Group and is published bimonthly by the International Advancement Center for Medicine & Health Research Co., Ltd. (IACMHR Co., Ltd.) and supported by the IRCA-BSSA and Shandong University China-Japan Cooperation Center for Drug Discovery & Screening (SDU-DDSC).

BioScience Trends devotes to publishing the latest and most exciting advances in scientific research. Articles cover fields of life science such as biochemistry, molecular biology, clinical research, public health, medical care system, and social science in order to encourage cooperation and exchange among scientists and clinical researchers.

BioScience Trends publishes Original Articles, Brief Reports, Reviews, Policy Forum articles, Case Reports, News, and Letters on all aspects of the field of life science. All contributions should seek to promote international collaboration.

Editorial Board

Editorial Office

Pearl City Koishikawa 603,
2-4-5 Kasuga, Bunkyo-ku, Tokyo 112-0003, Japan
E-mail: office@biosciencetrends.com

BioScience Trends

Editorial and Head Office

Pearl City Koishikawa 603, 2-4-5 Kasuga, Bunkyo-ku,
Tokyo 112-0003, Japan

E-mail: office@biosciencetrends.com
URL: www.biosciencetrends.com

Editorial Board Members

CONTENTS

Volume 14, Number 2, 2020

Review

Original Article

Brief Report

Communication

CONTENTS (*Continued*)

Letter

Review

DOI: 10.5582/bst.2020.01029

NEK7: a potential therapy target for NLRP3-related diseases

Ganglei Liu[1,§], Xueliang Chen[1,§], Qianqian Wang[2], Lianwen Yuan[1,*]

[1] Department of Geriatrics Surgery, The Second Xiangya Hospital, Central South University, Changsha, Hunan, China;
[2] Department of Oncology, The Affiliated Zhuzhou Hospital of Xiangya Medical College, Central South University, Zhuzhou, Hunan, China.

SUMMARY NLRP3 inflammasome plays an essential role in innate immunity, yet the activation mechanism of NLRP3 inflammasome is not clear. In human or animal models, inappropriate NLRP3 inflammasome activation is implicated in many NLRP3-related diseases, such as tumors, inflammatory diseases and autoimmune diseases. Until now, a great number of inhibitors have been used to disturb the related signaling pathways, such as IL-1β blockade, IL-18 blockade and caspase-1 inhibitors. Unfortunately, most of these inhibitors just disturb the signaling pathways after the activation of NLRP3 inflammasome. Inhibitors that directly regulate NLRP3 to abolish the inflammation response may be more effective. NEK7 is a multifunctional kinase affecting centrosome duplication, mitochondrial regulation, intracellular protein transport, DNA repair and mitotic spindle assembly. Researchers have made significant observations on the regulation of gene transcription or protein expression of the NLRP3 inflammasome signaling pathway by NEK7. Those signaling pathways include ROS signaling, potassium efflux, lysosomal destabilization, and NF-κB signaling. Furthermore, NEK7 has been proved to be involved in many NLRP3-related diseases in humans or in animal models. Inhibitors focused on NEK7 may regulate NLRP3 to abolish the inflammation response and NEK7 may be a potential therapeutic target for NLRP3-related diseases.

Keywords inhibitors, NF-κB signaling, NLRP3-related diseases, NEK7 , NLRP3 inflammasome

1. Introduction

Innate immunity provides the first line of defense to recognize pathogens and endogenous stress *via* the pathogen-associated molecular patterns (PAMPs) and danger-associated molecular patterns (DAMPs) (*1*). The danger signals can be identified by pattern recognition receptors (PRRs). Inflammasomes are activated to form a "danger" by innate immune cell defense through the maturation and secretion of pro-inflammatory cytokines, like IL-1β. Among all the known inflammasomes, the NLRP3 inflammasome plays a central role in innate immunity (*2*). NLRP3 inflammasome is a multiple protein complex composed of NLRP3, apoptosis-associated speck-like protein containing a caspase recruitment domain (ASC)and caspase-1 (*3,4*). The activation of caspase-1 results in the maturation and secretion of IL-1β and IL-18 (*5,6*) and the cleavage of GasderminD triggers pyroptosis (*7-9*). Thereafter, an inflammatory response is formed against the antigens of environmental or host origin.

The components of NLRP3 inflammasome often lead to susceptibilities to inflammatory diseases and cancer in humans (*10*). Until now, a great number of inhibitors have been used to disturb the related signaling pathways, such as IL-1β blockade, IL-18 blockade and caspase-1 inhibitors. Unfortunately, most of these inhibitors just disturb the signaling pathways after the activation of NLRP3 inflammasome. Inhibitors that directly regulate NLRP3 to abolish the inflammation response may be more effective. NIMA-related kinase 7 (NEK7) directly targets at NLRP3 inflammasome. Researchers have made significant observations on the regulation of gene transcription or protein expression of NLRP3 inflammasome signaling pathway by NEK7 in inflammatory diseases, which strongly suggests that NEK7 can be a new target for the clinical treatment of NLRP3-related diseases, such as squamous cell carcinoma of head and neck (*11*), Diabetic retinopathy (*12*), Hepatocellular carcinoma (*13*), systemic lupus erythematosus (*14*) and inflammatory bowel disease (*15*).

This review briefly discusses the immunological function of NEK7 and its potential regulatory role in NLRP3-related diseases, as well as the potential of NEK7 as a therapeutic target for NLRP3-related diseases.

2. The structure of NEK7 and its mechanism of action in basic biological functions (Table 1)

2.1. NEK7 structure and regulation

Table 1. The mechanism of action in basic biological functions of NEK7, and the potential diseases

Biological functions	Possible mechanism	Potential disease	*Ref*
Centrosome duplication, Mitochondrial regulation, DNA repair, Mitotic spindle assembly, proliferation of other resting cells	Promotes the recruitment of pericentriolar material(PCMs) to centrosomes in G1 and S phase; NEK9 activates NEK7 and NEK6 during mitosis to coordinate microtubule dynamics so as to promote spindle formation, centrosome nucleation and cytokinesis	Tumor, Inflammatory diseases, Autoimmune diseases	*20-26, 35, 94*
Nek7 is required for NLRP3 inflammasome activation induced by all NLRP3 stimuli tested including ATP, nigericin, monosodium urate crystals and Alum	Intracellular protein transport		

The NEK family was isolated by Ron Morris and his colleagues in cell division cycle mutants of Aspergillus nidulans (*16*). The NIMA-related kinase constitutes approximately 2% of all human kinases. NEK7 located in the centrosome is one of the smallest members of 11 NEK kinases, and is a highly conserved serine/threonine kinase among 302 kinases (*17*). NEK7 is expressed in a variety of organs, such as heart, brain, liver, lung and spleen (*18*). Human NEK7 consists of a non-conserved and disordered N-terminal regulatory domain as well as a conserved C-terminal catalytic domain (*19*). NEK7 promotes recruitment of pericentriolar material (PCMs) to centrosomes in G1 and S phase. The number of PCMs directly affects centrosome duplication efficiency (*20*). NEK7 is a multifunctional kinase affecting centrosome duplication, mitochondrial regulation, intracellular protein transport, DNA repair and mitotic spindle assembly (*21-24*). NEK7 may induce the proliferation of other resting cells, which indicates that NEK7 has cancer potential (*25,26*). NEK7-deficient mice results in lethality in late embryogenesis or in early postpartum stages to severe growth retardation, which shows that NEK7 plays a critical role in growth and survival (*27*).

2.2. NEK7 in mitosis (Figure 1)

NEK9, NEK6, and NEK7 are required for the module of downstream kinases implicated in mitotic signal transduction (*28*). Structurally, human NEK7 and NEK6 share 86% identity in their C-terminal domains and only 20% identity in their disordered N-terminal extensions (*29,30*). The mitotic regulatory factors cycle dependent kinase 1 (CDK1) and Polo-like kinase 1 (Plk1) activate NEK9 to bind directly to NEK6 and NEK7, thus controlling cytokinesis (*23,31*). In early mitosis, NEK9, NEK7, NEK6, and the kinesin Eg5 form a signaling module downstream of Cdk1 and Plk1 required for centrosomes separation and bipolar spindle formation (*32-34*). Both NEK7 and NEK6 kinase can phosphorylate α- and β-tubulin *in vitro*, as well as regulate the half-life of microtubules in interphase (*35*). NEK6 phosphorylates KIF11 to target centrosomes in order to promote centrosome separation (*36*). Nek6 controls microtubule binding activity of the

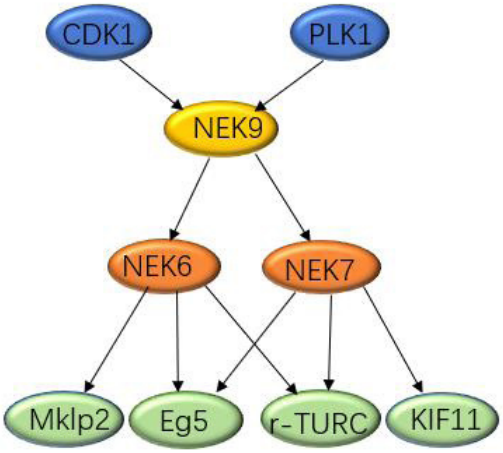

Figure 1. Mechanism of NEK9 regulating NEK7 and NEK6 in mitosis. In early mitosis, CDK1 phosphorylates many sites in NEK9, which are subsequently phosphorylated and activated by PLK1. through activation of NEK6 and NEK7. NEK9 subsequently phosphorylates components (kinesin Eg5, microtubules and the γ-TuRC) that are necessary for proper mitotic spindle formation.

central spindle in the telophase of Mklp2 (*23*). NEK9 activates NEK7 and NEK6 during mitosis to coordinate microtubule dynamics so as to promote spindle formation, centrosome nucleation and cytokinesis (*35*).Notably, both NEK6 and NEK9 do not interact with NLRP3 and are also dispensable for NLRP3 inflammasome activation.

3. The role of NEK7 in NLRP3-related diseases (Table 2)

3.1. NLRP3-related diseases and the regulation mechanism of NLRP3 inflammasome activation

Among the currently known inflammasomes, the nucleotide-binding oligomerization domain (NOD) and leucine-rich repeat pyrin (LRR) 3 domain (NLRP3) inflammasome are most widely studied (*37*). NLRP3 contains a pyrin domain at the N-terminus (PYD), a LRR at the C-terminus and the intermediate nucleotide triphosphatase domain (NACTH) mediated oligomerization (*37,38*). NLRP3 scaffold, apoptosis-

Table2. The role of NEK7 in NLRP3-related diseases

	Tumor	Inflammatory diseases	Autoimmune diseases	*Ref*
Research in animal model or in humans	MCC950 blocks the interaction between NEK7 and NLRP3. MCC950 inhibits the activation of NLRP3 inflammasome and IL-1β secretion in mice with head and neck squamous cell carcinoma, as well as enhances anti-tumor immunity.	The downregulation of NEK7 by siRNA inhibits the activation of NLRP3 inflammasome in diabetic retinopathy; MCC950 attenuates high glucose-induced retinal endothelial cell dysfunction by disrupting the binding of NEK7 to NLRP3.	The expression of NEK7-NLRP3 complex may play a protective role in the pathogenesis of systemic lupus erythematosus and is negatively correlated with disease activity; NEK7 interacts with NLRP3 to modulate the pyroptosis in inflammatory bowel disease *via* NF-κB signaling	*12, 14, 60, 93-95*
Pathways	NEK7 has been proved to be involved in the activation of NLRP3 inflammasome in several pathways , such as ROS signaling, potassium efflux, lysosomal destabilization, and NF-κB signaling			

associated speck-like protein (ASC) and pro-caspase-1 are assembled into the NLRP3 inflammasome, activated caspase-1 induces secretion, the maturation of IL-1β and IL-18 as well as the induction of pyroptosis (*39,40*).

The activation of NLRP3 inflammasome requires two steps. The priming signal enhances the production of NLRP3 and pro-IL-1β through the nuclear factor NF-κB pathway (*41*). The second signal is inflammasome activation, where caspase-1 induces the maturation of IL-1β and IL-18 for secretion, as well as pyroptosis (*42*). The exact mechanism of activating NLRP3 inflammasome remains unclear. Inactive NLRP3 inflammasome may be induced by Potassium (K^+) efflux (*43*), increased intracellular Ca^{2+}, decreased cellular cyclic AMP (cAMP) (*44*), oxidized mitochondrial DNA release (mtDN) (*45*), lysosomal destabilization, mitochondrial dysfunction as well as oxygen species(ROS) production (*46,47*).

Recently, NEK7 has been proved to be involved in the activation of NLRP3 inflammasome in several pathways, such as ROS signaling, potassium efflux, lysosomal destabilization, and NF-κB signaling (*18*). Researchers have made significant observations on the regulation of gene transcription or protein expression of NLRP3 inflammasome signaling pathway by NEK7 in NLRP3-related diseases, including tumors, inflammatory diseases, and autoimmune diseases, such as squamous cell carcinoma of head and neck (*11*), hepatocellular carcinoma (*13*), diabetic retinopathy (12), systemic lupus erythematosus (*14*), gout, atherosclerosis, type 2 diabetes, metabolic syndrome, age related macular degeneration, Alzheimer's disease, multiple sclerosis, and inflammatory bowel disease. (*15,18*)

3.2.1. NEK7 and tumors

Chronic inflammation plays a significant role in the occurrence and development of cancer (*48,49*). The tumor microenvironment contains many different inflammatory cells and mediators. Tumor pro-inflammation is considered to be one of the favorable features for cancer development. Both inflammation and innate immunity are essential causes of cancer (*50*). Numerous studies have shown that NLRP3 inflammasome is involved in the progression of liver failure and liver disease (*51-53*). The down-regulation of NLRP3 inflammasome in liver cancer inhibits the proliferation and metastasis of hepatoma cells (*13,54*). The activation of NLRP3 inflammasome leads to severe hepatic inflammation and fibrosis, and induces hepatocellular carcinoma apoptosis and pyroptosis (*55-57*).

Delayed cell cycle progression in knockout of NEK7 in head and neck squamous cell carcinoma suggests that NEK7 may play an important role in development of squamous cell carcinoma of head and neck through mitosis (*58*). NLRP3 is upregulated in head and neck squamous cell carcinoma as well as delays tumorigenesis in head and neck squamous cell carcinoma mice by reducing IL-1β secretion (*11,59*). MCC950 blocks interaction between NEK7 and NLRP3. MCC950 inhibits activation of NLRP3 inflammasome and IL-1β secretion in mice with head and neck squamous cell carcinoma, as well as enhances anti-tumor immunity (*60*). The combination of MCC950+oATP does not induce cell death in normal cells, yet it can specifically kill cancer cells of head and neck squamous cell carcinoma without harming normal cells (*59*). Kooi *et al.* (*25*) indicated that NEK7 expression is generally up-regulated in retinoblastoma cell lines when compared to normal retinal pigment epithelial cells. Downregulation of NEK7 inhibits cell proliferation by inducing cell cycle arrest in retinoblastoma cells (*61*).

3.2.2. NEK7 and inflammatory diseases

Diabetic retinopathy is a highly specific neurovascular complication associated with inflammation which can cause severe visual impairment or even blindness (*62,63*). NLRP3, caspase-1 and IL-18 levels are significantly elevated in patients with diabetic retinopathy (*63,64*). NLRP3 inflammasome plays a vital role in the late stage of diabetic retinopathy in Akimba Mice (*65*). Limiting IL-1β affects retinal microglial activation and proliferation, which may affect neurological changes in diabetic patients (*66*). Downregulation of NEK7 by

siRNA inhibits the activation of NLRP3 inflammasome in diabetic retinopathy, and MCC950 attenuates high glucose-induced retinal endothelial cell dysfunction by disrupting the binding of NEK7 to NLRP3 (*12*). The pulmonary ischemia-reperfusion injury is characterized by acute aseptic inflammation, alveolar damage and vascular permeability (*67*). Studies have shown that MCC950 significantly reduces the lung ischemia-reperfusion injury by blocking the interaction between some NEK7-NLRP3 (*65*). The mice deficient in NLRP3 inflammasome can regulate the inflammation of lung ischemia-reperfusion injury by reducing IL-1β production (*68*). Ozone protects lung from lung ischemia-reperfusion by reducing NRP3 and alleviating lung damage caused by oxidative stress and inflammation (*69*).

3.2.3. NEK7 and autoimmune diseases

Autoimmune diseases are characterized by excessive immune responses that cause damage and dysfunction in specific organs or tissues (*70*). Although the treatment of the disease continues to strengthen, the prognosis of most patients is not satisfactory. Therefore, new targets for clinical treatment are urgently sought. Current study finds that the expression of NEK7-NLRP3 complex may play a protective role in the pathogenesis of systemic lupus erythematosus and is negatively correlated with disease activity (*14*). With the progression of lupus nephritis, NLRP3 gene expression is significantly increased in MRL/lpr mice and inhibiting the activation of NLRP3 inflammasome in MRL/lpr mice can reduce lupus nephritis (*71,72*). Mice lacking caspase-1 are resistant to systemic lupus erythematosus-associated vascular injury (*73*). Improvement of survival and proteinuria in IL-18-deficient MRL/lpr mice or MRL/lpr is seen in mice treated with anti-IL-18 (*74*). The serum IL-18 levels are positively correlated with the lupus nephritis disease activity (*75*).

Although the specific cause of inflammatory bowel disease remains unclear, studies have shown that NLRP3 inflammasome plays a key role in the development of chronic intestinal inflammation, and the secretion of IL-1β and IL-18 is positively correlated with the colitis disease activity (76,77). Existing studies find the NEK7 mRNA, protein expression and cell-cause-related factors, including Caspase-1 (p45, p20), NLRP3 and GSDMD in inflammatory bowel disease. Currently, our study demonstrates the relationship between NEK7 and inflammatory bowel disease. Our research found that NEK7 interacts with NLRP3 to modulate the pyroptosis in inflammatory bowel disease *via* NF-κB signaling.

4. Mechanism and regulation of NEK7-NLRP3 inflammasome activation

4.1. The mechanism of NEK7 regulating the activation of NLRP3 inflammasome (Figure 2)

Although there is abundant evidence that the activation of NLRP3 inflammasome regulates inflammatory diseases, its upstream regulatory mechanism remains unclear. Recent studies have shown that NEK7 can directly regulate the activation of NLRP3 inflammasome (*78-80*). The N-terminal region of NEK7 interacts with the C-terminal leucine-rich repeats (LRRs) and the nucleotide-binding domain (NOD) of NLRP3 (*78,80*). NEK7 plays a key role in the reduction of microtubule dynamic stability during interphase and phosphorylation of α- and β-tubulin *in vitro*. Acetylated α-tubulin mediates the dynein-dependent transport of mitochondria as well as the subsequent apposition of ASC on mitochondria to NLRP3 on the endoplasmic reticulum. The integrity of the cellular microtubule network is crucial for the activation of NLRP3 inflammasome (*81,82*). The increase of α-tubulin acetylation in NEK7-knockout cells indicates that NEK7 is involved in microtubule acetylation during the activation of NLRP3 inflammasome. All these results indicate a close correlation between NEK7 and NLRP3 inflammasome.

Although NEK7 is related to NLRP3 inflammasome, the exact mechanism between NEK7 and NLRP3 still remains unknown. K^+ efflux is essential for inducing the activation of NLRP3 inflammasome through multiple stimuli. The assembly of NLRP3 inflammasome can be activated by a variety of exogenous stimuli, including nigericin, gramicidin, extracellular ATP, pore-forming protein toxins, and so forth. These NLRP3-activated stimuli directly disrupt the permeability of plasma membrane to K^+ and reduce $[K^+]$ in the cytoplasmic membrane (*83*). Recent results indicate that Nek7 is an essential mediator of NLRP3 activation downstream of K^+ efflux (*78*). Nek7 deficiency mice result in reduced IL-1β secretion, attenuated recruitment of immune cells and decreased disease severity when compared to wild-type mice (*78,80*). Nek7 binds to the NLRP3 LRRs in a kinase-independent manner downstream from the induction of mitochondrial ROS (*49,80*). ROS is a mediator that activates the binding of NEK7 and NLRP3 (*84*). Chloride intracellular channels (CLIC) act downstream of the K^+ efflux-mitochondrial ROS axis to promote the activation of NLRP3 inflammasome, and the CLICs-dependent chloride efflux is indispensable for the activation of NLRP3 inflammasome (*85*).

4.2. NEK7 as a switch for mitosis and NLRP3 inflammasome activation

Under homeostasis conditions, NEK7 appears to be in a low activity status. Nevertheless, when homeostasis is disturbed, NEK7 will show abnormal expression (*18*). The abnormal expression of NEK7 induces the production of abnormal cells, including apoptotic cells and multinucleate cells which are closely related to mitosis and inflammation (*58,80*). NEK7 is involved in the formation of microtubule structures

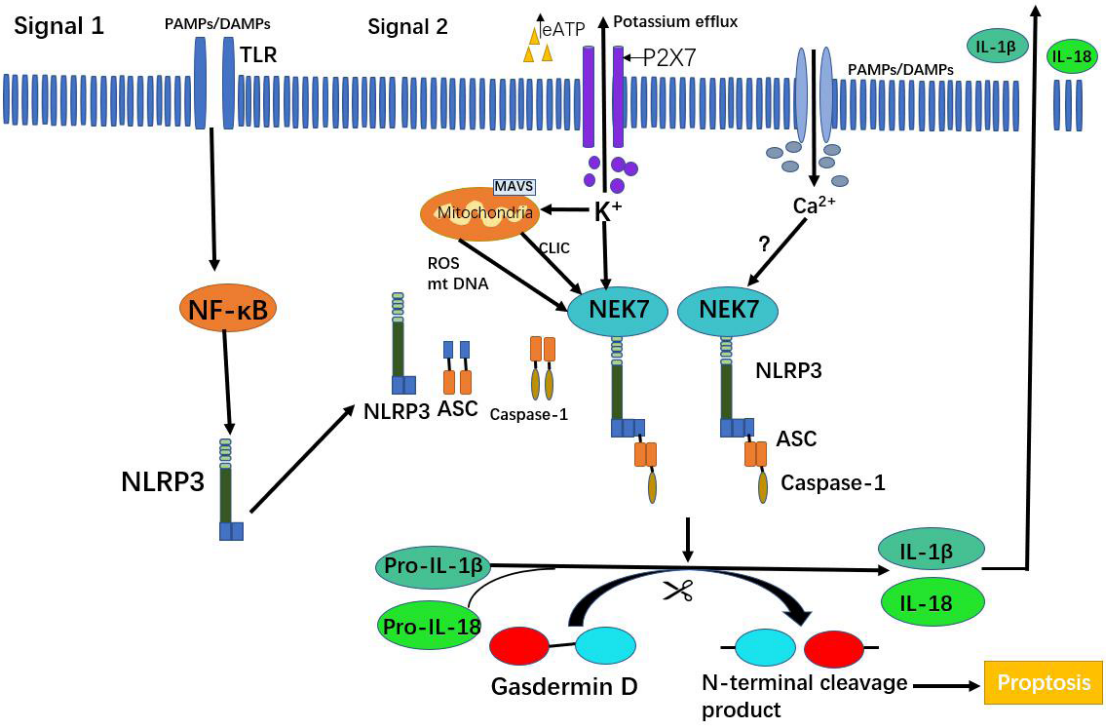

Figure 2. The mechanism of NEK7 regulating the activation of NLRP3 inflammasome. The Priming of signal 1 is mediated by the NF-κB-activating pathways, such as the Toll-like receptor (TLR) family. This signal cascade induces the expression of the functional NLRP3 inflammasome components. In signal 2, including K^+ efflux through ion channels and mitochondrial perturbations leads to the production and release of mitochondrial ROS and CLIC into the cytosol. The mammalian Nek7 activates NLRP3 and then promotes NLRP3 oligomerization and inflammasome assembly. The adaptor protein ASC is recruited to the inflammasome and nucleates into prion-like filaments. Caspase-1 is recruited by ASC and oligomerizes along the ASC filaments, leading to the autoproteolytic activation of caspase-1. Subsequently, active caspase-1 promotes the proteolytic cleavage and maturation of pro-IL-1β and pro-IL-18 into the biologically active IL-1β and IL-18. Caspase-1 also promotes the cleavage of gasdermin D to generate an N-terminal cleavage product that oligomerizes at the plasma membrane, causing the formation of pyroptotic pores. These pores disrupt the integrity of the cellular plasma membrane, and might contribute to the release of inflammatory mediators, including IL-1β and IL-18.

as well as the regulation of microtubule dynamic stability during interphase (*86,87*). The microtubules-mediated assembly and the activation of the NLRP3 inflammasome (*81,82*), and the NEK7-NLRP3 interaction are related to microtubule polymerization. Besides, NEK7 is required for the activation of both mitosis and NLRP3 inflammasome (*49,80*). The levels of acetylated α-tubulin are similar in NEK7-deficient and NEK7-sufficient macrophages, which suggests that NEK7 does not activate NLRP3 inflammasome by regulating the microtubule dynamics signals during mitosis (*49,80*). Nek6 and Nek9 are not associated with the activation of NLRP3 inflammasome. Thus, the activation of NLRP3 inflammasome is not associated with NEK7 kinase activity (*78*). The amount of NEK7 binding to NLRP3 in interphase is more than mitosis. Hence, the amount of NEK7 can only support mitosis or the activation of NLRP3 inflammasome (*80*). NEK7 acts as a cell switch during mitosis to avoid ineffective or potentially harmful inflammatory reactions (*80*). The expression of NEK7 in liver cancer is significantly higher than that in normal liver tissue, and the 5-year survival rate of patients with high expression of NEK7 is significantly lower (*88*). It is suggested that NEK7 may regulate the proliferation and metastasis of hepatoma cells by regulating the activation of NLRP3 inflammasome.

5. Discussion and future perspectives

As various diseases are linked to NLRP3-induced pyroptosis and IL-1β/18 secretion. IL-1β and IL-18 inhibitors have been widely used to disturb the related signaling pathways (*89-91*). Reported inhibitors include IL-1β blockade (neutralizing IL-1β antibody canakinumab, recombinant IL-1 receptor antagonist anakinra, the soluble decoy IL-1 receptor rilonacept), IL-18 blockade (GSK1070806), targeting inflammasome constituents (Parthenolide, Bay 11-7082, β-Hydroxybutyrate, VX-740 and VX-765), indirect NLRP3 inhibitors (Glyburide, 16673-34-0, JC124, FC11A-2), ASC inhibitors (cysteinyl leukotriene receptor antagonist), and P2X7 antagonists (AZD9056). (*92-93*) However, these inhibitors just disturb the signaling pathways of NLRP3 Inflammasome activation rather than directly regulate NLRP3 to abolish the inflammation response. Furthermore, inhibitors aimed at IL-1β or IL-18 can result in unintentional immunosuppressive effects. Therefore, inhibitors targeting the NLRP3 inflammasome only may be

a better option for treatment of NLRP3-associated diseases.

Until now, there are some reported direct inhibitors of NLRP3 Protein, including MCC950, 3,4-Methylenedioxy-β-nitrostyrene, CY-09, Tranilast, and Oridonin. Among these inhibitors, oridonin binds to cysteine 279 of NLRP3 to abolish NLRP3-NEK7 interaction, and then blocks the activation of NLRP3 inflammasome (*94*).

Based on the knowledge of available structure of NLRP3, future studies should focus on the development of structure-guided direct inhibitors and inhibitors, which may regulate NLRP3 to abolish the inflammation response. Recent research has made great progress in the mechanism of NEK7 in the activation of mitosis and NLRP3 inflammation. NLRP3-induced pyroptosis has been reported, and our own research also found that NEK7 interacts with NLRP3 to modulate the pyroptosis in inflammatory bowel disease *via* NF-κB signaling (*95*). Inhibitors focused on NEK7 may regulate NLRP3 to abolish the inflammation response with improved specificity and potency (*18*).

The source of NEK7 activation and regulation remains unclear. Understanding the molecular mechanisms of NEK7 assembly and activation may lead to novel therapeutic targets to formulate therapies in the treatment of NLRP3-related diseases.

Acknowledgement

This study was supported by the National Natural Science Foundation of China (81970493).

References

1. Laurent P, Sisirak V, Lazaro E, Richez C, Duffau P, Blanco P, Truchetet ME, Contin-Bordes C. Innate Immunity in Systemic Sclerosis Fibrosis: Recent Advances. Front Immunol. 2018; 9:1702.
2. Latz E, Xiao T S, Stutz A. Activation and regulation of the inflammasomes. Nat Rev Immunol. 2013; 13:397-411.
3. Martinon F, Mayor A, Tschopp J. The inflammasomes: guardians of the body. Annu Rev Immunol. 2009; 27:229-265.
4. Ahn H, Kang S G, Yoon SI, Kim P, Kim D, Lee G. Poly-gamma-glutamic acid from Bacillus subtilis upregulates pro-inflammatory cytokines while inhibiting NLRP3, NLRC4 and AIM2 inflammasome activation. Cell Mol Immunol. 2018; 15:111-119.
5. Orlowski G M, Sharma S, Colbert JD, Bogyo M, Robertson SA, Kataoka H, Chan FK, Rock KL. Frontline Science: Multiple cathepsins promote inflammasome-independent, particle-induced cell death during NLRP3-dependent IL-1beta activation. J Leukoc Biol. 2017; 102:7-17.
6. Yang J, Liu Z, Xiao TS. Post-translational regulation of inflammasomes. Cell Mol Immunol. 2017; 14:65-79.
7. Shi J, Zhao Y, Wang K, Shi X, Wang Y, Huang H, Zhuang Y, Cai T, Wang F, Shao F. Cleavage of GSDMD by inflammatory caspases determines pyroptotic cell death. Nature. 2015; 526 660-665.
8. Kayagaki N, Stowe IB, Lee B L, *et al*. Caspase-11 cleaves gasdermin D for non-canonical inflammasome signalling. Nature. 2015; 526:666-671.
9. He WT, Wan H, Hu L, Chen P, Wang X, Huang Z, Yang ZH, Zhong CQ, Han J. Gasdermin D is an executor of pyroptosis and required for interleukin-1beta secretion . Cell Res. 2015; 25:1285-1298.
10. Karki R, Man SM, Kanneganti TD. Inflammasomes and Cancer. Cancer Immunol Res. 2017; 5: 94-99.
11. Huang CF, Chen L, Li YC, Wu L, Yu GT, Zhang WF, Sun ZJ. NLRP3 inflammasome activation promotes inflammation-induced carcinogenesis in head and neck squamous cell carcinoma. J Exp Clin Cancer Res. 2017; 36:116.
12. Zhang Y, Lv X, Hu Z, Ye, X, Liu, Q. Protection of Mcc950 against high-glucose-induced human retinal endothelial cell dysfunction. Cell Death Dis. 2017; 8:e2941.
13. Wei Q, Mu K, Li T, Zhang Y, Yang ZW, Jia XQ, Zhao W, Huai WW, Guo PB, Han LH. Deregulation of the NLRP3 inflammasome in hepatic parenchymal cells during liver cancer progression. Lab Invest. 2014; 94:52-62.
14. Ma ZZ, Sun HS, Lv JC, Guo L, Yang QR. Expression and clinical significance of the NEK7-NLRP3 inflammasome signaling pathway in patients with systemic lupus erythematosus. J Inflamm (Lond). 2018; 15:16.
15. Lazaridis L D, Pistiki A, Giamarellos-Bourboulis EJ, Georgitsi M, Damoraki G, Polymeros D, Dimitriadis G D, Triantafyllou K. Activation of NLRP3 Inflammasome in Inflammatory Bowel Disease: Differences Between Crohn's Disease and Ulcerative Colitis . Dig Dis Sci. 2017; 62:2348-2356.
16. Oakley BR, Morris NR. A mutation in Aspergillus nidulans that blocks the transition from interphase to prophase. J Cell Biol. 1983; 96:1155-1158.
17. Fry AM, O'Regan L, Sabir SR, Bayliss R. Cell cycle regulation by the NEK family of protein kinases. J Cell Sci. 2012; 125:4423-433.
18. Xu J, Lu L, Li L. NEK7: a novel promising therapy target for NLRP3-related inflammatory diseases. Acta Biochim Biophys Sin (Shanghai). 2016; 48:966-968.
19. De Souza EE, Meirelles GV, Godoy BB, Perez AM, Smetana JHC, Doxsey SJ, McComb ME, Costello CE, Stephen A, Whelan SA, Kobarg J. Characterization of the human NEK7 interactome suggests catalytic and regulatory properties distinct from those of NEK6. J Proteome Res. 2014; 13:4074-4090.
20. Loncarek J, Hergert P, Magidson V, Khodjakov A. Control of daughter centriole formation by the pericentriolar material. Nat Cell Biol. 2008; 10:322-328.
21. Tan R, Nakajima S, Wang Q, Sun H, Xue J, Wu J, Hellwig S, Zeng XM, Yates N A, Smithgall T E, Lei M, Jiang Y, Levine A S, Su B, Lan L. Nek7 Protects Telomeres from Oxidative DNA Damage by Phosphorylation and Stabilization of TRF1. Mol Cell. 2017; 65:818-31 e5.
22. Haq T, Richards MW, Burgess SG, Gallego P, Yeoh S, O'Regan L, Reverter D, Roig J, Fry AM, Bayliss R. Mechanistic basis of Nek7 activation through Nek9 binding and induced dimerization. Nat Commun. 2015; 6:8771.
23. Fry AM, Bayliss R, Roig J. Mitotic Regulation by NEK Kinase Networks. Front Cell Dev Biol. 2017; 5:102.
24. Cullati SN, Kabeche L, Kettenbach AN, Gerber SA. A

bifurcated signaling cascade of NIMA-related kinases controls distinct kinesins in anaphase. J Cell Biol. 2017; 216:2339-2354.
25. Kooi IE, Mol BM, Massink MP, de Jong MC, de Graaf P, van der Valk P, Meijers-Heijboer H, Kaspers GJ, Moll AC, Te Riele H, Cloos J, Dorsman JC. A Meta-Analysis of Retinoblastoma Copy Numbers Refines the List of Possible Driver Genes Involved in Tumor Progression. PLoS One. 2016; 11:e0153323.
26. Gupta A, Tsuchiya Y, Ohta M, Shiratsuchi G, Kitagawa D.. NEK7 is required for G1 progression and procentriole formation. Mol Biol Cell. 2017; 28:2123-2134.
27. Salem H, Rachmin I, Yissachar N, Cohen S, Amiel A, Haffner R, Lavi L, Motro B. Nek7 kinase targeting leads to early mortality, cytokinesis disturbance and polyploidy. Oncogene. 2010; 29:4046-4057.
28. O'Regan L, Blot J, Fry A M. Mitotic regulation by NIMA-related kinases. Cell Div. 2007; 2:25.
29. Meirelles GV, Silva JC, Mendonça Yde A, Ramos H, Torriani IL, Kobarg J. Human Nek6 is a monomeric mostly globular kinase with an unfolded short N-terminal domain. BMC Struct Biol. 2011; 11:12.
30. Richards MW, O'Regan L, Mas-Droux C, M.Y.Blot J, Cheung J, Hoelder S, M.Fry A, Bayliss R. An autoinhibitory tyrosine motif in the cell-cycle-regulated Nek7 kinase is released through binding of Nek9. Mol Cell. 2009; 36:560-570.
31. Moraes EC, Meirelles GV, Honorato RV, de Souza Tde A, de Souza EE, Murakami MT, de Oliveira PS, Kobarg J. Kinase inhibitor profile for human nek1, nek6, and nek7 and analysis of the structural basis for inhibitor specificity. Molecules. 2015; 20:1176-1191.
32. Rapley J, Nicolàs M, Groen A, Regué L, Bertran MT, Caelles C, Avruch J, Roig J. The NIMA-family kinase Nek6 phosphorylates the kinesin Eg5 at a novel site necessary for mitotic spindle formation. J Cell Sci. 2008. 121:3912-3921.
33. Bertran MT, Sdelci S, Regué L, Avruch J, Caelles C, Roig J. Nek9 is a Plk1-activated kinase that controls early centrosome separation through Nek6/7 and Eg5. EMBO J. 2011; 30:2634-2647.
34. Freixo F, Martinez Delgado P, Manso Y, Sánchez-Huertas C, Lacasa C, Soriano E, Roig J , Lüders J. NEK7 regulates dendrite morphogenesis in neurons *via* Eg5-dependent microtubule stabilization. Nat Commun. 2018; 9:2330.
35. Van Hauwermeiren F, Lamkanfi M. The NEK-sus of the NLRP3 inflammasome. Nat Immunol. 2016; 17: 223-224.
36. Prosser SL, O'Regan L, Fry AM. Novel insights into the mechanisms of mitotic spindle assembly by NEK kinases. Mol Cell Oncol. 2016;3:e1062952.
37. Shen HH, Yang YX, Meng X, Luo XY, Li XM, Shuai ZW, Ye DQ, Pan HF. NLRP3: A promising therapeutic target for autoimmune diseases. Autoimmun Rev. 2018; 17: 694-702.
38. Jiang D, Chen S, Sun R, Zhang X, Wang D. The NLRP3 inflammasome: Role in metabolic disorders and regulation by metabolic pathways. Cancer Lett. 2018; 419:8-19.
39. Liu X, Zhang Z, Ruan J, Pan Y, Magupalli VG, Wu H, Lieberman J. Inflammasome-activated gasdermin D causes pyroptosis by forming membrane pores. Nature. 2016; 535:153-158.
40. Davidson S, Steiner A, Harapas CR, Masters SL. An Update on Autoinflammatory Diseases: Interferonopathies. Curr Rheumatol Rep. 2018; 20:38
41. Bauernfeind FG, Horvath G, Stutz A, Alnemri ES, MacDonald K, Speert D, Fernandes-Alnemri T, Wu J, Monks BG, Fitzgerald KA, Hornung V, Latz E. Cutting edge: NF-kappaB activating pattern recognition and cytokine receptors license NLRP3 inflammasome activation by regulating NLRP3 expression. J Immunol. 2009; 183:787-791.
42. Shi J, Gao W, Shao F. Pyroptosis: Gasdermin-Mediated Programmed Necrotic Cell Death. Trends Biochem Sci. 2017; 42:245-254.
43. Gross C J, Mishra R, Schneider K S, *et al*. K^+ Efflux-Independent NLRP3 Inflammasome Activation by Small Molecules Targeting Mitochondria. Immunity. 2016; 45:761-773.
44. Lee GS, Subramanian N, Kim AI, Aksentijevich I, Goldbach-Mansky R, Sacks DB, Germain RN, Kastner DL, Chae JJ. The calcium-sensing receptor regulates the NLRP3 inflammasome through Ca^{2+} and cAMP. Nature. 2012; 492:123-127.
45. Ding Z, Liu S, Wang X, Dai Y, Khaidakov M, Deng X, Fan Y, Xiang D, Mehta JL. LOX-1, mtDNA damage, and NLRP3 inflammasome activation in macrophages: implications in atherogenesis. Cardiovasc Res. 2014; 103:619-628.
46. Minutoli L, Puzzolo D, Rinaldi M, Irrera N, Marini H, Arcoraci V, Bitto A, Crea G, Pisani A, Squadrito F, Trichilo V, Bruschetta D, Micali A, Altavilla D. ROS-Mediated NLRP3 Inflammasome Activation in Brain, Heart, Kidney, and Testis Ischemia/Reperfusion Injury. Oxid Med Cell Longev. 2016; 2016: 2183026.
47. Rovira-Llopis S, Apostolova N, Bañuls C, Muntané J, Rocha M, Victor VM. Mitochondria, the NLRP3 Inflammasome, and Sirtuins in Type 2 Diabetes: New Therapeutic Targets. Antioxid Redox Signal. 2018; 29:749-91.
48. Cerwenka A, Lanier L L. Natural killer cell memory in infection, inflammation and cancer. Nat Rev Immunol. 2016; 16:112-23.
49. Zhong Z, Sanchez-lopez E, Karin M. Autophagy, Inflammation, and Immunity: A Troika Governing Cancer and Its Treatment. Cell. 2016; 166:288-98.
50. Crusz S M, Balkwill F R. Inflammation and cancer: advances and new agents. Nat Rev Clin Oncol. 2015; 12:584-96.
51. Ganz M, Csak T, Nath B, Szabo G. Lipopolysaccharide induces and activates the Nalp3 inflammasome in the liver. World J Gastroenterol. 2011. 17:4772-8.
52. Kim SJ, Lee SM. NLRP3 inflammasome activation in D-galactosamine and lipopolysaccharide-induced acute liver failure: role of heme oxygenase-1. Free Radic Biol Med. 2013; 65:997-1004.
53. Imaeda AB, Watanabe A, Sohail MA, Mahmood S, Mohamadnejad M, Sutterwala FS, Flavell RA, Mehal WZ. Acetaminophen-induced hepatotoxicity in mice is dependent on Tlr9 and the Nalp3 inflammasome. J Clin Invest. 2009; 119:305-14.
54. Fan SH, Wang YY, Lu J, Zheng YL, Wu DM, Li MQ, Hu B, Zhang ZF, Cheng W, Shan Q. Luteoloside suppresses proliferation and metastasis of hepatocellular carcinoma cells by inhibition of NLRP3 inflammasome. PLoS One. 2014; 9:e89961.
55. Wei Q, Guo P, Mu K, Zhang Y, Zhao W, Huai W, Qiu Y, Li T, Ma X, Liu Y, Chen X, Han L. Estrogen suppresses hepatocellular carcinoma cells through ERbeta-mediated upregulation of the NLRP3 inflammasome. Lab Invest. 2015; 95:804-816.

56. Wan L, Yuan X, Liu M, Xue B. miRNA-223-3p regulates NLRP3 to promote apoptosis and inhibit proliferation of hep3B cells. Exp Ther Med. 2018; 15:2429-2435.
57. Wree A, Eguchi A, McGeough MD, Pena CA, Johnson CD, Canbay A, Hoffman HM, Feldstein AE. NLRP3 inflammasome activation results in hepatocyte pyroptosis, liver inflammation, and fibrosis in mice. Hepatology. 2014; 59:898-910.
58. Saloura V, Cho HS, Kiyotani K, Alachkar H, Zuo Z, Nakakido M, Tsunoda T, Seiwert T, Lingen M, Licht J, Nakamura Y, Hamamoto R. WHSC1 promotes oncogenesis through regulation of NIMA-related kinase-7 in squamous cell carcinoma of the head and neck. Mol Cancer Res. 2015; 13:293-304.
59. Bae JY, Lee SW, Shin YH, Lee JH, Jahng JW, Park K. P2X7 receptor and NLRP3 inflammasome activation in head and neck cancer. Oncotarget. 2017; 8:48972-48982.
60. Chen L, Huang CF, Li YC, Deng WW, Mao L, Wu L, Zhang WF, Zhang L, Sun ZJ. Blockage of the NLRP3 inflammasome by MCC950 improves anti-tumor immune responses in head and neck squamous cell carcinoma. Cell Mol Life Sci. 2018; 75:2045-2058.
61. Zhang J, Wang L, Zhang Y. Downregulation of NIMA-related kinase-7 inhibits cell proliferation by inducing cell cycle arrest in human retinoblastoma cells. Exp Ther Med, 2018; 15:1360-1366.
62. Solomon SD, Chew E, Duh EJ, Sobrin L, Sun JK, Vanderbeek BL. Diabetic Retinopathy: A Position Statement by the American Diabetes Association. Diabetes Care. 2017; 40: 412-418.
63. Chen W, Zhao M, Zhao S, Lu Q, Ni L, Zou C, Lu L, Xu X, Guan H, Zheng Z, Qiu Q. Activation of the TXNIP/NLRP3 inflammasome pathway contributes to inflammation in diabetic retinopathy: a novel inhibitory effect of minocycline. Inflamm Res. 2017; 66:157-166.
64. Chen H, Zhang X, Liao N, Mi L, Peng Y, Liu B, Zhang S, Wen F. Enhanced Expression of NLRP3 Inflammasome-Related Inflammation in Diabetic Retinopathy. Invest Ophthalmol Vis Sci. 2018; 59: 978-985.
65. Xu KY, Wu CY, Tong S, Xiong P, Wang SH. The selective Nlrp3 inflammasome inhibitor Mcc950 attenuates lung ischemia-reperfusion injury. Biochem Biophys Res Commun. 2018; 503: 3031-3037.
66. Baptista FI, Aveleira CA, Castilho ÁF, Ambrósio AF. Elevated Glucose and Interleukin-1beta Differentially Affect Retinal Microglial Cell Proliferation. Mediators Inflamm. 2017; 2017:4316316.
67. Laubach VE, Sharma AK. Mechanisms of lung ischemia-reperfusion injury. Curr Opin Organ Transplant. 2016; 21:246-252.
68. Tian X, Sun H, Casbon AJ, Lim E, Francis KP, Hellman J, Prakash A. NLRP3 Inflammasome Mediates Dormant Neutrophil Recruitment following Sterile Lung Injury and Protects against Subsequent Bacterial Pneumonia in Mice. Front Immunol. 2017; 8:1337.
69. Wang Z, Zhang A, Meng W, Wang T, Li D, Liu Z, Liu H. Ozone protects the rat lung from ischemia-reperfusion injury by attenuating NLRP3-mediated inflammation, enhancing Nrf2 antioxidant activity and inhibiting apoptosis. Eur J Pharmacol. 2018; 835:82-93.
70. Ortona E, Pierdominici M, Maselli A, Veroni C, Aloisi F, Shoenfeld Y. Sex-based differences in autoimmune diseases. Ann Ist Super Sanita. 2016; 52: 205-212.
71. Honarpisheh M, Desai J, Marschner JA, Weidenbusch M, Lech M, Vielhauer V, Anders HJ, Mulay SR. Regulated necrosis-related molecule mRNA expression in humans and mice and in murine acute tissue injury and systemic autoimmunity leading to progressive organ damage, and progressive fibrosis. Biosci Rep. 2016; 36: e00425-e00425.
72. Zhang H, Liu L, Li L. Lentivirus-mediated knockdown of FcgammaRI (CD64) attenuated lupus nephritis *via* inhibition of NF-kappaB regulating NLRP3 inflammasome activation in MRL/lpr mice J Pharmacol Sci. 2018; 137: 342-349.
73. Kahlenberg JM, Yalavarthi S, Zhao W, Hodgin JB, Reed TJ, Tsuji NM, Kaplan MJ. An essential role of caspase 1 in the induction of murine lupus and its associated vascular damage. Arthritis Rheumatol. 2014. 66: 152-162.
74. Schirmer B, Wedekind D, Glage S, Neumann D. Deletion of IL-18 Expression Ameliorates Spontaneous Kidney Failure in MRLlpr Mice. PLoS One. 2015. 10: e0140173.
75. Jafari-Nakhjavani MR, Abedi-Azar S, Nejati B. Correlation of plasma interleukin-18 concentration and severity of renal involvement and disease activity in systemic lupus erythematosus. J Nephropathol. 2016; 5:28-33.
76. Liu L, Dong Y, Ye M, Jin S, Yang J, Joosse ME, Sun Y, Zhang J, Lazarev M, Brant SR, Safar B, Marohn M, Mezey E, Li X. The Pathogenic Role of NLRP3 Inflammasome Activation in Inflammatory Bowel Diseases of Both Mice and Humans. J Crohns Colitis. 2017; 11:737-750.
77. Mao L, Kitani A, Strober W, Fuss IJ. The Role of NLRP3 and IL-1beta in the Pathogenesis of Inflammatory Bowel Disease. Front Immunol. 2018; 9:2566.
78. He Y, Zeng MY, Yang D, Motro B, Núñez G. NEK7 is an essential mediator of NLRP3 activation downstream of potassium efflux. Nature. 2016; 530: 354-357.
79. Schmid-Burgk JL, Chauhan D, Schmidt T, Ebert TS, Reinhardt J, Endl E, Hornung V. A Genome-wide CRISPR (Clustered Regularly Interspaced Short Palindromic Repeats) Screen Identifies NEK7 as an Essential Component of NLRP3 Inflammasome Activation. J Biol Chem. 2016; 291: 103-109.
80. Shi H, Wang Y, Li X, *et al*. NLRP3 activation and mitosis are mutually exclusive events coordinated by NEK7, a new inflammasome component. Nat Immunol.2016; 17:250-258.
81. Misawa T, Takahama M, Kozaki T, Lee H, Zou J, Saitoh T, Akira S. Microtubule-driven spatial arrangement of mitochondria promotes activation of the NLRP3 inflammasome. Nat Immunol. 2013; 14:454-460.
82. Li X, Thome S, Ma X, Amrute-Nayak M, Finigan A, Kitt L, Masters L, James JR, Shi Y, Meng G, Mallat Z. MARK4 regulates NLRP3 positioning and inflammasome activation through a microtubule-dependent mechanism. Nat Commun. 2017; 8:15986.
83. Katsnelson MA, Rucker LG, Russo HM, Dubyak GR. K^+ efflux agonists induce NLRP3 inflammasome activation independently of Ca^{2+} signaling. J Immunol. 2015; 194:3937-3952.
84. Weinberg SE, Sena LA, CHANDEL NS. Mitochondria in the regulation of innate and adaptive immunity. Immunity. 2015; 42:406-417.
85. Tang T, Lang X, Xu C, Wang X, Gong T, Yang Y, Cui J, Bai L, Wang J, Jiang W, Zhou R. CLICs-dependent chloride efflux is an essential and proximal upstream event for NLRP3 inflammasome activation. Nat Commun. 2017; 8:202.

86. Cohen S, Aizer A, Shav-Tal Y, Yanai A, Motro B. Nek7 kinase accelerates microtubule dynamic instability. Biochim Biophys Acta. 2013; 1833:1104-1113.
87. Kim S, Lee K, Rhee K. NEK7 is a centrosomal kinase critical for microtubule nucleation . Biochem Biophys Res Commun. 2007; 360:56-62.
88. Zhou L, Wang Z, Xu X, Wan Y, Qu K, Fan H, Chen Q, Sun X, Liu C. Nek7 is overexpressed in hepatocellular carcinoma and promotes hepatocellular carcinoma cell proliferation *in vitro* and in vivo. Oncotarget. 2016; 7:18620-18630.
89. Grebe A, Hoss F, Latz E. NLRP3 Inflammasome and the IL-1 Pathway in Atherosclerosis. Circ Res. 2018; 122: 1722-1740.
90. Tang T, Gong T, Jiang W, Zhou R. GPCRs in NLRP3 Inflammasome Activation, Regulation, and Therapeutics. Trends Pharmacol Sci. 2018; 39: 798-811.
91. Munoz-wolf N, Lavelle EC. A Guide to IL-1 family cytokines in adjuvanticity. FEBS J. 2018; 285: 2377-2401.
92. Sarah D, Ema O, Matthew C. Targeting the NLRP3 inflammasome in chronic inflammatory diseases: current perspectives. J Inflamm Res. 2015; 8:15-27.
93. Zahid A, Li B, Kombe AJK, Jin T, Tao J. Pharmacological Inhibitors of the NLRP3 Inflammasome. Front. Immunol. 2019; 10:2538.
94. He H, Jiang H, Chen Y, Ye J, Wang A, Wang C, Liu Q, Liang G, Deng X, Jiang W, Zhou R. Oridonin is a covalent NLRP3 inhibitor with strong anti-inflammasome activity. Nat Commun. 2018; 9:2550.
95. Chen X, Liu G, Yuan Y, Wu G, Wang S, Yuan L. NEK7 interacts with NLRP3 to modulate the pyroptosis in inflammatory bowel disease *via* NF-κB signaling. Cell Death Dis. 2019; 10:906-918.

Received February 7, 2020; Revised April 2, 2020; Accepted April 9, 2020.

[§]These authors contributed equally to this work.
**Address correspondence to:*
Lianwen Yuan, Department of Geriatric Surgery, The Second Xiangya Hospital, Central South University, 139 # the Renmin Road, Changsha, 410011, Hunan, China.
E-mail: yuanlianwen@csu.edu.cn

Released online in J-STAGE as advance publication April 16, 2020.

Original Article

DOI: 10.5582/bst.2019.01272

Overexpression of DJ-1 enhances colorectal cancer cell proliferation through the cyclin-D1/MDM2-p53 signaling pathway

Xiaojian Zhu[§], Chen Luo[§], Kang Lin[§], Fanqin Bu, Fan Ye, Chao Huang, Hongliang Luo, Jun Huang, Zhengming Zhu[*]

The Second Affiliated Hospital Nanchang University, Nanchang University, Nanchang, Jiangxi, China.

SUMMARY Emerging evidence indicates that DJ-1 is highly expressed in different cancers. It modulates cancer progression, including cell proliferation, cell apoptosis, invasion, and metastasis. However, its role in colorectal cancer (CRC) remains poorly defined. The current study noted increased DJ-1 expression in CRC tumor tissue and found that its expression was closely related to clinical-pathological features. Similarly, DJ-1 increased in CRC cells (SW480, HT-29, Caco-2, LoVo, HCT116, and SW620), and especially in SW480 and HCT116 cells. Functional analyses indicated that overexpression of DJ-1 promoted CRC cell invasion, migration, and proliferation in vitro and in vivo. Mechanistic studies indicated that DJ-1 increased in CRC cell lines, activated specific protein cyclin-D1, and modulated the MDM2/p53 signaling pathway by regulating the levels of the downstream factors Bax, Caspase-3, and Bcl-2, which are related to the cell cycle and apoptosis. Conversely, knockdown of DJ-1 upregulated p53 expression by disrupting the interaction between p53 and MDM2 and inhibiting CRC cell proliferation, revealing the pro-oncogenic mechanism of DJ-1 in CRC. In conclusion, the current findings provide compelling evidence that DJ-1 might be a promoter of CRC cell invasion, proliferation, and migration via the cyclin-D1/MDM2-p53 signaling pathway. Findings also suggest its potential role as a postoperative adjuvant therapy for patients with CRC.

Keywords DJ-1, MDM2, p53, cyclin-D1, proliferation, CRC

1. Introduction

Colorectal cancer (CRC) is a malignancy that is prevalent worldwide. Recent statistics indicate that more than 1 million CRC cases are diagnosed annually. Moreover, the mortality rate of patients with CRC is as high as 33% in developed countries (*1*). In China, the incidence of CRC has risen annually given the changes in people's lifestyles and eating habits (*2*). Despite continuous advancements and improvements in comprehensive treatment of CRC over the past few years, the overall prognosis for CRC is poor, and its five-year survival rate is less than 50% (*3*). This is mainly due to the highly metastatic nature of CRC. Consequently, approximately 90% of CRC-related deaths occur as a result of metastatic disease (*4*). Numerous studies have been conducted to determine the biological (molecular) mechanism of CRC development in its early stages, and many metastasis-related oncogenes and tumor suppressor factors have been discovered (e.g. p53, K-ras, and APC). As an example, tumor invasion and growth is inhibited by targeting the gain-of-function mutant p53 in CRC *via* Stat3. Notably, patients with CRC and stable mutp53 have poorer survival rates and elevated Jak2/Stat3 activity (*5*). Peptidomimetic inhibitors of APC-Asef protein-protein interaction influence the migratory ability of CRC cells (*6*). Most of the prevailing evidence indicates that the presence of the K-ras mutation can predict the survival of patients with CRC (*7,8*). Despite these insights, the molecular pathways of CRC metastasis are diverse and are not well understood. Therefore, further studies are needed to better understand the drivers of CRC metastasis.

Originally, DJ-1 was discovered and named in a mouse NIH3T3 cell transformation study by a Japanese researcher, Nagakubo (*9*). It was described as a new mitogen-dependent oncogene and was found on the short arm of human chromosome 36 site 1 (1p36.12-1p36.33), which encodes the DJ-1 protein. This protein is highly conserved and is formed as a homodimer that is widely expressed in many human tissues. It participates in many pathological and physiological activities in cells, such as transcriptional regulation (*10*), oxidative stress (*11*), cell apoptosis, cell proliferation (*12*), and molecular

chaperoning (*13*). Early studies on DJ-1 mainly focused on its role in Parkinson's syndrome. Results from those studies suggested that a mutation in the DJ-1 gene is strongly linked to Parkinson's disease (of the human autosomal recessive early-onset type). However, DJ-1 was found to promote the transformation of normal immortalized fibroblasts with oncogenes such as H-Ras or c-MYC, so the relationship between DJ-1 and tumors has garnered considerable attention. Experiments have indicated that DJ-1 is overproduced in gastric, liver, pancreatic, and esophageal cancers (*14-17*) and is strongly correlated with the development, progression, and metastasis of and prognosis for numerous digestive system tumors. However, few studies have investigated the clinical value, function, and molecular mechanism of DJ-1 in CRC. Therefore, the current study explored whether DJ-1 participates in the development of CRC. The findings of this study should provide important scientific and clinical knowledge to prevent and treat CRC, and especially new methods and effective interventions for CRC invasion and metastasis.

2. Materials and Methods

2.1. Clinical samples

Ninety pairs of CRC specimens and adjacent nontumor tissue specimens were collected from patients (43 males and 47 females) seen at the Second Hospital Affiliated with Nanchang University from August 2016 to December 2018. Tumor-adjacent tissue was obtained at a distance of more than 5 cm from the periphery of the tumor in the aforementioned patients with CRC. No patient received radiotherapy or chemotherapy prior to surgery. The collected tissues samples were identified as CRC in a pathological examination. Each patient provided informed consent for tissue collection for research purposes (No. 2017[031]).

2.2. Cell preparation

The colorectal carcinoma cell lines SW480, HT29, HCT116, SW620, and LoVo were cultured in DMEM reconstituted with 1% penicillin-streptomycin and 10% North American FBS at 37°C in a humid atmosphere with 5% CO_2. All cells were washed with PBS every day, changed once, and then passaged for 2-3 days. All experiments were performed when the cells reached 75-85% confluence and were in the logarithmic growth phase.

2.3. Stable knockdown and overexpression of DJ-1 in CRC cells

To obtain cells overexpressing DJ-1, HCT116 and SW480 cells were transfected with the lentiviral vector carrying human DJ-1 (Shanghai China). Cells transfected with the empty vector (Mock) served as the negative control. HCT116 and SW480 cells were transfected with lentivirus-mediated control shRNA or shRNA targeting DJ-1, a designated vector, and shDJ-1. The lentivirus-mediated shRNA was obtained from Hanbio Biotechnology (Shanghai, China); specific fragments were inserted into a vector. The sequences used were as follows: vector shRNA, 5′-TTCTCCGAACGTGTCACGT-3′. shRNA-1, 5′-ACTCTGAGAATCGTGTGGAAA-3′ (DJ-1, 412 nt); shRNA-2, 5′-GCGCTTGCAATTGTTGAAGCC-3′ (DJ-1,499 nt); shRNA-3, 5′-GCAATTGTTGAAGCCCTGA AT-3′ (DJ-1, 541 nt).

The cells were subsequently harvested 72 h postinfection and cultured in a medium containing 5 μg/ml puromycin (Sigma, Missouri, USA) until all uninfected cells were killed by puromycin. The stably transfected cell lines were verified with RT-PCR and Western blotting before use in subsequent experiments.

2.4. Cell proliferation assay

SW480 and HCT116 cells in mock/OE-DJ-1 groups and vector/shDJ-1 groups were inoculated onto 6-well plates. When the cell density reached 75%-85%, 100 μL of 10 uM preheated Edu working fluid was pipetted into each well, and cells were cultured at 37°C for 2 h. After EDU labeling, 4% polyformaldehyde was used to fix the cells at room temperature for 15 min. Fifty uL of 2 mg/mL glycine solution was used to quench the reaction for 5 min, 0.3% TriX-100 PBS was incubated for 10 min, and Apollo and Hoechst staining were performed in a stepwise manner. After fluid staining, laser scanning confocal microscopy and photography were performed (Hoechst 33342 emits blue fluorescence).

An anchorage-independent colony formation assay was performed using soft agar growth of 3×10^3 cells for 10-14 days. Cell colonies were counted.

2.5. Analysis of apoptosis

Cells were grouped into: Control groups and a test group with CRC cells treated with shDJ-1-1# and shDJ-1-2# for 48 h followed by staining with Annexin V-FITC/PI (BD Pharmingen, USA). Apoptosis was determined as Annexin V +/PI + (late apoptotic) cells and Annexin V +/PI− (early apoptotic).

2.6. Cell cycle analysis

CRC cells were incubated with shDJ-1 for different time periods. Thereafter, they were fixed with 70% ice-cold ethanol at -20°C for 24 h. Cold PBS was used to wash the cells, which were then cultured with 300 uL of the staining solution (5 U/mL RNaseA and 5 ug/mL PI, BD Pharmingen, USA) for 30 min at 4°C. The results were examined with BD FASCanto II flow cytometry

and assessed with the software ModFitLT 3.2.

2.7. Cell invasion and migration assay

Transwell chambers were pre-coated with Matrigel. Matrigel was pre-cooled at 4°C and then added to cover the bottom of the Transwell chamber. Subsequently, the Transwell chamber was placed in an incubator until the Matrigel solidified, after which it was removed. After digestion and re-suspension, SW480 and HCT116 cells (control group and shDJ-1/OE-DJ-1 group) were inoculated onto the upper layer of the serum-free chamber at a density of 2×10^5/mL, and the lower chamber was filled with 20% FBS medium. After incubation for 24 h, unmigrated cells in the upper chamber were wiped away using a sterile cotton swab. Cells that migrated were examined using crystal violet (0.1%) staining and counted under a microscope (Migration experiment without Matrigel).

2.8. RNA isolation and qRT-PCR

TRIzol reagent (Invitrogen) was added to the samples to isolate total RNA, which was then used to synthesize cDNA with the PrimeScript reverse transcriptase reagent kit (TaKaRa, Shiga, Japan). qRT-PCR was performed to analyze the level of DJ-1, cyclin-D1, and p-MDM2 in patient samples and cell lines (all gene primer sequences are shown in Table 1). mRNA expression was calculated using the $2^{-\Delta\Delta CT}$ method, and the level of expression of target genes was normalized to that of GAPDH expression. All experiments were repeated at least thrice.

2.9. Western blotting

Following successful transfection of cells, cells were obtained at the indicated time-points. They were lysed to obtain total cell proteins. The quantity of protein was assessed with the BCA assay kit (Beyotime Biotechnology, China). Next, 30 μg of protein was separated using SDS-PAGE (concentration of 8% or 10%). Then, the protein was transferred to PVDF membranes. The membranes were treated with primary antibodies: GAPDH and Tubulin served as internal standards (8884s/2128s, CST, 1:1000), DJ-1 (ab18257, Abcam, 1:1000), p53(ab1101, Abcam, 1:1000), p-MDM2 (ab170880, Abcam, 1:5000), MDM2 (ab38618, Abcam, 1:1000), cyclin-D1 (55506T, CST, 1:1000), Bcl-2 (ab32124, Abcam, 1:1000), Bax (ab32503, Abcam, 1:1000), and cleaved caspase-3 (ab2302, Abcam, 1:1000).

2.10. HE and immunohistochemistry

The protein expression in the cancer specimens was determined immunohistochemically (IHC). The samples were from subjects with confirmed CRC who were seen at the Second Hospital Affiliated with Nanchang University from 2016 to 2018. The samples were cultured with p-MDM2 (ab170880, Abcam, 1:50), cyclin-D1 (55506T, CST, 1:500), and DJ-1 (ab18257, Abcam, 1:200) antibodies. The staining intensity of the cancer samples was scored as follows: 3 (strong staining, brown), 2 (moderate staining, yellowish-brown), 1 (weak staining, light yellow), and 0 (no staining). Intensity scores < 2 indicated low expression while intensity scores ≥ 2 indicated overexpression. Stained slides were independently examined by two researchers blinded to the clinical outcomes and patient allocation. Metastatic cancer nodules were confirmed with H&E staining.

Table 1. The sequences for RT-qPCR

GAPDH	
Forward Primer	5'-TGTGGGCATCAATGGATTTGG-3'
Reverse Primer	5'-ACACCATGTATTCCGGGTCAAT-3'
DJ-1	
Forward Primer	5'-AACGCTGAAGCGTCCAGAAT-3'
Reverse Primer	5'-TGACCACATCACGGCTACAC-3'
cyclin-D1	
Forward Primer	5'-CTGATTGGACAGGCATGGGT-3'
Reverse Primer	5'-GTGCCTGGAAGTCAACGGTA-3'
p-MDM2	
Forward Primer	5'-CTGTGTTGAGCCCTCTTCCAT-3'
Reverse Primer	5'-TTCTCCGTCAGGGACACTTC-3'

2.11. *In vivo* experiments

All animal experiments were approved by the Institutional Animal Care and Use Committee of the Second Hospital Affiliated with Nanchang University (No. 2017[028]). SW480 cells transfected with the shRNA/Vector were reconstituted in 100 μL of PBS. The cells were subcutaneously transplanted in 5-week-old female nude mice. Every 7 days, the tumor size was measured with Vernier calipers. The tumor volume was determined as: shortest diameter 2× longest diameter/2 at 7-day intervals post-transplantation. One month after cell implantation, mice were sacrificed and the xenografts specimens were used in Western blotting.

2.12. Statistics and data analysis

Groups were compared using the log-rank test; the Kaplan-Meier method was used to plot patient survival curves. Pearson's correlation test or an unpaired *t*-test was used to compare quantitative variables. Multivariate analysis was performed using the Cox regression model. Linear regression was calculated with the Spearman rank correlation. $P < 0.05$ was regarded as statistically significant.

3. Results

3.1. DJ-1 is upregulated in human CRC cells

To examine the effect of DJ-1 on CRC tissues, its level of expression was compared between 90 pairs of CRC samples and adjacent nontumor tissue samples. In both sets of samples, DJ-1 was largely localized in the cytoplasm, and a higher percentage of cells highly expressed DJ-1 in CRC tissues (62.2%, 56 of 90) compared to the level in adjacent normal tissues (13.3%, 12 of 90) (Figure 1A-B and Table 2). In addition, the level of DJ-1 protein expression was markedly higher in 39 CRC specimens compared to that in normal tissues (Figure 1C-D, $p < 0.01$). RT-qPCR revealed a consistently similar pattern of expression in 39 pairs of CRC samples (66.7%, 26 of 39) and matching normal colon samples (15.4%, 6 of 39), suggesting that DJ-1 mRNA was highly expressed in tumors (Figure 1E-F). In conclusion, these findings imply that levels of DJ-1 protein and mRNA expression were markedly higher in human CRC samples than those in adjacent noncancerous colon samples.

3.2. Increased DJ-1 expression in CRC is related to a poor prognosis and the TNM stage

Further experiments were conducted to explore the relationship between the level of DJ-1 protein and the pathological features of CRC. The results are shown in Tables 3 and 4. The level of DJ-1 expression was lower in samples from patients with early stage cancer than in samples from those with advanced disease (Figure 2A-B). The level of expression was strongly related to the tumor TNM stage ($p = 0.0001$) and lymphatic metastasis ($p = 0.0003$). That said, the level of expression did not differ significantly in terms of tumor histological grade and location (Table 4). Kaplan–Meier survival curves indicated that high levels DJ-1 were inversely correlated with the survival rate (Figure 2C, $p < 0.001$). Thus, the current results indicate that DJ-1 contributes to the

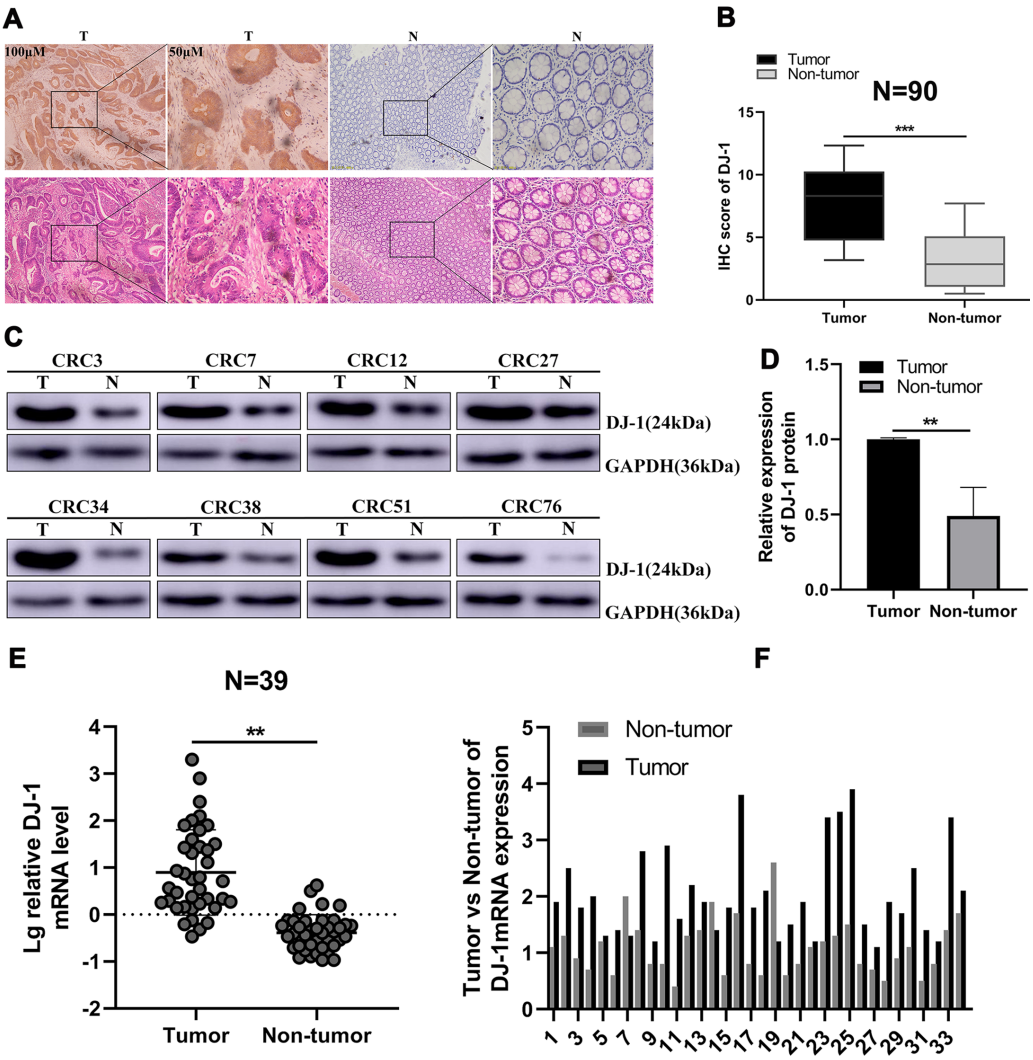

Figure 1. DJ-1 is overexpressed in human CRC tissues. (**A**), Typical IHC and H&E staining images of DJ-1 in normal colon tissue and CRC samples (N: normal colon tissue; T: tumor; scale bar = 100 μM, 50 μM); (**B**), IHC scores for 90 pairs of normal and CRC samples; (**C**), Typical Western blot indicating DJ-1 expression (N: normal colon tissue; T: tumor); (**D**), DJ-1 protein levels in CRC tumor tissues and matching adjacent normal tissues were determined with Western blotting; (**E**), Level of DJ-1 mRNA in39 paired CRC and adjacent normal specimens; (**F**), Ratio of expression (DJ-1/GAPDH) for each the 39 paired CRC and normal specimens. ($^{**}p < 0.01$, $^{***}p < 0.001$).

progression of CRC and is closely related to a poor prognosis.

3.3. Knockdown and overexpression of DJ-1 in CRC cell lines

The baseline level of DJ-1 was measured with Western blotting and RT-qPCR in 6 CRC cell lines: SW480, HT-29, Caco-2, LoVo, HCT116, and SW620. DJ-1 increased particularly in the HCT116 and SW480 cell lines (Figure 3A-B). Therefore, HCT116 and SW480 cells were selected to construct stably transfected cell lines with lentivirus-mediated shRNA targeting DJ-1 to knockdown DJ-1 expression. Transfection efficiency was verified with Western blotting. Silencing efficiency was 82.64% in SW480 cells and 85.26% in HCT116 cells (Figure 3C-D). Analysis was performed with ImageJ. mRNA levels consistently indicated a similar level of silencing efficiency; the mRNA level was reduced by 58.13% in SW480 cells and by 61.92% in HCT116 cells (Figure 3E).

3.4. DJ-1 enhances the invasion, proliferation, and migration of CRC cells

To assess the impact of DJ-1 on the progression of CRC, DJ-1 was knocked down or overexpressed in SW480 and HCT116 cells (Figure 3C-E). Results indicated that SW480 and HCT116 cells with knocked down DJ-1 invaded and migrated into the lower chamber at a slower rate than the vector groups (Figure 4C-F, 24h, $p < 0.05$; 48, $p < 0.01$). After transfection with OE-DJ-1, there were more migrating and invading CRC cells compared to the number in mock cells (Figure 4C-F, $p < 0.001$). Similar findings were noted in HCT116 cells. The role of DJ-1 in the development of colon cancer was evaluated. Results revealed that DJ-1 inhibition decreased the growth of colon cancer cells while DJ-1 overexpression significantly facilitated their growth and proliferation (Figure 4A-B, $p < 0.05$). In addition, DJ-1 regulation of

Table 2. DJ-1 levels in CRC and adjacent nontumor tissues

	DJ-1 (High)	DJ-1 (Low)	*p* value
Tumor	62	28	$p < 0.001$
Adjacent nontumor tissue	12	78	

Table 3. The clinical characteristics of the CRC samples used in this study

Feature	WHO grade		
	I ($n = 6$)	II ($n = 43$)	III ($n = 41$)
Gender			
Male	2	22	19
Female	4	21	22
Age at diagnosis			
< 65	1	2	7
≥ 65	5	41	34
Depth of invasion			
Submucosa	1	2	1
Muscular layer	1	3	9
Serous layer	2	31	20
Every layer	2	7	11
Location			
Transverse colon	2	3	7
Ascending colon	0	1	5
Descending colon	1	17	14
Sigmoid colon	3	12	16

Table 4. The correlation of DJ-1 expression and clinical-pathological characteristics of CRC

Group	Expression of DJ-1 protein		
	DJ-1 (High, $n = 62$)	DJ-1 (Low, $n = 28$)	*p* value
Age at diagnosis			0.733
< 65	13 (21.0%)	5 (17.9%)	
≥ 65	49 (79.0%)	23 (82.1%)	
Gender			0.626
Male	30 (48.4%)	12 (42.9%)	
Female	32 (51.6%)	16 (57.1%)	
Location			0.929
Transverse colon	12 (19.4%)	6 (21.4%)	
Ascending colon	10 (16.1%)	5 (17.9%)	
Descending colon	15 (24.2%)	5 (17.9%)	
Sigmoid colon	25 (40.3%)	12 (42.8%)	
Lymph node status			0.0003*
Positive	41 (66.1%)	7 (25.0%)	
Negative	21 (33.9%)	21 (75.0%)	
Histological grade			0.55
Highly/Moderately differentiated	29 (8.3%)	15 (53.6%)	
Poorly differentiated	33 (66.7%)	13 (46.4%)	
TNM stage			0.0001**
I + II	19 (30.7%)	22 (80%)	
III + IV	43 (69.3%)	6 (20%)	

*$p < 0.001$; **$p < 0.0001$.

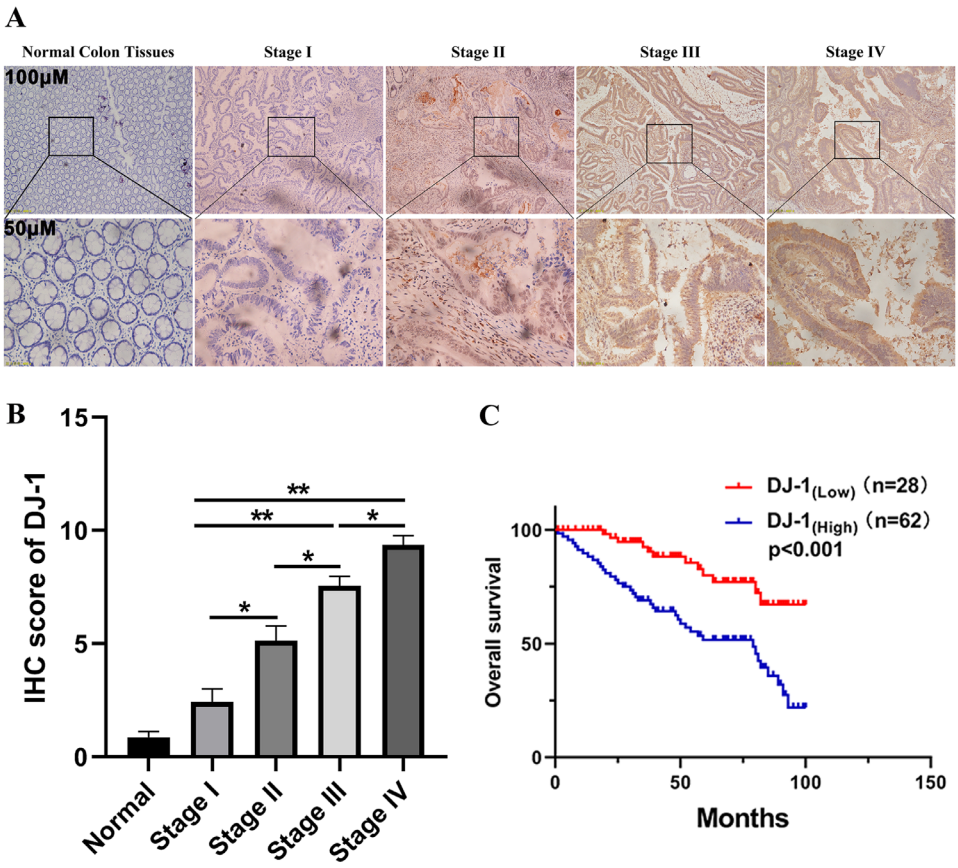

Figure 2. The prognostic value of DJ-1 expression in CRC. (**A**), Results of DJ-1 staining of CRC tumors and normal colorectal mucosa samples obtained from patients with cancer in various TNM stages (scale bar = 100 μM, 50 μM); (**B**), Results of an IHC assay of DJ-1 expression for all stages of cancer. Tumors with a low TNM stage had lower DJ-1 expression than those with a high TNM stage; (**C**), Kaplan-Meier survival curves revealed that increased DJ-1 expression ($n = 62$) in the 90 CRC samples was related to a shorter overall survival compared to samples with low DJ-1 levels ($n = 28$) ($p < 0.001$) ($^{*}p < 0.05$, $^{**}p < 0.01$).

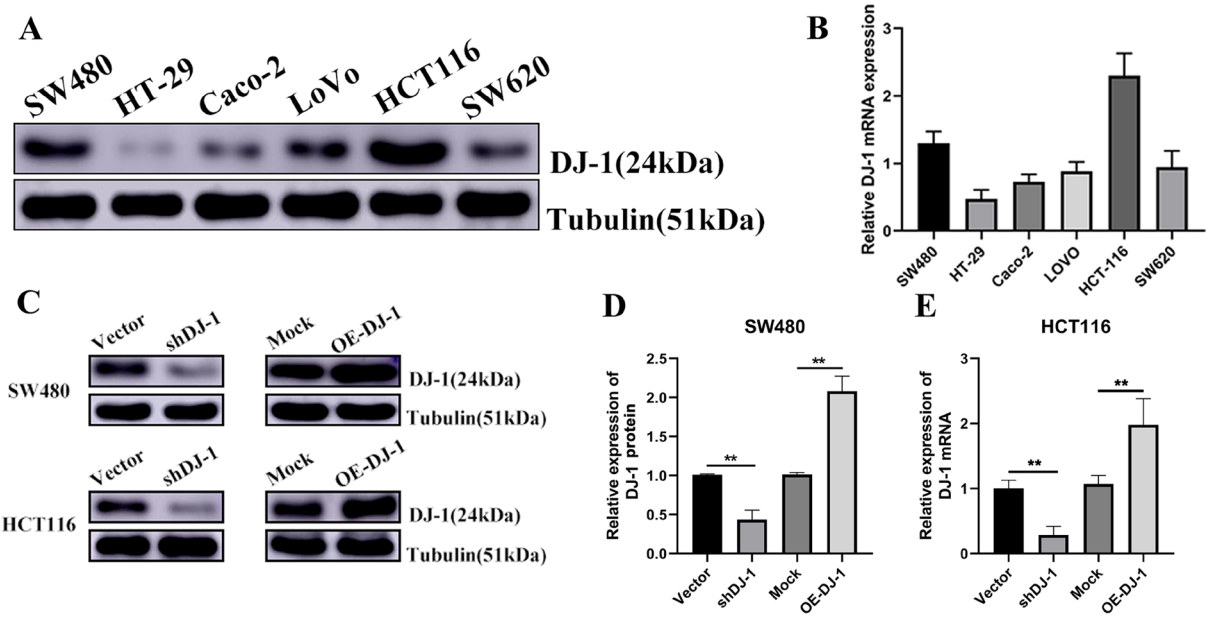

Figure 3. DJ-1 knockdown and overexpression in CRC cell lines. HCT116 and SW480 cells were transfected with lentiviral vectors to inhibit or overexpress DJ-1; An empty vector and scrambled shRNA served as negative controls. (**A-B**), The level of expression of DJ-1 protein and mRNA in 6 CRC cell lines; (**C-E**), The level of expression of DJ-1 protein and mRNA was verified with Western blotting ($p < 0.01$) and RT-qPCR. (OE-DJ-1: Overexpressed DJ-1, $^{**}p < 0.01$).

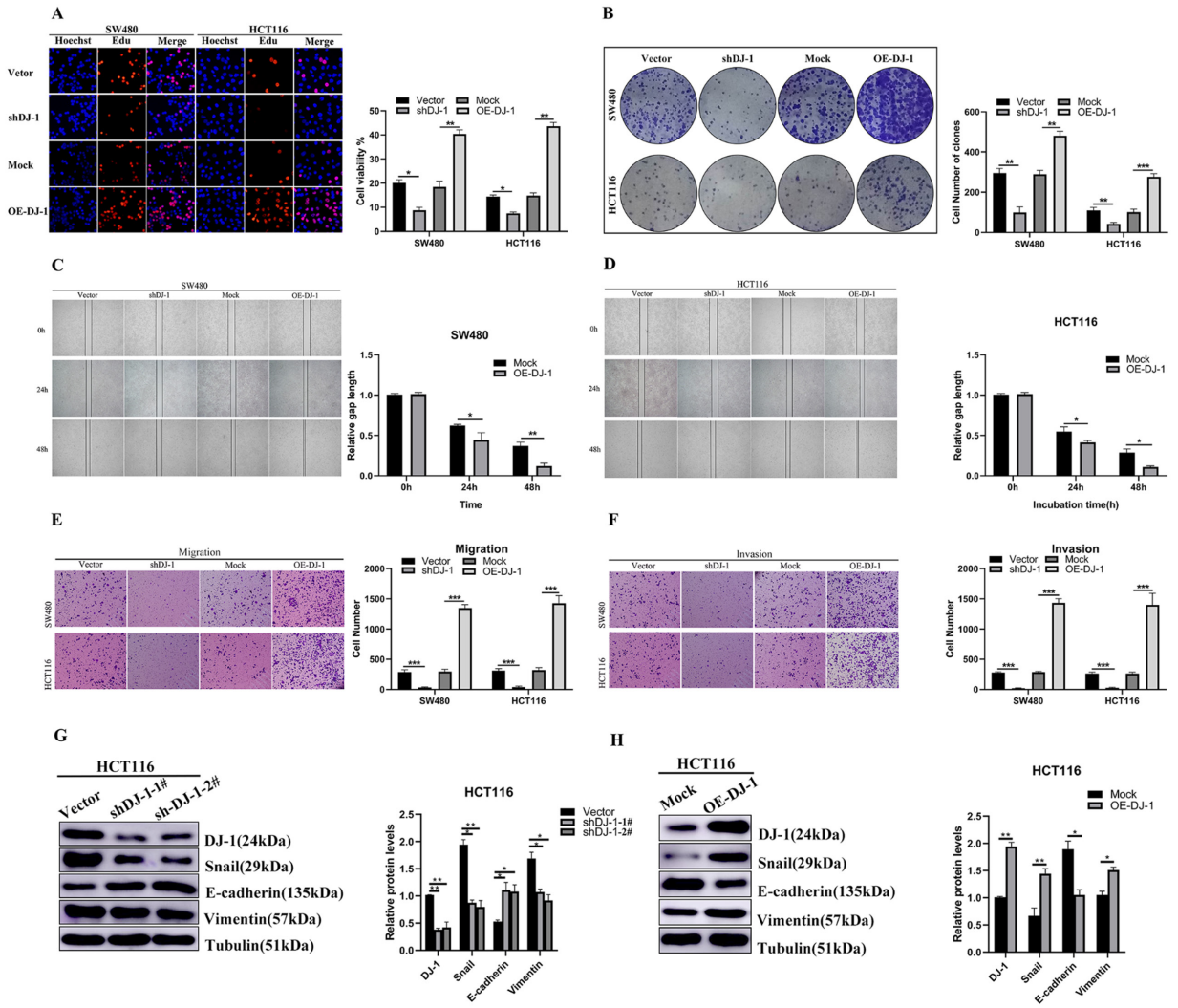

Figure 4. DJ-1 enhances the invasion, proliferation, and migration of CRC cell lines. (**A**), The Edu kit cell proliferation assay was performed in different groups; (**B**), A colony formation assay of the Vector/shDJ-1 and Mock/OE-DJ-1 groups was performed after 14 days of culturing; (**C-D**), Wound-healing migration at the indicated times (Scale bar, 100μm); (**E-F**), A cell Matrigel assay and migration & invasion assay were performed as quantitative assays. The migratory process was assessed at 24 h, and invasion at 48 h (Scale bar, 50μm); (**G-H**), Western blotting was performed to evaluate the effect of DJ-1 on levels of Snail, E-cadherin, and Vimentin expression in HCT116 cells. Data are expressed as the mean ± SD of 3 replicates. (OE-DJ-1: Overexpressed DJ-1, $^{*}p < 0.05$, $^{**}p < 0.01$, $^{***}p < 0.001$).

the expression of proteins involved in tumor metastasis was determined in CRC cell lines. Results indicated that the expression of Snail and Vimentin, two important proteins related to tumour metastasis, decreased markedly ($p < 0.05$) whereas that of E-cadherin increased significantly in shDJ-1 CRC cells (Figure 4G, $p < 0.05$), suggesting that changes in levels of these proteins may play a role in shDJ-1-mediated malignant progression. When DJ-1 was overexpressed in CRC cells, the opposite results were noted (Figure 4H, $p < 0.05$).

3.5. DJ-1 regulates the proliferation and apoptosis of CRC cells

To explore the potential function of DJ-1 in CRC cell apoptosis and proliferation, the impact of DJ-1 knockdown was examined in CRC cell lines. Results indicated that DJ-1 knockdown slightly increased the quantity of cells in the G1 phase and decreased the proportion of cells in the S phase (Figure 5A, $p < 0.05$). In other words, cell viability markedly decreased as a result of inhibition with DJ-1 compared to that in the shRNA groups. That said, SW480 and HCT116 cells transfected with shDJ-1 had an increased rate of apoptosis (Figure 5B, $p < 0.05$).

3.6. DJ-1 promotes CRC cell proliferation *via* the cyclin-D1/MDM2-p53 signaling pathway

DJ-1 may antagonize p53 by inhibiting the expression of the p53 and eventually promoting the proliferation of cancerous cells (*18*). Unfortunately, a co-immunoprecipitation assay revealed that DJ-1 does not directly interact with p53 in CRC (data not shown). Several studies have reported that an oncogene signaling pathway contributes to apoptosis by targeting

MDM2 and indirectly activating the p53 pathway (*19,20*). Thus, the state of the MDM2/p53 pathway was assessed to determine whether it underlies the oncogenic functions of DJ-1 in CRC. Western blotting was performed to evaluate the mechanism responsible for the suppressive effects of DJ-1 on proliferation *in vitro*. Results indicated that the expression of p-MDM2 (MDM2, no significant change) decreased in CRC cells treated with shDJ-1 ($p < 0.05$). However, the expression of p53 increased for some unknown reason ($p < 0.05$). DJ-1 knockdown reduced the level of the apoptotic protein Bcl-2 and enhanced the level of the proteins Bax and Caspase-3 ($p < 0.05$). In contrast, DJ-1 overexpression produced similar results (Figure 6C-D). Thus, DJ-1 is involved in regulating the process of cell apoptosis. In addition, the level of cyclin-D1 protein increased after DJ-1 overexpression compared to that in cells transfected with the control DJ-1-free vector ($p < 0.05$). DJ-1 influenced the amount of cyclin-D1 and promoted expression of Bax and cleaved caspase-3 but inhibited the level of Bcl-2 protein (Figure 6A-B, $p < 0.05$). Similarly, IHC revealed that DJ-1 inhibition decreased the expression of cyclin-D1 and p-MDM2 in the same human CRC tissues (Figure 7A-B, $p < 0.05$). The level of DJ-1 protein was related to that of cyclin-D1 and p-MDM2 in the same CRC tissue samples (Figure 7C-D, and Table 5, $r = 0.2137$, $p = 0.0068$; $r = 0.2056$, $p = 0.0037$).

3.7. The DJ-1-cyclin-D1/p53-MDM2 pathway enhances CRC progression *in vivo*

Additional tests were performed to examine the impact of DJ-1 suppression on the oncogenic activity of SW480

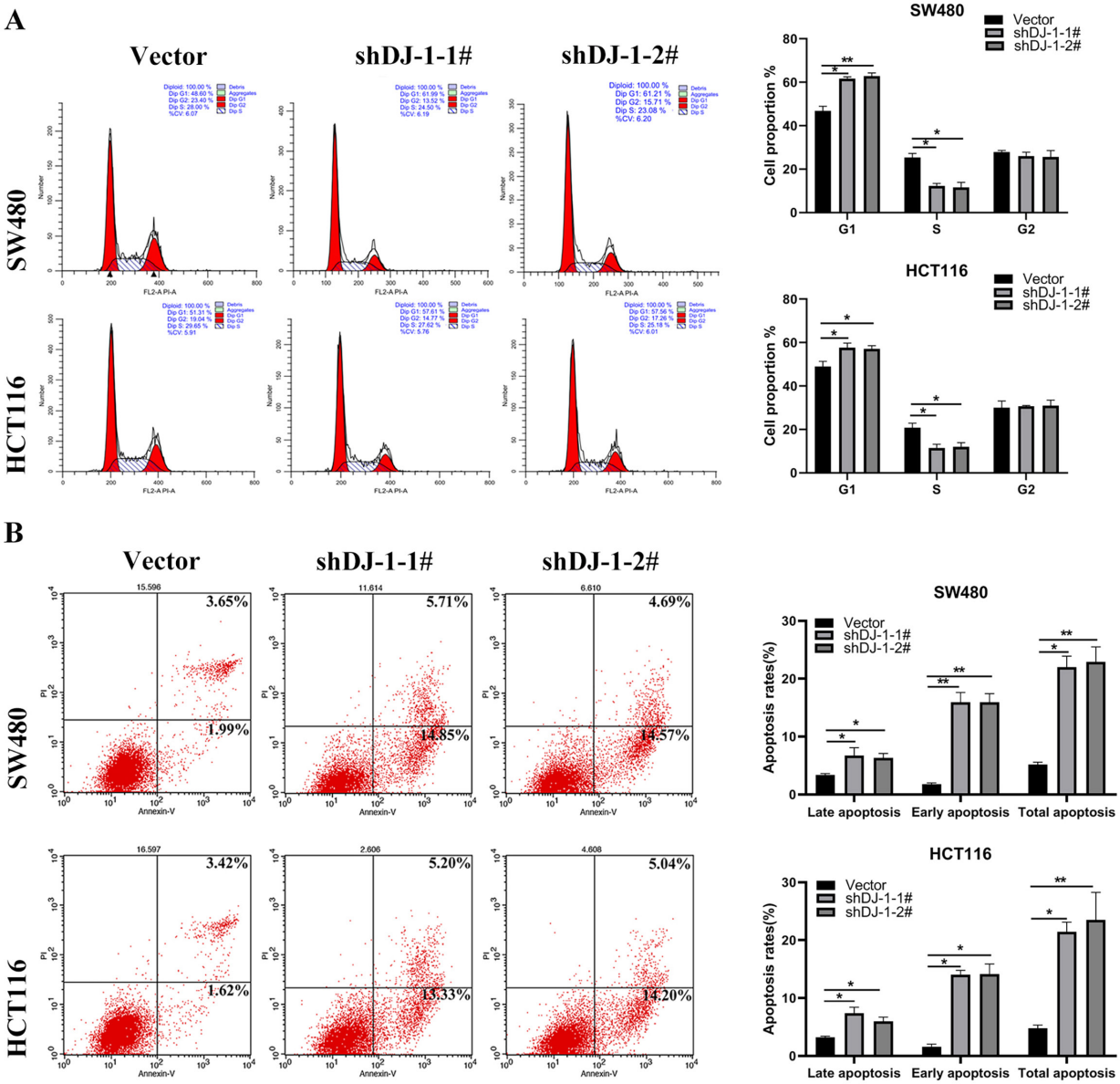

Figure 5. DJ-1 promotes cell cycle progression and decreases cell apoptosis. (**A**), Cell cycle analyses were performed with HCT116 and SW480 cells transfected with shDJ-1-1# and shDJ-1-2#; (**B**), Flow cytometry indicated that DJ-1 knockdown increased cell apoptosis in CRC cells ($^{*}p < 0.05$, $^{**}p < 0.01$).

cells, and a subcutaneous xenograft model was created in nude mice. Implantation of DJ-1-knockdown cells produced xenograft tumors with a smaller average weight compared to those formed by control cells (Figure 8A, B and D, $p < 0.01$), and those tumors displayed slower growth (Figure 8E, $p < 0.01$). Furthermore, H&E staining indicated successful subcutaneous tumor formation in nude mice (Figure 8C). In addition, p53 expression increased while p-MDM2 and cyclin-D1 decreased in tumors obtained from DJ-1-knockdown cells compared to those obtained from control cells (Figure 8F-H, $p < 0.05$). This suggested that the DJ-1/cyclin-D1/MDM2-p53 pathway participated in the development of colon cancer cells *in vivo*.

4. Discussion

At present, tumor metastasis and invasion are the leading factors that decrease the efficacy of tumor therapy, leading to death in patients with CRC (*21*). Thus, more detailed molecular studies need to be conducted to reveal the mechanisms involved in CRC metastasis to promote the development of an early intervention for high-risk cases involving metastasis. Numerous studies have indicated that DJ-1 is a key modulator of metastasis in various types of cancer (*22,23*). The current results revealed that DJ-1 expression increased in CRC, and levels were closely related to the pathological features of the

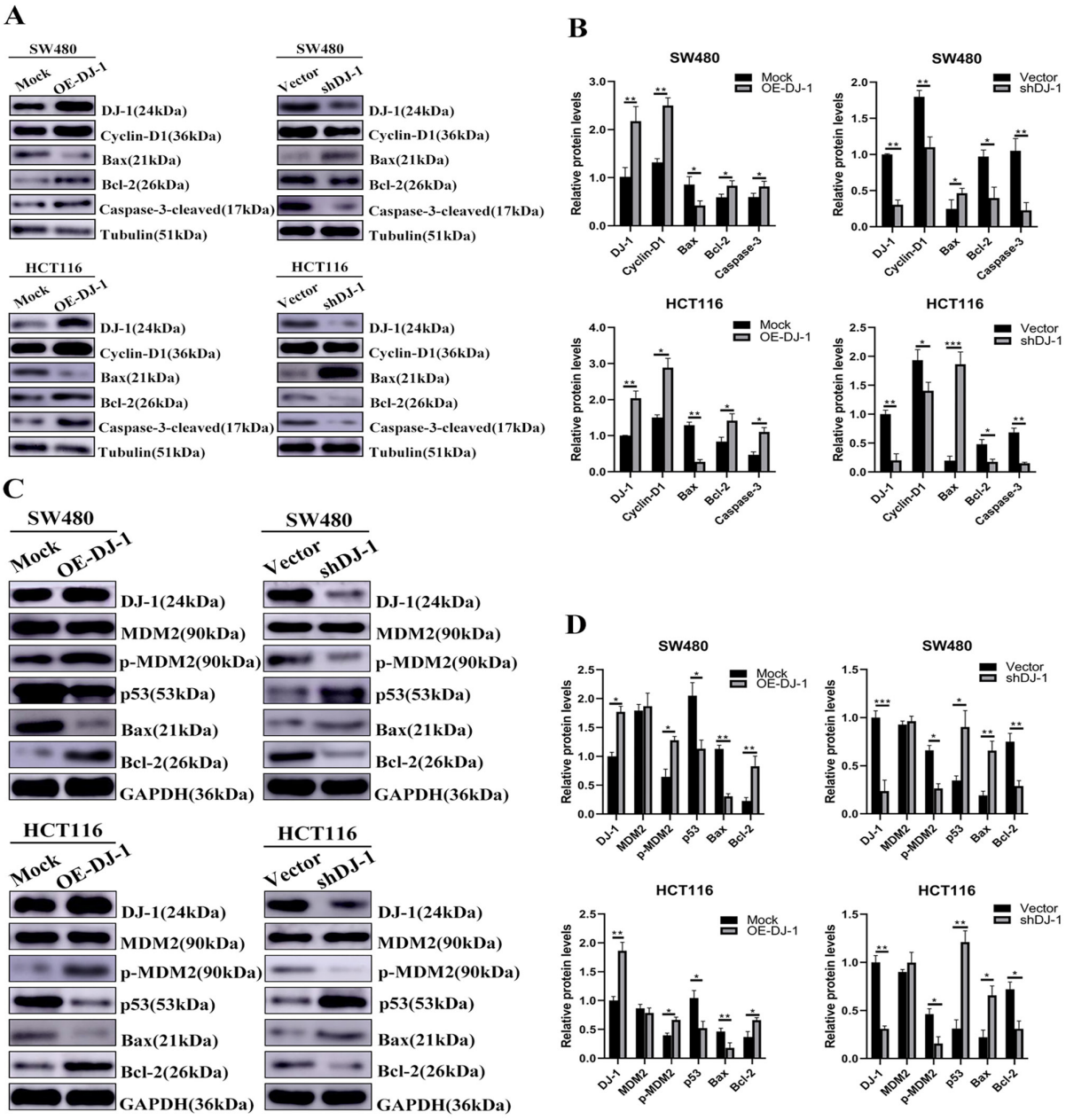

Figure 6. DJ-1 promotes CRC cell proliferation *via* the cyclin-D1/MDM2-p53 signaling pathway. (**A-D**), The effect of DJ-1 on cyclin-D1, Bax, Bcl-2, Caspase-3, p53, p-MDM2, and MDM2 protein levels was evaluated with Western blotting in SW480 and HCT116 cells. Data are expressed as the mean ± SD of 3 replicates. (OE-DJ-1: Overexpressed DJ-1, $^{*}p < 0.05$, $^{**}p < 0.01$).

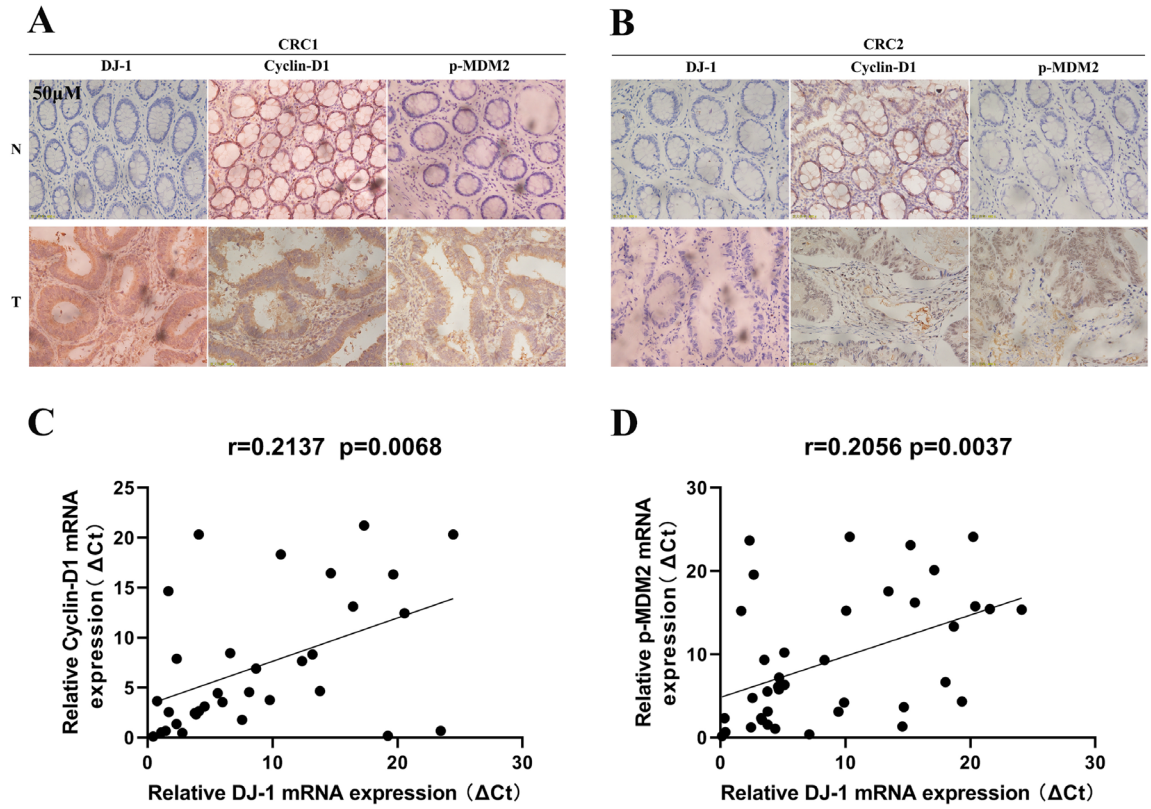

Figure 7. DJ-1 and cyclin-D1 and DJ-1 and p-MDM2 are correlated in CRC. (**A-B**), Representative immunohistochemistry images of DJ-1, cyclin-D1, and p-MDM2 protein levels in tumor specimens from two patients with CRC are shown. In Patient 1, DJ-1 overexpression upregulated cyclin-D1 and p-MDM2, while the opposite occurred in Patient 2 (N: normal colon tissue; T: tumor; scale bar = 50 μM); (**C**), The linear correlation between levels of DJ-1 and cyclin-D1 mRNA in CRC tissues (r = 0.2137) (p = 0.0068); (**D**), The linear correlation between levels of DJ-1 and p-MDM2 mRNA in CRC tissues (r = 0.2056) (p = 0.0037).

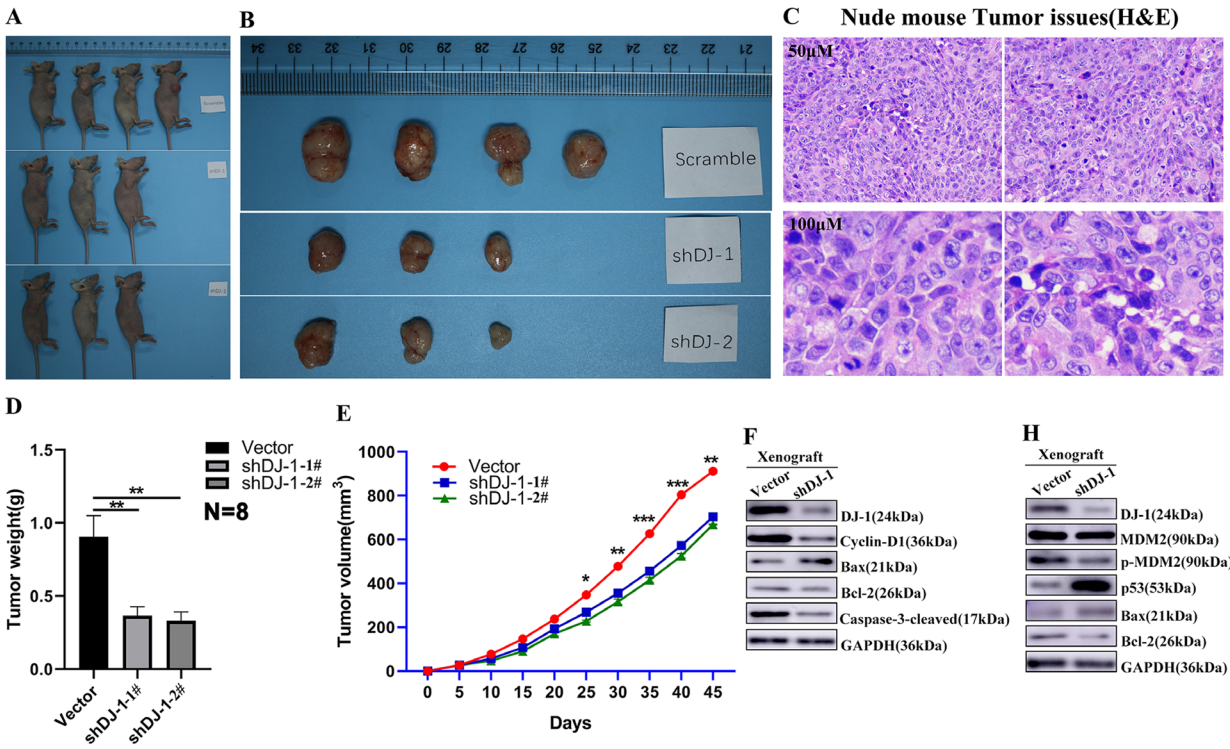

Figure 8. Knockdown of DJ-1 inhibits CRC growth *in vivo*. (**A**), Typical images of nude mice transfected with SW480 cells with shDJ-1-1#, shDJ-1-2#; (**B**), Subcutaneous implantation of SW480 cells; (**C**), Representative images of HE staining of a tumor; (**D**), Tumor weight, n = 4; (**E**), Growth curves for tumors; (**F-H**), Expression of DJ-1, cyclin-D1, p53, p-MDM2, Bax, and Bcl-2 in xenograft tumors obtained from control cells and DJ-1-knockdown. ($^{*}p < 0.05$, $^{**}p < 0.01$, $^{***}p < 0.001$).

Table 5. Association between cyclin-D1 and MDM2 expression and DJ-1 expression in CRC

Gene	*n* (%)	DJ-1 expression		
		High	Low	*r/p-value*
cyclin-D1 expression				
Low	31 (34.4%)	21	18	$r = 0.2137$
High	59 (65.6%)	41	10	$p = 0.0068^*$
p-MDM2 expression				
Low	37 (41.1%)	26	19	$r = 0.2056$
High	53 (58.9%)	36	9	$p = 0.0037^*$

$^*p < 0.001$

disease. This implies that DJ-1 is not only involved in the tumorigenesis of CRC but can also predict the prognosis for this cancer. Moreover, DJ-1 was found to enhance the metastasis and growth of CRC tumors both *in vivo* and *in vitro*. In conclusion, these findings indicate that DJ-1 plays a crucial role in the progression and development of CRC.

Similarly, many previous studies have found that DJ-1 participates in cancer initiation, progression, and multidrug resistance through multiple mechanisms in a context-dependent manner. For instance, the role of DJ-1 in mitochondrial metabolic function is modulated by 14-3-3β. DJ-1 modulation of this novel molecular mechanism of mitochondrial metabolic efficiency is potentially involved in promoting the proliferation of cancer cells (*24*).DJ-1 enhances tumor metastasis and invasion *via* activation of the PLAGL2/Wnt/BMP4 axis in CRC (*22*). In addition, DJ-1 activates the pKB/Akt signaling pathway by inhibiting PTEN, thereby promoting the progression of ovarian, lung, and breast cancer (*25-27*).

Malignant proliferation, migration, and invasion by cancer cells through the basal membrane into the lymphatic vessels, adjacent tissues, and blood is a basic characteristic of cancers and a contributor to local tumor metastasis. The current study explored the molecular mechanism of DJ-1 in CRC cell proliferation, invasion, and migration. Results showed that DJ-1 activated cyclin-D1 and MDM2-p53 signaling, which modulate CRC pathogenesis and progression. A previous study reported that DJ-1 induced G1 arrest by decreasing cyclin-E1 in HCT8 cells (*28*). The results indicated that DJ-1 triggered G1-S phase arrest in HCT116 and SW480 cells (Figure 5, A-H). During G1-S phase arrest, cyclin-D1 is a cardinal factor that orchestrates the transition from the G1 to the S phase in many cancers (*29,30*). cyclin-D1 is highly expressed during the initiation of many cancers such as CRC, indicating that downregulating cyclin-D1 may be a novel target for treatment of CRC.

Western blotting revealed that the level of cyclin-D1 protein increased following overexpression of DJ-1 in SW480 cells compared to that in cells transfected with the control DJ-1-free vector. Equivalent findings were obtained in HCT116 cells. Moreover, DJ-1 overexpression decreased the expression of the apoptosis-related proteins cleaved Caspase-3 and Bax and increased the level of Bcl-2 expression, thereby enhancing the malignant proliferation of CRC cells.

Given that the exact mechanism of DJ-1 signaling in CRC cells is not clearly known, the current study explored the involvement of p53 signaling in DJ-1-enhanced CRC aggressiveness. Mutations in p53, APC, or β-catenin, which are classic tumor suppressor genes, account for over 50% of CRC cases. These mutations often increase gene expression (c-Myc and CCND1), promote nuclear β-catenin accumulation, and increase TCF/LEF transcription activity, leading to uncontrolled proliferation (*31-33*). Moreover, prior studies have revealed that stimulation of p53 and Snail/β-catenin signaling enhances CRC metastasis (*34,35*). Decreased PDLIM claudin-3 or 1PTEN expression has been found to trigger metastasis and/or CRC EMT by promoting Wnt/β-catenin signaling, while surface-expressed FZD8 GPCR48, and FGFR4 respond to paracrine or autocrine cytokines or growth factors in a tumor microenvironment to activate p53 signaling, thereby promoting cancer aggressiveness.

Therefore, the current explored whether DJ-1 regulates p53 and promotes the malignant proliferation and metastasis of CRC cells. Interestingly, a co-immunoprecipitation assay revealed that DJ-1 does not directly interact with p53 in CRC. An oncogene signaling pathway has been found to contribute to apoptosis by targeting MDM2 and indirectly activating the p53 pathway (*36-37*). Therefore, the current study explored whether activation of the MDM2/p53 pathway mediated the oncogenic effects of DJ-1 in CRC. Western blotting was performed to assess how DJ-1 regulates anti-proliferative action *in vitro*. Several p53 targets were positively affected by DJ-1. Bax was the most markedly altered protein. Moreover, p53 knockdown ameliorated DJ-1-induced CRC cell proliferation but not invasion and migration.

Taken together, the current findings indicate that DJ-1 indirectly reduced p53 expression by upregulating p-MDM2 and then activated apoptosis signaling by decreasing expression of Bax and cleaved Caspase-3, all of which enhanced malignant proliferation of CRC cells. Interestingly, results indicated that DJ-1 activated EMT signaling and regulated Snail signaling-targeted gene expression and CRC cell proliferation (Figure 4 M-P). These findings add to the knowledge of the underlying mechanism of the pro-proliferative effects of DJ-1 and reveal new avenues for CRC therapy.

5. Conclusion

This study has provided compelling evidence that as an oncogene DJ-1 might be a promoter of CRC cell invasion, proliferation, and migration *via* the cyclin-D1/MDM2-p53 signaling pathway, and this study has

described its potential role as a postoperative adjuvant therapy for patients with CRC.

Acknowledgements

The study was supported by grants from the National Natural Science Foundation of China (81560389, 81860433, 81960436, and 81560396), the Natural Science Foundation of Jiangxi Province (20181BBG70015, 2018BBG70019), the Natural Science Youth Foundation of Jiangxi Province (20192BAB215036), and the Foundation for Fostering Young Scholars of Nanchang University (PY201822).

References

1. Siegel RL, Miller KD, Jemal A. Cancer statistics, 2019. CA Cancer J Clin. 2019; 69:7-34.
2. Chen W, Zheng R, Baade P D, Zhang S, Zeng H, Bray F, Jemal A, Yu XQ, He J. Cancer statistics in China, 2015. CA Cancer J Clin. 2016; 66:115-132.
3. Brody H. Colorectal cancer. Nature. 2015; 521:S1.
4. Paauwe M, Schoonderwoerd MJ, Helderman RFCP, *et al.* Endoglin expression on cancer-associated fibroblasts regulates invasion and stimulates colorectal cancer metastasis. Clin Cancer Res. 2018; 24:6331-6344.
5. Schulz-Heddergott R, Stark N, Edmunds SJ, Li J, Conradi LC, Bohnenberger H, Ceteci F, Greten FR, Dobbelstein M, Moll UM. Therapeutic ablation of gain-of-function mutant p53 in colorectal cancer inhibits stat3-mediated tumor growth and invasion. Cancer Cell. 2018; 34:298-314.e7.
6. Jiang H, Deng R, Yang X, *et al.* Peptidomimetic inhibitors of APC-Asef interaction block colorectal cancer migration. Nat Chem Biol. 2017; 13:994-1001.
7. Vincenzi B, Cremolini C, Sartore-Bianchi A, *et al.* Prognostic significance of K-Ras mutation rate in metastatic colorectal cancer patients. Oncotarget, 2015; 6:31604-31612.
8. Rui YY, Zhang D, Zhou ZG, Wang C, Yang L, Yu YY, Chen HN. Can K-ras gene mutation be utilized as prognostic biomarker for colorectal cancer patients receiving chemotherapy? A meta-analysis and systematic review. PLoS One. 2013; 8:e77901.
9. Nagakubo D, Taira T, Kitaura H, Ikeda M, Tamai K, Iguchi-Ariga SM, Ariga H. DJ-1, a novel oncogene which transforms mouse NIH3T3 cells in cooperation with ras. Biochem Biophys Res Commun. 1997; 231:509-513.
10. Yang J, Kim KS, Iyirhiaro GO, Marcogliese PC, Callaghan SM, Qu D, Kim WJ, Slack RS, Park DS. DJ-1 modulates the unfolded protein response and cell death *via* upregulation of ATF4 following ER stress. Cell Death Dis. 2019; 10:135.
11. Oh S , Mouradian MM. Cytoprotective mechanisms of DJ-1 against oxidative stress through modulating ERK1/2 and ASK1 signal transduction. Redox Biol. 2018; 14:211-217.
12. Junn E, Taniguchi H, Jeong BS, Zhao X, Ichijo H, Mouradian MM. Interaction of DJ-1 with Daxx inhibits apoptosis signal-regulating kinase 1 activity and cell death. Proc Natl Acad Sci U S A. 2005; 102:9691-9696.
13. Lee D H, D K, ST K, *et al.* PARK7 modulates autophagic proteolysis through binding to the N-terminally arginylated form of the molecular chaperone HSPA5. Autophagy. 2018; 14:1870-1885.
14. Zhu ZM, Li ZR, Huang Y, Yu HH, Huang XS, Yan YF, Shao JH, Chen HP. DJ-1 is involved in the peritoneal metastasis of gastric cancer through activation of the Akt signaling pathway. Oncol Rep. 2014; 31:1489-1497.
15. Qiu B, Wang J, Yu Y, Zhen C, Gu J, Liu W, Wen Y, Chen L, Gao Y, Xia Q, Kong X. DJ-1 promotes development of DEN-induced hepatocellular carcinoma and proliferation of liver cancer cells. Oncotarget. 2016; 8:8499-8511.
16. He X, Zheng Z, Li J, Ben Q, Liu J, Zhang J, Ji J, Yu B, Chen X, Su L, Zhou L, Liu B, Yuan Y. DJ-1 promotes invasion and metastasis of pancreatic cancer cells by activating SRC/ERK/uPA. Carcinogenesis. 2012; 33:555-562.
17. Yuen H F, Chan Y P, Law S, Srivastava G, El-Tanani M, Mak TW, Chan KW. DJ-1 could predict worse prognosis in esophageal squamous cell carcinoma. Cancer Epidemiol Biomarkers Prev. 2008; 17:3593-3602.
18. Vasseur S, Afzal S, Tomasini R, Guillaumond F, Tardivel-Lacombe J, Mak TW, Iovanna JL. Consequences of DJ-1 upregulation following p53 loss and cell transformation. Oncogene. 2012; 31:664-670.
19. Klimovich B, Stiewe T, Timofeev O. Inactivation of Mdm2 restores apoptosis proficiency of cooperativity mutant p53 *in vivo*. Cell Cycle. 2020; 19:109-123.
20. Nietzold F, Rubner S, Berg T. The hydrophobically-tagged MDM2-p53 interaction inhibitor Nutlin-3a-HT is more potent against tumor cells than Nutlin-3a. Chem Commun (Camb), 2019; 55:14351-14354.
21. Zhou J, Liu H, Zhang L, Liu X, Zhang C, Wang Y, He Q, Zhang Y, Li Y, Chen Q, Zhang L, Wang K, Bu Y, Lei Y. DJ-1 promotes colorectal cancer progression through activating PLAGL2/Wnt/BMP4 axis. Cell Death Dis. 2018; 9:865.
22. El-Sokkary GH, Ismail IA, Saber SH. Melatonin inhibits breast cancer cell invasion through modulating DJ-1/KLF17/ID-1 signaling pathway. J Cell Biochem. 2019; 120:3945-3957.
23. Weinert M, Millet A, Jonas E A, Alavian KN. The mitochondrial metabolic function of DJ-1 is modulated by 14-3-3beta. FASEB J. 2019; 33:8925-8934.
24. Ismail I A, Kang HS, Lee HJ, Kim JK, Hong SH. DJ-1 upregulates breast cancer cell invasion by repressing KLF17 expression. Br J Cancer. 2014; 110:1298-1306.
25. Kim R H, Peters M, Jang Y, *et al.* DJ-1, a novel regulator of the tumor suppressor PTEN. Cancer Cell. 2005; 7:263-273.
26. Davidson B, Hadar R, Schlossberg A, Sternlicht T, Slipicevic A, Skrede M, Risberg B, Flørenes VA, Kopolovic J, Reich R. Expression and clinical role of DJ-1, a negative regulator of PTEN, in ovarian carcinoma. Hum Pathol. 2008; 39:87-95.
27. Robert G, Puissant A, Dufies M, Marchetti S, Jacquel A, Cluzeau T, Colosetti P, Belhacene N, Kahle P, Da Costa CA, Luciano F, Checler F, Auberger P. The caspase 6 derived N-terminal fragment of DJ-1 promotes apoptosis *via* increased ROS production. Cell Death Differ. 2012; 19:1769-1778.
28. Zheng F, Wang M, Li Y, Huang C, Tao D, Xie F, Zhang H, Sun J, Zhang C, Gu C, Wang Z, Jiang G. CircNR3C1 inhibits proliferation of bladder cancer cells by sponging miR-27a-3p and downregulating cyclin D1 expression. Cancer Lett. 2019; 460:139-151.
29. Jeong K, Kim J H, Murphy J M, *et al.* Nuclear focal adhesion kinase controls vascular smooth muscle cell

proliferation and neointimal hyperplasia through GATA4-mediated cyclin D1 transcription. Circ Res. 2019; 125:152-166.
30. Kimata Y. APC/C ubiquitin ligase: Coupling cellular differentiation to G1/G0 phase in multicellular systems. Trends Cell Biol. 2019; 29:591-603.
31. Hafner A, Bulyk M L, Jambhekar A, Lahav G. The multiple mechanisms that regulate p53 activity and cell fate. Nat Rev Mol Cell Biol. 2019; 20:199-210.
32. Perugorria M J, Olaizola P, Labiano I, Esparza-Baquer A, Marzioni M, Marin JJG, Bujanda L, Banales JM. Wnt-beta-catenin signalling in liver development, health and disease. Nat Rev Gastroenterol Hepatol. 2019; 16:121-136.
33. Lee SH, Shen GN, Jung YS, Lee SJ, Chung JY, Kim HS, Xu Y, Choi Y, Lee JW, Ha NC, Song GY, Park BJ. Antitumor effect of novel small chemical inhibitors of Snail-p53 binding in K-Ras-mutated cancer cells. Oncogene. 2010; 29:4576-4587.
34. Kurrey NK, Jalgaonkar SP, Joglekar AV, Ghanate AD, Chaskar PD, Doiphode RY, Bapat SA. Snail and slug mediate radioresistance and chemoresistance by antagonizing p53-mediated apoptosis and acquiring a stem-like phenotype in ovarian cancer cells. Stem Cells. 2009; 27:2059-2068.
35. Duplan E, Giaime E, Viotti J, Sévalle J, Corti O, Brice A, Ariga H, Qi L, Checler F, Alves da Costa C. ER-stress-associated functional link between Parkin and DJ-1 *via* a transcriptional cascade involving the tumor suppressor p53 and the spliced X-box binding protein XBP-1. J Cell Sci. 2013; 126:2124-2133.
36. Kato I, Maita H, Takahashi-Niki K, Saito Y, Noguchi N, Iguchi-Ariga SM, Ariga H. Oxidized DJ-1 inhibits p53 by sequestering p53 from promoters in a DNA-binding affinity-dependent manner. Mol Cell Biol. 2013; 33:340-359.
37. Deng X, Li S, Kong F, Ruan H, Xu X, Zhang X, Wu Z, Zhang L, Xu Y, Yuan H, Peng H5, Yang D, Guan M. Long noncoding RNA PiHL regulates p53 protein stability through GRWD1/RPL11/MDM2 axis in colorectal cancer. Theranostics. 2020; 10:265-280.

Received October 9, 2019; Revised February 6, 2020; Accepted February 15, 2020.

[§]These authors contributed equally to this work.

**Address correspondence to:*
Zhengming Zhu, The Second Affiliated Hospital of Nanchang University, Nanchang University, No. 1 Minde Road, Nanchang, Jiangxi 330006, China.
E-mail: zzm8654@163.com

Released online in J-STAGE as advance publication March 4, 2020.

Original Article

DOI: 10.5582/bst.2019.01302

Novel conjugates of endoperoxide and 4-anilinoquinazoline induce myeloma cell apoptosis by inhibiting the IGF1-R/AKT/mTOR signaling pathway

Yujia Xu[1], Kun Zeng[1], Xiaoge Wang[1,2], Jieyu Zhang[1], Biyin Cao[1], Zubin Zhang[1], Chunhua Qiao[3], Xiaofeng Xu[4], Qi Wang[2], Yuanying Zeng[5,*], Xinliang Mao[1,2,6,*]

[1] Department of Pharmacology, College of Pharmaceutical Sciences, Soochow University, Suzhou, Jiangsu, China;
[2] Institute of Clinical Pharmacology, Guangzhou University of Chinese Medicine, Guangzhou, China;
[3] Department of Medicinal Chemistry, College of Pharmaceutical Sciences, Soochow University, Suzhou, Jiangsu, China;
[4] Department of Urology, Nanjing Jinling Hospital, School of Medicine, Nanjing University, Nanjing, Jiangsu, China;
[5] Department of Oncology, Suzhou Municipal Hospital, Suzhou, Jiangsu, China;
[6] School of Basic Medical Sciences, Guangzhou Medical University, Guangzhou, China.

SUMMARY 4-anilinoquinazoline-containing inhibitors of the epidermal growth factor receptor (EGFR) are widely used in non-small cell lung cancer patients with mutated EGFR, but they are less effective in multiple myeloma (MM), a fatal malignancy derived from plasma cells. The present study designed a series of novel compounds by conjugating a peroxide bridge to the 4-anilinoquinazoline pharmacophore. Further studies showed that these agents such as 4061 and 4065B displayed potent activity to induce MM cell apoptosis by upregulating pro-apoptotic p53 and Bax while downregulating pro-survival Bcl-2. The mechanistic analysis revealed that both 4061 and 4065B inhibited IGF1-R, AKT and mTOR activation in a concentration dependent manner but had no effects on the expression of their total proteins, suggesting the conjugates of endoperoxide and 4-anilinoquinazoline may exert its anti-myeloma activity by targeting the IGF1-R/AKT/mTOR pathway.

Keywords cell death, endoperoxide bridge, multiple myeloma, signaling transduction

1. Introduction

Multiple myeloma (MM) is a fatal hematological malignancy derived from plasma cells and accounts for approximately 2% of total cancer-associated death. The last few decades have witnessed the development of several lines of novel agents for the treatment of MM from immunomodulators, proteosomal inhibitors to monoclonal antibodies and CAR-T-based cell therapies. However, due to genetic heterogeneity and other factors, most patients quickly develop resistance and the general outcomes are not favorable (*1*). Until now, MM is still incurable and the five-year survival rate remains only 30 to 40 percent.

Insulin-like growth factor (IGF1) is a potent activator and promoter of the proliferation and survival of MM cells by activating the receptor tyrosine kinase (RTK) IGF-1 receptor (IGF1-R). It is reported that IGF1-R is hyperactivated in most MM cell lines and patient samples. As an RTK, IGF1-R activates phosphoinositide-3 kinase (PI3K) and subsequent downstream signals, mainly the protein kinase B (AKT) and mammalian target of rapamycin (mTOR), therefore promoting MM cell proliferation and survival. Targeting the PI3K/AKT/mTOR signaling pathway has been regarded as a promising strategy for MM therapy and a number of specific inhibitors of this signaling pathway have been developed. Notably, PI3K is also activated by other RTKs, such as the epidermal growth factor receptor (EGFR), especially in solid cancers such as non-small cell lung cancers (NSCLCs). Inhibition of the EGFR pathway led to the discovery of specific inhibitors of EGFR (*2*), including gefitinib, erlotinib, afatinib and dacomitinib, all of which have been applied in the clinic for lung cancer patients. However, these inhibitors are less effective in liquid tumors such as MM (*3*). By comparing the chemical structure of these inhibitors, we found that all these inhibitors share the 4-anilinoquinazoline core scaffold (*4*). Therefore, it will be interesting to develop a second class of these inhibitors based on this scaffold for the treatment of MM. To develop such inhibitors, We took artemisinin

into consideration because it contains an endoperoxide pharmacophore and displays anti-MM activity (*5*). We therefore developed some novel conjugates of 4-anilinoquinazoline and endoperoxide pharmocophore (*4*). These novel compounds showed potency against NSCLC cell lines with L858R/T790M mutation in the EGFR (*4*). The present study found that 4061 and 4065B, two representative agents, displayed potent anti-MM activity by inhibiting the IGF1-R/AKT/mTOR signaling pathway.

2. Materials and Methods

2.1. Cell lines

MM cell lines OPM2, KMS11, OCI-My5 and JJN3 were generously provided by Dr. Aaron Schimmer from Ontario Cancer Center and the University of Toronto, Canada. MM cell lines RPMI-8226 and LP1 were purchased from American Type Culture Collection (Manassas, VA). All cell lines were maintained in Iscove's modified Dulbecco's medium. All media were supplemented with 10% fetal bovine serum, 100 μg/mL of penicillin, and 100 units/mL of streptomycin.

2.2. Gefitinib and novel conjugates of 4-anilinoquinazoline and endoperoxide

Gefitinib was purchased from Sigma-Aldrich Chemicals (St. Louis, MO, USA). The novel conjugates of the 4-anilinoquinazoline and endoperoxide pharmacophore were synthesized and characterized by NMR as described previously (*4*).

2.3. Cell proliferation analysis

MM cells were treated with increasing concentrations of compounds of interest for 72 hrs before being subjected to MTT (3-(4,5-dimethylthiazol-2-yl)-2,5-diphenyltetrazolium bromide) assay as described previously (*6*).

2.4. Annexin V staining and flow cytometric analysis

Apoptosis was quantitatively assessed using Annexin V-FITC and propidium iodide (PI) staining (MultiSciences Biotech Co., Ltd., Hangzhou, China). After being treated with 4061 and 4065B at indicated concentrations for 24 hrs, cells were collected and rinsed with ice-cold PBS, re-suspended in 500 μL of 1 × binding buffer, and then labeled with 5 μL Annexin V-FITC and 10 μL PI for 10 min in the dark. The samples were mixed slightly before being analyzed on a flow cytometer (*6*).

2.5. Reverse transcription polymerase chain reaction (RT-PCR)

Total RNA was extracted using the Trizol®reagent (Sangon Biotech, Shanghai, China). Total RNA (2.5 μg) was reverse transcribed using a Superscript™-III kit (Invitrogen) according to the manufacturer's instruction. The polymerase chain reaction amplification was carried out in 25 μL of PCR reaction mixture containing 10 mM Tris-HCl (pH 8.3), 50 mM KCl, 2 mM $MgCl_2$, 20 pmol of each primer set, two units of Taq DNA polymerase (Transgen, Beijing, China), 0.2 mM dNTPs, and 2 μL cDNA. The Primers used were as follows: EGFR1, forward 5'-TTGCCGCAAAGTGTGTAACG-3' and reverse 5'-GTTGCACTTGTCCACGCATT-3'; EGFR2, forward 5'-GCTCCTCCTCGCCCTCTT-3' and reverse 5'-GCCAGCTGGTTGTTCTTGTG-3'; FGFR3, forward 5'-CTGAAGAACGGCAGGGAGTT-3' and reverse 5'-CTGTGCGTCACTGTACACCT-3'; GAPDH, forward 5'-AATCCCATCACCATCTTCC-3' and reverse 5'-CATCACGCCACAGTTTCC-3'. Reaction cycling conditions were 3 min at 95°C, followed by 30 cycles at 95°C for 30 s, 60°C for 30 s, and 72°C for 40 s, and 1 cycle at 72°C for 10 min. Products were analyzed on 2% agarose gels.

2.6. Analyses of the oncomine datasets

Several datasets from the Oncomine Database (*https://www.oncomine.org/*) were retrieved by searching genes of interest in association with MM and several solid cancers including NSCLC, breast cancer, liver cancer and prostate cancer tissues.

2.7. Western blotting

Cells (3×10^6) in 60-mm dishes were treated with 4061 and 4065B at indicated concentrations for 24 hrs before being collected for total cell lysates preparation in ice-cold lysis buffer. After clarifying using high speed centrifugation at 4°C, protein concentrations were determined with the BCA assay (Beyotime Institute of Biotechnology, Nantong, China). Equal amounts of proteins (30-40 μg) were fractionated using SDS-PAGE, and transferred to polyvinylidene difluoride membranes. The blots were subjected to analysis against appropriate antibodies, including monoclonal PARP, Bcl-2, Bax, p53, IGF1-R, p-IGF1-R, p-AKT(S473), AKT, p-mTOR(S2448) and mTOR. All these antibodies were purchased from Cell Signaling Technology (Danvers, MA, USA). An anti-GAPDH antibody was purchased from Affinity Biosciences (Cincinnati, OH, USA).

2.8. Phosphorylation analysis

MM cell lines were stored overnight in Iscove's modified Dulbecco's medium containing 0.5% fetal bovine serum and low concentrations of 4061 and 4065B. One plate of cells was then treated with BENC-

511 for 2 hrs as a positive control. Cells were then stimulated with 100 ng/mL human recombinant insulin-like growth factor-1 (hrIGF-1, PeproTech, Rocky Hill, NJ) for 15 min before being lysed in Tris-buffered saline containing 1 mM sodium orthovanadate. After clarification, cell lysates were subjected to Western blotting analysis with anti-phospho-AKT (S473), anti-AKT, anti-phospho-mTOR (S2448) and anti-mTOR antibodies.

3. Results

3.1. 4061 and 4065B induce MM cell apoptosis

The EGFR inhibitors gefitinib, erlotinib, afatinib and dacomitinib share 4-anilinoquinazoline as the pharmacophore (Figure 1A), and artemisinin and derivatives have endoperoxide moiety as the pharmacophore (*7*). To take advantage of both pharmacophores of these two classes of anti-cancer compounds, we designed and synthesized a series of novel agents by conjugating an endoperoxide bridge to the 4-anilinoquinazoline core scaffold (Figure 1B) (*4*). From a series of agents, two compounds, 4061 and 4065B (Figure 1B), had displayed improved activity to induce NSCLC cell death (*4*). To evaluate their anti-MM activity, MM cell lines RPMI-8226, LP1, and OPM2 were treated with 4061 and 4065B for 24 hrs, followed by Western blot assays to evaluate the cleaved level of PARP, a hallmark of apoptosis. As shown in Figure 1C, gefitinib, 4-anilinoquinazoline (YY) and endoperoxide (3022) failed to induce cleavage of PARP, in contrast, both 4061 and 4065B induced marked cleavage of PARP. To confirm this finding, MM

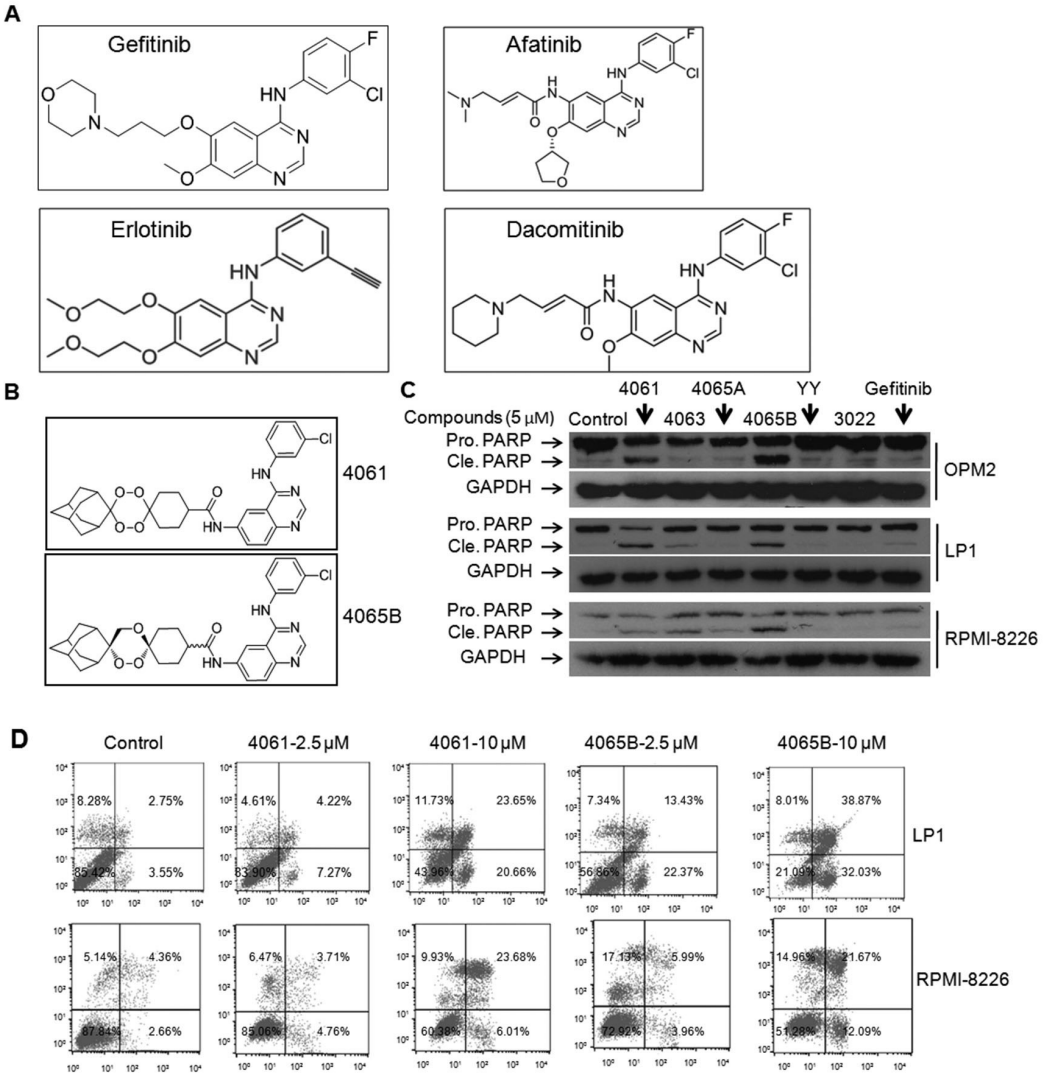

Figure 1. 4061 and 4065B induce MM cell apoptosis. (**A**) The chemical structure of Gefitinib and other EGFR inhibitors; (**B**) The chemical structure of 4061 and 4065B. (**C**) OPM2, LP1, and RPMI-8226 cells were treated with various compounds including gefitinib, 4061, 4065B and negative controls YY and 3022 for 24 hrs. Cell lysates were prepared and subjected to immunoblotting assay against apoptosis-associated proteins PARP. GAPDH was used as a loading control. (**D**) Apoptosis of LP1 and RPMI-8226 cells treated with various concentrations of 4061 and 4065B were determined by Annexin V-FITC and PI staining using flow cytometric analysis.

cells treated with these two compounds were stained with Annexin V and propidium iodide followed by flow cytometry analysis. When cells are undergoing apoptosis, phosphatidylserine inside the plasma membrane will turn over and appear on the cell surface and thus could be identified by Annexin V, therefore, Annexin V staining-positive cells are regarded as a gold criterion of apoptosis (*6*). Our study found that both 4061 and 4065B induced Annexin V positive cells in a concentration-dependent manner (Figure 1D). Therefore, 4061 and 4065B induce MM cell apoptosis.

3.2. 4061 and 4065B inhibit MM cell proliferation

To find out whether these two compounds also inhibit MM cell proliferation, a panel of MM cells were treated with 4061 and 4065B in increasing concentrations for 72 hrs, followed by the MTT assay. The results demonstrated that both 4061 and 4065B suppressed proliferation of all MM cell lines tested (Figure 2). Therefore, these conjugates of 4-anilinoquinazoline and endoperoxide suppress MM cell proliferation and induce MM cell apoptosis.

3.3. 4061 and 4065B upregulate pro-apoptotic signals

The above findings suggest both 4061 and 4065B induce MM cell apoptosis and suppress proliferation, to find out whether pro-apoptotic signals were activated, RPMI-8226 and LP1 cells were treated for 24 hrs followed by Western blotting assays to evaluate typical pro-apoptotic and pro-survival proteins. The results showed that these two analogs downregulated the protein level of Bcl-2, a typical pro-survival protein in cancer cells (Figure 3A and 3B), which was consistent with apoptosis and PRAP cleavage. In contrast, p53 and Bax, two typical pro-apoptotic proteins, were upregulated by both compounds (Figure 3A and 3B). Therefore, these results further demonstrated that these novel agents with conjugated endoperoxide bridge and the 4-anilinoquinazoline core scaffold display potent activity in inducing MM cell apoptosis.

3.4. EGFR expression is dispensable for 4061 and 4065B to induce MM cell apoptosis

Gefitinib and derivatives are selective EGFR inhibitors mainly prescribed for NSCLC patients with mutated and overactivated EGFR (*8*), while it was ineffective in MM cells (*3*). Therefore, we wondered whether EGFR might not be expressed in MM cells. To this end, we first evaluated the expression profile of EGFR in various types of cancers, including NSCLC, breast cancer, colorectal cancer, lymphoma, melanoma and ovarian cancer. The result showed that EGFR was highly expressed in solid cancers but not in liquid cancers (Figure 4A). We next evaluated EGFR in two different MM datasets, the Zhan Myeloma dataset (*9*) and the Agnelli Myeloma 3 dataset (*10*), it turned out that EGFR is not in MM cells as expected (Figure 4B and 4C). To confirm these findings, EGFR expression in MM and representative solid tumor cell lines was further measured by RT-PCR. The results showed that EGFR1 and EGFR2, two major EGFR isoforms in cancers, were highly expressed in solid tumor cell lines, such as NSCLC cell line A549, breast cancer cell line H47D, cervical cancer cell line HeLa and prostate cancer cell line PC3, while neither was detected by RT-PCR in six MM cell lines including LP1 and RPMI-8226 (Figure 4D). This finding was consistent with previous studies that EGFRs are high in solid tumors (*11*), but it was not identified in RPMI-8226 cells (*12*). However, both RPMI-8226 and LP1 were sensitive to 4061 and 4065B, and these findings suggested that EGFR is dispensable for apoptosis induced by the conjugates of the endoperoxide and 4-anilinoquinazoline.

3.5. 4061 and 4065B inhibit the IGF1-R/AKT/mTOR signaling pathway

It is well known that growth factor IGF1 is a key stimulator to increase MM cell proliferation *via* its specific receptor IGF1-R. To find out the expression

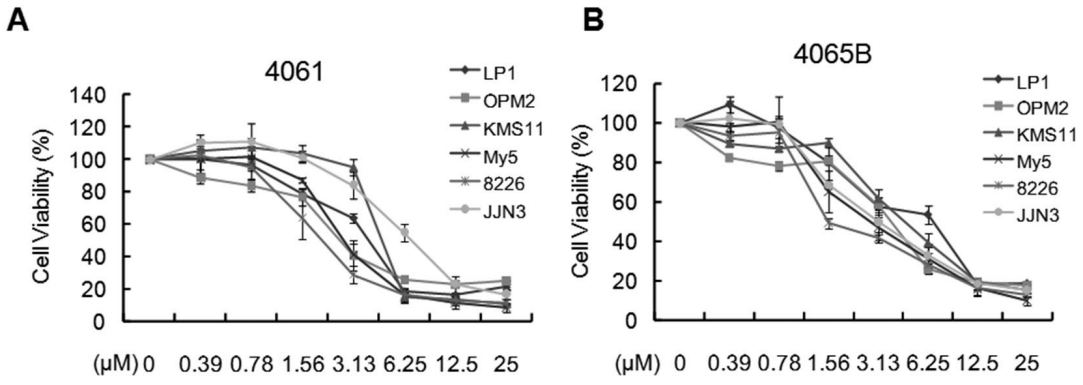

Figure 2. 4061 and 4065B inhibit MM cell proliferation. Various MM cell lines were treated with 4061 (**A**) or 4065B (**B**) at indicated concentrations for 72 hrs. Cells were then subjected to MTT assays as described in the Methods section.

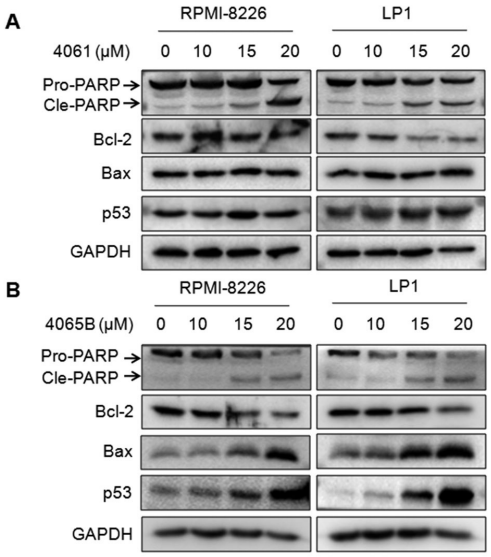

Figure 3. 4061 and 4065B activate apoptotic signaling in MM cells. RPMI-8226 and LP1 cells were treated with increasing concentrations of 4061 (**A**) and 4065B (**B**) for 24 hrs. Cell lysates were then prepared and subjected to immunoblotting assays against specific proteins as indicated. GAPDH was used as a loading control.

profile of IGF1-R, the mRNA levels of IGF1-R were analyzed by retrieving the Chapman Myeloma dataset based on 239 MM patients retrieved from the Oncomine Database (*13*). As shown in Figure 5A, compared with that from normal bone marrow cells, IGF1-R was significantly increased in MM cells and smoldering MM, an early stage of MM. Because IGF1/IGF1-R leads to the activation of the AKT/mTOR signaling pathway in MM survival (*12,14*), we wondered whether 4061 and 4065B could inhibit the AKT/mTOR pathway in MM cells stimulated by IGF1. To this end, starved LP1 and RPMI-8226 cells were treated with 4061 and 4065B or the known inhibitor BENC-511 (*15*), followed by stimulation with IGF1, a typical ligand of IGFR. The phosphorylation levels of IGFR1, AKT and mTOR kinases were strikingly increased by IGF1, but this activation was inhibited by both BENC-511 and the tested compounds 4061 and 4065B. Notably, 4061 and 4065B suppressed the activation of AKT and mTOR in a concentration-dependent manner but had no effects on their total protein expression (Figure 5B and 5C).

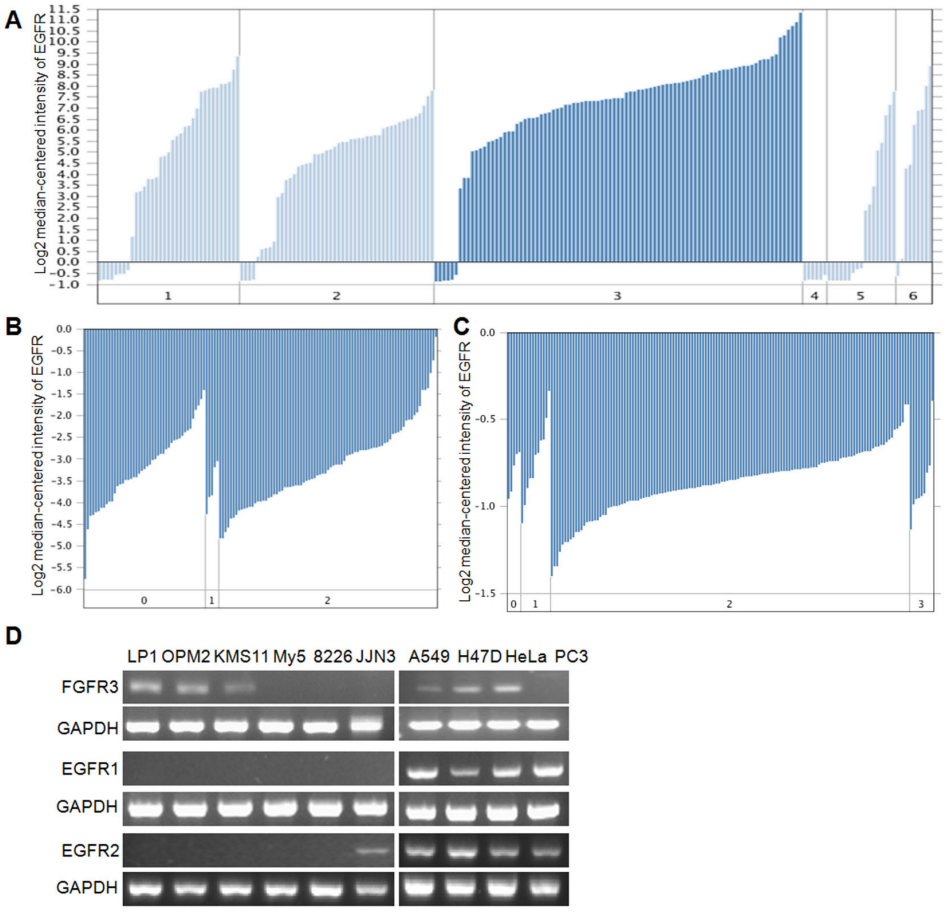

Figure 4. EGFR is not expressed in MM cells. (**A**) EGFR expression in various solid cancers and lymphoma retrieved from the Adai Cell Line dataset of Oncomine database.1. Breast Cancer (n = 35); 2. Colorectal Cancer (n = 48); 3. Lung Cancer (n = 91); 4. Lymphoma (n = 6); 5. Melanoma (n = 17); 6. Ovarian Cancer (n = 9). (**B**) EGFR expression retrieved from the Zhan Myeloma dataset of Oncomine database. 0. normal (n = 45); 1. MGUS (n = 5); 2. MM (n = 81). (**C**) EGFR expression retrieved from the Agnelli Myeloma 3 dataset of Oncomine database. 0. Normal (n = 5); 1. MGUS (n = 11); 2. MM (n = 133); 3. plasma cell leukemia (n = 9). (**D**) Representative cancer cell lines were collected to isolate total RNA, followed by RT-PCR. The products were isolated on agarose gels.

Therefore, 4061 and 4065B displayed potent activity against MM by inhibiting IGF1-R/AKT/mTOR signaling transduction.

4. Discussion

The AKT/mTOR signaling pathway is activated by receptor tyrosine kinases including EGFR, FGFR, IGFR, PDGFR and others, upon individual ligand binding, thus this pathway plays a critical role in proliferation and survival of various cancers including solid tumors such as NSCLC and liquid tumors such as MM (*16*). Inhibitors of EGFR and IGF1-R have been developed for the treatment of various cancers (*8,17*). The most well known one is gefitinib, the first-in-class EGFR inhibitor, which has been widely used for the treatment of NSCLC patients with mutated and overactivated EGFR. However, this powerful drug is not effective in most liquid tumors, such as MM (*3*). The present study found that the endoperoxide bridge conjugated to the 4-anilinoquinazoline core scaffold displayed potent anti-MM activity.

EGFR is the target of gefitinib in NSCLC but it is less expressed or not expressed in MM cells (*18*). The present study also demonstrated that EGFR1 and EGFR2, two major isoforms of EGFRs, were not detected from most MM cell lines examined, which is consistent with previous studies in which EGFR1 and other isoforms

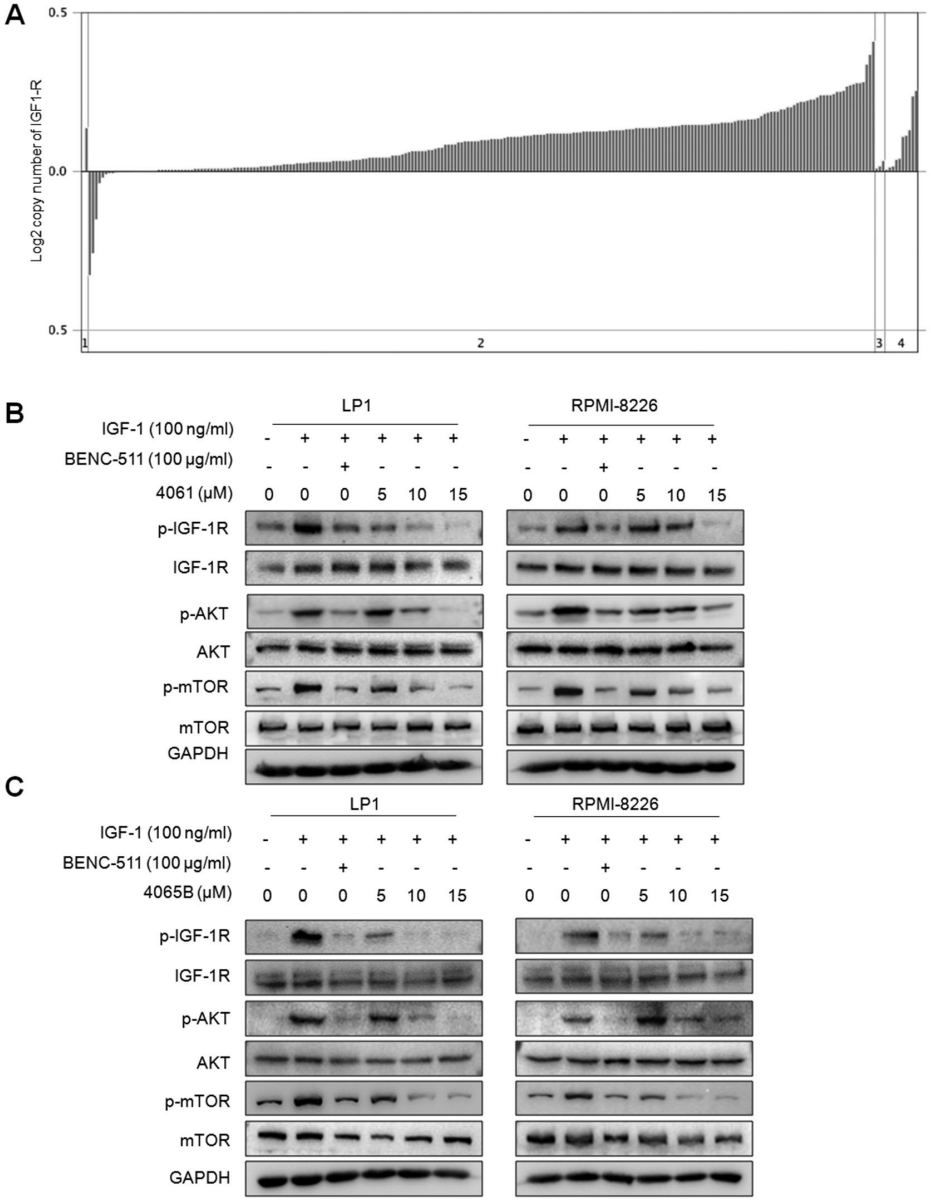

Figure 5. 4061 and 4065B inhibit the IGFR/AKT/mTOR signaling transduction. (**A**) The expression profile of IGF1-R in MM cells retrieved from the Chapman Myeloma 2 dataset of Oncomine Dataset. 1. MGUS (*n* = 2); 2. MM (*n* = 239); 3. plasma cell leukemia (*n* = 3); 4. SMM (*n* = 10). (**B, C**) RPMI-8226 and LP1 were stored with 4061 **(B)** or 4065B **(C)** overnight or BENC-511 for 2 hrs. Cells were further treated with 100 μg/mL of IGF-1 for 15 min. Cells were then harvested for immunoblotting assays against indicated antibodies. GAPDH was measured as an internal control.

are not detected in RPMI-8226, a typical MM cell line (*18*) or at a relative low level compared with solid cancers (*19*). Therefore, there is no wonder that gefitinib is ineffective in MM. However, 4061 and 4065B that conjugate 4-anilinoquinazoline, the pharmacophore of gefitinib, and peroxide bridge, the pharmacophore of artemisinin, displayed great activity in MM cell apoptosis. The underlying mechanisms of these two compounds in MM cell apoptosis are probably associated with the production of reactive oxygen species (ROS). ROS is believed to be a major mechanism in the anti-cancer activity of some compounds such as artemisinin and derivatives that contain an endoperoxide group (*20*). The *in vivo* studies demonstrated that the ferrous iron mediated cleavage of the endoperoxide group to release ROS and/or carbon centered radicals that further induce DNA damage, mitochondrial depolarization and apoptosis. In the RTK-associated signaling transduction, IGF1/IGF1-R activated AKT/mTOR signaling pathway is probably another target because activation of IGF1-R by phosphorylation is inhibited by both 4061 and 4065B. The IGF1/IGF1-R pathway including its constitutive ligands and receptors not only contributes to the survival, proliferation, and homing of MM cells, but also leads to MM-associated angiogenesis and osteolysis (*21,22*). IGF1/IGF1-R overexpression is closely correlated to poor prognosis in MM patients (*22*). Targeting the IGF system has been developed for MM treatment, *e.g*. IGFR monoclonal antibodies such as AVE1642 (*23*) and small chemical compound inhibitors OSI-906 (*24*) have been developed in preclinical models with great potential for MM treatment. In the present study, the growth factor IGF1 drastically induces the phosphorylation of both AKT and mTOR, but these signals were suppressed by both 4061 and 4065B in a concentration-dependent manner, suggesting that 4061 and 4056B at least inhibit IGF1/IGF1-R-mediated AKT/mTOR signaling. This is probably one major mechanism in that 4061 and 4056B go beyond gefitinib that is not effective in MM cell apoptosis.

In conclusion, this present study reported novel agents by conjugating endoperoxide bridge to 4-anilinoquinazoline that display potential for the treatment of liquid cancers such as MM by suppressing the IGF1-R/AKT/mTOR signaling pathway. These compounds might represent a novel class of anti-MM drugs.

Acknowledgements

This study was partly supported by grants from the National Natural Science Foundation of China (81770215 to BC; 81972841 to XX).

References

1. Manni S, Carrino M, Semenzato G, Piazza F. Old and young actors playing novel roles in the drama of multiple myeloma bone marrow microenvironment dependent drug resistance. Int J Mol Sci. 2018; 19. pii: E1512.
2. Chang GC, Yu CT, Tsai CH, Tsai JR, Chen JC, Wu CC, Wu WJ, Hsu SL. An epidermal growth factor inhibitor, Gefitinib, induces apoptosis through a p53-dependent upregulation of pro-apoptotic molecules and downregulation of anti-apoptotic molecules in human lung adenocarcinoma A549 cells. Eur J Pharmacol. 2008; 600:37-44.
3. Chen Y, Huang R, Ding J, Ji D, Song B, Yuan L, Chang H, Chen G. Multiple myeloma acquires resistance to EGFR inhibitor *via* induction of pentose phosphate pathway. Sci Rep. 2015; 5:9925.
4. Yang J, Tu Z, Xu X,Luo J,Yan X, Ran C,Mao X, Ding K, Qian C. Novel conjugates of endoperoxide and 4-anilinoquinazoline as potential anticancer agents. Bioorg Med Chem Lett. 2017; 27:1341-1345.
5. Holien T, Olsen OE, Misund K, Hella H, Waage A, Rø TB, Sundan A. Lymphoma and myeloma cells are highly sensitive to growth arrest and apoptosis induced by artesunate. Eur J Haematol. 2013; 91:339-346.
6. Mao H, Du Y, Zhang Z, Cao B, Zhao J, Zhou H, Mao X. Nitroxoline shows antimyeloma activity by targeting the TRIM25/p53 axle. Anticancer Drugs. 2017; 28:376-383.
7. Hartwig CL, Rosenthal AS, D'Angelo J, Griffin CE, Posner GH, Cooper RA. Accumulation of artemisinin trioxane derivatives within neutral lipids of Plasmodium falciparum malaria parasites is endoperoxide-dependent. Biochem Pharmacol. 2009; 77:322-336.
8. Lee DH. Treatments for EGFR-mutant non-small cell lung cancer (NSCLC): the road to a success, paved with failures. Pharmacol Ther. 2017; 174:1-21.
9. Zhan F, Hardin J, Kordsmeier B, *et al.* Global gene expression profiling of multiple myeloma, monoclonal gammopathy of undetermined significance, and normal bone marrow plasma cells. Blood. 2002; 99:1745-1757.
10. Agnelli L, Mosca L, Fabris S, Lionetti M, Andronache A, Kwee I, Todoerti K, Verdelli D, Battaglia C, Bertoni F, Deliliers GL, Neri A. A SNP microarray and FISH-based procedure to detect allelic imbalances in multiple myeloma: an integrated genomics approach reveals a wide gene dosage effect. Genes Chromosomes Cancer. 2009; 48:603-614.
11. Wang J, Li X, Xue X, Ou Q, Wu X, Liang Y, Wang X, You M, Shao YW, Zhang Z, Zhang S. Clinical outcomes of EGFR kinase domain duplication to targeted therapies in NSCLC. Int J Cancer. 2019; 144:2677-2682.
12. Sprynski AC, Hose D, Caillot L, *et al.* The role of IGF-1 as a major growth factor for myeloma cell lines and the prognostic relevance of the expression of its receptor. Blood. 2009; 113:4614-4626.
13. Chapman MA, Lawrence MS, Keats JJ, *et al.* Initial genome sequencing and analysis of multiple myeloma. Nature. 2011; 471:467-472.
14. Zhu J, Wang M, Cao B, Hou T, Mao X. Targeting the phosphatidylinositol 3-kinase/AKT pathway for the treatment of multiple myeloma. Curr Med Chem. 2014; 21:3173-3187.
15. Han K, Xu X, Chen G, Zeng Y, Zhu J, Du X, Zhang Z, Cao B, Liu Z, Mao X. Identification of a promising PI3K inhibitor for the treatment of multiple myeloma through the structural optimization. J Hematol Oncol. 2014; 7:9.
16. Zhu J, Hou T, Mao X. Discovery of selective phosphatidylinositol 3-kinase inhibitors to treat

hematological malignancies. Drug Discov Today. 2015; 20:988-994.
17. Gariboldi MB, Ravizza R, Monti E. The IGFR1 inhibitor NVP-AEW541 disrupts a pro-survival and pro-angiogenic IGF-STAT3-HIF1 pathway in human glioblastoma cells. Biochem Pharmacol. 2010; 80:455-462.
18. Zhang XD, Baladandayuthapani V, Lin H, *et al.* Tight junction protein 1 modulates proteasome capacity and proteasome inhibitor sensitivity in multiple myeloma *via* EGFR/JAK1/STAT3 signaling. Cancer Cell. 2016; 29:639-652.
19. Mahtouk K, Jourdan M, De VJ, Hertogh C, Fiol G, Jourdan E, Rossi JF, Klein B. An inhibitor of the EGF receptor family blocks myeloma cell growth factor activity of HB-EGF and potentiates dexamethasone or anti-IL-6 antibody-induced apoptosis. Blood. 2004; 103:1829-1837.
20. Terzic N, Opsenica D, Milic D, Tinant B, Smith KS, Milhous WK, Solaja BA. Deoxycholic acid-derived tetraoxane antimalarials and antiproliferatives (1). J Med Chem. 2007; 50:5118-5127.
21. Bieghs L, Johnsen HE, Maes K, Menu E, Van Valckenborgh E, Overgaard MT, Nyegaard M, Conover CA, Vanderkerken K, De Bruyne E. The insulin-like growth factor system in multiple myeloma: diagnostic and therapeutic potential. Oncotarget. 2016; 7:48732-48752.
22. Bataille R, Robillard N, Avet-Loiseau H, Harousseau JL, Moreau P. CD221 (IGF-1R) is aberrantly expressed in multiple myeloma, in relation to disease severity. Haematologica. 2005; 90:706-707.
23. Descamps G, Gomez-Bougie P, Venot C, Moreau P, Bataille R, Amiot M. A humanised anti-IGF-1R monoclonal antibody (AVE1642) enhances Bortezomib-induced apoptosis in myeloma cells lacking CD45. Br J Cancer. 2009; 100:366-369.
24. Kuhn DJ, Berkova Z, Jones RJ, *et al.* Targeting the insulin-like growth factor-1 receptor to overcome bortezomib resistance in preclinical models of multiple myeloma. Blood. 2012; 120:3260-3270.

Received November 9, 2019; Revised February 18, 2020; Accepted March 3, 2020

**Address correspondence to:*
Yuanying Zeng, Department of Oncology, Suzhou Municipal Hospital, 16 Baita West Rd., Suzhou, Jiangsu 215100, China.
E-mail: zengyuanying@163.com

Xinliang Mao, Department of Pharmacology, College of Pharmaceutical Sciences, Soochow University, 199 Ren Ai Road, Suzhou, Jiangsu 215123, China.
E-mail: xinliangmao@gzhmu.edu.cn

Released online in J-STAGE as advance publication March 13, 2020.

Original Article

DOI: 10.5582/bst.2019.01345

Comparative transcriptome analysis of transcultured human skin-derived precursors (tSKPs) from adherent monolayer culture system and tSKPs-derived fibroblasts (tFBs) by RNA-Seq

Ru Dai[1,2,§], Wei Chen[3,§], Wei Hua[1], Lidan Xiong[1], Yiming Li[1], Li Li[1,*]

[1] Department of Dermatology, West China Hospital, Sichuan University, Chengdu, Sichuan, China;
[2] Department of Dermatology, Ningbo First Hospital, Ningbo University, Ningbo, Zhejiang, China;
[3] Department of Medical Cosmetology, The Second People's Hospital of Chengdu, Chengdu, Sichuan, China.

SUMMARY Transcultured human skin derived precursors (tSKPs) from adherent monolayer culture system have similar characteristics as traditional skin derived precursors (SKPs), making tSKPs a suitable candidate for regenerative medicine. tSKPs can differentiate into fibroblasts. However, little is known about the molecular mechanism of the transition from tSKPs to fibroblasts. Here, we compared the transcriptional profiles of human tSKPs and tSKPs-derived fibroblasts (tFBs) by RNA-Sequence aiming to determine the candidate genes and pathways involving in the differentiation process. A total of 1042 differentially expressed genes (DEGs) were identified between tSKPs and tFBs, with 490 genes up-regulated and 552 genes down-regulated. Our study showed that these DEGs were significantly enriched in tumor necrosis factor signaling pathway, focal adhesion, extracellular matrix-receptor interaction and phosphatidylinositol 3 kinase (PI3K)/protein kinase B (Akt) signaling pathway. A further transcription factors (TFs) analysis of DEGs revealed the significantly down-expressed TFs (p21, Foxo1and Foxc1) in tFBs were mostly the downstream nodes of PI3K-Akt signaling pathway, which suggested PI3K-Akt signaling pathway might play an important role in tSKPs differentiation. The results of our study are useful for investigating the molecular mechanisms in tSKPs differentiation into tFBs, making it possible to take advantage of their potential application in regenerative medicine.

Keywords skin derived precursors, fibroblasts, stem cell, RNA-Seq, adherent culture system

1. Introduction

Skin-derived precursors (SKPs) from dermis, firstly described by Toma *et al*. in 2001 (*1*), are adult stem cells with the capacities of self-renewal and multipotency (*2*). Conventionally, SKPs are cultured as floating spheres in suspending serum-free medium with required growth factors (*3*); however, many studies have reported that isolating human SKPs by this protocol has many limitations such as relatively low yield (*4*), slow growth rate (*3*), and heterogeneous spheres (*5*). Therefore, it is unsurprising that several studies have demonstrated a new technique to transculture human SKPs from adherent monolayer culture system (henceforth termed tSKPs), and these tSKPs are similar to traditional SKPs in morphology and function (*6-8*). Developments in tSKPs research have indicated their potential application in regenerative medicine.

Under proper stimulus, tSKPs can differentiate into cells of both neural and mesodermal lineages, including neurons (*7*), Schwann cells (*6,7*), smooth muscle cells (*6,8*), osteogenic (*6,7*) and adipogenic cells (*6,7*). It has also been reported that tSKPs can differentiate into fibroblasts (FBs) (*8*). Cultured in low-glucose medium with 15% fetal bovine serum, tSKPs presented fibroblast-like morphology and expressed fibroblast marker of prolyl-4-hydroxylase beta-an enzyme involved in collagen synthesis (*8*). Previous studies have demonstrated that SKPs became morphologically similar to the endogenous fibroblasts and expressed fibroblast markers when transplanted into dermis, while did not express markers of neurons or peripheral glia (*9,10*). Moreover, SKPs could integrate throughout the thickness of the dermis, mostly locating in the dermal papilla and dermal sheath of hair follicles (*9*). As the principal cellular target of skin regeneration, FBs play a pivotal role in maintaining the morphology and function of normal skin. Since tSKPs can differentiate

into fibroblasts, they may serve as potential sources for treating aged skin, atrophic skin diseases or skin repair by replenishing the lost or damaged FBs.

As a requisite to potential applications in cell-based therapies, it is essential to understand the molecular mechanisms that why and how tSKPs can differentiate into FBs. Actually, any biological changes of stem cells including whether they self-renew, remain quiescence, proliferate, differentiate or undergo apoptosis, is ultimately the alterations of gene expression (*11*). Therefore, it is necessary to investigate gene evolution of related cells at the expression level for which may provide further insights into mechanisms.

To date, no studies have compared the transcriptomic profiles between human tSKPs and tSKPs-derived FBs (tFBs). Hence, this study aims to perform a comparative transcriptomes between tSKPs and tFBs by RNA-Sequence (RNA-Seq). We assume that our study may help determine the candidate genes and pathways that involve in the differentiation of tSKPs to fibroblasts, thus broaden the potential application of tSKPs in the treatment of skin-related diseases.

2. Materials and Methods

2.1. Cell Preparation

Human skin samples were collected from patients undergoing circumcisions with informed consents signed. Our study was conducted in accordance with the ethical guidelines of West China Hospital (Chengdu, China) and had Ethics Committee approval (No. 2017064A).

The protocol for isolating tSKPs has been described previously in our study (*6*). For directing tSKPs into tFBs, spheres were collected, resuspended in dulbecco's modified eagle medium (DMEM) containing 10% fetal bovine serum, and then seeded into cell culture dishes.

2.2. Immunocytochemistry

Cells were plated onto slides and fixed with 4% paraformaldehyde for 30 minutes at room temperature. The fixed cells were permeabilized with 0.25% Triton X-100 for 10 minutes and subsequently blocked with 3% bull serum albumin for 30 minutes. Then, cells were incubated with primary antibodies overnight at 4℃ and with secondary antibodies for 1 hour at room temperature. Finally, cells were incubated with DAPI (Dojindo, Japan) for 1 minute before visualizing under a fluorescence microscope (Olympus, Japan). Primary antibodies were anti-Versican (Abcam, UK, 1:200), anti-Fibronectin (Abcam, UK, 1:250), anti-Collagen I (Abcam, UK, 1:250), anti-Vimentin (Abcam, UK, 1:250), anti-Sox2 (Abcam, UK, 1:250) and anti-Nestin (Abcam, UK, 1:250). The secondary antibodies were Alexa Fluro® 488 donkey anti-mouse IgG (Abcam, UK, 1:500) and Alexa Fluro® 488 goat anti-rabbit IgG (Abcam, UK, 1:500). The protocol was performed in triplicate for each cell type described.

2.3. RNA-Seq

2.3.1. Library Preparation

cDNA library preparation was prepared at Novogene Co., LTD, Beijing. Total RNA was extracted from samples by Trizol (Ambion, USA). mRNA was purified using olidgo (dT) magnetic beads, and broken into short fragments in fragmentation buffer. Taking mRNA as a temple, first strand cDNA was synthesized using random hexamers. Second strand cDNA was subsequently synthesized in the condition of deoxyribonucleoside triphosphates (dNTPs), DNA polymerase I, and buffer. cDNA was purified with AMPure XP beads and then performed end reparation and 3'-end single nucleotide A addition. At last, the resulting fragments were screened by AMPure XP beads and enriched by PCR amplication. The quality of library products was determined on the Agilent Bioanalyzer 2100 system, and the qualified products were used for sequencing on Illumina HiSeq™ 2000.

2.3.2. Mapping Reads to the Reference Genome

The original image data generated from HiSeq was transferred into sequence using base calling, and these sequences were defined as "raw reads". The resulting sequences were filtered as follows: remove adaptor sequences, N sequences and low-quality sequences. The remaining reads were mapped to the human genome using Tophat v2.0.12, and no more than 2 mismatches were allowed in the alignment. The RNA-Seq data is provided on GEO with the accession number of GSE133190.

2.3.3. Statistical Analysis and Screening of Differentially Expressed Genes (DEGs)

The gene expression level was presented by the Reads Per Kb per Million reads (RPKM) method, which was calculated based on the length of the gene and sequencing discrepancies. HTSeq v0.6.1 was used to count the read numbers mapped to each gene. RPKM values could be used for comparing the difference of gene expression in different samples using DEGSeq v1.12.0. *p*-value was used corresponding to a differential gene expression test at statistically significant levels. "|log2 (Fold change)| ≥ 1 and False Discovery rate < 0.001" were set to identify DEGs as the threshold.

2.3.4. Functional Annotation of DEGs

Gene ontology (GO) enrichment analysis of DEGs that were significantly enriched in all GO terms compared

to genome background using GOSeq (Release 2.23). The corresponding biological functions related to the DEGs were also presented. The calculated *p* value was adjusted through Benjamini and Hochberg's approach, using an adjusted $p < 0.05$ as a threshold. GO terms with adjusted $p < 0.5$ were regarded as significantly enriched by DEGs.

The analysis of kyoto encyclopedia of genes and genomes (KEGG) was the major public pathway-related database, which provided all KEGG pathways that are significantly enriched in DEGs. The calculating formula was the same as that in GO analysis, using KOBAS v2.0.

The regulation of gene transcription, which is important for many biological functions, relies largely on transcription factors (TFs). TFs can active or inhibit downstream gene transcription by binding to specific upstream nucleotide sequences. TFCat (*http://www.tfcat.ca/*) is a curated catalog of mouse and human TFs based on a reliable core collection of annotation obtained by expert review of the scientific literature (*12*), which provides reliable data of functional category and confidence level of candidate TFs. In this study, TFCat was used to characterize and annotate TFs in DEGs.

2.4. Quantitative Real Time Reverse Transcription PCR (qRT-PCR) for Validation

Main DEGs involved in important KEGG pathways or related to TFs were selected to verify the RNA-Seq data by qRT-PCR: Mmp9, Ccl20, Vcam1, Csf3, Cxcl5, Foxo1, Nr4a1, Foxc1, Foxm1, Cited2, Mylk, Thbs1, Hmgb2, Dhcr24, Dhcr7 and Vegfc. Total RNA was extracted from cells using Trizol, then was converted to cDNA using the iScript™ cDNA Synthesis Kit (Bio-Rad, USA) according to the manufacturer's instructions. qRT-PCR was carried out using the CFX Connect™ Real-Time PCR Detection System (Bio-Rad, USA) with SsoAdvanced™ Universal SYBR® Green Supermix (Bio-Rad, USA). The primers were described in Table S1 (*http://www.biosciencetrends.com/action/getSupplementalData.php?ID=63*). The mRNA expression levels were normalized by the internal β-actin control and the relative expression of each gene was calculated using the $2^{-\Delta\Delta Ct}$ method. Three independent biological experiments and two technical replicate were performed. Pearson correlation coefficient between qRT-PCR data and RNA-Seq data was calculated to validate RNA-Seq experiments.

3. Results

3.1. Differentiation of tSKPs into Fibroblasts

tSKPs were successfully isolated from primary adherent monolayer culture system established from human skin tissue. The tSKPs demonstrated a sphere-like structure in suspension 7 days after transculturing (Figure 1A). Being cultured in the medium differentiated toward tFBs, cells adhered to the plastic and presented a flattened and spindle-shaped morphology (Figure 1B), similar to the characteristic morphology of primary-cultured FBs (pFBs) (Figure 1C).

The protein expressions of cells were analyzed by immunocytochemistry. As shown in Figure 2, tSKPs expressed Versican (Figure 2A), Fibronectin (Figure 2D), Vimentin (Figure 2J), Sox2 (Figure 2M) and Nestin (Figure 2P), while did not express Collagen I (Figure 2G), which was consistent with traditional

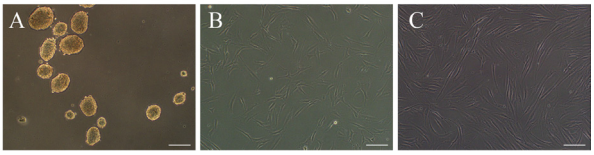

Figure 1. Morphology of tSKPs and fibroblasts. (**A**) tSKPs presented a sphere-like structure. (**B**) tFBs differentiated from tSKPs had same morphology as pFBs. (**C**) pFBs presented a flattened and spindle-shaped morphology. Scar bars: 100 μm.

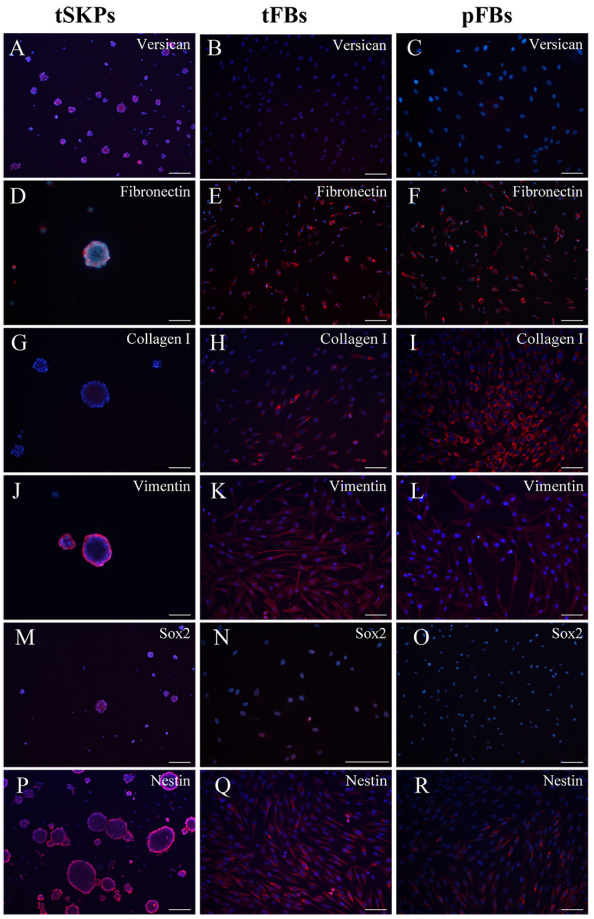

Figure 2. Immunocytochemical analysis of tSKPs and fibroblasts. tSKPs spheres expressed Versican (**A**), Fibronectin (**D**), Vimentin (**J**), Sox2 (**M**) and Nestin (**P**), did not express Collagen I (**G**); tFBs expressed Fibronectin (**E**), Collagen I (**H**), Vimentin (**K**) and Nestin (**Q**), did not express Versican (**B**) and Sox2 (**N**). PFBs expressed Fibronectin (**F**), Collagen I (**I**) and Vimentin (**L**), weakly expressed nestin (**R**), and did not express Sox2 (**O**) and Versican (**C**). Scar bars: 100 μm.

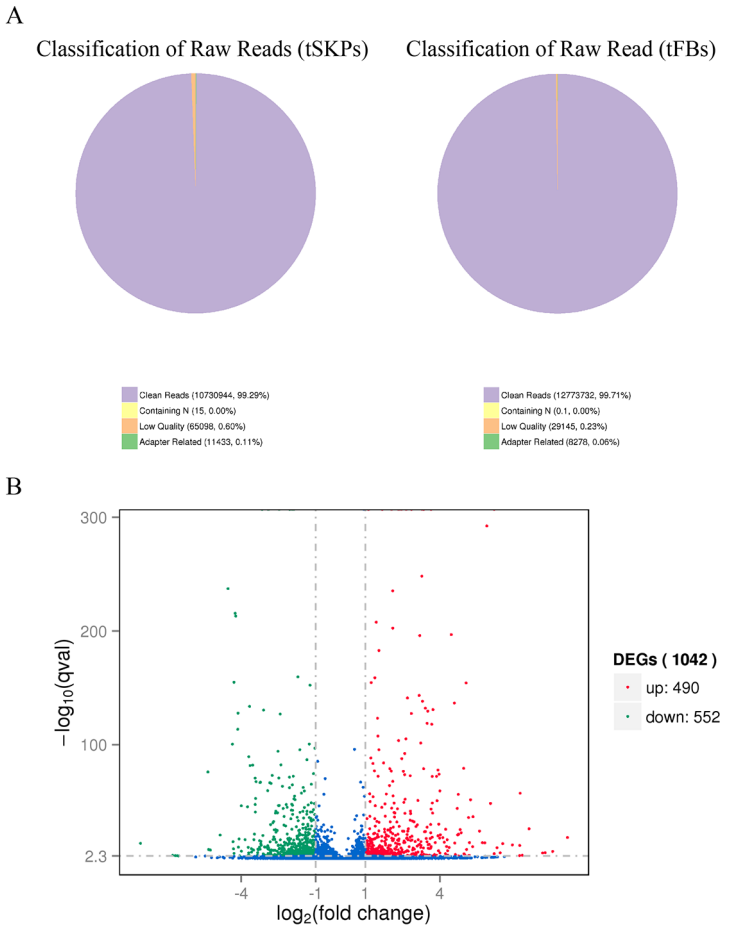

Figure 3. Quality assessment of reads and DEGs between tSKPs and tFBs. (**A**) Classification of raw reads in tSKPs and tFBs. (**B**) Scattered plot of DEGs identified between tSKPs and tFBs.

Table 1. Summary of mapping results (mapping to reference genes)

Sample name	Total reads	Total mapped	Multiple mapped	Uniquely mapped	Non-splice reads	Splice reads
tSKPs_RNA	10730944	10389834 (96.82%)	600661 (5.6%)	9789173 (91.22%)	7759368 (72.31%)	2029805 (18.92%)
tFBs_RNA	12773732	12522653 (98.03%)	668801 (5.24%)	11853852 (92.8%)	9627457 (75.37%)	2226395 (17.43%)

tSKPs: transcultured skin-derived precursors; tFB: tSKPs-derived fibroblasts.

SKPs (*4*). tFBs expressed Fibronectin (Figure 2E), Collagen I (Figure 2H), Vimentin (Figure 2K), and Nestin (Figure 2Q), while were negative for Versican (Figure 2B) and Sox2 (Figure 2N). As for pFBs, they were positive for Fibronectin (Figure 2F), Collagen I (Figure 2I), Vimentin (Figure 2L) and Nestin (Figure 2R). However, the expression level of Collagen I was stronger and the Nestin expression level was weaker in pFBs compared with tFBs. pFBs also did not express Versican (Figure 2C) and Sox2 (Figure 2O). The results of immunofluorescence staining of tFBs and pFBs were similar. Herein, our data showed that tSKPs could differentiate into fibroblast in adhesive culture with serum, which was consistent with previous studies on mouse (*13*), and porcine (*14*). Concomitantly, they gradually lost the neural potential while appeared certain mesodermal capacity during this process.

3.2. Quality Assessment of Samples by RNA-Seq

More than 10 million raw reads were generated from tSKPs or tFBs. The percentage of clean reads of each library was 99.29% and 99.71% respectively (Figure 3A). The mapping rate of each one was 96.82% and 98.03% of the total read (Table 1). The detailed information of quality assessment of reads and statistics of alignment were presented in Figure 3A and Table 1.

3.3. Analysis of DEGs between tSKPs and tFBs

A total of 1042 DEGs were identified between tSKPs and tFBs, with 490 genes up-regulated and 552 genes down-regulated (Figure 3B). The full lists of up-regulated and down-regulated DEGs were shown in Table S2 (*http://www.biosciencetrends.com/action/*

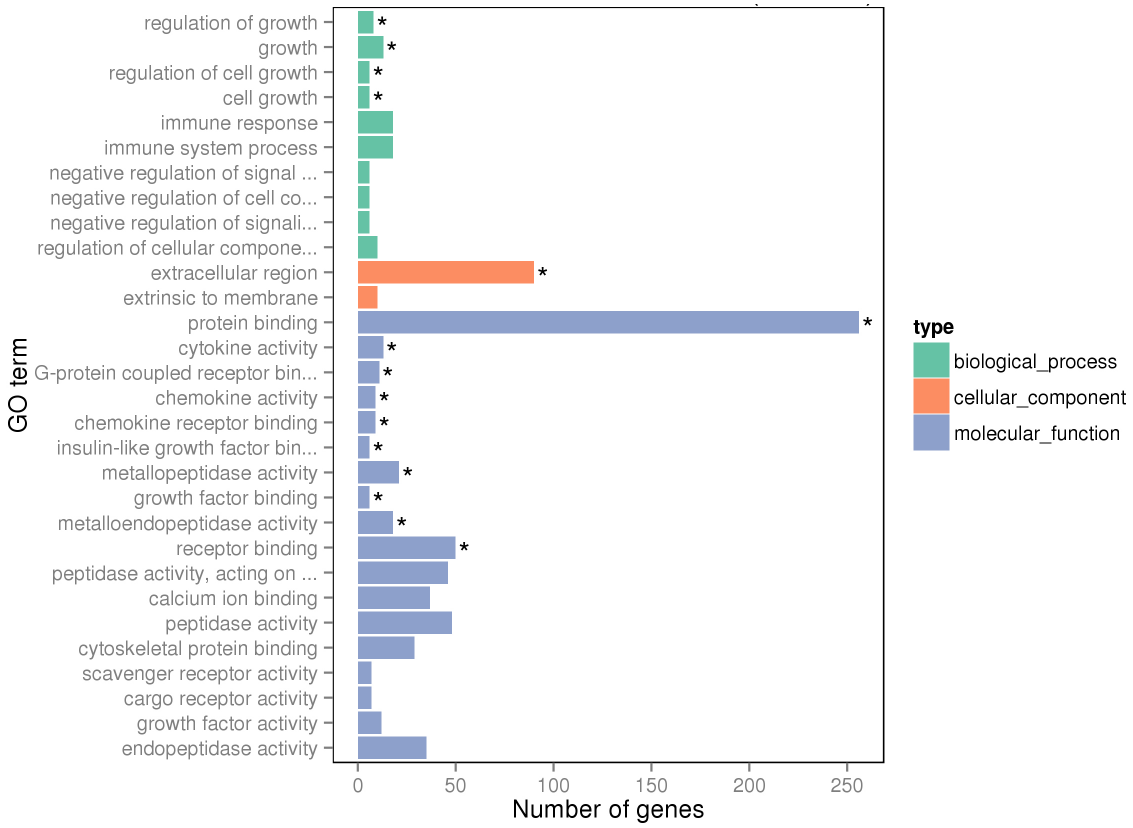

Figure 4. GO terms of DEGs. The top 30 enriched GO terms in the three main domains: biological process (10), cellular component (2), and molecular function (18). *Significantly enriched GO term.

getSupplementalData.php?ID=63).

3.4. GO Enrichment Analysis of DEGs

The 1042 DEGs could be categorized into 1971 GO terms. GO functional analysis identified the top 30 DEGs enriched GO terms (Figure 4). Among the GO annotations, 18 GO terms were in the domain of molecular function, and terms protein binding, cytokine activity, G-protein coupled receptor binding, chemokine activity, chemokine receptor binding, insulin-like growth factor binding, metallopeptidase activity, growth factor binding, metalloendopepetidase activity and receptor binding were dominant; 2 GO terms were in the domain of cellular component, and the term extracellular region was significantly enriched; 10 GO terms were related to biologic process, and the terms regulation of growth, growth, regulation of cell growth and cell growth were also significantly enriched.

3.5. KEGG Enrichment Analysis of DEGs

KEGG analysis identifies the pathways where DEGs are significantly enriched, which is beneficial for further understanding of DEGs biological functions. In our study, the top 20 enriched KEGG pathways were presented in Figure 5, and 9 pathways were identified to be significantly enriched in DEGs between tSKPs and FBs (Table S3, *http://www.biosciencetrends.com/action/getSupplementalData.php?ID=63*), including tumor necrosis factor (TNF) signaling pathway (Figure S1, *http://www.biosciencetrends.com/action/getSupplementalData.php?ID=63*), focal adhesion (Figure S2, *http://www.biosciencetrends.com/action/getSupplementalData.php?ID=63*), extracellular matrix (ECM)-receptor interaction (Figure S3, *http://www.biosciencetrends.com/action/getSupplementalData.php?ID=63*) and phosphatidylinositol 3 kinase (PI3K)-protein kinase B (Akt) signaling pathway (Figure S4, *http://www.biosciencetrends.com/action/getSupplementalData.php?ID=63*). The main DEGs involved in these signaling pathways were listed in Table 2.

3.6. TF Annotation Analysis of DEGs

Regulation at the transcriptional level is important for gene expression. TFs can bind to specific upstream nucleotide sequences, thereby controlling the rate of transcription of downstream genes (*15*). Their activity determines how cells function and respond to external environments. The annotation analysis of TFs identified the differentially expressed TFs of DEGs between tSKPs and tFBs, and the main up-regulated and down-regulated TFs with strong evidence and their function were listed in Table 3.

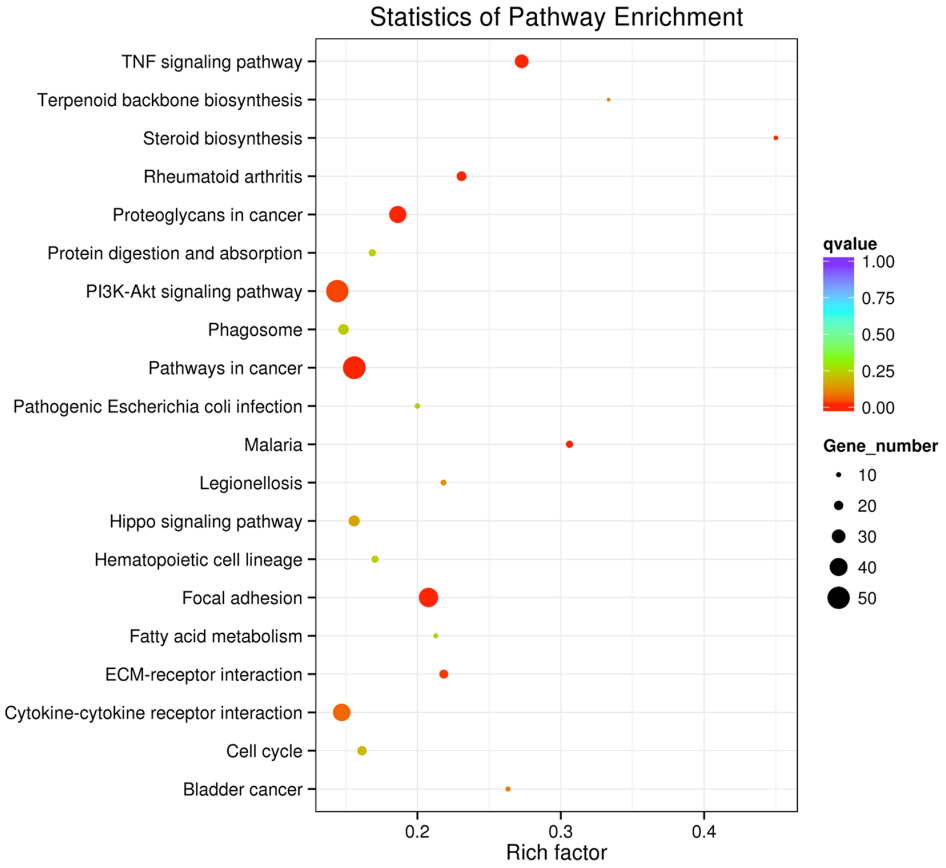

Figure 5. KEGG analysis of DEGs. Scattered plot of DEGs enriched KEGG pathways.

Table 2. List of possible signaling pathways and major DEGs involved in these pathways

Items	Up-regulated DEGs	Down-regulated DEGs
TNF signaling pathway	MMP9, CCL5/20, VCAM1, LIF, TNFAIP3, CXCL1/2/3/5, BIRC3, PTGSZ, IL18R1, IL6, IL1B	CREB3L1, VEGFC, CSF1
Focal adhesion	LAMC2/3, HGF, VEGFA, BIRC3, COL4A1, SHC2	MYLK, MYL9, FLNC, DAPK2, VEGFC, THBS1, ACTB, ITGA4, FLT1
ECM-receptor interaction	LAMC2/3, COL4A2/1, COL5A3, COMP, COL3A1	SDC1, THBS1, ITGA4
PI3K-Akt signaling pathway	LAMC2/3, BCL2L11, IL6, COMP, NGFR, COL4A1, CSF3	FGF1/5, CREB3L1, EPHA2, VEGFC, THBS1, ITGA4, FLT1, Itga6, Angpt1, Csf1, Il7r

DEGs: differentially expressed genes; TNF: tumor necrosis factor; ECM: extracellular matrix; PI3K: phosphatidylinositol 3 kinase; Akt: protein kinase B.

Table 3. List of major up-regulated and down-regulated transcription factors with strong evidence

Function	Up-regulated transcription factor	Down-regulated transcription factor
DNA binding	Snail2, Foxc1, Nfkb2, Xbp1, Mef2d, Cdkn1a, Nr1d1, Creg1, Foxo1, Nr4a2, Klf10, Tgif1	Foxm1, Hic1, Nr2f2, Tead1
Transactivation	Foxc1, Notch3, Xbp1, Mef2d, Foxo1, Nr4a2, Tgif1, Nr2f2, Tead1	Cited2, AR, Hic1, Nr2f2, Tead1
Co-activation	Notch3, Ncoa7, Nr4a2	Cited2
TF PPI	Nfkbia, Bag1	Runx1t1, Hmgb2, Cited2, AR
Other	Mxi1	/

TF: transcription factor.

Table 4. Validation of RNA-Seq results and comparison of selected genes expression between tSKPs and tFBs by qRT-PCR

Gene	Category	RNA-Seq (tSKPs/tFBs) Fold Change	qRT-PCR (tSKPs/tFBs) Fold Change (Mean ± SE)
Mmp9	Up-regulated	9.13	10.87 ± 1.35
Ccl20	Up-regulated	8.14	9.03 ± 0.08
Vcam1	Up-regulated	7.21	6.58 ± 0.50
Csf3	Up-regulated	6.04	5.91 ± 0.31
Cxcl5	Up-regulated	4.96	5.14 ± 1.17
Foxo1	Up-regulated	3.24	3.40 ± 0.39
Nr4a2	Up-regulated	3.92	4.21 ± 0.37
Foxc1	Up-regulated	2.87	2.24 ± 0.35
Foxm1	Down-regulated	2.32	2.38 ± 0.21
Cited2	Down-regulated	1.93	1.71 ± 0.01
Mylk	Down-regulated	4.12	4.18 ± 0.69
Thbs1	Down-regulated	3.16	3.16 ± 0.25
Hmgb2	Down-regulated	1.37	1.23 ± 0.03
Dhcr24	Down-regulated	3.64	3.37 ± 0.48
Dhcr7	Down-regulated	4.00	3.90 ± 0.32
Vegfc	Down-regulated	2.07	2.12 ± 0.05

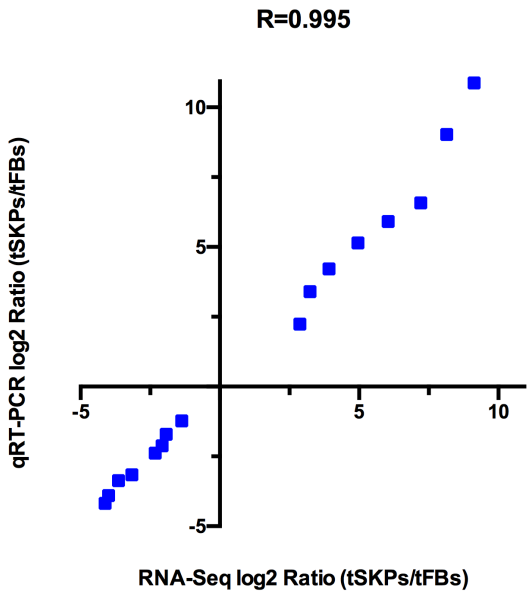

Figure 6. Correlation of selected genes between RNA-Seq and qRT-PCR. Pearson correlation coefficient (R = 0.995) was used to determine the consistency in gene expression pattern between RNA-Seq and qRT-PCR.

3.7. qRT-PCR for Data Validation

Sixteen main DEGs (up-regulated: Mmp9,Ccl20, Vcam1, Csf3, Cxcl5, Foxo1, Nr4a2 and Foxc1; down-regulated: Foxm1, Cited2, Mylk, Thbs1, Hmgb2, Dhcr24, Dhcr7 and Vegfc) related to TF or involved in important KEGG pathways were selected to verify the RNA-Seq data by qRT-PCR (Table 4). Pearson correlation coefficient between RNA-Seq data and qRT-PCR data was 0.995 (Figure 6), which indicated that RNA-Seq could provide reliable data for mRNA differential expression analysis.

3.8. RNA-Seq Analysis of tFBs and pFBs

The genomic profiles of tFBs and pFBs from same human dermis sample were also compared by RNA-Seq. A total of 268 DEGs were identified between pFBs and tFBs, with 139 genes up-regulated and 129 genes down-regulated (Figure 7A). GO function analysis revealed that no significant GO term enriched with DEGs was found (Figure 7B). KEGG pathway enrichment analysis showed that candidate genes were most significantly enriched in the terpenoid backbone biosynthesis, ECM-receptor interaction, focal adhesion and steroid biosynthesis (Figure 7C), most of which were associated with metabolism and morphogenesis.

4. Discussion

In present study, we compared the transcriptional profiles of human tSKPs and tFBs by RNA-Seq. RNA-Seq is an application of next-generation sequencing technique to analyze transcriptome at a given moment and can be used for revealing different gene expression among different samples (*16-18*). RNA-Seq is widely used for laboratory research and clinical studies now, because it provides a more accurate measurement of levels of transcripts and their isoforms over other methods such as microarrays (*19*). To the best of our knowledge, this is the first article performing transcriptomic comparison between tSKPs and tFBs in human.

A total of 1042 genes were found to be differentially expressed between tSKPs and tFBs. Compared with the results of mouse counterpart (*13*), the amount of DEGs is slightly smaller, which indicates that the molecular mechanism underlying differentiation process from SKPs to fibroblasts is not completely same between different species. GO is a common classification scheme for gene function which provides an up-to-date, comprehensive, comparable descriptions of homologous gene and protein sequence across the phylogenetic spectrum (*20,21*). GO functional enrichment reflects the candidate genes are significantly enriched in multiple cellular functions, including cellular component,

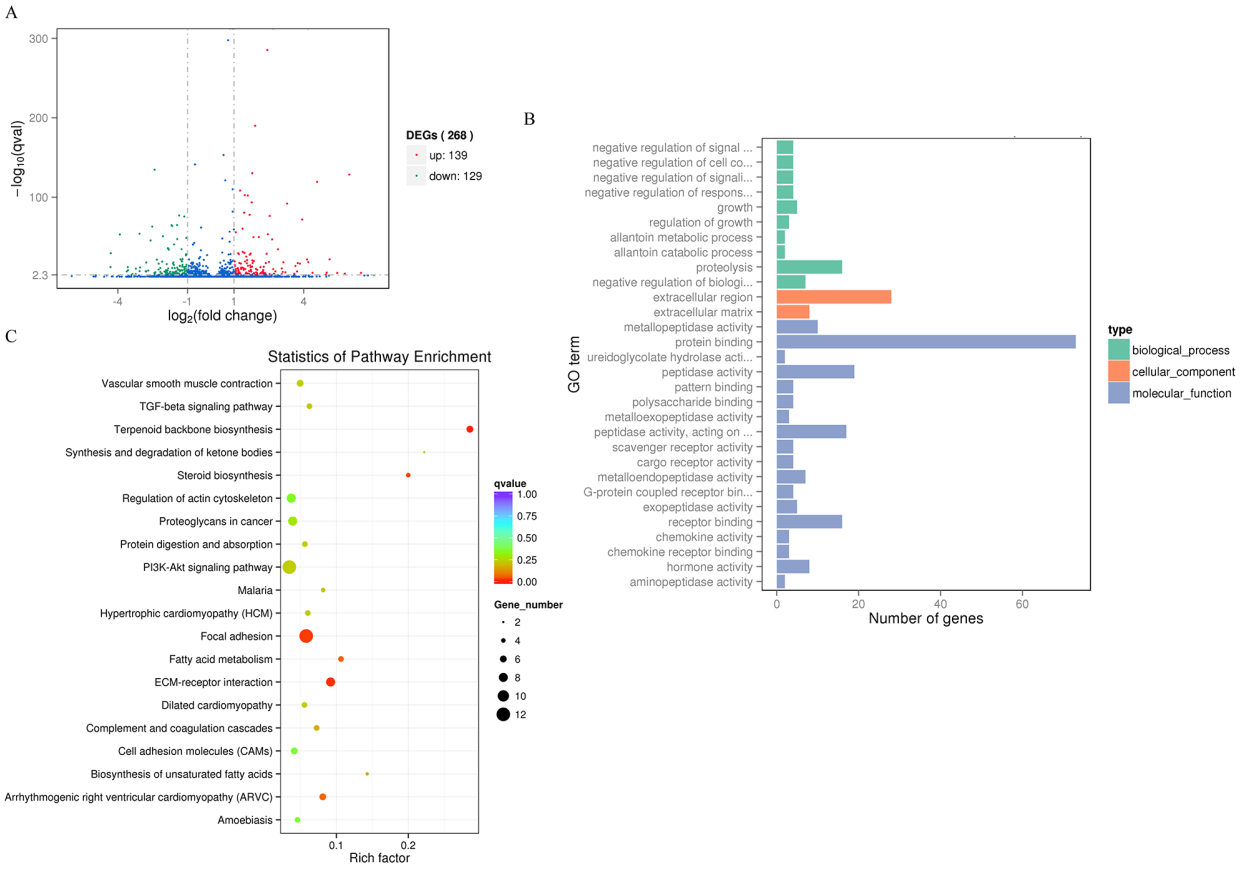

Figure 7. Results of RNA-Seq between pFBs and tFBs. (**A**) Scattered plot of DEGs. (**B**) GO terms of DEGs. *Significantly enriched GO term. (**C**) Scattered plot of DEGs enriched KEGG pathways.

molecular function and biological process. In this study, GO analysis of DEGs showed that these genes were mostly enriched in cell growth, extracellular region, protein binding, peptidase activity and chemokine activity, indicating complex mechanisms were involved in the differentiation of tSKPs towards tFBs.

KEGG analysis detects the pathways where the target genes are most significantly enriched. The result of KEGG identified four major developmental signaling pathways, including TNF signal pathway, focal adhesion, ECM-receptor interaction, and PI3K-Akt signaling pathway. The TNF protein superfamily affects a range of cell biological phenomena, including immune regulation, inflammation, proliferation and differentiation (*22*). In this pathway, tSKPs *vs.* tFBs up-regulated 25 DEGs and down-regulated 5 DEGs (tFBs *vs.* tSKPs up-regulated 5 DEGs and down-regulated 25 DEGs conversely). Numerous studies reported the TNF family is closely related to biological functions of stem cells. TNFα can promote mesendodermal lineage differentiation of mesenchymal stem cells *via* induction of NF-κB, such as myofibroblast (*23*), and osteocytes (*24,25*). The regulation of TNF signaling pathway may play an important role in the transition from tSKPs to fibroblasts. The focal adhesion pathway affects biological processes of cell motility, proliferation and differentiation (*26*). In the focal adhesion, tSKPs *vs.* tFBs up-regulated 20 DEGs and down-regulated 23 DEGs (tFBs *vs.* tSKPs up-regulated 23 DEGs and down-regulated 20 DEGs conversely), indicating the differentiation process from tSKPs to tFBs involves the regulation of focal adhesion pathway. The ECM consists of a complex mixture of structure and functional macromolecules that serves as an essential role in tissue and organ morphogenesis (*27*). In ECM-receptor interaction signaling, tSKPs *vs.* FBs up-regulated 14 DEGs and down-regulated 5 DEGs (tFBs *vs.* tSKPs up-regulated 5 DEGs and down-regulated 14 DEGs conversely), which indicated specific interactions occurred between cells and extracellular environment during the differentiation activity of tSKPs and tFBs. The PI3K-Akt signaling pathway is an intracellular signaling pathway that regulates many aspects of cellular functions, including transcription, growth, proliferation, metabolism and survival (*28*). In our study, tSKPs *vs.* tFBs up-regulated 31 DEGs and down-regulated 19 DEGs (tFBs *vs.* tSKPs up-regulated 19 DEGs and down-regulated 31 DEGs conversely). PI3K activation phosphorylates and activates Akt, which is recruited to the plasma membrane along with PI3K-dependent kinase-1 (*29*). Akt can phosphorylate many target proteins, most notably the forkhead box O (FOXO) (*30*), glycogen synthase kinase 3 (GSK3) (*31*), cell cycle regulators p21 and p27 (*31*) and target of

rapamycin (mTOR) (*32*), which explains its relatively wide effects on cell function (*33*). In many cancers, the pathway is well defined in context of tumorigenesis. However, recent studies have highlighted that the pathway is also important for development and cellular differentiation of adult stem cell (*33*). Studies using kinase inhibitors and genetic approaches have shown that both human embryonic stem cells (ESCs) and mouse ESCs require active PI3K/AKT signaling to maintain their undifferentiated properties (*34,35*). Under culture condition conducive for both naive and primed human pluripotent stem cells (PSCs) propagation, high level of PI3K/Akt signaling acts to maintain pluripotency while preventing aberrant differentiation (*36*). Specification of neuro-differentiation requires the sustained status of PI3K/Akt/mTOR signaling (*37*). However, inhibition of this signaling in PSCs promotes the specification of mesoderm differentiation (*38,39*). Under cultured condition permissive for differentiation, the alleviation of PI3K/Akt/mTOR-mediated inhibition of activin/Smad2/3 and Wnt/β-catenin pathways drives PSCs to differentiate into mesendodermal fates (*40*). Therefore, the PI3K/Akt signaling has negative effect on mesodermal differentiation while presenting positive effect on neural differentiation. tSKPs are reported for similar properties as neural stem cells, and tFBs present the function of mesodermal fibroblasts. The KEGG analysis revealed that PI3K/Akt signaling was mostly enriched by down-regulated DEGs when differentiating tSKPs into tFBs. Therefore, we assume that PI3K/Akt signaling may be important in the differentiation process from tSKPs to tFBs and the regulation of PI3K/Akt signaling may activate tSKPs differentiation.

TFs regulate gene expression by binding to specific upstream nucleotide sequences to achieve biological functions. Analysis of TFs between tSKPs and tFBs may also help us lift the veil on the transition from tSKPs and FBs. Among the TFs down-expressed in tFBs, many genes have been reported to encode for functions in the neural system. Nr4a2 is associated with neuron progenitors and neurogenesis of hippocampus neural stem cells (*41,42*). The Klf family can promotes self-renewal and cellular programing of stem cells (*43*). Snail2 involves in the regulation of neural crest development (*44*). Inhibiting the expression of the above genes in tFBs, which are related to neural system, may be important for tSKPs differentiation into mesodermal lineages rather than neural cells. Ceg1 is highly expressed in both embryonic and adult heat, which is required for differentiation of mouse embryonic cell into cardiomyocytes and the formation of cohesive myocardium-like structure in a cell-autonomous fashion (*45*). Tgif1 has been showed to regulate quiescence and self-renewal of hematopoietic stem cells (*45*). Silencing of Tgif1 in tendon-derived stem cells can improve the tendon-to-bone insertion site regeneration (*46*). Cdkn1a (alternatively p21), Foxo1 (*47*) and Foxc1 (*8*) are key multifunctional downstream signaling nodes of PI3K/Akt signaling. The down-regulation of above genes in tFBs suggests the inhibition of PI3K/Akt signaling may involve in the process of transition from tSKPs to tFBs, which was consistent with the results of KEGG. Among the TFs up-expressed in tFBs, Foxm1 is a proliferation-associated TF, which stimulates cell cycle progression by promoting the entry into S-phase and M-phase (*49*). The knockout of Foxm1 in mice is lethal with defective development of heart, lung and liver (*49*). Thus, Foxm1 is essential for the maintenance of genomic stability and chromosome integrity. Thbs1, a transient component of extracellular matrix in developing and repairing tissue, functions as a cell adhesion molecule and modulates cell movement and cell proliferation (*9*). Thbs1 has been shown to be involved in the activation of latent transforming growth factor (TGF) β (*50*). The up-regulation of Thbs1 indicates that it may associate with the formation process of tFBs through TGFβ signaling pathway.

A further comparison of tFBs and pFBs identified 268 DEGs. Compared with the results of tSKPs and tFBs, the amount of DEGs was much smaller. In addition, no GO term was significantly enriched by DEGs and KEGG analysis revealed only few pathways related to metabolism and morphogenesis were enriched by DEGs. The comparative transcriptome analysis of two fibroblasts suggested that no major difference of biological function was found between tFBs and pFBs.

In conclusion, we compared the transcriptional profiles between tSKPs and tFBs by RNA-Seq. Our studies showed that the up-regulated and down-regulated genes were significantly enriched in TNF signaling pathway, focal adhesion, ECM-receptor interaction and PI3K/Akt signaling pathway. A further TF analysis of DEGs revealed that the down-expressed TFs (p21, Foxo1and Foxc1) in tFB were the downstream nodes of PI3K-Akt signaling pathway, which suggested PI3K-Akt signaling pathway might play an important role in tSKPs differentiation. The results of our study are useful for investigating the molecular mechanisms in tSKPs differentiation into tFBs, making it possible to take advantage of their potential application in regenerative medicine.

Acknowledgements

The work was supported by grants from Natural Science Foundation of China (No. 81673084), Natural Science Foundation of Zhejiang province (LQ20H110002) and 1.3.5 project for disciplines of excellence, West China Hospital, Sichuan University.

References

1. Toma JG, Akhavan M. Isolation of multipotent adult stem cells from the dermis of mammalian skin. Nat Cell Biol.

2001; 3:778-784.
2. Dai R, Hua W, Xie H, Chen W, Xiong L, Li L. The human skin-derived precursors for regenerative medicine: current state, challenges, and perspectives. Stem Cells Int. 2018; 2018:8637812.
3. Biernaskie JA, McKenzie IA, Toma JG, Miller FD. Isolation of skin-derived precursors (SKPs) and differentiation and enrichment of their Schwann cell progeny. Nat Protoc. 2007; 1:2803-2812.
4. Toma JG, Mckenzie IA, Bagli D, Miller FD. Isolation and characterization of multipotent skin-derived precursors from human skin. Stem Cells 2005; 23:727-737.
5. Fernandes KJL, McKenzie IA, Mill P, Smith KM, Akhavan M, Barnabé-Heider F, Biernaskie J, Junek A, Kobayashi NR, Toma JG, Kaplan DR, Labosky PA, Rafuse V, Hui CC, Miller FD. A dermal niche for multipotent adult skin-derived precursor cells. Nat Cell Biol. 2004; 6:1082-1093.
6. Dai R, Hua W, Chen W, Xiong L, Li L, Li Y. Isolation , characterization , and safety evaluation of human skin-derived precursors from an adherent monolayer culture system. Stem Cell Int. 2019; 2019:9194560.
7. Hill RP, Gledhill K, Gardner A, Higgins CA, Crawford H, Lawrence C, Hutchison CJ, Owens WA, Kara B, James SE, Jahoda CAB. Generation and characterization of multipotent stem cells from established dermal cultures. PLoS One. 2012; 7:e50742.
8. Wenzel V, Roedl D, Gabriel D, Gordon LB, Herlyn M, Schneider R, Ring J, Djabali K. Naive adult stem cells from patients with Hutchinson-Gilford progeria syndrome express low levels of progerin *in vivo*. Biol Open. 2012; 1:516-526.
9. Biernaskie J, Miller FD. Skin-derived precursors(SKPs): *in vivo* cell fate is limited to the neural crest lineage, and is determined by tissue-specific factors. Int J Dev Neruoscience. 2006; 24:495-603.
10. Biernaskie J, Paris M, Morozova O, Fagan BM, Marra M, Pevny L, Miller FD. SKPs derived from hair follicle precursors and exhibit properties of adlut dermal stem cells. Cell Stem Cell. 2009; 5:610-623.
11. Fushan AA, Turanov AA, Lee S, Kim EB, Lobanov AV, Yim SH, Buffenstein R, Lee S, Chang K, Rhee H, Kim J, Yang K, Gladyshev VN. Gene expression defines natural changes in mammalian lifespan. Aging Cell. 2015; 14:352-365.
12. Fulton DL, Sundararajan S, Badis G, Hughes TR, Wasserman WW, Roach JC, Sladek R. TFCat : the curated catalog of mouse and human transcription. Genome Biol. 2009; 10:R29.
13. Mao Y, Xiong L, Wang S, Zhong J, Zhou R, Li L. Comparison of the transcriptomes of mouse skin derived precursors (SKPs) and SKP-derived fibroblasts (SFBs) by RNA-Seq. PLoS One. 2015; 10:e0117739.
14. Zhao M, Whitworth KM, Zhang X, Zhao J, Miao Y, Zhang Y, Prather RS. Deciphering the mesodermal potency of porcine skin-derived progenitors (SKP) by microarray analysis. Cell Reprogram. 2010; 12:161-173.
15. Vaquerizas JM, Kummerfeld SK, Teichmann SA, Luscombe NM. A cesus of human transcription factors: function, expression and evolution. Nat Rev Genet. 2009; 10:252-263.
16. Chu Y, Corey DR. RNA sequencing : platform selection , experimental design, and data interpretation. Nucleic Acid Ther. 2012; 22:271-274.
17. Wilhelm BT, Landry J. RNA-Seq-quantitative measurement of expression through massively parallel RNA-sequencing. Methods. 2009; 48:249-257.
18. Wang Z, Gerstein M, Snyder M. RNA-Seq : a revolutionary tool for transcriptomics. Nat Rev Genet. 2009; 10:57-63.
19. Fu X, Fu N, Guo S, Yan Z, Xu Y, Hu H, Menzel C, Chen W, Li Y, Zeng R, Khaitovich P. Estimating accuracy of RNA-Seq and microarrays with proteomics. BMC Genomics. 2009; 10:161.
20. Michael A, Catherine A B, Judith A B, *et al*. Gene Ontology : tool for the unification of biology. The Gene Ontology Consortium. Nat Commun. 2000; 25:25-29.
21. The Gene Ontology Consortium. The Gene Ontology Resource: 20 years and still GOing strong. Nucleic Acids Res. 2019; 47:D330-D338.
22. Sabio G, Davis RJ. TNF and MAP kinase signaling pathways. Semin Immunol. 2014; 26:237-245.
23. Zhou J, Ma T, Cao H, Chen Y, Wang C, Chen X, Xiang Z, Han X. TNF-α-induced NF-κB activation promotes myofibroblast differentiation of LR-MSCs and exacerbates bleomycin-induced pulmonary fibrosis. J Cell Physiol. 2018; 233:2409-2419.
24. Feng X, Feng G, Xing J, Shen B, Li L, Tan W, Xu Y, Liu S, Liu H, Jiang J, Wu H, Tao T, Gu Z. TNF-α triggers osteogenic differentiation of human dental pulp stem cells *via* the NF-κB signalling pathway. Cell Biol Int. 2013; 37:1267-1275.
25. Kotake S, Nanke Y. Effect of TNFα on osteoblastogenesis from mesenchymal stem cells. Biochim Biophsica Acta. 2014; 1840:1209-1213.
26. Mathieu PS, Loboa EG. Cytoskeletal and focal adhesion influences on mesenchymal stem cell shape, mechanical properties, and differentiation down osteogenic, adipogenic, and chondrogenic pathways. Tissue Eng Part B Rev. 2012; 18:436-444.
27. Rozario T, Desimone DW. The extracellular matrix in development and morphogenesis: a dynamic view. Dev Biol. 2010; 341:126-140.
28. Vanhaesebroeck B, Stephens L, Hawkins P. PI3K signalling: the path to discovery and understanding. Nat Publ Gr. 2012; 13:195-203.
29. Vanhaesebroeck B, Guibert JG, Graupera M. The emerging mechanisms of isoform-specific PI3K signalling. Nat Rev Mol Cell Biol. 2010; 11:329-341.
30. Kops GJ, de Ruiter ND, De Vries-Smits AM, Powell DR, Bos JL, Burgering BM. Direct control of the Forkhead transcription factor AFX by protein kinase B. Nature. 1999; 398:630-634.
31. Cross DE, Alessi DR, Cohen P, Andjelkovich M, Hemmings BA. Inhibition of glycogen synthase kinase-3 by insulin mediated by protein kinase B. Nature. 1995; 378:785-789.
32. Jacinto E, Facchinetti V, Liu D, Soto N, Wei S, Jung SY, Huang Q, Qin J, Su B. SIN1/MIP1 maintains rictor-mTOR complex integrity and regulates Akt phosphorylation and substrate specificity. Cell. 2006; 127:125-137.
33. Yu JSL, Cui W. Proliferation, survival and metabolism: the role of PI3K/AKT/mTOR signalling in pluripotency and cell fate determination. Deveopment. 2016; 143:3050-3060.
34. Paling NRD, Wheadon H, Bone HK, Welham MJ. Regulation of embryonic stem cell self-renewal by phosphoinositide 3-kinase-dependent signaling. J Biol Chem. 2004; 279:48063-48070.
35. Kingham E, Welham M. Distinct roles for isoforms of

the catalytic subunit of class-IA PI3K in the regulation of behaviour of murine embryonic stem cells. J Cell Sci. 2009; 122:2311-2321.
36. Betschinger J, Nichols J, Dietmann S, Corrin PD, Paddison PJ, Smith A. Exit from pluripotency is gated by intracellular redistribution of the bHLH transcription factor Tfe3. Cell. 2013; 153:335-347.
37. Fishwick KJ, Li RA, Halley P, Deng P, Storey KG. Initiation of neuronal differentiation requires PI3-kinase/TOR signalling in the vertebrate neural tube. Dev Biol. 2010; 338:215-225.
38. McLean AB, D'Anour KA, Jones KL, Krishnamoorthy M, Kulik MJ, Reynolds DM, Sheppard AM, Liu H, Xu Y,Baetge EE, Dalton S. Activin a efficiently specifies definitive endoderm from human embryonic stem cells only when phosphatidylinositol 3-kinase signaling is suppressed. Stem Cells. 2007; 25:29-38.
39. Zhou J, Su P, Wang L, Chen J, Zimmermann M, Genbacev O, Afonja O, Horne MC, Tanaka T, Duan E, Fisher SJ, Liao J, Chen J, Wang F. mTOR supports long-term self-renewal and suppresses mesoderm and endoderm activities of human embryonic stem cells. Proc Natl Acad Sci U S A. 2009; 106:7840-7845.
40. Yu JSL, Ramasamy TS, Murphy N, Holt MK, Czapiewski R, Wei SK, Cui W. PI3K/mTORC2 regulates TGF-β/Activin signalling by modulating Smad2/3 activity *via* linker phosphorylation. Nat Commun. 2015; 6:7212.
41. Shao CZ, Xia KP. Sevoflurane anesthesia represses neurogenesis of hippocampus neural stem cells *via* regulating microRNA-183-mediated NR4A2 in newborn rats. J Cell Physiol. 2019; 234:3864-3873.
42. Chen S, Luo GR, Li T, Liu TX, Le W. Correlation of Nr4a2 Expression with the Neuron Progenitors in Adult Zebrafish Brain. J Mol Neurosci. 2013; 51:719-723.
43. Bialkowska AB, Yang VW, Mallipattu SK. Krüppel-like factors in mammalian stem cells and development. Deveopment. 2017; 144:737-754.
44. Tien CL, Jones A, Wang H, Gerigk M, Nozell S, Chang C. Snail2/Slug cooperates with Polycomb repressive complex 2 (PRC2) to regulate neural crest development. Deveopment. 2015; 142:722-731.
45. Liu J, Qi Y, Li S, Hsu SC, Saadat S, Hsu J, Rahimi SA, Lee LY, Yan C, Tian X, Han Y. CREG1 Interacts with Sec8 to promote cardio-myogenic differentiation and cell-cell adhesion. Stem Cells. 2016; 34:2648-2660.
46. Chen L, Jiang C, Tiwari SR, Shrestha A, Xu P, Liang W, Sun Y, He S, Cheng B. TGIF1 gene silencing in tendon-derived stem cells improves the tendon-to-bone insertion site regeneration. Callular Physilogy Biochem. 2015; 37:2101-2114.
47. Paradis S, Ruvkun G. Caenorhabditis elegans Akt / PKB transduces insulin receptor-like signals from AGE-1 PI3 kinase to the DAF-16 transcription factor. Genes Dev. 1998; 12:2488-2498.
48. Yu Z, Xu H, Wang H, Wang Y. Foxc1 promotes the proliferation of fibroblast-like synoviocytes in rheumatoid arthritis *via* PI3K/AKT signalling pathway. Tissue Cell. 2018; 53:15-22.
49. Wierstra I. The transcription factor FOXM1 (Forkhead box M1): proliferation-specific expression, transcription factor function, target genes, mouse models, and normal biological roles. Adv Cancer Res. 2013; 118:97-398.
50. Murphy-ullrich JE, Poczatek M. Activation of latent TGF-β by thrombospondin-1: mechanisms and physiology. Cytokine Growth Factor Rev. 2000; 11:59-69.

Received December 24, 2019; Revised April 1, 2020; Accepted April 6, 2020

[§]These authors contributed equally to this work.
**Address correspondence to:*
Li Li, Department of Dermatology, West China Hospital, Sichuan University, No. 37, Guo Xue Xiang, Chengdu, 610041, China
E-mail: hxskincos2017@qq.com

Released online in J-STAGE as advance publication April 23, 2020.

Original Article

DOI: 10.5582/bst.2019.01351

Dimethylarginine dimethylaminohydrolase-1 contributes to exercise-induced cardiac angiogenesis in mice

Xiaowei Shi[1], Xueting Luo[1], Xin Xu[1,2,*]

[1] School of Kinesiology, Shanghai University of Sport, Shanghai, China;
[2] Department of Exercise Rehabilitation, Shanghai University of Sport, Shanghai, China.

SUMMARY Dimethylarginine dimethylaminohydrolase-1 (DDAH1) maintains nitric oxide (NO) bioavailability by degrading asymmetric dimethylarginine (ADMA), which is an endogenous inhibitor of nitric oxide synthase (NOS). It has been well established that DDAH1 and exercise play crucial roles in promoting cardiac angiogenesis under pathological conditions. However, the role of DDAH1 in exercise-induced cardiac angiogenesis remains unclear. In this study, we focused on the change in DDAH1 in response to moderate exercise and the underlying mechanism of exercise-induced cardiac angiogenesis. Eight-week-old male DDAH1 global knockout (KO) mice and DDAH1$^{flox/flox}$ mice (wild-type) were randomly divided into sedentary groups (control) and swimming groups (exercise). After eight weeks of swimming at five days per week, all the mice were anesthetized and sacrificed. Histological examination and Western blot analysis were performed. There were low levels of myocardial capillaries in DDAH1 KO mice under control and exercise conditions. Notably, exercise elevated DDAH1 protein expression, as observed by Western blot analysis. The common cardiac angiogenesis biomarkers vascular endothelial growth factor (VEGF) and Caveolin-1 were increased during exercise. A significant difference in VEGF was observed between the DDAH1 KO and wild-type groups. Similarly, increased Caveolin-1 expression was abrogated in DDAH1 KO mice. Furthermore, we tested the R-Ras/AKT/GSK3β signaling pathway to study the underlying molecular mechanism. DDAH1 may regulate the R-Ras/AKT/GSK3β pathway due to distinct protein changes in this pathway in the DDAH1 KO and wild-type groups. Our findings suggest that DDAH1 plays an important role in exercise-induced cardiac angiogenesis by regulating the R-Ras/AKT/GSK3β signaling pathway.

Keywords swim, cardiac capillary density, eNOS, VEGF, Caveolin-1, R-Ras

1. Introduction

Angiogenesis is the process of generating new blood vessels from existing ones. Homeostasis of angiogenesis plays an important role in human cardiac health. In animal experiments, myocardial ischemia (*1*), diabetic heart disease (*2*) and myocardial aging (*3*) are all characterized by poor angiogenesis. Inadequate angiogenesis has been viewed as one of the key reasons for the occurrence of these diseases. The cardioprotective effects of regular exercise are an efficient therapeutic strategy to preserve the balance of angiogenesis, including improving cardiac angiogenesis in myocardial infarction (*4,5*), heart transplantation (*6*), diabetes (*7,8*) and aging (*9,10*). It is well recognized that exercise protects cardiac structure and function *via* elevating capillary density under pathological conditions (*5,11*). Exercise-induced angiogenesis plays a vital role in maintaining the homeostasis of angiogenesis in the myocardium.

Dimethylarginine dimethylaminohydrolase-1 (DDAH1) degrades asymmetric dimethylarginine (ADMA), which is an endogenous inhibitor of nitric oxide synthase (NOS). Previous studies have demonstrated that DDAH1 is involved in the occurrence and development of multiple diseases, such as vascular disease (*12*), heart failure (*13*) and myocardial ischemia (*14,15*). Moreover, Zhang found direct evidence that DDAH1 expression is upregulated with a decline in ADMA and may take part in a protective effect against myocardial ischemia *via* promoting angiogenesis (*15*). DDAH1 and DDAH2 are two isoforms of DDAH. DDAH1 plays a leading role in degrading ADMA. The protein level of DDAH2 is not changed in DDAH1 global KO mice (*16*) and endothelial DDAH1 gene deletion mice (*17*). However, these mice show a lack of DDAH activity (increased ADMA level, and blood

pressure and decreased NO generation). Interestingly, the vital role of DDAH1 in regulating cardiac angiogenesis under pathological conditions may be attributed to the distribution of DDAH1. In the myocardium, DDAH1 is mainly distributed in the sarcolemma of cardiomyocytes and the endothelium of cardiac microvessels (*18*), which provides a basis for the role of DDAH1 in regulating myocardial angiogenesis. However, the role of DDAH1 in exercise-induced angiogenesis in the myocardium remains unclear.

The aim of this study was to focus on changes in DDAH1 in response to moderate exercise and to investigate the underlying mechanism of exercise-induced cardiac angiogenesis in mice. Our data indicated a pivotal role of DDAH1 in contributing to exercise-induced cardiac angiogenesis.

2. Materials and Methods

2.1. Experimental animals

DDAH1 KO mice (*16*) and DDAH1$^{flox/flox}$ mice (*16*) were generated in the lab of the Cardiovascular Division (University of Minnesota Medical School, Minneapolis, USA). The mice were kept in the animal experimental center (SPF level) at Shanghai University of Sport. Twenty-six eight-week-old mice were randomly divided into four groups according to their genotypes and exercise states: the DDAH1 KO sedentary group (KO SED, n = 7), the DDAH1$^{flox/flox}$ sedentary group (WT SED, n = 6), the DDAH1 KO swimming group (KO EXE, n = 7), and the DDAH1$^{flox/flox}$ swimming group (WT EXE, n = 6). All mice were freely fed normal rodent chow and water during the experiments. The mice received a 12 h: 12 h alternating dark and light cycle in well-controlled settings with constant temperature (22-26°C) and humidity (55-60%). All experimental animals conformed to the laboratory rules. The studies were approved by the Institutional Animal Care and Use Committee and the Ethics Committee for Science Research at Shanghai University of Sport.

2.2. Exercise protocol

Mice from the KO EXE group and the WT EXE group were trained to swim in two respective tanks (45 cm × 35 cm × 25 cm), in which the water temperature ranged from 32 to 33°C. The mice were familiarized with the water tank during the first week. The exercise protocol began with a 30 min/day swimming session and increased gradually to 90 min/day for 7 consecutive days. Subsequently, the mice were maintained for seven weeks of swimming (90 min daily, 5 days per week) without any workload increase. Mice in the KO SED and WT SED groups were kept sedentary throughout the study (Figure 1).

2.3. Sample processing

All mice were anesthetized and sacrificed after eight weeks. A portion of the myocardium was fixed in 4% paraformaldehyde and placed in a 4°C refrigerator for histological observation. Another part of the myocardium was placed in liquid nitrogen and then transferred to a -80°C freezer for Western blotting.

2.4. Isolectin B4 and DAPI staining

The cardiac tissue samples were embedded in paraffin and cut at a thickness of 4 μm. After dewaxing in water, repairing antigens and blocking, the sections were labeled with isolectin B4 (10 μg/mL, DL-1207, Vector laboratories, USA) and DAPI (1 μg/mL, D1306, Thermo Fisher Scientific, Waltham, MA, USA) for angiogenesis observation. The procedures were carried out in accordance with the manufacturer's instructions. Sections (6 sections per group, 5 fields per section) were observed with fluorescence microscopy (Olympus, Japan) and laser scanning confocal microscopy (Zeiss, Germany).

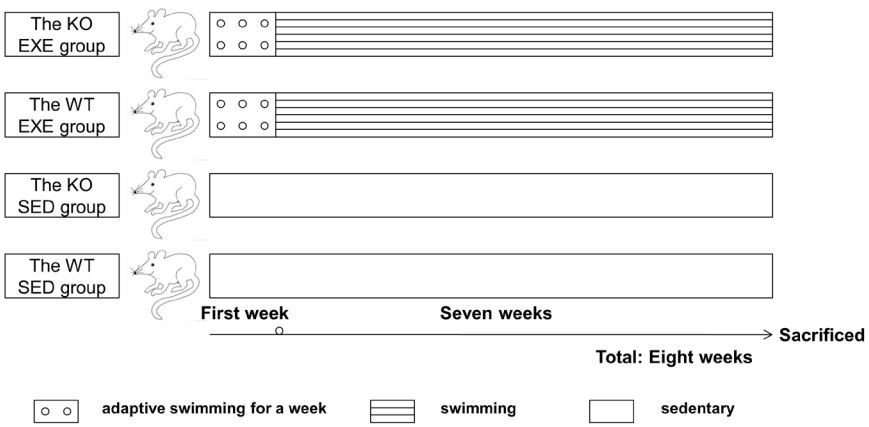

Figure 1. Exercise protocol. Mice from the KO EXE group and the WT EXE group were trained to swim in two tanks. They were trained to swim for the first week (30-90 min/day for 7 consecutive days) and then went into formal exercises for seven weeks (90 min/day, 5 day/week).

2.5. Western blot analysis and antibodies

After the lysis of cardiac tissue homogenates, sodium dodecyl sulfate polyacrylamide gel electrophoresis (SDS-PAGE) was utilized, and the remaining steps were the same as those of conventional Western blotting procedures. The primary antibodies used for Western blotting were as follows: rabbit anti-DDAH1 (1:500, Absin, abs133884), rabbit anti-phospho-eNOS Ser1177 (1:1000, Abcam, ab215717), rabbit anti-eNOS (1:1000, Abcam, ab199956), rabbit anti-vascular endothelial growth factor (VEGF) (1:500, Absin, abs131208), rabbit anti-Caveolin-1 (1:1000, Cell Signaling, 3267), rabbit anti-R-Ras (1:1000, Abcam, ab191791), rabbit anti-AKT (1:1000, Cell Signaling, 4691), rabbit anti-phospho-AKT Ser473 (1:1000, Cell Signaling, 4060), rabbit anti-GSK3β (1:1000, Cell Signaling, 9315), rabbit anti-phospho-GSK3β Ser9 (1:1000, Cell Signaling, 9323) and rabbit anti-GAPDH (1:1000, Cell Signaling, 5174).

2.6. Statistical analysis

All values are expressed as the mean ± standard deviation and significance was regarded as $p < 0.05$. SPSS (19.0 version) was used to analyze the experimental data. Two groups of data were analyzed by unpaired *t*-test. Data between four groups were analyzed by two-way ANOVA and post hoc comparisons with the Fisher LSD test.

3. Results

3.1. Effect of exercise on the heart weight/body weight ratio and the left ventricular weight/body weight ratio in WT and DDAH1 KO mice

The heart weight/body weight ratio and the left ventricular weight/body weight ratio had no significant changes in DDAH1 KO and wild-type mice ($p > 0.05$) (Figure 2A and 2B). The results suggested that eight weeks of swimming couldn't induce cardiac hypertrophy in WT and DDAH1 KO mice.

3.2. Role of DDAH1 in exercise-induced myocardial capillary density

At a basal level, the WT SED group manifested higher cardiac microvessel density than that in the KO SED group ($p < 0.05$). After eight weeks of swimming, compared with the angiogenesis levels in the WT SED and KO SED groups, exercise enhanced cardiac angiogenesis in both WT EXE ($p < 0.01$) and KO EXE ($p < 0.01$) groups. Interestingly, capillary density in the KO EXE group was blunted compared with that in the WT EXE group ($p < 0.01$) (Figure 3A and 3B), indicating that DDAH1 exerted a key effect on exercise-induced cardiac angiogenesis.

3.3. Upregulation of DDAH1, p-eNOS/eNOS, VEGF, and Caveolin-1 protein expression following exercise

According to the histological results, DDAH1 played a crucial role in exercise-induced angiogenesis, but the exercise-induced change in DDAH1 was unknown. Western blot results showed that eight weeks of swimming elevated DDAH1 protein expression in the WT EXE group compared with that of the WT SED group ($p < 0.01$) (Figure 4A and 4B). Similarly, p-eNOS/eNOS was also increased in the WT EXE ($p < 0.01$) and KO EXE ($p < 0.01$) groups (Figure 4A and 4B). Under sedentary and exercise conditions, p-eNOS/eNOS showed a significant difference in the KO EXE group compared with that of the WT EXE group ($p < 0.01$). Moreover, we examined changes in cardiac angiogenesis-related indicators, such as VEGF and Caveolin-1. Eight weeks of swimming increased VEGF and Caveolin-1 expression ($p < 0.01$) (Figure 4A and 4B). The data demonstrated that exercise enhanced cardiac capillary density in mice. The effect of exercise on VEGF and Caveolin-1 was obvious. Exercise for eight weeks upregulated VEGF and Caveolin-1. In addition, the expression of VEGF and Caveolin-1 protein in the KO EXE and KO SED groups was lower

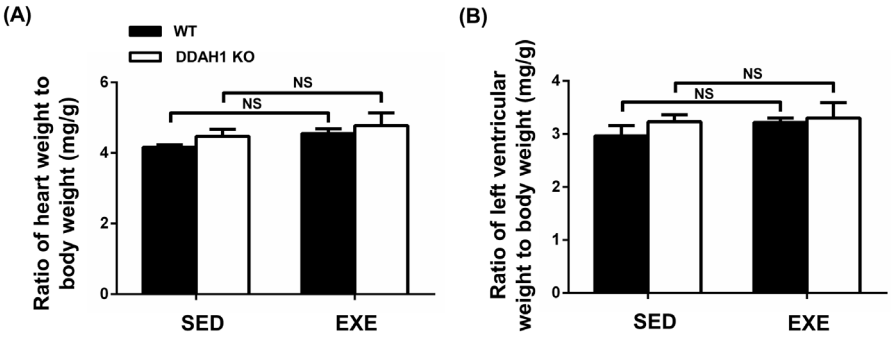

Figure 2. The heart weight/body weight ratio and the left ventricular weight/body weight ratio in WT and DDAH1 KO mice. (**A**) The heart weight/body weight ratio in WT and DDAH1 KO mice. (**B**) The left ventricular weight/body weight ratio in WT and DDAH1 KO mice. (NS: no significant difference).

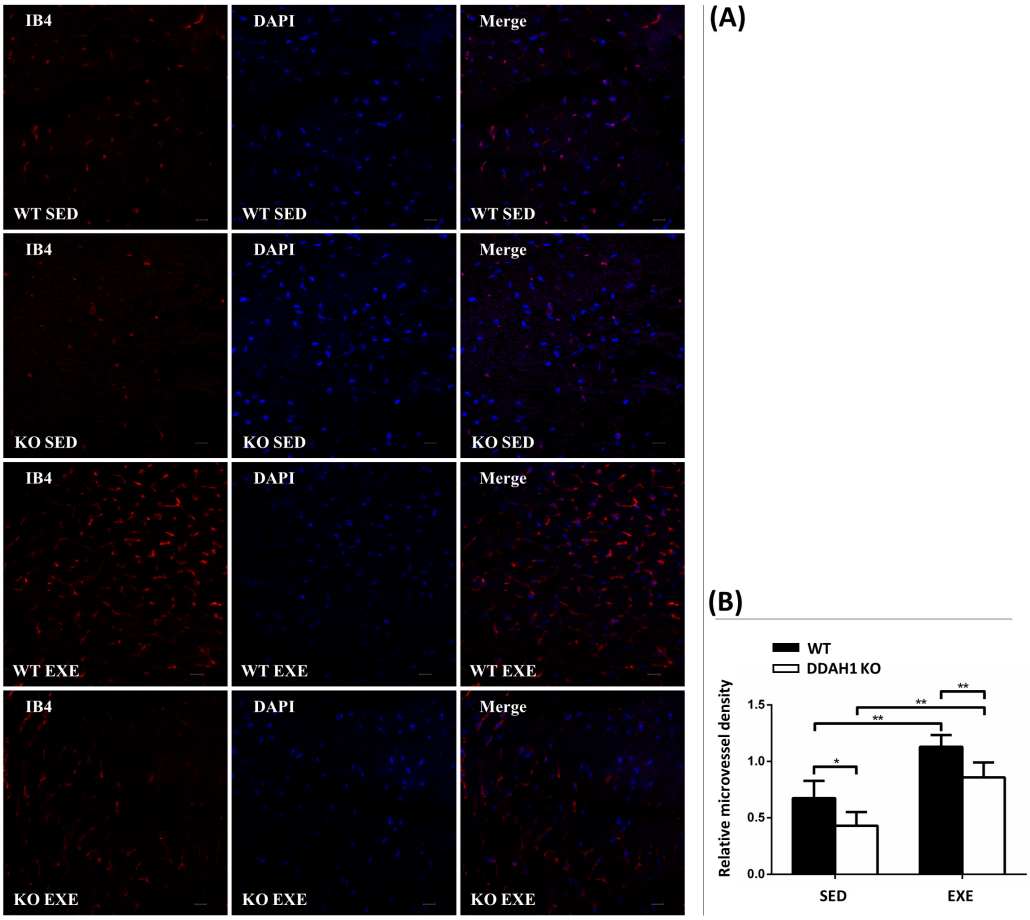

Figure 3. Myocardial angiogenesis staining and relative microvessel density. (**A**) Isolectin B4 (IB4) staining of wild-type and DDAH1-/- cardiac tissue samples. The number of nuclei was analyzed using DAPI staining (blue fluorescence marker). As shown in the images, microvessels are exhibited in a series of tiny red rings. (**B**) Measurement of microvessel density reflected angiogenesis. Angiogenesis was determined *via* capillary number and the ratio of capillary number to nuclei number. Scale bars: 10 μm. ($^{*}p < 0.05$, $^{**}p < 0.01$) Original magnification, ×400 in A.

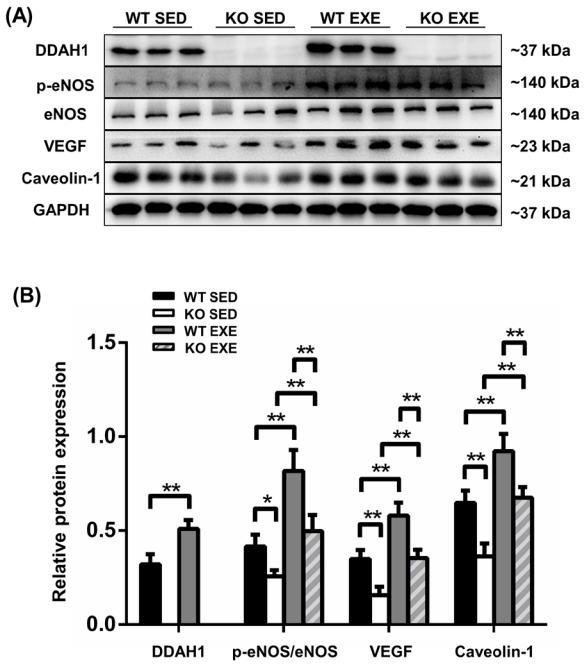

Figure 4. Exercise enhances DDAH1, p-eNOS/eNOS, VEGF, and Caveolin-1 protein expression. (**A-B**) The changes in DDAH1, p-eNOS/eNOS, VEGF, and Caveolin-1 in wild-type and DDAH1 KO mice under sedentary and exercise conditions ($^{*}p < 0.05$, $^{**}p < 0.01$).

than those in the WT EXE ($p < 0.01$) and WT SED ($p < 0.01$) groups (Figure 4A and 4B), regardless of exercise or sedentary state.

3.4. Role of DDAH1 in regulating the R-Ras/AKT/GSK3β pathway following exercise-induced cardiac angiogenesis

To further determine the potential molecular mechanism by which DDAH1 affects exercise-induced angiogenesis, we examined the changes in the R-Ras/AKT/GSK3β signaling pathway. R-Ras, p-AKT/AKT and p-GSK3β/GSK3β protein expression was changed under basal conditions in sedentary mice, which showed a novel pathway by which DDAH1 affects myocardial capillary density ($p < 0.05$) (Figure 5A and 5B). After eight weeks of swimming, compared with the expression levels in the WT SED and KO SED groups, R-Ras, p-AKT/AKT and p-GSK3β/GSK3β were expressed at high levels in the WT EXE ($p < 0.01$) and KO EXE ($p < 0.05$) groups (Figure 5A and 5B). Furthermore, the elevation in the protein expression of R-Ras, p-AKT/AKT and p-GSK3β/GSK3β was abrogated in the KO EXE group compared with that of the WT EXE group ($p < 0.01$) (Figure 5A

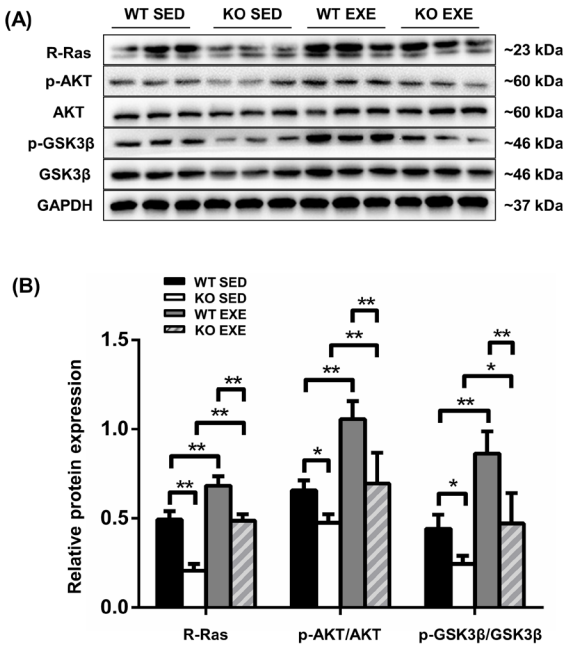

Figure 5. DDAH1 is involved in exercise-induced cardiac angiogenesis *via* regulating the R-Ras/AKT/GSK3β pathway. (**A-B**) The alterations in R-Ras, p-AKT/AKT, and p-GSK3β/GSK3β in wild-type and DDAH1 KO mice under sedentary and exercise conditions ($^{*}p < 0.05$, $^{**}p < 0.01$).

and 5B). Corroborating these changes in the R-Ras/AKT/GSK3β signaling pathway, our data suggest that DDAH1 regulates the R-Ras/AKT/GSK3β signaling pathway and plays a crucial role in cardiac angiogenesis.

4. Discussion

The main finding of the current study indicates the essential role of DDAH1 in exercise-induced cardiac angiogenesis. DDAH1 deletion abated myocardial capillary density under sedentary and exercise conditions. At a basal level, DDAH1 global KO mice exhibited increased levels of ADMA in plasma and tissue, decreased NOS, and increased systemic blood pressure (*16*). ADMA accumulation in DDAH1-/-mice also led to a reduction in angiogenesis and impairment of vascular repairing capacity (*12,19*). Of note, ADMA accumulation can induce endothelial cell apoptosis. Consequently, it was shown that DDAH1 is pivotal in regulating angiogenesis through degrading ADMA and maintaining NO signaling in a strain of DDAH1 global KO mice. Furthermore, Dowsett confirmed that endothelial deletion of DDAH1 profoundly impaired the angiogenic responses both ex vivo and *in vivo* (*20*). In addition, other researchers found that angiogenesis was enhanced in response to overexpression of DDAH1 (*21*). These findings suggest that DDAH1 increases capillary formation in important organs and blood vessels, including the brain, heart, liver, lung, kidney, skeletal muscle and carotid artery. Under sedentary conditions, DDAH1 KO (*16*) or DDAH1 silencing (*22*) reduces the degradation of ADMA, implying that endothelial cell apoptosis increases, while angiogenesis is inhibited. Conversely, overexpression of DDAH1 (*22*) increases the degradation of ADMA, suggesting that endothelial cell function is protected and angiogenesis is promoted. As the major enzyme for degrading ADMA, DDAH1 can protect against ADMA accumulation induced endothelial cell apoptosis, maintain endothelial function and regulate angiogenesis under sedentary conditions. In the present study, according to our angiogenesis staining results, loss of DDAH1 reduced capillary density in the myocardium under sedentary conditions, which is consistent with previous studies and added robust evidence.

There are two subtypes of DDAH including DDAH1 and DDAH2, which are encoded by distinct genes. Different subcellular distributions and physiological functions of the two isoforms determine that DDAH1 plays a role in cardiac angiogenesis. In terms of subcellular distribution of DDAH, DDAH1 is predominantly distributed in vascular endothelial cells (*18*) and the heart (*23*). Based on the physiological functions of DDAH, the leading enzyme degrading ADMA is DDAH1 rather than DDAH2. A large amount of evidence has shown that DDAH1 gene deletion does not change protein expression of DDAH2 (*16,17*). Unexpectedly, DDAH1 gene deletion increases ADMA levels. To our best knowledge, until now, there is no powerful evidence that DDAH2 plays a role in cardiac angiogenesis. Conversely, a series of strong evidence shows the important effects of DDAH1 on cardiac angiogenesis.

It is well established that exercise promotes cardiac angiogenesis in animals and human studies (*6,24*). The increase in myocardial capillaries is an important manifestation of exercise benefits to the heart. Exercise-induced cardiac angiogenesis in both WT and KO mice showed that our designed swim protocol was effective. In this exercise protocol (90 min/day, 8 weeks, without any workload increase), the intensity for the mice was moderate. Evangelista (*25*) demonstrated that different swim training volumes (min), body weight loads (%), frequencies (sessions/day) and durations (weeks) played essential roles in triggering cardiac hypertrophy in mice. As evidences showed in the heart weight/body weight ratio and the left ventricular weight/body weight ratio, our protocol did not meet the minimum requirement of exercise training-induced cardiac hypertrophy caused by swimming. There may be a threshold in the model of swim training induced cardiac hypertrophy. Thus, in this study, exercise-induced cardiac angiogenesis did not belong to myocardial remodeling caused by high-intensity exercise training-induced cardiac hypertrophy. Although moderate and high intensity exercise (*4*) can both increase myocardial capillaries, they should be essentially different, which may facilitate the future study of their respective mechanisms.

After eight weeks of swimming, the protein expression of DDAH1 in wild-type mice was increased compared with that of the control group. The results of this study demonstrate a direct role of DDAH1 in exercise-induced capillary formation. Combined with the decrease in angiogenesis in KO mice under exercise conditions, DDAH1 deficiency indeed reduced exercise-induced myocardial capillary density. Thus, to the best of our knowledge, these findings provide the first evidence that exercise elevates the protein expression of DDAH1. The protein expression of DDAH1 was upregulated during exercise. It may be hypothesized that DDAH1 directly increases in the endothelium of cardiac microvessels, which is the basis by which DDAH1 participates in exercise-induced cardiac angiogenesis. In fact, DDAH1 is involved in the regulation of myocardial capillary formation and has a protective effect on the heart. Other researchers had similar results in heart diseases, such as heart failure (*13*) and myocardial infarction (*14*), for DDAH1 protecting myocardium. In the present study, we have found that exercise elevated the expression of DDAH1 and increased angiogenesis, suggesting that exercise could inhibit ADMA to promote angiogenesis by increasing the expression level of DDAH1. The result is consistent with the findings that regular aerobic exercise can reduce ADMA levels in human experiments (*26,27*). Therefore, studying the regulatory angiogenesis mechanism of DDAH1 is essential.

Our finding that exercise increased myocardial eNOS expression is well established in many studies (*28,29*). DDAH1, which directly interacts with eNOS in cardiac tissues (*13*), degrades ADMA to preserve eNOS activity and NO. It has been noted that exercise elevates both DDAH1 and p-eNOS/eNOS in the myocardium. Thus, the changes in DDAH1 and p-eNOS/eNOS are consistent. In addition, p-eNOS/eNOS in the DDAH1 KO mice was blunted compared with that in wild-type mice under sedentary or exercise conditions. Thus, DDAH1 plays an important part in cardiac angiogenesis by regulating NO signaling. This is consistent with previous research (*22*). However, the question of whether there is synergism between exercise and DDAH1 needs further study.

It is already known that DDAH1 takes part in the regulation of exercise-induced angiogenesis, but how DDAH1 regulates angiogenesis still needs more research regarding related indicators and pathways of angiogenesis. VEGF and Caveolin-1 are crucial to the vascular system. A recent report confirmed that exercise improves angiogenesis through the Caveolin-1/VEGF pathway in the ischemic penumbra (*30*). However, the evidence above was determined in the brain and not in the heart. Other research demonstrated that the Caveolin-1/VEGF signaling pathway is an important target in angiogenesis in acute myocardial infarction (*31*). However, the purpose of the study was drug treatment rather than exercise intervention. In this study, the results are not different. Exercise induced the expression of VEGF and Caveolin-1, which demonstrated that exercise directly increases myocardial capillary density. Our finding that VEGF and Caveolin-1 are affected by the deletion of DDAH1 showed that DDAH1 may play an important role in modulating myocardial angiogenesis induced by exercise through VEGF and Caveolin-1. VEGF is a leading regulator of angiogenesis. A large amount of evidence has demonstrated that the VEGF signaling pathway could directly promote blood vessel formation (*32,33*). Thus, the results indicated that DDAH1 contributes to exercise-induced cardiac angiogenesis. Different from the widespread use of VEGF in angiogenesis, Caveolin-1 begins to show new features. Chen demonstrated the primary colocalization of DDAH1 and Caveolin-1 in the endothelium of cardiac microvessels (*18*). In fact, Caveolin-1 is mainly expressed in endothelial cells (*34*). It is conceivable that similar localization of DDAH1 and Caveolin-1 substantiates the same function in regulating cardiac angiogenesis. Caveolin-1 plays an important role in controlling the biological process of angiogenesis by binding to eNOS. VEGF and Caveolin-1 are key indexes of cardiac angiogenesis. Since DDAH1 regulates cardiac angiogenesis rather than DDAH2, DDAH1 has a dominant effect on the expressions of VEGF and Caveolin-1. In this paper, DDAH1 played an important role in exercise-induced cardiac angiogenesis. The expressions of VEGF and Caveolin-1, which are key indexes of cardiac angiogenesis, changed significantly, suggesting that DDAH1 has an important effect on the expressions of VEGF and Caveolin-1. There is no strong evidence that DDAH2 has an effect on the expression of VEGF and Caveolin-1. To our best knowledge, DDAH1 has a dominant effect on the expression of VEGF and Caveolin-1 in the myocardium. Based on the explanations above, our data provide new direct evidence for the impact of DDAH1 on VEGF and Caveolin-1 in exercise-induced cardiac angiogenesis.

To explore the potential mechanism by which DDAH1 regulates exercise-induced myocardial angiogenesis, a new pathway regulating vascular density has been found in recent years. In 2005, Komatsu reported that R-Ras is a pivotal regulator of vascular regeneration in tumors by employing R-Ras-null mice (*35*). Based on this evidence, Komatsu and colleagues found that the R-Ras/AKT axis induces endothelial lumenogenesis and regulates the patency of regenerating vasculature in vitro and *in vivo* (*36*). The integrity of angiogenesis includes proliferation, migration, increased permeability and lumenogenesis of endothelial cells because the vessels are three-dimensional and form a complicated reticular structure. The sequential steps of angiogenesis should recapitulate sprouting, branching, and lumen formation (*36*). R-Ras, a member of the Ras family of small GTPases, not only increases AKT,

GSK3β phosphorylation and microtubule stabilization in endothelial cells (*36*) but also compensates for the conventionally insufficient effect of VEGF on angiogenesis. R-Ras activates AKT (*37*) and GSK3β, which is a known downstream substrate of AKT (*38*). Thus, we observed exercise-induced changes in the expression of R-Ras, p-AKT, AKT, p-GSK3β and GSK3β in the R-Ras/AKT/GSK3β signaling pathway. Our data demonstrates that exercise increased R-Ras, p-AKT/AKT, and p-GSK3β/GSK3β. It seems that exercise activates the R-Ras/AKT/GSK3β pathway. Exercise promotes angiogenesis in terms of improving the quantity and quality of microvessels. In addition, the expression of R-Ras and the ratio of p-AKT to AKT and p-GSK3β to GSK3β in DDAH1 KO mice was significantly different from those in wild-type mice. These results show that DDAH1 directly regulates this pathway. Consistent with Komatsu's finding, the R-Ras/AKT/GSK3β pathway indeed plays a crucial role in regulating angiogenesis. Combined with the data of this study, DDAH1 may play an important role in exercise-induced myocardial angiogenesis by regulating the R-Ras/AKT/GSK3β signaling pathway. On the one hand, the current study expands the understanding of increased capillary density by exercise; on the other hand, this study provides a new pathway in the regulation of angiogenesis by DDAH1. The new discovery of the function of the R-Ras/AKT/GSK3β pathway also reveals a novel role of DDAH1, which is of great significance in explaining the regulatory role of DDAH1 on angiogenesis. DDAH1 promotes exercise-induced angiogenesis, which may be exerted partly through the regulation of DDAH1 on the R-Ras/AKT/GSK3β signaling pathway. DDAH1 may be a potential molecular target to regulate angiogenesis with exercise in future gene therapy studies.

DDAH1 plays a major role in exercise-induced cardiac angiogenesis not DDAH2. In this study, DDAH1 played a key role in exercise-induced cardiac angiogenesis through regulating the R-Ras/AKT/GSK3β signaling pathway. So we found a novel role for DDAH1. Does DDAH2 have this new role? It depends on whether DDAH2 affects exercise-induced cardiac angiogenesis. Until now, there is no powerful evidence that DDAH2 plays a role in cardiac angiogenesis. Thus, DDAH1 has a leading effect on the regulation of the R-Ras/AKT/GSK3β signaling pathway in the myocardium.

Based on the above analysis, we think that DDAH1 plays a leading role in our experiments. Therefore, we have not studied DDAH2. If there are sufficient conditions in the future, we will also consider further research on DDAH2.

Acknowledgements

This work was supported by the National Natural Science Foundation of China (grant number 81370197).

References

1. Badimon L, Borrell M. Microvasculature recovery by angiogenesis after myocardial infarction. Curr Pharm Des. 2018; 24:2967-2973.
2. Khazaei M, Fallahzadeh AR, Sharifi MR, Afsharmoghaddam N, Javanmard SH, Salehi E. Effects of diabetes on myocardial capillary density and serum angiogenesis biomarkers in male rats. Clinics (Sao Paulo). 2011; 66:1419-1424.
3. Ahluwalia A, Narula J, Jones MK, Deng X, Tarnawski AS. Impaired angiogenesis in aging myocardial microvascular endothelial cells is associated with reduced importin alpha and decreased nuclear transport of HIF1 alpha: Mechanistic implications. J Physiol Pharmacol. 2010; 61:133-139.
4. Tang XY, Hong HS, Chen LL, Lin XH, Lin JH, Lin Z. Effects of exercise of different intensities on the angiogenesis, infarct healing, and function of the left ventricle in postmyocardial infarction rats. Coron Artery Dis. 2011; 22:497-506.
5. Leosco D, Rengo G, Iaccarino G, *et al*. Exercise promotes angiogenesis and improves β-adrenergic receptor signalling in the post-ischaemic failing rat heart. Cardiovasc Res. 2008; 78:385-394.
6. Yardley M, Ueland T, Aukrust P, Michelsen A, Bjørkelund E, Gullestad L, Nytrøen K. Immediate response in markers of inflammation and angiogenesis during exercise: a randomised cross-over study in heart transplant recipients. Open Heart. 2017; 4:e000635.
7. Naderi R, Mohaddes G, Mohammadi M, Alihemmati A, Khamaneh A, Ghyasi R, Ghaznavi R. The effect of garlic and voluntary exercise on cardiac angiogenesis in diabetes: the role of miR-126 and miR-210. Arq Bras Cardiol. 2019; 112:154-162.
8. Chodari L, Mohammadi M, Ghorbanzadeh V, Dariushnejad H, Mohaddes G. Testosterone and voluntary exercise promote angiogenesis in hearts of rats with diabetes by enhancing expression of VEGF-A and SDF-1a. Can J Diabetes. 2016; 40:436-441.
9. Soori R, Amini AA, Choobineh S, Eskandari A, Behjat A, Ghram A, Voltarelli FA. Exercise attenuates myocardial fibrosis and increases angiogenesis-related molecules in the myocardium of aged rats. Arch Physiol Biochem. 2019:1-6.
10. Naderi-boldaji V, Joukar S, Noorafshan A, Raji-amirhasani A, Naderi-boldaji S, Bejeshk M-a. The effect of blood flow restriction along with low-intensity exercise on cardiac structure and function in aging rat: role of angiogenesis. Life Sci. 2018; 209:202-209.
11. Marini M, Falcieri E, Margonato V, Treré D, Lapalombella R, di Tullio S, Marchionni C, Burattini S, Samaja M, Esposito F, Veicsteinas A. Partial persistence of exercise-induced myocardial angiogenesis following 4-week detraining in the rat. Histochem Cell Biol. 2008; 129:479-487.
12. Zhang P, Xu X, Hu X, Wang H, Fassett J, Huo Y, Chen Y, Bache RJ. DDAH1 deficiency attenuates endothelial cell cycle progression and angiogenesis. PLoS One. 2013; 8:e79444.
13. Xu X, Zhang P, Kwak D, Fassett J, Yue W, Atzler D, Hu X, Liu X, Wang H, Lu Z, Guo H, Schwedhelm E, Böger RH, Chen P, Chen Y. Cardiomyocyte dimethylarginine dimethylaminohydrolase-1 (DDAH1) plays an important role in attenuating ventricular hypertrophy and

dysfunction. Basic Res Cardiol. 2017; 112:55.
14. Hou L, Guo J, Xu F, Weng X, Yue W, Ge J. Cardiomyocyte dimethylarginine dimethylaminohydrolase1 attenuates left-ventricular remodeling after acute myocardial infarction: involvement in oxidative stress and apoptosis. Basic Res Cardiol. 2018; 113:28.
15. Zhang P, Fassett JT, Zhu G, Li J, Hu X, Xu X, Chen Y, Bache RJ. Repetitive ischemia increases myocardial dimethylarginine dimethylaminohydrolase 1 expression. Vasc Med. 2017; 22:179-188.
16. Hu X, Atzler D, Xu X, Zhang P, Guo H, Lu Z, Fassett J, Schwedhelm E, Böger RH, Bache RJ, Chen Y. Dimethylarginine dimethylaminohydrolase-1 is the critical enzyme for degrading the cardiovascular risk factor asymmetrical dimethylarginine. Arterioscler Thromb Vasc Biol. 2011; 31:1540-1546.
17. Hu X, Xu X, Zhu G, Atzler D, Kimoto M, Chen J, Schwedhelm E, Lüneburg N, Böger RH, Zhang P, Chen Y. Vascular endothelial-specific dimethylarginine dimethylaminohydrolase-1-deficient mice reveal that vascular endothelium plays an important role in removing asymmetric dimethylarginine. Circulation. 2009; 120:2222-2229.
18. Chen Y, Li Y, Zhang P, Traverse JH, Hou M, Xu X, Kimoto M, Bache RJ. Dimethylarginine dimethylaminohydrolase and endothelial dysfunction in failing hearts. Am J Physiol Heart Circ Physiol. 2005; 289:H2212-2219.
19. Leiper J, Nandi M, Torondel B, *et al.* Disruption of methylarginine metabolism impairs vascular homeostasis. Nat Med. 2007; 13:198-203.
20. Dowsett L, Piper S, Slaviero A, Dufton N, Wang Z, Boruc O, Delahaye M, Colman L, Kalk E, Tomlinson J, Birdsey G, Randi AM, Leiper J. Endothelial dimethylarginine dimethylaminohydrolase 1 is an important regulator of angiogenesis but does not regulate vascular reactivity or hemodynamic homeostasis. Circulation. 2015; 131:2217-2225.
21. Jacobi J, Sydow K, von Degenfeld G, Zhang Y, Dayoub H, Wang B, Patterson AJ, Kimoto M, Blau HM, Cooke JP. Overexpression of dimethylarginine dimethylaminohydrolase reduces tissue asymmetric dimethylarginine levels and enhances angiogenesis. Circulation. 2005; 111:1431-1438.
22. Zhang P, Hu X, Xu X, Chen Y, Bache RJ. Dimethylarginine dimethylaminohydrolase 1 modulates endothelial cell growth through nitric oxide and Akt. Arterioscler Thromb Vasc Biol. 2011; 31:890-897.
23. Chen Y, Park S, Li Y, Missov E, Hou M, Han X, Hall JL, Miller LW, Bache RJ. Alterations of gene expression in failing myocardium following left ventricular assist device support. Physiol Genomics. 2003; 14:251-260.
24. Ardakanizade M. The effects of mid- and long-term endurance exercise on heart angiogenesis and oxidative stress. Iran J Basic Med Sci. 2018; 21:800-805.
25. Evangelista FS, Brum PC, Krieger JE. Duration-controlled swimming exercise training induces cardiac hypertrophy in mice. Braz J Med Biol Res. 2003; 36:1751-1759.
26. Teplan V, Mahrova A, Pitha J, Racek J, Gurlich R, Teplan V, Jr., Valkovsky I, Stollova M. Early exercise training after renal transplantation and asymmetric dimethylarginine: the effect of obesity. Kidney Blood Press Res. 2014; 39:289-298.
27. Schlager O, Giurgea A, Schuhfried O, Seidinger D, Hammer A, Groger M, Fialka-Moser V, Gschwandtner M, Koppensteiner R, Steiner S. Exercise training increases endothelial progenitor cells and decreases asymmetric dimethylarginine in peripheral arterial disease: a randomized controlled trial. Atherosclerosis. 2011; 217:240-248.
28. Iemitsu M, Maeda S, Jesmin S, Otsuki T, Miyauchi T. Exercise training improves aging-induced downregulation of VEGF angiogenic signaling cascade in hearts. Am J Physiol Heart Circ Physiol. 2006; 291:H1290-1298.
29. Broderick TL, Sennott JM, Gutkowska J, Jankowski M. Anti-inflammatory and angiogenic effects of exercise training in cardiac muscle of diabetic mice. Diabetes Metab Syndr Obes. 2019; 12:565-573.
30. Chen Z, Hu Q, Xie Q, Wu S, Pang Q, Liu M, Zhao Y, Tu F, Liu C, Chen X. Effects of treadmill exercise on motor and cognitive function recovery of MCAO mice through the caveolin-1/VEGF signaling pathway in ischemic penumbra. Neurochem Res. 2019; 44:930-946.
31. Zhu JZ, Bao XY, Zheng Q, Tong Q, Zhu PC, Zhuang Z, Wang Y. Buyang Huanwu decoction exerts cardioprotective effects through targeting angiogenesis *via* caveolin-1/VEGF signaling pathway in mice with acute myocardial infarction. Oxid Med Cell Longev. 2019; 2019:4275984.
32. Kokubun T, Saitoh SI, Miura S, Ishida T, Takeishi Y. Telomerase plays a pivotal role in collateral growth under ischemia by suppressing age-induced oxidative stress, expression of p53, and pro-apoptotic proteins. Int Heart J. 2019; 60:736-745.
33. Takada M, Yasui T, Oka T, Shioyama W, Kuroda T, Nakai Y, Nishimura K, Mukai M, Fujita M. Aortic dissection and cardiac dysfunction emerged coincidentally during the long-term treatment with angiogenesis inhibitors for metastatic renal cell carcinoma. Int Heart J. 2018; 59:1174-1179.
34. Jiang Y, Lin X, Tang Z, *et al.* Critical role of caveolin-1 in ocular neovascularization and multitargeted antiangiogenic effects of cavtratin *via* JNK. Proc Natl Acad Sci U S A. 2017; 114:10737-10742.
35. Komatsu M, Ruoslahti E. R-Ras is a global regulator of vascular regeneration that suppresses intimal hyperplasia and tumor angiogenesis. Nat Med. 2005; 11:1346-1350.
36. Li F, Sawada J, Komatsu M. R-Ras-Akt axis induces endothelial lumenogenesis and regulates the patency of regenerating vasculature. Nat Commun. 2017; 8:1720.
37. Osada M, Tolkacheva T, Li W, Chan TO, Tsichlis PN, Saez R, Kimmelman AC, Chan AM. Differential roles of Akt, Rac, and Ral in R-Ras-mediated cellular transformation, adhesion, and survival. Mol Cell Biol. 1999; 19:6333-6344.
38. Cantley LC. The phosphoinositide 3-kinase pathway. Science. 2002; 296:1655-1657.

Received December 30, 2019; Revised February 9, 2020; Re-revised February 25, 2020; Accepted March 19, 2020

**Address correspondence to:*
Xin Xu, Department of Exercise Rehabilitation, Shanghai University of Sport, No.188 Hengren Road, Shanghai 200438, China.
E-mail: xxu2000@outlook.com

Released online in J-STAGE as advance publication April 1, 2020.

Original Article

DOI: 10.5582/bst.2020.01005

A steroidal saponin form *Paris vietnamensis* (Takht.) reverses temozolomide resistance in glioblastoma cells *via* inducing apoptosis through ROS/PI3K/Akt pathway

Shan Zhang[1,§], Yang Liu[2,§], Yunyang Lu[2,§], Hua Li[2], Yuqiang Ji[3], Fei Fang[3], Haifeng Tang[1,2,*], Pengcheng Qiu[2,*]

[1] School of Pharmacy, Shaanxi University of Chinese Medicine, Xianyang, China;
[2] Institute of Materia Medica, School of Pharmacy, Fourth Military Medical University, Xi'an, China;
[3] Central Laboratory of Xi'an No.1 Hospital, Xi'an, China.

SUMMARY Glioblastoma is one of the most difficult cancers to treat with a 5-year overall survival rate less than 5%. Temozolomide (TMZ) is an effective drug for prolonging the overall survival time of patients, while drug-resistance is an important clinical problem at present. Pennogenin-3-α-L-rhamnopyranosyl-(1→4)-[α-Lrhamno-pyranosyl-(1→2)]- β-D-glucopyranoside (N45), a steroidal saponin, was isolated from the rhizomes of *Paris vietnamensis* (Takht.), which is used as a Traditional Chinese Medicine and has been reported to possess preclinical anticancer efficacy in various cancer types. However, the mechanism of the inhibition of N45 on glioblastoma cells and its possible application in the treatment of chemotherapy-resistant glioblastoma cells are still unknown. In this study, we use cellular methodological experiments including cell counting kit-8 (CCK-8) assay, terminal deoxynucleotidyl transferase dUTP nick end labeling (TUNEL) staining assay, flow cytometry assay, transmission electron microscopy (TEM) and Western blot. The results show that N45 significantly suppresses the proliferation of glioblastoma cells and TMZ-resistant glioblastoma cells (U87R) by inducing mitochondrial apoptosis through reactive oxygen species (ROS)/phosphoinositide 3-kinase (PI3K)/Akt signal pathway, and the N-acetyl-L-cysteine (NAC) combined with N45 effectively reduced N45-mediated apoptosis and reversed the inhibition of PI3K/Akt signal pathway. In addition, N45 decreased the drug-resistance by down-regulation of nuclear factor kappa-B p65 (NF-κB p65) to attenuate O^6-methylguanine-DNA methyltransferase (MGMT) in TMZ-resistant glioblastoma cells (U87R). Our findings proved that N45 might be a potential therapeutic agent against glioblastoma and TMZ-resistant glioblastoma, promising to be a potential agent to reduce drug resistance.

Keywords *Paris vietnamensis* (Takht.) (N45), glioblastoma cells, temozolomide resistance, apoptosis, ROS/PI3K/Akt pathway

1. Introduction

Glioblastoma is the most common malignant primary brain tumor in adults, and the high rate of mortality and relapse makes it remain to be one of the most difficult cancers to treat with a 5-year overall survival rate less than 5% (*1*). Despite this the treatment has evolved from only single surgery to a combination treatment of surgery with radiotherapy and chemotherapy, and the average survival time is only 12-15 months for the patient with glioblastoma. Especially for elders, the survival period is less than 12 months (*2,3*). However, commonly used clinical drugs cannot effectively prolong the survival time of patients. Tumor recurrence limits the efficacy of glioblastoma treatment, which is mainly associated with the drug-resistance property of glioblastoma cells (*4*). Temozolomide (TMZ) is a clinical chemotherapy drug with broad-spectrum antitumor activity. The cytotoxicity of temozolomide is mainly achieved by methylation of O^6-guanine. However, because of the single mechanism of action and widespread drug-resistance its drug efficacy is limited (*5*). Therefore, it is urgent to develop new therapeutic drugs for glioblastoma treatment.

Natural products are a source of leading compounds for new drug development, especially for tumor

treatment. For example, taxol, a natural compound, was first isolated from the bark of *Taxus brevifoliac* and has showed significant therapeutic effect against several tumors, such as ovarian cancer, breast cancer and so on (*6,7*). Steroidal saponins, a group of natural products consisting of a steroidal aglycone moiety and oligosaccharide moiety, with a character of resource diversity, structural diversity and bioactive diversity, have become an important branch of natural drug discovery. Studies have shown that steroidal saponins exhibit multiple pharmacological effects, such as anti-inflammatory, anti-cancer, antiviral, immune regulatory and cardiovascular protection, among which anti-cancer is the most attractive one (*8-10*). For instance, ginsenoside Rg3 demonstrates significant anti-cancer effects on various tumors, such as gastric cancer (*11*), liver cancer (*12*), ovarian cancer (*13*), lung cancer (*14*), and melanoma (*15*).

The genus *Paris* (Liliaceae) is a famous Traditional Chinese Medicine listed in the Chinese Pharmacopoeia, with 32 species and more than 10 varieties (*16*). *Paris vietnamensis* (Takht.) is one of the varieties of the genus *Paris*, mainly distributed in Guangxi and Yunnan provinces of China and in North Vietnam (*17*). Modern phytochemical and pharmacological research showed that the genus *Paris* had anti-tumor effects and steroidal saponins were the chief active components. For example, Polyphyllin I (D), Polyphyllin II, Polyphyllin III, Polyphyllin VII and *paris* saponin H, which were isolated from *Paris*, have significant anti-cancer effects, including ovarian cancer, liver cancer, stomach cancer, colon cancer, breast cancer, osteosarcoma, melanoma and glioblastoma (*18,19*). Liu *et al.* reported Polyphyllin I induced G2/M phase arrest and apoptosis in U251 human glioblastoma cells *via* JNK signaling pathway (*20*). Pang *et al.* discovered that Polyphyllin VII promoted glioblastoma cells apoptosis and autophagic cell death through ROS-inhibited Akt activity (*21*). These studies demonstrate the potential of the genus *Paris* in anti- glioblastoma studies.

N45 is a steroidal saponin isolated from the rhizomes of *Paris vietnamensis*, and the structures were identified as pennogenin-3-α-L-rhamnopyranosyl-(1→4)-[α-Lrhamnopyranosyl-(1→2)]-β-D-glucopyranoside. Our previous study revealed that N45 exhibited significant cytotoxic effects against glioblastoma cell lines U87 and U251 (*22*). However, the mechanism and the possible application in the treatment of chemotherapy-resistant glioblastoma are still unknown. This study was designed to evaluate the antitumor mechanism of N45 on glioblastoma cells and TMZ-resistant glioblastoma cells, and examine the correlation between apoptosis and the ROS/PI3K/Akt signal pathway. Besides, we also investigated the mechanism of N45 reversal of drug resistance in glioblastoma cells.

2. Materials and Methods

2.1. Materials

TMZ was supplied by Yuanye Biological Co., Ltd. (Shanghai, China). The Cell Counting Kit-8 (CCK-8) and the terminal deoxynucleotidyl transferase dUTP nick end labeling (TUNEL) assay cell death kit were purchased from Seven-sea Biotech (Shanghai, China). N-acetyl-L-cysteine (NAC) was supplied by Solarbio (Beijing, China). ROS assay kit was purchased from Beyotime Biotechnology (Shanghai, China).

2.2. Cell culture

Human glioblastoma cell lines U251 and U87 were purchased from the Chinese Academy of Sciences Cell Bank (Shanghai, China). TMZ-resistant variant cell line (U87R) was obtained by exposing U87 to an increasing concentration of TMZ (1, 5, 25, 50, 100, 200 μg/mL) for 6 months. The cell lines were cultured in DMEM (Corning, Beijing, China) supplemented with 10% FBS (Ausbian, Harbin, China), maintained at 37℃ with 5% CO_2. The medium was changed every 3 days.

2.3. Cell proliferation assay

The logarithmic phase cells were seeded in 96-well plates at a density of 5×10^3 cells/well. After 24 h, the cells were incubated with different doses (40, 20, 10, 5, 2.5, 1.25, 0.625 0.3125 μg/mL) of N45 for 24 h. Four replicated wells were used for each experimental condition. After treatment, cell proliferation and cytotoxicity were assessed using CCK-8, 10 μL CCK-8 was added to each well and incubated at 37℃ for 2 h, measuring the absorbance at a wavelength of 450 nm using a microplate reader.

2.4. TUNEL assay

Cells were cultured on cell plates coated with Poly-L-Lysine (PLL) and incubated 24 h. After incubation with N45 for 24 h, and phosphate-buffered saline (PBS) washing twice, the cells were incubated with fluorescein isothiocyanate (FITC)-dUTP for 15 minutes at room temperature in the dark. Thereafter, the cells were washed twice more with PBS. Then using a fluorescence microscope obtained five random fields of vision, recorded apoptotic cells (green fluorescence cells) and normal cells (red fluorescence cells), and calculated the apoptosis rate.

2.5. Cell apoptosis analysis

The logarithmic phase cells were cultured on 6-well plates at density of 2×10^5 cells and incubated for 24 h, The cells were collected after treatment with different

doses (0, 2, 4 μg/mL) of N45 for 24 h, three replicate wells were used for each experimental condition. Then washed twice in cold PBS (4℃), cells apoptosis were performed using Annexin V-FITC/ propidine iodide (PI) double staining. The result of AV/PI-positive cells was evaluated with a flow cytometer (BD FACSCalibur, USA).

2.6. Transmission electron microscopy analysis

Cells were fixed in 2% glutaraldehyde for 2 h and washed twice with PBS for 10 min. Then fixed in 1% OsO_4 for 2 h. After gradient dehydration with ethanol, the cells were embedded in epoxy resin and cut into 50-60 nm sections. Sections were stained with uranyl acetate combined with lead citrate. Samples were cut and analyzed with a JEM-1400 transmission electron microscope (JEM-1400, JEOL, Japan).

2.7. Reactive oxygen species (ROS) detection

ROS assay kit was used according to the manufacturer's instructions. 2×10^7 glioblastoma cells were incubated with N45 (0, 4 μg/mL) for 24 h, then the cells were harvested, the cells were washed twice more with PBS and loaded with 10 μM 2', 7'-Dichlorodi-hydrofluorescein diacetate (DCFH-DA) in serum-free medium for 30 min at 37°C in the dark. After washing three more times with PBS, the samples were analyzed for fluorescence by flow cytometer, with excitation at 485 nm and emission at 525 nm.

2.8. Real time cellular analysis (RTCA)

The proliferation assay and the cell growth index were recorded using iCELLigence system (ACEA Biosciences, Inc. San Diego, CA, USA) as the RTCA system. This system can monitor cell growth status in real time. All monitoring was performed at 37℃ with regulated CO_2 content of 5%. E-plates (culture plates for the iCELLigence system) containing 200 μL culture medium per well were equilibrated to 37℃, and the cells were seeded at 1×10^4 cells per well in cell culture media.

2.9. Western blot analysis

Cells were treated with different doses (0, 4 μg/mL in medium) of N45 for 24 h, and washed twice in cold PBS. Then the treated cells were collected and lysed in radio immunoprecipitation assay (RIPA) lysis buffer, a bicinchoninic acid (BCA) kit was used to determine protein concentration, and all protein samples were quantified to be the same concentration. Cell lysates were subjected to sodium dodecyl sulfate (SDS)-polyacrylamide gel electrophoresis (PAGE) and transferred onto polyvinylidene difluoride (PVDF) membrane. Then incubated with the primary antibody at 4℃ overnight after blocking with 5% non-fat dry milk, and then incubated again with the secondary antibody in the dark for 1 h. The protein level was corrected using glyceraldehyde-3-phosphate dehydrogenase (GAPDH). The band density was quantified by densitometry using Image J software.

2.10. Statistical analysis

Results were analyzed by GraphPad Prism software 7.0, and all the data were expressed as mean ± standard deviation. One-way Analysis of Variance (ANOVA) was used to analyze the multi-group differences, *t* test was used to examine the differences between two groups. The value of $p < 0.05$ suggested that the difference was a statistically significant difference.

3. Results

3.1. Established the TMZ-resistant U87 cells (U87R) expressed high MGMT

We successfully cultured U87R cells for 175 days and observed with light microscopy (Figure 1A). Western blot assay was used to evaluate the levels of MGMT. The Western blot result showed that the expression of MGMT proteins in U87R was significantly increased compared with the parental U87 cells ($p < 0.05$ and $p < 0.01$) (Figure 1B), and flow cytometry showed TMZ (100, 200 μg/mL) could not induce apoptosis in U87R cells (Figure 1C). These results indicated that U87R resistant to TMZ 200 μg/mL doses was successfully established and we observed normal cell morphology under light microscopy.

3.2. N45 exhibited cytotoxicity against general glioblastoma cells *in vitro*

Light microscopy confirmed that 24 h treatment with N45 on U87 and U251 cells was the optimal time for this study (Figure 2B). The effect on general glioblastoma cells proliferation with N45 was determined by CCK-8 assay. The results showed that compared with control group N45 could significantly decrease the optical density (OD) value of U87 and U251 cells after 24h treatment ($p < 0.05$ and $p < 0.001$). Respectively, the IC_{50} values (concentration of drug inhibiting cell growth by 50%) of U87 and U251 cells were 3.808 μg/mL and 3.39 μg/mL (Figure 2C). The results revealed that N45 suppressed cell proliferation in a dose dependent manner in U87 and U251 glioblastoma cell lines.

3.3. N45 inhibited the viability of general glioblastoma cells by inducing mitochondrial apoptosis

The TUNEL staining assay showed that, numbers of

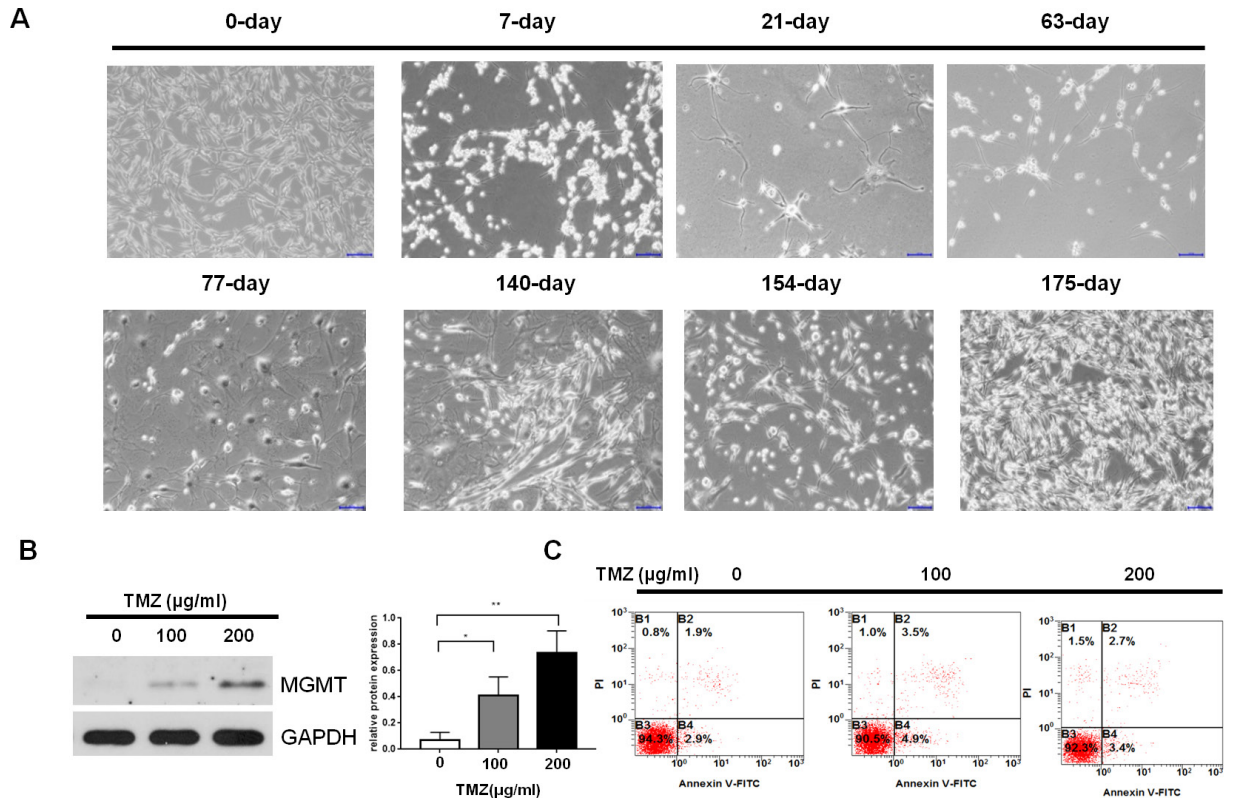

Figure 1. Culture of U87R cell lines (**A**) The parental cells were treated with repeatedly increased concentrations of TMZ (1, 5, 25, 50, 100 μg/mL) for 6 months to establish U87R cells. (**B**) Western blot assay was used to evaluate the expression of MGMT in parental U87 and U87R (100, 200 μg/mL) cells, and the density of MGMT was semi-quantitative by Image J software. (**C**) Annexin V-FITC/PI double staining was used to detect the cell apoptosis rate after treatment with TMZ (100, 200 μg/mL) for 24 h. Data is expressed as means ± SD of three independent experiments. ($^{*}p < 0.05$, $^{**}p < 0.01$), as compared with the control.

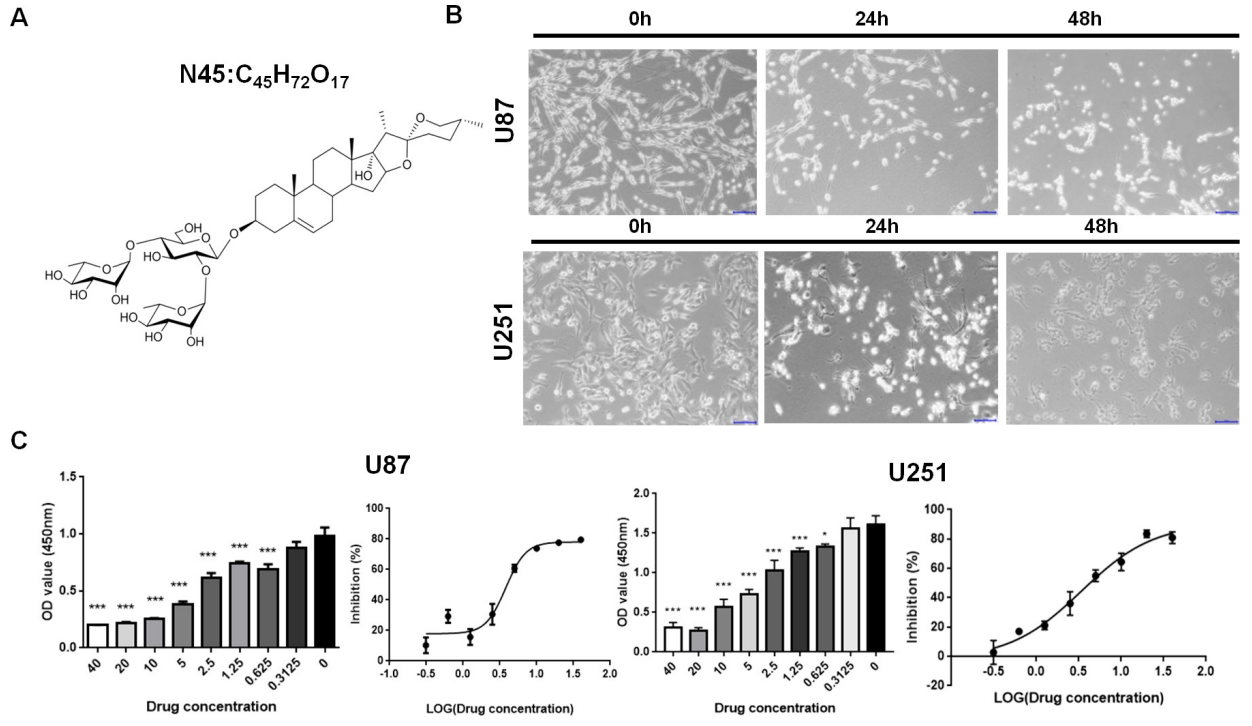

Figure 2. N45 showed cytotoxicity against U87 and U251 cells in a dose dependent manner. (**A**) Structure of compound N45. (**B**) U87 and U251 cells morphology were observed under light microscope after treatment with N45 10 μg/mL (24 h and 48 h). (**C**) U87 and U251 cells were treated with various concentrations of N45 for 24 h and the dose response curves of U87 and U251 cells were assessed by CCK8 assay. Data is expressed as means ± SD of three independent experiments. ($^{*}p < 0.05$, $^{***}p < 0.001$), as compared with the control group.

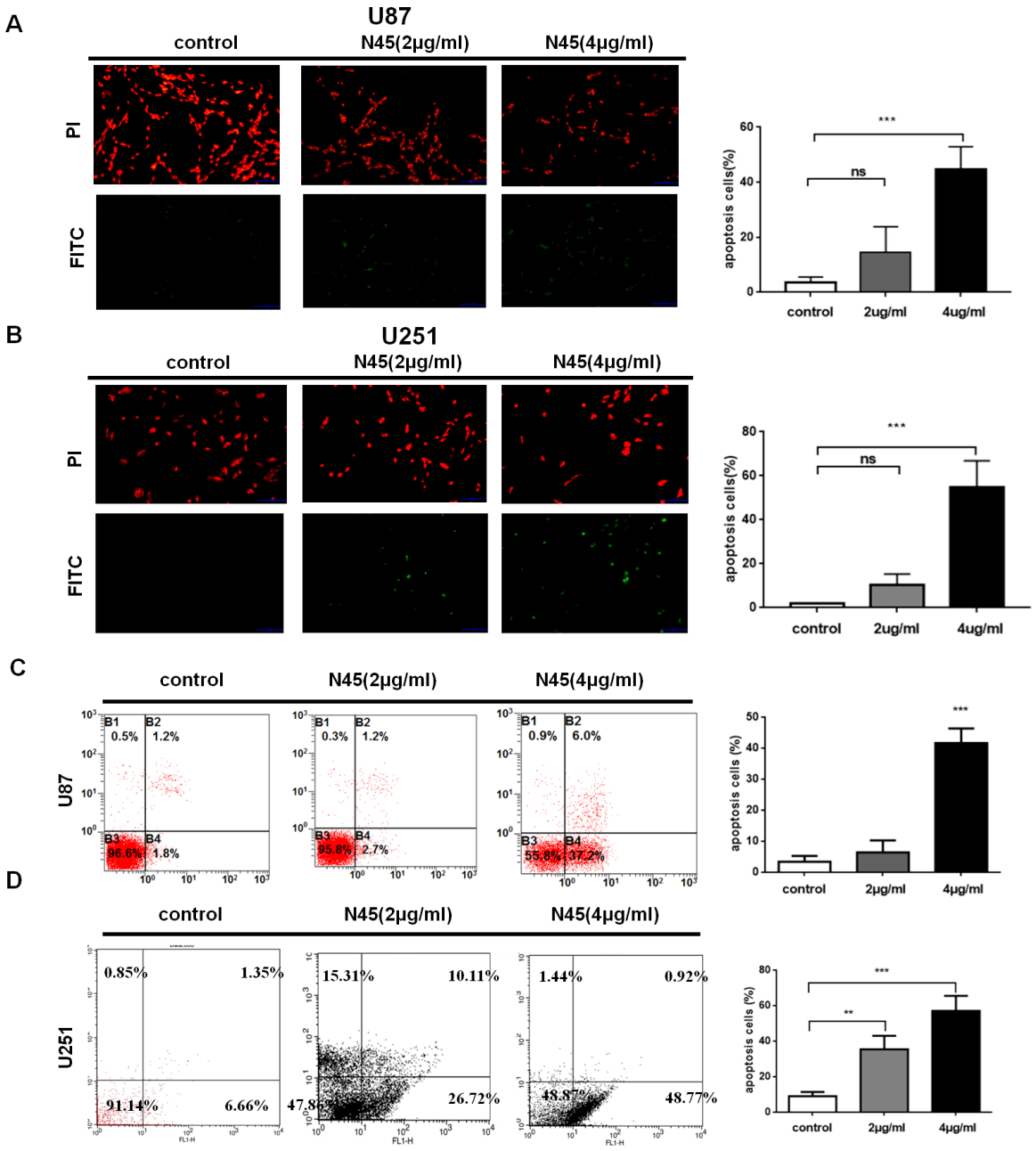

Figure 3. N45 induced apoptosis of U87 and U251 cells. (**A**) (**B**) The apoptotic cell rates were determined using TUNEL staining assay after treatment with N45 (2, 4 μg/mL) for 24 h. Green fluorescence indicates the apoptotic cells. Red fluorescence indicates both apoptotic and non-apoptotic cells. The histograms present the apoptosis rate (positive cells/total cells). (**C**) (**D**) The proportions of living and dead cells were determined using flow cytometry analysis after treatment with N45 (2, 4 μg/mL) for 24 h. The histograms represent the apoptosis rate. Data is expressed as means ± SD of three independent experiments. ($^{**}p < 0.01$ and $^{***}p < 0.001$), as compared with the control group. ns, not significant.

green fluorescence cells significantly increased in 4 μg/mL N45 treated U87 and U251 cells compared with the control group ($p < 0.001$) (Figure 3A and B). The flow cytometry assay showed that 4 μg/mL N45 significantly promoted the percentage of apoptotic cells in the U87 and U251 cells compared with the control group ($p < 0.01$ and $p < 0.001$) (Figure 3C and D). According to the results expressed in Figure 3, the concentration of N45 was determined to be 4 μg/mL for the following experiments.

Morphological changes of mitochondria apoptosis were observed using TEM. TEM revealed that, untreated cells exhibited intact cell membranes and normal nuclei, after treatment with N45 the majority of cells had apoptosis features, mainly including cytoplasmic shrinkage, dilation of the ERs, and turgidity of the mitochondrion, disarrangement, diminution and vacuolization (Figure 4A and B).

Furthermore, we detected expression of mitochondrial apoptosis-related proteins. Western blot showed that, after treatment with N45 (4 μg/mL) for 24 hours, the expressions of caspase 3, cleaved-caspase 3 and cytochrome c, and the value of Bax/Bcl-2 were significantly increased ($p < 0.01$ and $p < 0.001$) (Figure

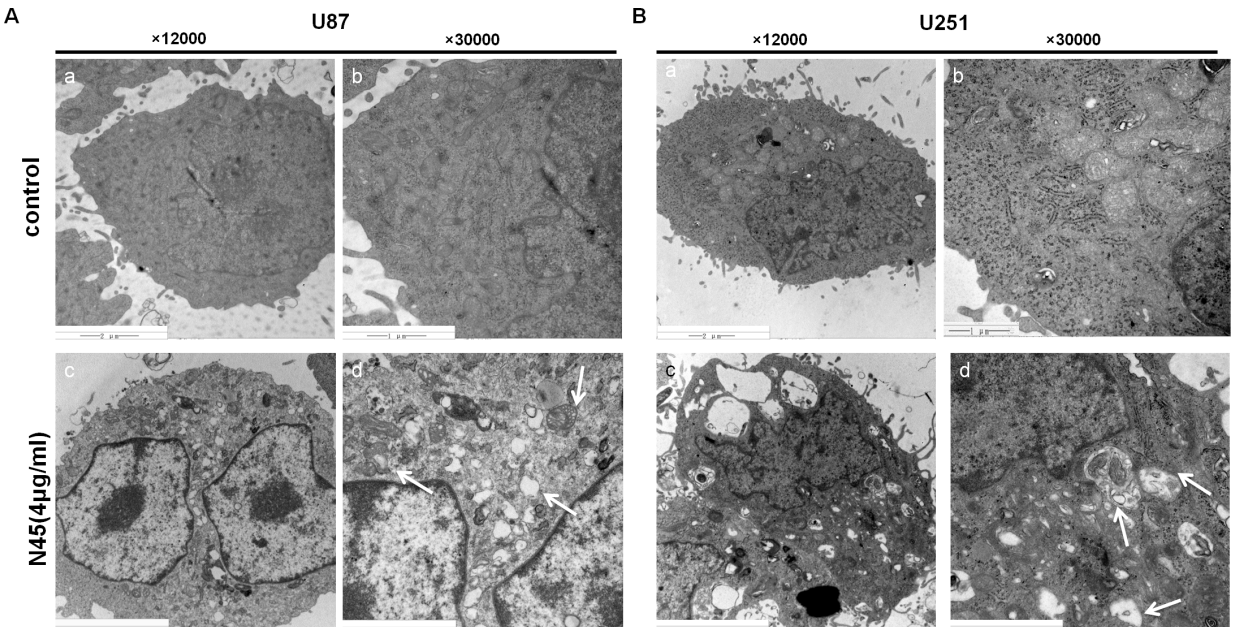

Figure 4. The mitochondria morphological changes of U87 and U251 cells. TEM was used to determine the morphological changes after treatment with N45 (4μg/mL). (**A**) (**B**) Cytoplasmic shrinkage, the dilation of the ERs, and turgidity of the mitochondrion, the disarrangement and vacuolization are shown as arrows.

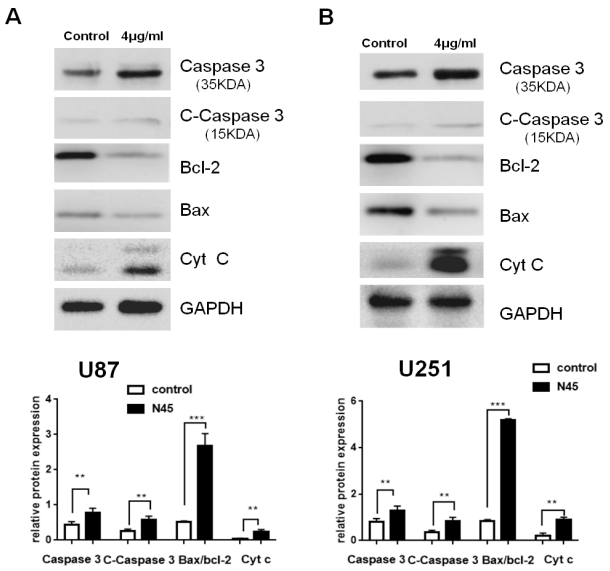

Figure 5. N45 induced mitochondrial apoptosis in U87 and U251 cells. After treatment with N45 (4 μg/mL) for 24 h, the expression of Bax/Bcl-2, Caspase 3, Cleaved-Caspase 3 and cytochrome c in the U87 (**A**), and U251 (**B**) were analyzed by Western blot, the relative density was semi-quantitative by Image J software. Data is expressed as means ± SD of three independent experiments. ($^{**}p < 0.01$ and $^{***}p < 0.001$), as compared with the control group.

5A and B). These results demonstrated that N45 induced mitochondrial apoptosis in U87 and U251 cells.

3.4. N45 induced mitochondrial apoptosis in U87R cells

CCK-8 assay and RTCA assay were performed to explore the effect of N45 on U87R cells. The results of CCK-8 assay showed that compared with control group, N45 significantly decreased the proliferation of U87R cells (24 h) in a dose dependent manner ($p < 0.001$) (Figure 6A). Furthermore, the iCELLigence system revealed that the logarithmic phase U87R cells were given N45 (4 μg/mL) at 125 h. The cell index of U87R decreased rapidly, and viability of U87R cells was inhibited in a short time compared with the control group (Figure 6B). TUNEL staining assay showed that, after treatment with N45 (4 μg/mL) for 24 h, the numbers of green fluorescence cells significantly increased compared with control group ($p < 0.01$) (Figure 6C). The flow cytometry assay showed that, 4 μg/mL N45 significantly increased the percentage of apoptotic cells in the U87R cells compared with the control group ($p < 0.001$) (Figure 6D). TEM observed that untreated cells exhibited intact cell membranes and normal nuclei, while after treatment with N45 (4 μg/mL) for 24 h, the majority of cells showed dilation of the ERs, turgidity of the mitochondrion, disarrangement, diminution and vacuolization (Figure 7A). Western blot showed that, the U87R cells after treatment with N45 (4 μg/mL) for 24h, the expressions of caspase 3, c-caspase 3 and cytochrome c, and the value of Bax/Bcl-2 were significantly increased ($p < 0.01$) (Figure 7B). These results revealed that N45 suppressed the cell viability of TMZ-resistant glioblastoma cells in a dose dependent manner, and induced mitochondrial apoptosis.

3.5. N45 reduced MGMT in U87R cells

Western blots were used to detect the resistance indicator proteins. Western blot showed that, the level of MGMT and NF-κB p65 were significantly increased in the U87R group compared with the parental U87 cells. After treatment with N45 (4 μg/mL) for 24h, N45 down-regulated the level of MGMT and NF-κB p65 in U87R

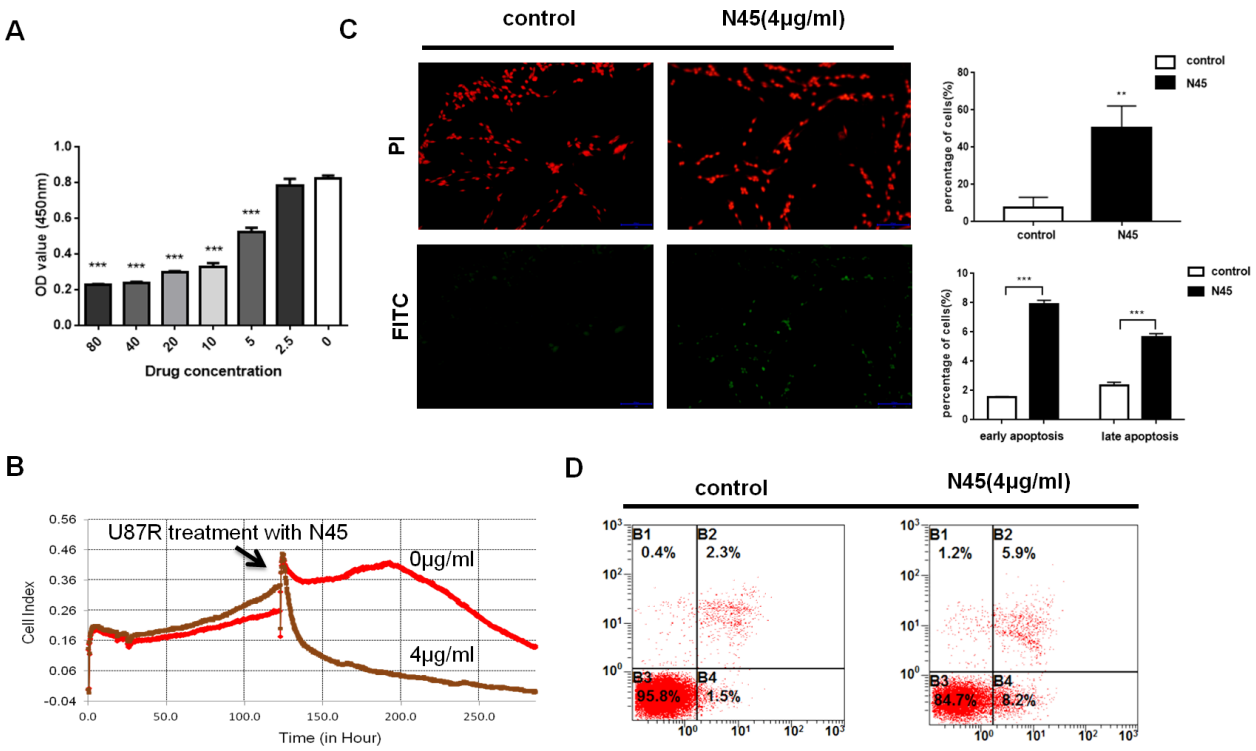

Figure 6. N45 showed cytotoxicity against U87R cells in a dose dependent manner. (**A**) U87R cells were treated with various concentrations of N45 for 24 h and cell viability was assessed by CCK8 assay. (**B**) The cell growth index was recorded using iCELLigence system. U87R was treated with N45 (125 h) and decreased in a short time. (**C**) The apoptotic cell rates were determined using TUNEL staining assay after treatment with N45 (4 μg/mL) for 24 h. The histograms represent the apoptosis rate (positive cells/total cells). (**D**) The proportions of living and dead cells were determined using flow cytometry analysis after treatment with N45 (4 μg/mL) for 24 h. The histograms represent the percentage of early apoptosis and late apoptosis. Data is expressed as means ± SD of three independent experiments. ($^{**}p < 0.01$ and $^{***}p < 0.001$), as compared with the control group.

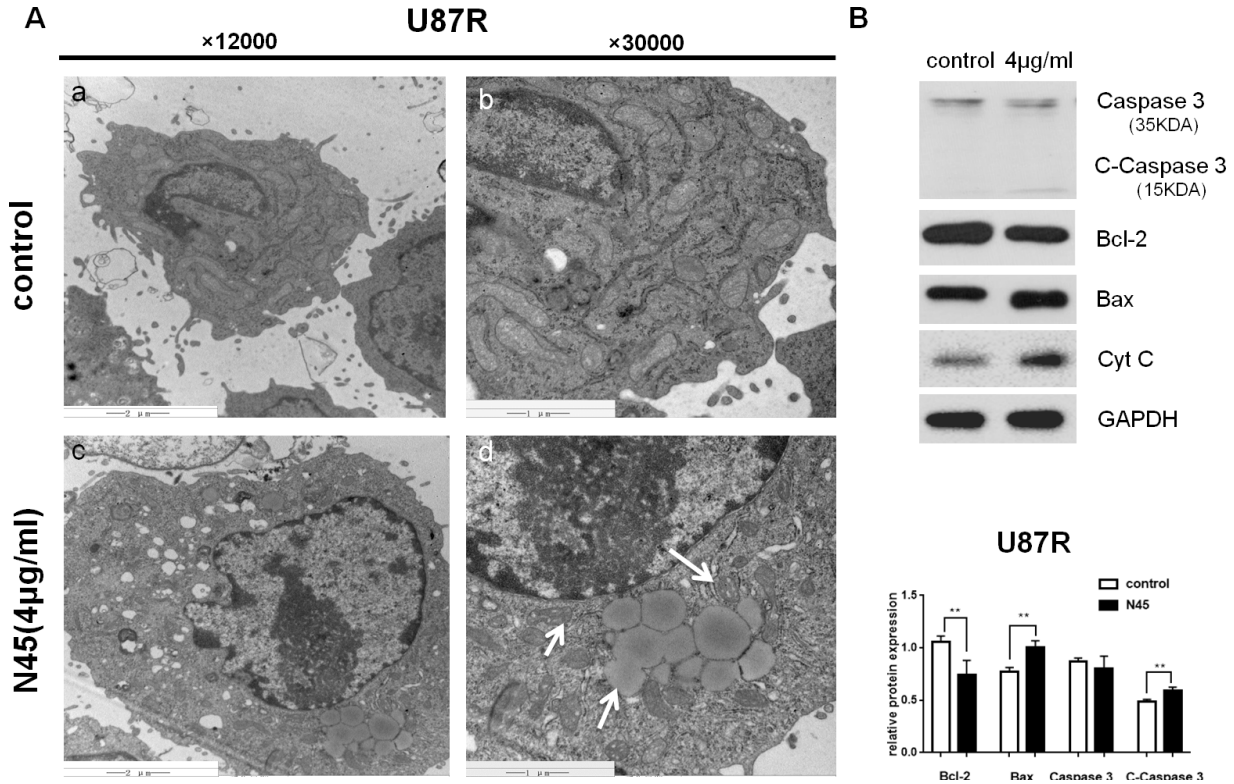

Figure 7. N45 induced mitochondrial apoptosis in U87R cells. (**A**) TEM was used to determine the morphological changes of U87R cells. Cytoplasmic shrinkage, the dilation of the ERs, and turgidity of the mitochondrion, the disarrangement and vacuolization are shown as arrows. (**B**) After treatment with N45 (4 μg/mL) for 24 h, the expression of Bax, Bcl-2, Caspase 3, Cleaved-Caspase 3 and cytochrome c in the U87R cells were analyzed by Western blot. The relative density was semi-quantitative by Image J software. Data is expressed as means ± SD of three independent experiments. ($^{**}p < 0.01$), as compared with the control group.

cells compared with the U87R N45 group ($p < 0.05$ and $p < 0.01$) (Figure 8A). These results suggested N45 down-regulated the expression of the drug resistance related proteins (MGMT), and indicated that N45 could reduce TMZ resistance.

3.6. N45 induced mitochondrial apoptosis through ROS-mediated inactivation of PI3K/Akt signal pathway

In order to determine whether intracellular ROS involved mitochondrial apoptosis in U87, U251 and U87R cells, intracellular ROS was assessed after 24 h and measured using flow cytometry assay. The results showed that N45 (4 μg/mL) treatment increased the levels of intracellular ROS compared with control group (Figure 9A). Western blot showed that, after treatment with N45 (4 μg/mL) for 24 hours, the expression of PI3K, Akt and phosphorylated Akt (p-Akt) were significantly decreased in U87, U251 and U87R cells ($p < 0.05$, $p < 0.01$ and $p < 0.001$) (Figure 9C-E).

3.7. NAC (ROS scavenger) counteract N45-mediated mitochondrial apoptosis

The CCK8 assay showed that, the cell viability of N45 (4 μg/mL) + NAC (4 mg/ml) group was higher than the N45 (4 μg/mL) group, and indicated that NAC reversed the N45 inhibition in U87, U251 and U87R cells (Figure 9B). Western blot showed that, in the N45 (4 μg/mL) + NAC (4 mg/mL) group, the levels of PI3K and p-Akt were up regulated compared with the N45 (4 μg/mL) treatment group ($p < 0.01$ and $p < 0.001$) (Figure 9C-E). These results demonstrated that ROS were negatively correlated with the PI3K/Akt pathway. Moreover, the NAC effectively reduced N45-mediated apoptosis in U87, U251 and U87R cells.

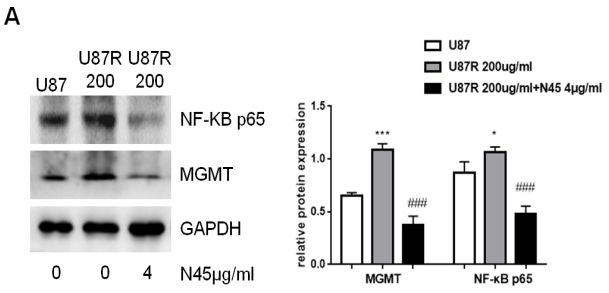

Figure 8. N45 reduced MGMT in U87R cells. (**A**) The expression of MGMT and NF-κB p65 in the parental U87 cells group, U87R cells group and U87R cells + N45 (4 μg/mL) group were analyzed by Western blot, the relative density was semi-quantitative by Image J software. Data is expressed as means ± SD of three independent experiments. ($^{*}p < 0.05$ and $^{***}p < 0.001$ *vs*. the control group. $^{\#\#\#}p < 0.001$ *vs*. the N45 treated group).

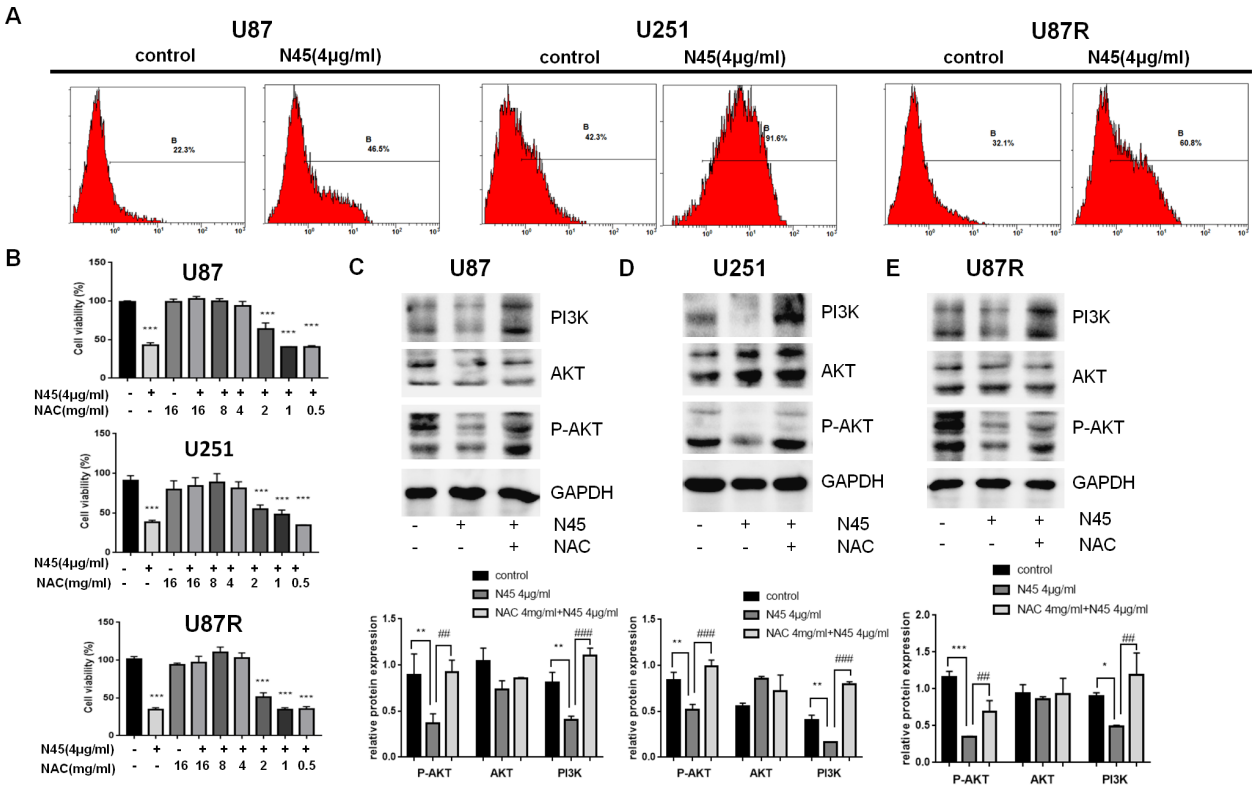

Figure 9. Effects of N45 on ROS/PI3K/Akt signaling pathway in U87, U251 and U87R cells. (**A**) Intracellular ROS were assessed by flow cytometry after treatment with N45 (4 μg/mL) for 24 h, the relative fluorescence percentage was used to estimate intracellular ROS increase. (**B**) The CCK8 assay determined that 4 mg/mL NAC was the optimal dose, in combination with N45 and could reverse the inhibition in U87, U251 and U87R cells. (**C-E**) Cells were treated with N45 (4 μg/mL) and N45 (4 μg/mL) + NAC (4 mg/ml) for 24 h. the expression of PI3K, Akt and p-Akt in the U87, U251 and U87R cells were analyzed by Western blot, the relative density was semi-quantitative by Image J software. Data is expressed as means ± SD of three independent experiments. ($^{*}p < 0.05$, $^{**}p < 0.01$ and $^{***}p < 0.001$ *vs*. the control group. $^{\#\#}p < 0.01$ and $^{\#\#\#}p < 0.001$ *vs*. the N45 treated group).

4. Discussion

Natural products are a main resource for leading compounds for new drug discovery, which have played a critical role in cancer therapy and chemoprevention study. Steroidal saponins with the character of resource diversity, structural diversity and bioactive diversity have become an important branch of natural drug discovery and one of the most likely sources of innovative drugs in the future. The work undertaken by our team has isolated many anti-tumor saponins from many plants and animals, such as *Paris vietnamensis* (*22*), *Culcita novaeguineae* (*23*), and *Anthenea chinensis* (*24*), and many of them have demonstrated significant effects on various tumors. *Paris vietnamensis* (Takht.) is used as a Traditional Chinese Medicine and has been reported to possess preclinical anticancer efficacy in various cancer types (*18,22*). N45 was isolated from the rhizomes of *Paris vietnamensis* (Takht.) and was supposed to have a good antitumor effect. In this study, we investigated the antitumor mechanism of N45 on glioblastoma cells and TMZ-resistant glioblastoma cells.

The results showed that N45 significantly suppressed the cell proliferation of glioblastoma cells in a dose dependent manner (Figure 2C). Furthermore, N45 induced cell apoptosis of U87 and U251 cells, which was verified by TUNEL and flow cytometry experiments (Figure 3A and B). Noticeably, morphological changes of mitochondrial swelling and crista disorder were observed under TEM in U87 and U251 cells, which indicated that mitochondria might be involved in the cell apoptosis induced by N45 (Figure 4A and B).

The participation of mitochondria in apoptosis is one of the most important cell apoptotic pathways. PI3K is a key signal molecule that regulates the mitochondrial apoptosis pathway. The downstream signal molecule of PI3K signal pathway was mainly related to caspase family, Bax, Bcl-2 family and PI3K, Akt indicators. Akt is activated by phosphorylation and is the primary mediator of PI3K-initiated signaling, while Bcl-2 is a member of its downstream apoptosis-inhibitory molecule (*25,26*). Apoptosis-inhibitory protein Bcl-2 and pro-apoptotic protein Bax are both members of the Bcl-2 family. The ratio of Bax/Bcl-2 is a key factor in balancing mitochondrial apoptosis pathway (*27*). The inactivation of PI3K/Akt could down-regulate the expression of Bcl-2, in order to change the ratio of Bax/Bcl-2. Increasing the ratio of Bax/Bcl-2 could release cytochrome C from mitochondria to cytoplasm, and then activate caspase 3, which is an important apoptosis implementing protein. In the current study, N45 decreased the levels of PI3K, p-Akt and Bcl-2, while it increased the expression of cytochrome C, capase 3, cleaved caspase 3 and the ratio of Bax/Bcl-2, which resulted in proliferation inhibition and cell apoptosis in U87 (Figure 5A, Figure 9C) and U251 cells (Figure 5B, Figure 9D). The results revealed that N45 inhibited proliferation and induced mitochondrial apoptosis in glioblastoma cells through the PI3K/Akt pathway.

Intracellular ROS are mainly produced from mitochondria. Intracellular or extracellular stimuli lead to intracellular ROS production and increased membrane permeabilization, whereas excessively high levels of ROS promote cell apoptosis by activating internal and external pathways (*28*). ROS interact with many factors that directly affect cell viability and promote cell death, thus, ROS are widely studied as antitumor agents (*29*). Previous studies have reported several bioactive compounds generated ROS to activate apoptosis signaling in cancer cells, while ROS-dependent compounds suppressed the activity of the PI3K/Akt signaling pathway. Fucoxanthin induced apoptosis in human glioblastoma cells *via* triggering of ROS-mediated oxidative damage and regulation of MAPKs and PI3K-Akt pathways (*30*). Thioridazine enhanced TRAIL-mediated apoptosis *via* the ROS-mediated inhibition of Akt signaling in renal carcinoma Caki cells (*31*). In this paper, N45 increased ROS generation, which was observed by flow cytometry experiments (Figure 9A). NAC, a ROS scavenger, was used for the following rescue experiments. A CCK-8 experiment showed that NAC significantly attenuated the proliferation inhibition effect of N45 in U87 and U251 cells (Figure 9B). Moreover, NAC also reversed the levels of PI3K and p-Akt, both of which were the primary mediator of PI3K-initiated signaling (Figure 9C and D). That confirmed N45 induced glioblastoma cells' mitochondrial apoptosis *via* ROS-mediated inactivation of PI3K/Akt.

TMZ is the first-line chemotherapy drug for glioblastoma and possesses a relatively good efficacy. However, in recent years endogenous or acquired resistance to TMZ limits its efficacy in the therapy of glioblastoma. TMZ-induced injury can be repaired by O^6-methylguanine-DNA methyltransferase (MGMT), which is a DNA repair enzyme and plays a key role in TMZ resistance and has now been commonly recognized (*32*). These findings suggested that reducing the expression of MGMT might be an effective therapeutic strategy in TMZ-resistant cancers. Previous studies reported reducing MGMT expression to augment chemo-sensitivity to TMZ and induced cell apoptosis in cancers. Lingchao Chen *et al.* (*33*) and Mao Li *et al.* (*34*) showed that the PI3K inhibitor (BKM120 and LY294002) could reduce MGMT, and overcome TMZ resistance sensitivity in glioblastoma cells *via* suppression of the PI3K/Akt signaling pathway. However, there are few studies on steroid saponins to reverse TMZ resistance. Thus, we cultured U87R cells to test the effect of N45 on TMZ-resistant glioblastoma, the result of Figure 1 showed that TMZ-resistant glioblastoma cells were successfully established. The

results of CCK-8, TUNEL, flow cytometry, TEM and iCELLigence systems confirmed that N45 inhibited proliferation and induced mitochondrial apoptosis in U87R cells (Figure 6A-D, Figure 7A). Western blots revealed that N45 treated U87R cells reacted the same as it worked in U87 and U251 cells (Figure 7B, Figure 9E). The results of rescue experiments also confirmed N45 induced mitochondrial apoptosis *via* ROS-mediated inactivation of PI3K/Akt signal pathway in U87R cells.

NF-κB is a member substrate in the downstream PI3K/Akt pathway, which contributes to the resistance of chemotherapy. NF-κB p65, a transcription factor, is the key subunit in the NF-κB family (*35-37*). In glioblastoma cells, due to the over-activation of PI3K/Akt signaling pathway, NF-κB p65 translocated into the nucleus and subsequently initiated transcription of numerous genes, including MGMT (*33,38*). In this paper, U87R cells significantly expressed NF- κB p65 and MGMT. After treatment with N45, the expression of MGMT and NF-κB p65 was decreased compared with the untreated U87R cells (Figure 8A). The results indicated that N45 suppressed TMZ-resistance and induced apoptosis in U87R cells by decreasing the expression of PI3K/Akt and its downstream protein NF- κB p65 to attenuate MGMT.

In conclusions, these results suggest that ROS-mediated inactivation of PI3K/Akt played an important role in N45 induced mitochondrial apoptosis in glioblastoma cells and TMZ-resistant glioblastoma cells.

Acknowledgements

This study was supported by the National Natural Science Foundation of China (No. 81973192 and No.81903862), and Shaanxi Provincial Administration of Traditional Chinese Medicine (No. ZYMS012).

Statement of Ethics This investigation was approved by the Institutional Review Board of Tangdu Hospital, Fourth Military Medical University.

References

1. Lapointe S, Perry A, Butowski NA. Primary brain tumours in adults. Lancet. 2018; 392:432-446.
2. Palanichamy K, Erkkinen M, Chakravarti A. Predictive and prognostic markers in human glioblastomas. Curr Treat Options Oncol. 2006; 7:490-504.
3. Stupp R, Hegi ME, van den Bent MJ, Mason WP, Weller M, Mirimanoff RO, Cairncross JG, European Organisation for Research and Treatment of Cancer Brain Tumor and Radiotherapy Groups, National Cancer Institute of Canada Clinical Trials Group. Changing paradigms--an update on the multidisciplinary management of malignant glioma. Oncologist. 2006; 11:165-180.
4. Mrugala MM. Advances and challenges in the treatment of glioblastoma: a clinician's perspective. Discov Med. 2013; 15:221-230.
5. Fan TY, Wang H, Xiang P, Liu YW, Li HZ, Lei BX, Yu M, Qi ST. Inhibition of EZH2 reverses chemotherapeutic drug TMZ chemosensitivity in glioblastoma. Int J Clin Exp Pathol. 2014; 7:6662-6670.
6. Galic VL, Wright JD, Lewin SN, Herzog TJ. Paclitaxel poliglumex for ovarian cancer. Expert Opin Investig Drugs. 2011; 20:813-821.
7. Megerdichian C, Olimpiadi Y, Hurvitz SA. nab-Paclitaxel in combination with biologically targeted agents for early and metastatic breast cancer. Cancer Treat Rev. 2014; 40:614-625.
8. Xiang L, Yi X, Wang Y, He X. Antiproliferative and anti-inflammatory polyhydroxylated spirostanol saponins from Tupistra chinensis. Sci Rep. 2016; 6:31633.
9. Khan M, Maryam A, Zhang H, Mehmood T, Ma T. Killing cancer with platycodin D through multiple mechanisms. J Cell Mol Med. 2016; 20:389-402.
10. Zheng M, Zhao M, Tang L, Zhang C, Song L, Wang W. Ginsenoside Rg1 attenuates hypoxia and hypercapnia-induced vasoconstriction in isolated rat pulmonary arterial rings by reducing the expression of p38. J Thorac Dis. 2016; 8:1513-1523.
11. Park EH, Kim YJ, Yamabe N, Park SH, Kim HK, Jang HJ, Kim JH, Cheon GJ, Ham J, Kang KS. Stereospecific anticancer effects of ginsenoside Rg3 epimers isolated from heat-processed American ginseng on human gastric cancer cell. J Ginseng Res. 2014; 38:22-27.
12. Cheong JH, Kim H, Hong MJ, Yang MH, Kim JW, Yoo H, Yang H, Park JH, Sung SH, Kim HP, Kim J. Stereoisomer-specific anticancer activities of ginsenoside Rg3 and Rh2 in HepG2 cells: disparity in cytotoxicity and autophagy-inducing effects due to 20(S)-epimers. Biol Pharm Bull. 2015; 38:102-108.
13. Liu T, Zhao L, Zhang Y, Chen W, Liu D, Hou H, Ding L, Li X. Ginsenoside 20(S)-Rg3 targets HIF-1α to block hypoxia-induced epithelial-mesenchymal transition in ovarian cancer cells. PLoS One. 2014; 9:e103887.
14. Park D, Bae DK, Jeon JH, *et al.* Immunopotentiation and antitumor effects of a ginsenoside Rg3-fortified red ginseng preparation in mice bearing H460 lung cancer cells. Environ Toxicol Pharmacol. 2011; 31:397-405.
15. Shan X, Tian LL, Zhang YM, Wang XQ, Yan Q, Liu JW. Ginsenoside Rg3 suppresses FUT4 expression through inhibiting NF-κB/p65 signaling pathway to promote melanoma cell death. Int J Oncol. 2015; 47:701-709.
16. Wang YH, Shi M, Niu HM, Yang J, Xia MY, Luo JF, Chen YJ, Zhou YP, Li H. Substituting one Paris for another? In vitro cytotoxic and *in vivo* antitumor activities of Paris forrestii, a substitute of *Paris polyphylla* var. yunnanensis. J Ethnopharmacol. 2018; 218:45-50.
17. Li, H. *The Genus Paris* (Trilliaceae). Science Press, Beijing, China, 1998; pp. 26-28. (in Chinese)
18. Wei JC, Gao WY, Yan XD, Wang Y, Jing SS, Xiao PG. Chemical constituents of plants from the genus Paris. Chem Biodivers. 2014; 11:1277-1297.
19. Xu XH, Li T, Fong CM, Chen X, Chen XJ, Wang YT, Huang MQ, Lu JJ. Saponins from Chinese Medicines as Anticancer Agents. Molecules. 2016; 21:E1326.
20. Liu J, Zhang Y, Chen L, Yu F, Li X, Dan Tao, Zhao J, Zhou S. Polyphyllin I induces G2/M phase arrest and apoptosis in U251 human glioma cells *via* mitochondrial dysfunction and the JNK signaling pathway. Acta Biochim Biophys Sin (Shanghai). 2017; 49:479-486.
21. Pang D, Li C, Yang C, Zou Y, Feng B, Li L, Liu W, Geng Y, Luo Q, Chen Z, Huang C. Polyphyllin VII

Promotes Apoptosis and Autophagic Cell Death *via* ROS-Inhibited AKT Activity, and Sensitizes Glioma Cells to Temozolomide. Oxid Med Cell Longev. 2019; 2019:1805635.
22. Liu Y, Wang M, Liu K, Qiu P, Zhang S, Lu Y, Tang N, Tang H. New Steroidal Saponins from the Rhizomes of *Paris vietnamensis* and Their Cytotoxicity. Molecules. 2018; 23: E588
23. Cheng G, Zhang X, Tang HF, Zhang Y, Zhang XH, Cao WD, Gao DK, Wang XL, Jin BQ. Asterosaponin 1, a cytostatic compound from the starfish *Culcita novaeguineae*, functions by inducing apoptosis in human glioblastoma U87MG cells. J Neurooncol. 2006; 79:235-241.
24. Ma N, Tang HF, Qiu F, Lin HW, Tian XR, Yao MN. Polyhydroxysteroidal glycosides from the starfish *Anthenea chinensis*. J Nat Prod. 2010; 73:590-597.
25. Manning BD, Cantley LC. AKT/PKB signaling: navigating downstream. Cell. 2007; 129:1261-1274.
26. Yang E, Korsmeyer SJ. Molecular thanatopsis: a discourse on the BCL2 family and cell death. Blood. 1996; 88:386-401.
27. Gao C, He XF, Xu QR, Xu YJ, Shen J. Sevoflurane downregulates insulin-like growth factor-1 to inhibit cell proliferation, invasion and trigger apoptosis in glioma through the PI3K/AKT signaling pathway. Anticancer Drugs. 2019; 30:e0744.
28. Zhou S, Wen H, Li H. Magnolol induces apoptosis in osteosarcoma cells *via* G0/G1 phase arrest and p53-mediated mitochondrial pathway. J Cell Biochem. 2019; 120:17067-17079.
29. Giampazolias E, Tait SW. Mitochondria and the hallmarks of cancer. FEBS J. 2016; 283:803-814.
30. Wu HL, Fu XY, Cao WQ, Xiang WZ, Hou YJ, Ma JK, Wang Y, Fan CD. Induction of Apoptosis in Human Glioma Cells by Fucoxanthin *via* Triggering of ROS-Mediated Oxidative Damage and Regulation of MAPKs and PI3K-AKT Pathways. J Agric Food Chem. 2019; 67:2212-2219.
31. Min KJ, Seo BR, Bae YC, Yoo YH, Kwon TK. Antipsychotic agent thioridazine sensitizes renal carcinoma Caki cells to TRAIL-induced apoptosis through reactive oxygen species-mediated inhibition of Akt signaling and downregulation of Mcl-1 and c-FLIP(L). Cell Death Dis. 2014; 5:e1063.
32. Lai SW, Huang BR, Liu YS, Lin HY, Chen CC, Tsai CF, Lu DY, Lin C. Differential Characterization of Temozolomide-Resistant Human Glioma Cells. Int J Mol Sci. 2018; 19:E127.
33. Li M, Liang RF, Wang X, Mao Q, Liu YH. BKM120 sensitizes C6 glioma cells to temozolomide *via* suppression of the PI3K/Akt/NF-κB/MGMT signaling pathway. Oncol Lett. 2017; 14:6597-6603.
34. Chen L, Han L, Shi Z, Zhang K, Liu Y, Zheng Y, Jiang T, Pu P, Jiang C, Kang C. LY294002 enhances cytotoxicity of temozolomide in glioma by down-regulation of the PI3K/Akt pathway. Mol Med Rep. 2012; 5:575-579.
35. Kumar A, Takada Y, Boriek AM, Aggarwal BB. Nuclear factor-kappaB: its role in health and disease. J Mol Med (Berl). 2004; 82:434-448.
36. Van der Heiden K, Cuhlmann S, Luong le A, Zakkar M, Evans PC. Role of nuclear factor kappaB in cardiovascular health and disease. Clin Sci (Lond). 2010; 118:593-605.
37. Senftleben U, Cao Y, Xiao G, Greten FR, Krähn G, Bonizzi G, Chen Y, Hu Y, Fong A, Sun SC, Karin M. Activation by IKKalpha of a second, evolutionary conserved, NF-kappa B signaling pathway. Science. 2001; 293:1495-1499.
38. Zhang LH, Yin AA, Cheng JX, Huang HY, Li XM, Zhang YQ, Han N, Zhang X. TRIM24 promotes glioma progression and enhances chemoresistance through activation of the PI3K/Akt signaling pathway. Oncogene. 2015; 34:600-610.

Received January 9, 2020; Revised February 9, 2020; Accepted February 15, 2020.

[§]These authors contributed equally to this work.
**Address correspondence to:*
Haifeng Tang, School of Pharmacy, Shaanxi University of Chinese Medicine, Xianyang 712046, China;
E-mail: tanghaifeng71@163.com

Pengcheng Qiu, Institute of Materia Medica, School of Pharmacy, Fourth Military Medical University, Xi'an 710032, China.
E-mail: qpc023@126.com

Released online in J-STAGE as advance publication March 14, 2020.

Brief Report

DOI: 10.5582/bst.2020.01482

Analysis of COVID-19 infection spread in Japan based on stochastic transition model

Kenji Karako[1], Peipei Song[2,*], Yu Chen[1,*], Wei Tang[3]

[1] Department of Human and Engineered Environmental Studies, Graduate School of Frontier Sciences, The University of Tokyo, Chiba, Japan;
[2] Institute for Global Health Policy Research, Bureau of International Health Cooperation, National Center for Global Health and Medicine, Tokyo, Japan;
[3] International Health Care Center, National Center for Global Health and Medicine, Tokyo, Japan.

SUMMARY To assess the effectiveness of response strategies of avoiding large gatherings or crowded areas and to predict the spread of COVID-19 infections in Japan, we developed a stochastic transmission model by extending the Susceptible-Infected-Removed (SIR) epidemiological model with an additional modeling of the individual action on whether to stay away from the crowded areas. The population were divided into three compartments: Susceptible, Infected, Removed. Susceptible transitions to Infected every hour with a probability determined by the ratio of Infected and the congestion of area. The total area consists of three zones crowded zone, mid zone and uncrowded zone, with different infection probabilities characterized by the number of people gathered there. The time for each people to spend in the crowded zone is curtailed by 0, 2, 4, 6, 7, and 8 hours, and the time spent in mid zone is extended accordingly. This simulation showed that the number of Infected and Removed will increase rapidly if there is no reduction of the time spent in crowded zone. On the other hand, the stagnant growth of Infected can be observed when the time spent in the crowded zone is reduced to 4 hours, and the growth number of Infected will decrease and the spread of the infection will subside gradually if the time spent in the crowded zone is further cut to 2 hours. In conclusions The infection spread in Japan will be gradually contained by reducing the time spent in the crowded zone to less than 4 hours.

Keywords coronavirus disease 2019 (COVID-19), Japan, transmission, infection, modeling, Susceptible-Infected-Removed (SIR)

1. Introduction

In December 2019 an outbreak of coronavirus disease 2019 (COVID-19) occurred in Wuhan (*1*). At present, some countries are facing on a crisis of outbreak and trying to prevent the spread of 2019-nCoV infections (*2-7*). Japan is also one of them. As of February 29, 2020, in addition to the confirmed 619 cases (passengers and crew members) from a virus-hit cruise ship docked in Yokohama near Tokyo and 15 cases returning to Japan by charter flight from Wuhan, 215 locally transmitted cases have been confirmed to have the 2019-nCoV infection in Japan (*8,9*).

To contain the outbreak, the government of Japan shifted the response strategy from "prevention of domestic invasion" to "prevention infection spread". On February 25, the Japanese government officially released the latest countermeasures for COVID-19 infections (*10*). The Japanese government asked the public not to flock to hospitals without prior consultation, with the purpose of reducing the risk of exposure to cross-contamination at medical facilities or on the way. To stay away from large gatherings or crowded areas, the Japanese government promoted the adoption of telecommuting, encourage staggering commuting hours and ensure that workers with cold-like symptoms can take sick leave. In addition, on February 27, the government requested all elementary, junior high and high schools in Japan to close from March 2 until the end of a spring break through early April 2020 (*11*).

It is unknown whether these strategies have had an impact, and how long they should avoid large gatherings or crowded areas. To assess the effectiveness of these response strategies and to predict the spread of COVID-19 infections in Japan, we thus developed a stochastic transmission model by extending the Susceptible-Infected-Removed (SIR) epidemiological model with an additional modeling of the individual

action on whether to stay away from the crowded areas.

2. Methods

2.1. Model structure

We implemented a stochastic state transition model with reference to SIR model (*12,13*) dividing population into three compartments: Susceptible, Infected, Removed. Flow of the state transition is shown in Figure 1. Susceptible transitions to Infected every hour with a probability determined by the ratio of Infected and the congestion of area. The total area consists of three zones crowded zone, mid zone and uncrowded zone, with different infection probabilities characterized by the number of people gathered there. The probability of infection at each hour is decided as:

$$P_{infection}(t,d) = P_{zone}(t)\, R_{Infected}(d) \quad (1)$$

$$R_{Infected}(d) = \frac{N_{Infected}(d)}{N_{Infected}(d) + N_{Susceptible}(d)} \quad (2)$$

Where $P_{zone}(t)$ denotes the infection probability at the zone where Susceptible exist at time (t), $R_{Infected}(d)$ denotes the ratio of Infected determined by the number of Infected and Susceptible at day (d). In addition, Infected transitions to Removed every day by segregation with a certain probability: $P_{Removed}$ and hence Removed will not infect others any more.

2.2. Estimation of model parameters

In order to apply our model to Japan's situation, we need to estimate the parameters $P_{crowded\ zone}$, $P_{mid\ zone}$, $P_{uncrowded\ zone}$ and $P_{Removed}$. To estimate the P_{zone}, we reference the infected ratio of the cases at diamond princess and returning to Japan by charter flight from Wuhan. In the case of diamond princess, there were 3,711 people on board, of which 619 were infected, and the ratio of infected was 17% (*9*). Out of 829 returnees from Wuhan, 15 were infected and the ratio of infected was 1.8% (*14*). The ratio of infected in spatially isolated ship were 10 times greater than those in returnees from potentially dangerous area. Crowded zone is considered as not an isolated space like diamond princess but an area with a high probability of infection, thus we set the infection probability at crowded zone as 1.8%. Also, according to the difference between diamond princess and returnees from Wuhan, we set the probability at mid zone and uncrowded zone as 0.18% and 0.018%. As of February 25, 140 out of 1,017 people were detected as infected by PCR test in Japan (*7*). According to detection rate, we set $P_{Removed}$ as 14%.

To set action policy on where to spend, we refer to the average Japanese behavior obtained from the basic survey on social life (*15*). The total time for work, meals, study, and travel was 467 minutes. According

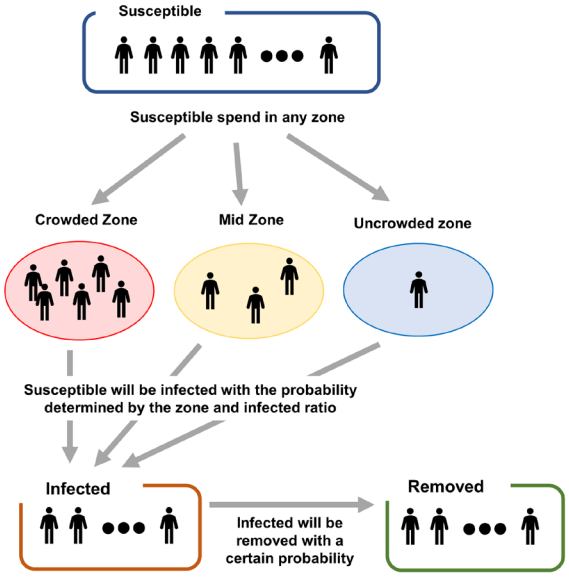

Figure 1. The flow of transition between three compartments.

the time spending at places where many people gather, we set 8 hours as the time in crowded zone per day. And also, we set 8 hours as the time in mid and uncrowded zone per day.

The result using above settings and initial Susceptible:120,000,000 and initial Infected:10 is shown in Figure 2. The number of Removed was 65 at 30th day. The number does not match the situation in Japan, where the infection was confirmed for the first time on January 14 and reached 165 on February 25. Therefore, we changed the parameters as $P_{crowded\ zone}$: 2%, $P_{mid\ zone}$: 0.2%, $P_{uncrowded\ zone}$: 0.02% and $P_{Removed}$: 10% , and simulate the infection spread (Figure 3). The number of Removed reached 159 at 30th day and it was close to the situation in Japan.

3. Results and Discussion

Prediction of the spread in Japan Reflecting the Japanese strategy to prevent outbreaks and control the spread of infection, we simulated infection spread using some scenarios with different hour in crowded zone. Assuming Japan response strategy "prevention infection spread" reduces time in crowded zone, we simulate the spread continuing 30 days of Figure 3 with same probabilities.

As a parameter study of the model, the time for each people to spend in the crowded zone is curtailed by 0, 2, 4, 6, 7, and 8 hours, and the time spent in mid zone is extended accordingly. These results were shown in Figure 4.

Results of simulation showed that *i*) the number of Infected and Removed will increase rapidly if there is no reduction of the time spent in crowded zone; *ii*) the stagnant growth of Infected can be observed when the time spent in the crowded zone is reduced to 4 hours;

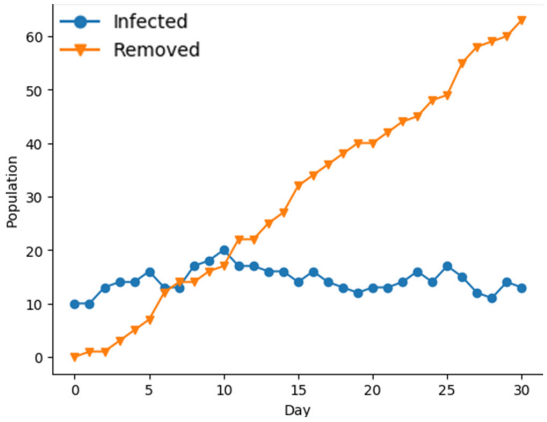

Figure 2. Infected and Removed population transition simulated with $P_{crowded\ zone}$: 1.8%, $P_{mid\ zone}$: 0.18%, $P_{uncrowded\ zone}$: 0.018%, and $P_{Removed}$: 14%.

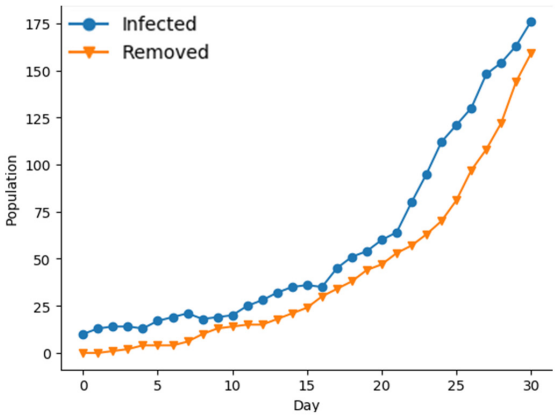

Figure 3. Infected and Removed population transition simulated with $P_{crowded\ zone}$: 2%, $P_{mid\ zone}$: 0.2%, $P_{uncrowded\ zone}$: 0.02%, and $P_{Removed}$: 10%.

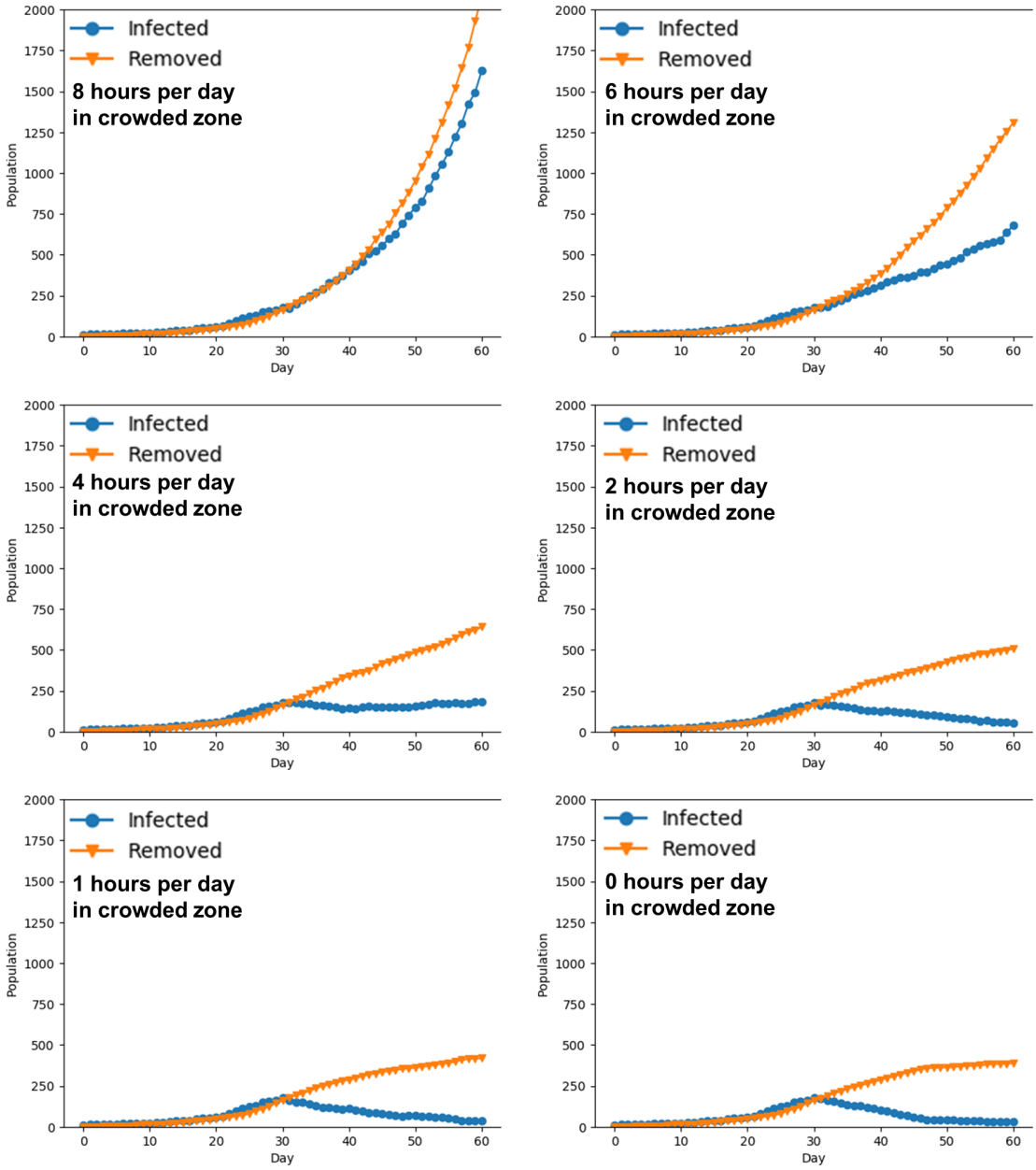

Figure 4. Infected and Removed population transition simulated with changing the time spending in crowded zone after 30 days.

and *iii*) the growth number of Infected will decrease and the spread of the infection will subside gradually if the time spent in the crowded zone is further cut to 2 hours.

As can be seen in Figure 4, the infection spread in Japan will be gradually contained by reducing the time spent in the crowded zone to less than 4 hours. Otherwise, the outbreak of infection in Japan will remain.

The Japanese government has already advice all people to stay away from large gatherings or crowded areas. In addition, the government requested all elementary, junior high and high schools in Japan to close from March 2 and promoted the adoption of telecommuting and encourage staggering commuting hours. Through these policies, minimizing exposure risks of the public (*16,17*) will be effective and feasible measure to contain mass COVID-19 infection in Japan.

On the other hand, if the time in crowded zone does not decrease enough by these policies, there is a way to control the spread by increasing the probability of Removed.

Although there are some voices in the public questioning that the number of people tested every day is too small, from the perspective of policies to prevent infectious diseases, performing PCR test on everyone is not an effective measure against this virus because of the risk of exposure to cross-contamination at medical facilities or on the way as well as the low positive rate, high false-negative rate, low patient viral load, or improper clinical sampling, *etc* (*18-21*). However, if exposure to cross-contamination can be prevented, increasing the number of tests will be a measure to control the spread of infection.

In conclusion, we developed a COVID-19 spread prediction model analysis with the stochastic transition model using existence ratio of influencer and the areas characterized by the number of people gathered. Results of simulation showed that preventing mass COVID-19 infection and control the spread of infection need to reduce the time spent in the crowded zone to less than 4 hours. Everyone should follow the Japan response strategies and avoid crowded areas as possible.

References

1. Li Q, Guan X, Wu P, *et al*. Early Transmission Dynamics in Wuhan, China, of Novel Coronavirus-Infected Pneumonia. N Engl J Med. 2020; doi: 10.1056/NEJMoa2001316.
2. World Health Organization. Coronavirus disease (COVID-2019) situation reports. *https://www.who.int/emergencies/diseases/novel-coronavirus-2019/situation-reports* (accessed March 11, 2020).
3. Guan WJ, Ni ZY, Hu Y, *et al*. Clinical Characteristics of Coronavirus Disease 2019 in China. N Engl J Med. 2020; doi: 10.1056/NEJMoa2002032.
4. Gilbert M, Pullano G, Pinotti F, Valdano E, Poletto C, Boëlle PY, D'Ortenzio E, Yazdanpanah Y, Eholie SP, Altmann M, Gutierrez B, Kraemer MUG, Colizza V. Preparedness and vulnerability of African countries against importations of COVID-19: a modelling study. Lancet. 2020; 395:871-877.
5. Hoehl S, Berger A, Kortenbusch M, *et al*. Evidence of SARS-CoV-2 Infection in Returning Travelers from Wuhan, China. N Engl J Med. 2020; doi: 10.1056/NEJMc2001899.
6. Adalja AA, Toner E, Inglesby TV. Priorities for the US Health Community Responding to COVID-19. JAMA. 2020; doi: 10.1001/jama.2020.3413.
7. Porcheddu R, Serra C, Kelvin D, Kelvin N, Rubino S. Similarity in case fatality rates (CFR) of COVID-19/SARS-COV-2 in Italy and China. J Infect Dev Ctries. 2020; 14:125-128.
8. Ministry of Health, Labour and Welfare, Japan. About New Coronavirus Infections. February 29, 2020. *https://www.mhlw.go.jp/stf/seisakunitsuite/bunya/0000164708_00001.html* (accessed March 11, 2020).
9. National Institute of Infectious Diseases. Field Briefing: Diamond Princess COVID-19 Cases, 20 Feb Update . *https://www.niid.go.jp/niid/en/2019-ncov-e/9417-covid-dp-fe-02.html* (accessed March 11, 2020).
10. Ministry of Health, Labour and Welfare, Japan. Basic policy for countermeasures against SARS-Cov-2 infection. February 25, 2020. *https://www.mhlw.go.jp/content/10900000/000599698.pdf* (accessed March 11, 2020).
11. NHK World-Japan. Abe to ask all schools to close during March. February 27, 2020. *https://www3.nhk.or.jp/nhkworld/en/news/20200227_47* (accessed March 11, 2020).
12. Kermack WO, McKendrick AG. A contribution to the mathematical theory of epidemics. Proceedings of the royal society of london. Series A. 1927; 115:700-721.
13. Britton T. Stochastic epidemic models: a survey. Math Biosci. 2009; 225:24-35.
14. Ministry of Health, Labour and Welfare, Japan. About the Present Situation of New Coronavirus Infections and Correspondence of Ministry of Health, Labor and Welfare. February 25, 2020. *https://www.mhlw.go.jp/stf/newpage_09747.html* (accessed March 11, 2020).
15. Statistics Bureau of Japan. Basic Survey on Social Life in 2016. September 15, 2017. *https://www.stat.go.jp/data/shakai/2016/pdf/gaiyou3.pdf* (accessed March 11, 2020).
16. Hellewell J, Abbott S, Gimma A, Bosse NI, Jarvis CI, Russell TW, Munday JD, Kucharski AJ, Edmunds WJ; Centre for the Mathematical Modelling of Infectious Diseases COVID-19 Working Group, Funk S, Eggo RM. Feasibility of controlling COVID-19 outbreaks by isolation of cases and contacts. Lancet Glob Health. 2020; pii: S2214-109X(20)30074-7. doi: 10.1016/S2214-109X(20)30074-7.
17. Chinazzi M, Davis JT, Ajelli M, *et al*. The effect of travel restrictions on the spread of the 2019 novel coronavirus (COVID-19) outbreak. Science. 2020; pii: eaba9757. doi: 10.1126/science.aba9757.
18. Tang A, Tong ZD, Wang HL, Dai YX, Li KF, Liu JN, Wu WJ, Yuan C, Yu ML, Li P, Yan JB. Detection of Novel Coronavirus by RT-PCR in Stool Specimen from Asymptomatic Child, China. Emerg Infect Dis. 2020; 26: doi: 10.3201/eid2606.200301.
19. Fang Y, Zhang H, Xie J, Lin M, Ying L, Pang P, Ji W. Sensitivity of Chest CT for COVID-19: Comparison to RT-PCR. Radiology. 2020; doi: 10.1148/radiol.2020200432.

20. Ai T, Yang Z, Hou H, Zhan C, Chen C, Lv W, Tao Q, Sun Z, Xia L. Correlation of Chest CT and RT-PCR Testing in Coronavirus Disease 2019 (COVID-19) in China: A Report of 1014 Cases. Radiology. 2020; doi: 10.1148/radiol.2020200642
21. World Health Organization. Report of the WHO-China Joint Mission on Coronavirus Disease 2019 (COVID-19). *https://www.who.int/docs/default-source/coronaviruse/who-china-joint-mission-on-covid-19-final-re* (accessed March 11, 2020).

Received March 14, 2020; Revised March 18, 2020; Accepted March 18, 2020.

**Address correspondence to:*
Peipei Song, Institute for Global Health Policy Research, Bureau of International Health Cooperation, National Center for Global Health and Medicine, Tokyo, Japan.
E-mail: ppsong-tky@umin.ac.jp

Yu Chen, Department of Human and Engineered Environmental Studies, Graduate School of Frontier Sciences, The University of Tokyo, Chiba, Japan.
E-mail: chen@edu.k.u-tokyo.ac.jp

Released online in J-STAGE as advance publication March 19, 2020.

Brief Report

DOI: 10.5582/bst.2020.03082

Neuropsychiatric adverse events of chloroquine: a real-world pharmacovigilance study using the FDA Adverse Event Reporting System (FAERS) database

Kenichiro Sato[1], Tatsuo Mano[1], Atsushi Iwata[1,2,*], Tatsushi Toda[1]

[1] Department of Neurology, Graduate School of Medicine, University of Tokyo, Tokyo, Japan.
[2] Department of Neurology, Tokyo Metropolitan Geriatric Medical Center Hospital, Tokyo, Japan.

SUMMARY In late March and early April 2020, the antimalarial drug, chloroquine, has been approved as an emergency treatment for the coronavirus disease 2019 (COVID-19) in the United States and in Europe. Although infrequent, neuropsychiatric symptoms have been reported in patients who received chloroquine for the treatment of malaria or autoimmune diseases. In this study, aiming to investigate these adverse events (AEs) using a large self-reporting database, we conducted a disproportionality analysis for the detection of neuropsychiatric AE signals associated with the use of chloroquine (or hydroxychloroquine), reported to FDA Adverse Event Reporting System (FAERS) database between the fourth quarter of 2012 and the fourth quarter of 2019. We included 2,389,474 AE cases, among which 520 cases developed neuropsychiatric AE following the use of chloroquine. Adjusted reporting odds ratio (ROR) for the development of each of the neuropsychiatric AEs following the use of chloroquine was calculated using a multilevel model: exposure to chloroquine was associated with a statistically significant high reporting of amnesia, delirium, hallucinations, depression, and loss of consciousness, (lower 95% confidence interval of the adjusted ROR > 1), although the degree of increase in their ROR was limited. There was no statistically significant high reporting of any other neuropsychiatric AE, including suicide, psychosis, confusion, and agitation. Current pharmacovigilance study results did not suggest any potential link between the use of chloroquine and an increased risk of suicide, psychosis, confusion, and agitation, which would be informative during the emergency use of chloroquine for the treatment of COVID-19.

Keywords COVID-19, chloroquine, adverse events, pharmacovigilance, FAERS, real-world data

1. Introduction

The coronavirus disease 2019 (COVID-19) outbreak is a global emergency situation (*1*), for which the development of drugs and vaccines has been intensively investigated worldwide. In late March and early April 2020, the US Food and Drug Administration (FDA) (*2*) and the European Medicines Agency (EMA) (*3*) have approved the use of chloroquine and hydroxychloroquine for an emergency treatment of COVID-19, based on their potential effectiveness in this setting (*4,5*).

While chloroquine has a long history in the treatment of malaria and autoimmune diseases, its safety and efficacy in the treatment of COVID-19 remain unknown (*5*). In the treatment of malaria and autoimmune diseases, chloroquine can cause numerous side effects such as nausea, headache, pruritus, worsening of psoriasis, retinopathy, and cardiac dysfunction. While neuropsychiatric symptoms such as seizure, coma, and psychosis, were also reported in patients who received chloroquine (*6,7*), it is still unknown which neuropsychiatric symptoms are directly associated with the use of chloroquine, partly because of their relatively low frequency (*8*). Understanding in advance the types of neuropsychiatric symptoms that may occur in patients treated with chloroquine, may be useful, particularly in patients with COVID-19 in intensive care units, where rapid clinical judgement is required.

In the current study, we investigated the link between the use of chloroquine and the occurrence of neuropsychiatric symptoms, using the FDA Adverse Event Reporting System (FAERS) database that is provided by the FDA (*9*). Since this database contains a very large number of case reports of drug AEs, it is widely used in identifying potential link between drugs and AEs during post-marketing surveillance of drug

safety (*10*), despite the risk of bias that is associated with its self-reported data (*11*).

2. Materials and Methods

2.1. Data acquisition and preprocessing

This was a retrospective pharmacovigilance study that used the FAERS database. This database contains more than 9 million global case reports of potential adverse events of drugs. On April 1, 2020, we downloaded from the FDA's website (*https://www.fda.gov*) patient data that were reported between the fourth quarter of 2012 and the fourth quarter of 2019. The FAERS database contains data tables named 'DEMO', 'DRUG', 'REAC', 'OUTC', 'RPSR', 'THER', and 'INDI', of which we mainly used the following 3 tables: 1) 'DEMO', which provides the case ID, sex, age, year of event occurrence, country of event occurrence, and the reporter's type of occupation (*e.g.*, medical doctor, pharmacist, lawyer, consumer); 2) 'REAC', which contains all adverse events that are potentially caused by the drug used by each patient, and 3) 'DRUG', which includes the name, dose, indication, and date of administration and discontinuation of each drug that is possibly associated with that AE. In the 'DRUG' table, the causality assessment of the relationship between each drug and its reported AE is classified by the reporter as 'primary suspected', 'secondary suspected', 'concomitant', or 'interacting'. In our analysis, we included only reports that were classified as 'primary suspected' and 'secondary suspected', to reduce the risk of false positive association in deriving our conclusions. In addition, we included only reports that were reported from medical doctor, pharmacist, or other medical staffs, and not from lawyers or consumers. Duplicate reports were excluded such that only the latest version of the report that was obtained from the same case ID was retained.

2.2. Database search

In the FAERS database, the AEs are mainly identified by their Preferred Terms (PTs), as determined by the Medical Dictionary for Regulatory Activities (MedDRA). To search for cases that were associated with chloroquine (including hydroxychloroquine) or mefloquine treatment and presented with any of the AEs of interest, we used the following neurological or psychiatric AE terms, as summarized in Table S1 (*http://www.biosciencetrends.com/action/getSupplementalData.php?ID=64*) : 'Seizure' (PT: 10039906), 'Loss of consciousness' (PT: 10024855), 'Confusional state' (PT: 10010305), 'Coma' (PT: 10010071), 'Stupor' (PT: 10042264), 'Somnolence' (PT: 10041349), 'Sedation' (PT: 10039897), 'Lethargy' (PT: 10024264), 'Delirium' (PT: 10012218), 'Disorientation' (PT: 10013395), 'Hallucination' (PT: 10019063), 'Delusion' (PT: 10012239), 'Paranoia' (PT: 10033864), 'Anxiety' (PT: 10002855), 'Anger' (PT: 10002368), 'Aggression' (PT: 10001488), 'Nervousness' (PT: 10029216), 'Irritability' (PT: 10022998), 'Mood altered' (PT: 10027940), 'Abnormal behavior' (PT: 10061422), and 'Restlessness' (PT: 10038743). In addition, several AE terms were similar, and were therefore treated collectively, based on a single AE category, as follows: 'Dizziness' (PT: 10013573) and 'Dizziness postural' (10013578) were treated as dizziness, 'Amnesia' (PT: 10001949) and 'Anterograde amnesia' (PT: 10002711) were treated as amnesia, 'Altered state of consciousness' (PT: 10001854) and 'Mental status changes' (PT: 10048294) were treated as altered mental status (AMS), 'Acute psychosis' (PT: 10001022) and 'Psychotic disorder' (PT: 10061290) were treated as psychosis, 'Agitation' (PT: 10001497) and 'Psychomotor hyperactivity' (PT: 10037211) were treated as agitation, 'Depressed mood' (PT: 10012374) and 'Depression' (PT: 10012378) were treated as depression, 'Panic attack' (PT: 10033664) and 'Panic reaction' (PT: 10033670) were treated as panic, 'Nightmare' (10029412) and 'Abnormal dreams' (10000125) were treated as nightmare, and 'Suicidal ideation' (PT: 10042458), 'Completed suicide' (PT: 10010144), 'Suicide attempt' (PT: 10042464), and 'Suspected suicide' (PT: 10082458) were treated suicide.

We included mefloquine as one of our drugs of interest because it is an antimalarial drug that is known to cause neuropsychiatric AEs (*12*). We classified each case report based on the following binomial factors: 'with' or 'without' exposure to the drugs of interest, and 'with' or 'without' the development of each of the AEs of interest, irrespective of the timing of drug administration or the time of AE development.

2.3. Statistical analyses

All data handling and statistical analyses were performed using R software (version 3.5.1). For each included drug (chloroquine or mefloquine), we calculated the reporting odds ratio (ROR), to assess the potential drug-AE links for chloroquine (or mefloquine) and the reported neuropsychiatric symptoms. The crude ROR was calculated by a 2 × 2 contingency table as described previously (*13-15*), where all the reports were classified by two factors for each AE term and for each drug, as described above. When the lower limit of the 95% confidential interval (CI) for the adjusted ROR was > 1, the AE was considered to be significantly highly reported following the use of the drug of interest, compared with the report of the same AE following the use of all other drugs.

In calculating ROR, we used a multilevel model, to adjust for covariates in a hierarchical design, as described previously (*16,17*): we incorporated into the model the year of AE occurrence and the country of AE

occurrence as random effect terms, to reduce bias in the data. Accordingly, the adjusted ROR was calculated by the following formula (*16*):

$$Odds = \frac{P(Y_i = 1|x_i, z_i)}{P(Y_i = 0|x_i, z_i)} = exp(x_i^T\beta + z_i^T u)$$

where, Y_i is binomial status for with/without AE of interest in each case i, β is the vector of fixed effect parameters, x_i is the covariates matrix for fixed effect, u is the vector of random effect parameters, and z_i is the covariates matrix of random effect. Covariates to measure fixed effect include age, sex, binomial exposure to chloroquine (0 if not used, and 1 if used), and binomial exposure to mefloquine (0 if not used, and 1 if used). And covariates to measure random effect (as random intercepts) are the calendar year between 1990 and 2019, and the regional code of the country (*e.g.*, the United States, Great Britain, Canada, Germany, Japan). We used the R package lme4 (*18*) to perform the above multilevel model analysis.

2.4. Ethics

This study was approved by the University of Tokyo Graduate School of Medicine institutional ethics committee [ID: 11754-(1)]. An informed consent was not required for this type of study. The work was conducted in accordance with the ethical standards laid out in the Declaration of Helsinki, 1964.

3. Results and Discussion

In total, our analysis included 2,389,474 unique case reports. There were 4,336 case reports with exposure to chloroquine, of which 520 (12.0%) reported neuropsychiatric AEs. The number of reported cases with exposure to mefloquine was only 67, of which 28 (41.8%) included neuropsychiatric AEs. Patients treated with chloroquine were predominantly female (3452 females (81.9%) versus 762 males) and the median age of the patients was 56.0 (IQR: 45.0-65.0).

Patients treated with mefloquine were predominantly male (40 males (62.5%) versus 24 females) with a median age of 40.0 (IQR: 27.0-72.0). There were no cases of concomitant exposure to chloroquine and mefloquine.

Figure 1 provides forest plots of the adjusted RORs and their 95% CI for each neuropsychiatric AE following the use of chloroquine (Figure 1A) or mefloquine (Figure 1B). In the case of chloroquine-associated AEs (Figure 1A), only 5 AE types, including loss of consciousness (LOC) (adjusted ROR, 1.31; 95% CI, 1.03-1.66), amnesia (adjusted ROR, 1.30; 95% CI, 1.02-1.66),

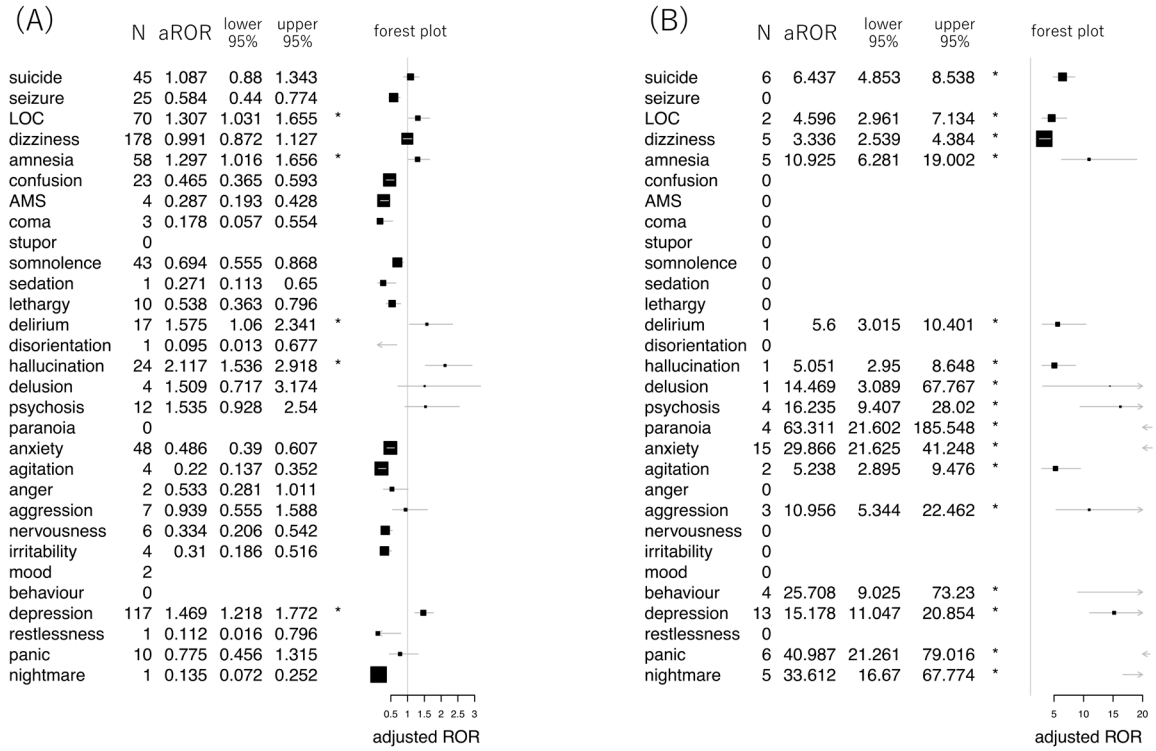

Figure 1. Forest plots of each AE. Forest plots showing the aROR of each AE following the use of chloroquine (**A**) and mefloquine (**B**). The number of reports of each AE, the reporting odds ratios that were adjusted based on age and sex for each AE, and their 95% CI are provided in the adjacent tables. Note that the vertical bar shows the line of ROR = 1. For AEs that were not reported after the use of chloroquine or mefloquine (n = 0), the aROR was not calculated and appear as blank. (*Abbreviations:* AE, adverse event; aROR, adjusted reporting odds ratio; LOC, loss of consciousness; AMS, altered mental status, N, number of observations; lower 95%, the lower limit of the 95% confidence interval; upper 95%, the upper limit of the 95% confidence interval.)

delirium (adjusted ROR, 1.58; 95% CI, 1.06-2.34), hallucination (adjusted ROR, 2.12; 95% CI, 1.54-2.92), and depression (adjusted ROR, 1.47; 95% CI, 1.22-1.77) had significantly high reporting (lower limit of the 95% CI > 1). As for mefloquine (Figure 1B), all of the neuropsychiatric AEs, except for somnolence, showed high reporting, with adjusted ROR values higher that 2 in almost all cases.

In this study, we investigated reports of neuropsychiatric AEs that were developed following exposure to chloroquine as a treatment for malaria or autoimmune diseases. The major strength of our study is that it was based on a database that includes global real-world data from a very large number of patients. Our results showed a statistically significant association (albeit marginal) between the use of chloroquine and the reporting of LOC, amnesia, delirium, hallucination, and depression, however, there was no statistically significant association between the use of chloroquine and the reporting of suicide, psychosis, confusion, or agitation, suggesting that there is no link between the use of chloroquine and the increased risk of these AEs. Conversely, mefloquine showed to be associated with statistically significant high reporting of most of the neuropsychiatric AEs, which is consistent with some of the earlier literature reports (*12,19*).

Our study has some limitations, resulting from the use of self-reported data (*11*), and it therefore includes some bias that cannot be eliminated. First, this setting may be associated with a reporting bias, that is, over- or under-reporting of neuropsychiatric AEs following the use of chloroquine. Second, due to the absence of denominators, we were not able to discuss the incidence rate of each neuropsychiatric AE. Third, in our multivariate adjustment, we did not consider the use of concomitant medications or the medical history of the patients, both of which could have potentially contributed to the development or to the worsening of some neuropsychiatric symptoms. Fourth, while suicide was included as one of the AEs in our analysis, it is possible that some of the suicide cases represent suicide by chloroquine overdose, which is known to be cardiotoxic, and not an AE of chloroquine (*6*). Fifth, we have not included the timing or the total dose of chloroquine and mefloquine in the analysis. Lastly, it is possible that our final dataset included duplicated cases that should have been excluded.

To conclude, the current pharmacovigilance study, using the FAERS database, did not suggest a potential link between the use of chloroquine and an increased risk of suicide or psychosis. These results provide information that can be essential when the use of chloroquine is considered for the treatment of patients with COVID-19. Since this study was based on a self-reporting database that inevitably contains several biases, cohort studies are needed, to validate these results and to confirm the neuropsychiatric safety of chloroquine.

Acknowledgements

This study was performed using the FDA Adverse Event Reporting System (FAERS) database that was provided by the FDA. The information, results, or interpretation of the current study do not represent any opinion of the FDA. This study was supported by JSPS KAKENHI Grant Number 20H03587.

References

1. Verity R, Okell LC, Dorigatti I, *et al.* Estimates of the severity of coronavirus disease 2019: a model-based analysis. Lancet Infect Dis. 2020; pii: S1473-3099(20)30243-7.
2. FDA. Coronavirus (COVID-19) Update: Daily Roundup March 30, 2020. *https://www.fda.gov/news-events/press-announcements/coronavirus-covid-19-update-daily-roundup-march-30-2020* (accessed April 6, 2020).
3. EMA. COVID-19: chloroquine and hydroxychloroquine only to be used in clinical trials or emergency use programmes. EMA/170590/2020. *https://www.ema.europa.eu/en/documents/press-release/covid-19-chloroquine-hydroxychloroquine-only-be-used-clinical-trials-emergency-use-programmes_en.pdf* (accessed April 6, 2020).
4. Gao J, Tian Z, Yang X. Breakthrough: Chloroquine phosphate has shown apparent efficacy in treatment of COVID-19 associated pneumonia in clinical studies. Biosci Trends. 2020; 14:72-73.
5. Cortegiani A, Ingoglia G, Ippolito M, Giarratano A, Einav S. A systematic review on the efficacy and safety of chloroquine for the treatment of COVID-19. J Crit Care. 2020; pii: S0883-9441(20)30390-7.
6. AlKadi HO. Antimalarial drug toxicity: a review. Chemotherapy. 2007; 53:385-91.
7. Anna Bogaczewicz, Tomasz Sobów. Psychiatric adverse effects of chloroquine. Psychiatr Psychol Klin. 2017; 17:11-114.
8. Taylor WR, White NJ. Antimalarial drug toxicity: a review. Drug Saf. 2004; 27:25-61.
9. U.S. Food & Drug Administration. *https://www.fda.gov* (accessed April 6, 2020).
10. Yokoyama S, Ieda S, Nagano M, Nakagawa C, Iwase M, Hosomi K, Takada M. Association between oral anticoagulants and osteoporosis: Real-world data mining using a multi-methodological approach. Int J Med Sci. 2020; 17:471-479.
11. Michel C, Scosyrev E, Petrin M, Schmouder R. Can Disproportionality Analysis of Post-marketing Case Reports be Used for Comparison of Drug Safety Profiles? Clin Drug Investig. 2017; 37:415-422.
12. Nevin RL, Byrd AM. Neuropsychiatric Adverse Reactions to Mefloquine: a Systematic Comparison of Prescribing and Patient Safety Guidance in the US, UK, Ireland, Australia, New Zealand, and Canada. Neurol Ther. 2016; 5:69-83.
13. Van Puijenbroek EP, Egberts AC, Meyboom RH, Leufkens HG. Signalling possible drug-drug interactions in a spontaneous reporting system: delay of withdrawal bleeding during concomitant use of oral contraceptives and itraconazole. Br J Clin Pharmacol. 1999; 47:689-93.
14. Rothman KJ, Lanes S, Sacks ST. The reporting odds ratio

and its advantages over the proportional reporting ratio. Pharmacoepidemiol Drug Saf. 2004; 13:519-23.
15. Sato K, Mano T, Iwata A, Toda T. Neurological and related adverse events in immune checkpoint inhibitors: a pharmacovigilance study from the Japanese Adverse Drug Event Report database. J Neurooncol. 2019; 145:1-9.
16. Larsen K, Petersen JH, Budtz-Jørgensen E, Endahl L. Interpreting parameters in the logistic regression model with random effects. Biometrics. 2000; 56:909-914.
17. Casals M, Girabent-Farrés M, Carrasco JL. Methodological quality and reporting of generalized linear mixed models in clinical medicine (2000-2012): a systematic review. PLoS One. 2014; 9:e112653.
18. Bates D, Mächler M, Bolker B, Steve Walker S. Fitting linear mixed-effects models using lme4. Journal of Statistical Software. 2015; 67: 1-48. doi: 10.18637/jss.v067.i01
19. Thomas KH, Martin RM, Potokar J, Pirmohamed M, Gunnell D. Reporting of drug induced depression and fatal and non-fatal suicidal behaviour in the UK from 1998 to 2011. BMC Pharmacol Toxicol. 2014; 15:54.

Received April 12, 2020; Revised April 16, 2020; Accepted April 17, 2020

*Address correspondence to:
Atsushi Iwata, Department of Neurology, Tokyo Metropolitan Geriatric Medical Center Hospital
35-2 Sakaecho Itabashi-ku, Tokyo 173-0015, Japan.
E-mail: iwata@m.u-tokyo.ac.jp

Released online in J-STAGE as advance publication April 22, 2020.

Brief Report

DOI: 10.5582/bst.2019.01331

Identification and characterization of the V3 promoter of the *ST3GAL4* gene

Patricia L. Martínez-Morales[1], Claudia A. Ortiz-Mateos[2], Jonatan Reyes-Pineda[2], Tania Reyes-Vallejo[3], Adriana Aguilar-Lemarroy[4], Luis F. Jave-Suárez[4], Gerardo Santos-López[5], Julio Reyes-Leyva[5], Lorena Milflores-Flores[2,*], Verónica Vallejo-Ruiz[5,*]

[1] CONACYT- Instituto Mexicano del Seguro Social, Centro de Investigación Biomédica de Oriente, Metepec, Puebla, Mexico;
[2] Facultad de Ciencias Biológicas, Benemérita Universidad Autónoma de Puebla, Puebla, Mexico;
[3] Escuela de Ciencias, Universidad de las Américas, Puebla, Mexico;
[4] Instituto Mexicano del Seguro Social, Centro de Investigación Biomédica de Occidente, Guadalajara, Jalisco, Mexico;
[5] Instituto Mexicano del Seguro Social, Centro de Investigación Biomédica de Oriente, Laboratorio de Biología Molecular, Metepec, Puebla, Mexico.

SUMMARY The *ST3GAL4* gene encodes the enzyme Galβ1-4GlcNAc α2,3 sialyltransferase (ST3Gal IV). This enzyme participates in the synthesis of the sialyl Lewis x antigen. In different cancer types altered expression of this antigen has been reported. The transcriptional regulation of this gene is very complex, different mRNA variants (V1-V10) have been reported and are originated by the activity of different promoters and alternative splicing. Only the promoter that gives rise to the V3 variant has not been previously reported. The objective of this work was to identify and characterize the V3 promoter of the *ST3GAL4* gene. For this, the putative V3 promoter of the *ST3GAL4* gene was delimited by *in silico* analysis. The complete promoter and smaller versions were cloned in a reporter plasmid. The constructs were transfected in the HaCaT cells and the promoter activity was evaluated by luciferase reporter assays. The cloned region showed promoter activity, and the basal activity was not dependent on TATA boxes. However, the GC boxes, an initiator element (Inr) and downstream promoter element (DPE) could contribute to basal activity. The promoter contains several binding sites for the nuclear factor of activated T-cells (NFAT) that could participate in inducible activity during the immune response. The minimal promoter corresponds to a fragment of approximately 300 bp, located in the position -347 b to -40 b. The characterization of the V3 promoter of the *ST3GAL4* gene completes the study of the four promoters of this gene, this contributes to the understanding of its complex transcription regulation.

Keywords ST3Gal IV, transcriptional regulation *ST3GAL4*, V3 promoter

1. Introduction

The *ST3GAL4* gene encodes the Galβ1-4GlcNAc α2,3 sialyltransferase (ST3Gal IV), which transfers sialic acid to glycoconjugates containing the terminal structure Galβ1-4GlcNAc or Galβ1-3GalNAc (*1*). This enzyme participates in the synthesis of the sialyl Lewis x antigen, which is a tetra-saccharide highly expressed in different cancer types and during inflammation (*2-4*). Abnormal expression of *ST3GAL4*, either decreased (*5,6*) or increased (*7*), has been reported in several types of cancer.

This gene spans approximately 59 kb (GeneID 6484) in GenBank (*8*) and displays intricate regulation since it contains different promoter regions that participate in the transcription of several mRNA variants. Previously, the presence of mRNA variants named A1, A2, B1, B2, B3, and BX in several human tissues and cancer cell lines has been reported (*9-14*); nevertheless, the current variants described in RefSeq RNA are named V1 to V10 (*15*). Thus, the previously reported variants correspond to those described in RefSeq as follows B1:V1, BX:V2 and B3:V4; the rest of the variants (A1, A2, B2) are no longer listed in GenBank (*6*). The expression of the mRNA variants results from alternative splicing and from the activity of different promoters (named pV1, pV2 and pV4) (*5,9,10,16-18*). Promoter pV1 gives rise to the variants V1, V6 and V8; promoter pV2 gives rise to the variants V2, V5, V7 and V9; pV4 gives rise to the variant V4

and only the pV3 promoter that gives rise to the V3 variant has not been characterized. Molecular studies indicate that the promoter pV4 displays activity in testicular, ovarian, cervical, colon and leukaemia cancer cell lines (*17*). Specifically, the promoter lacks TATA or CAAT boxes but contains regulatory elements as binding sites for MAF, AP2, SP1, LFA1, and HLH (*10*). In a cervical cancer cell line, the binding sites for the transcription factor AP2 are involved in its regulation (*18*). The promoter pV2 contains neither canonical TATA nor CAAT boxes but carries several putative binding sites for SP1, AP-1, and NF-kB transcription factors. Moreover, this promoter showed constitutive activity as well as inducible activity by TNF in a lung cancer cell line, which has been associated with high levels of the transcript isoform V2 (*9*). pV1 has been previously identified but not characterized (*10*). The way that transcription initiation is regulated is important for understanding the cellular processes and diseases in which the transcribed gen is involved.

Our research group recently reported the presence of the variants V1, V2, and V3 (not characterized previously) in keratinocytes and cervical cancer cells. Whereas V1 and V2 were present in all the cell lines (HaCaT, SiHa, C33A and HeLa), V3 was expressed in HaCaT, SiHa, and HeLa cells but it was not detected in C33A, suggesting differential regulation of this variant (*5*). Since the promoter for the V3 variant and its putative regulatory elements have not been described, here we identify and characterize the promotor of the V3 variant of the *ST3GAL4* gene to better understand its complex transcription regulation.

2. Materials and Methods

2.1. Cell culture

The human keratinocyte cell line HaCaT was cultured in Dulbecco's modified Eagle's medium (Sigma-Aldrich; Merck KGaA, Darmstadt, Germany) with 10 mmol/L HEPES, supplemented with 10% foetal bovine serum, 100 IU/mL penicillin and 100 µg/mL streptomycin (Sigma-Aldrich; Merck KGaA) at 37°C with 5% CO_2. Cells were harvested using trypsin (0.025%) and EDTA (0.02%) (Sigma-Aldrich; Merck KGaA) and were washed with phosphate-buffered saline.

2.2. Bioinformatic analysis

Alignment among the V mRNA variants was performed to localize the V3 variant in the genomic map of the human *ST3GAL4* gene and its putative promoter. Then, the putative promoter region was delimited using the promoter prediction program Transcriptional Regulatory Element Database. Additionally, we used the Elements Navigation Tool (ElemeNT) to predict the core promoter elements. The software *PATCH Public 1.0* (Pattern Search for Transcription Factor Binding Sites) was employed to determine possible regulation sites inside the promoter and to design deleted versions of the complete promoter.

2.3. Cloning of the putative pV3 promoter region

Genomic DNA was extracted from HaCaT cell line from keratinocytes of human skin (*Wizard Genomic DNA Purification Kit*, Promega, Madison, WI). Then, the putative promoter of 1735 bp was amplified by PCR using the forward primer 5'-GAGGAAAACCTcgAGGGAATCTTGA-3' and the reverse primer 5'-GGAAAAAGcTTTGGCGTCAGAGG-3'. The underlined nucleotides represent the restriction sites for *XhoI* (forward) and *HindIII* (reverse), and lower-case letters correspond to the nucleotides incorporated into the cloned-promoter sequence. Smaller versions of 689 bp and 484 bp were generated by enzymatic restriction with *KpnI/HindIII* and *SmaI/HindIII*, respectively, of the 1735 bp construction. The promoter fragments were purified and cloned into the reporter vector. The forward primers for the other versions correspond to 5'-GGCTTTGCTCgaGCCCTTTATG-3' for 364 bp, 5'-CTCAGAGCTcGAgCAGCAATGT-3' for 342 bp, 5'-GAAAGGtacCATGTTGTCTTG-3' for 308 bp and 5'-GGCTCGaGAAATTCCTGATTG-3' for 207 bp. The restriction site for the 364 bp, 342 bp and 207 bp versions corresponds to *XhoI*, and that for the 308 bp version corresponds to *Kpn I*. The reverse primer was the same for all versions. The PCR contained 25 µl of PCR Master Mix (Promega, Madison, WI), 0.5 µM of each primer, and 100 ng of DNA template in a final volume of 50 µL, with the following PCR conditions: 95°C for 5 min and 40 cycles at 95°C for 1 min, 58°C for 1 min and 72°C for 2 min, followed by a final extension at 72°C for 7 min. Next, each fragment was electrophoresed in agarose gel, and the band was purified and cloned into the pGL4.12[*luc2CP*] vector (Promega, Madison, WI) using T4 DNA Ligase (Promega). The constructs were verified by digestion with restriction enzymes and subsequent sequencing.

2.4. Luciferase assay

HaCaT cells were seeded in 24-well plates, and when the cells reached 80% confluence, they were transiently transfected with 600 ng of each pGL4.12 construct and 20 ng of the pGL4.74[*hRlucCP*] vector as a reference plasmid (Promega, Madison, WI) using the Lipofectamine 3000 reagent protocol (Invitrogen, Carlsbad, CA). Cells were lysed 24 h after transfection, and firefly and *Renilla* luciferase activities were determined using the commercially available Dual-Luciferase Reporter Assay System (Promega) according to the manufacturer's instructions. Luciferase activities were measured in a luminometer

Glomax 20/20 (Promega). The firefly luciferase activity was normalized to the *Renilla* luciferase activity. All transfections were performed in triplicate in three different experiments. Student's *t*-test was used to determine statistical significance between the different constructs; $p < 0.05$ was considered statistically significant.

3. Results and Discussion

The *ST3GAL4* gene encodes the enzyme ST3GAL IV, which participates in the synthesis of the sialyl Lewis X antigen. The expression change of this glycan has been implicated in different pathologies, such as cystic fibrosis and cancer (*2,4,9*). Regulation of *ST3GAL4* gene expression is very complex, giving rise to 10 different mRNA variants (V1-V10), currently reported in the RefSeq RNA database (*15*). These mRNA variants are the result of the activity of different promoters (pV1, pV2, pV3 and pV4) and of alternative splicing. The promoters pV1, pV2 and pV4 have been previously characterized (*10,17*). Recently, we identified the presence of V3 mRNA in cervical cancer cell lines HeLa and SiHa, but not in C33A, nevertheless the promoter of this variant has not been previously reported (*5*). The characterization of promoters that participate in the expression of this gene is of interest, considering the importance of the enzyme ST3Gal IV in cancer and inflammatory disease and the fact that the promoters could respond in a different manner according to the stimulus and cell type (*9*). The promoter of V3 mRNA has not been characterized to date. The objective of this work was to delimitate and characterize the V3 promoter region of the *ST3GAL4* gene and to identify its minimal promoter.

In silico analysis showed that the putative promoter is located from position 126401632 to 126403373 of chromosome 11 and extends up to 1735 bp upstream of the transcription start site of the V3 mRNA variant (GenBank NC_000011.10). The promoter contains five TFIID/TBP (TATA box binding protein) binding sites, four of which are localized far from the transcription start site. Additionally, the promoter contains four initiator elements (Inr), several GC and CCAAT boxes and a downstream promoter element (DPE) (Figure 1). The CCAAT box, GC boxes, and TATA box are promoter elements that have been reported within core promoters (*19*). Other common sequences found close to the transcriptional start site are DPE and Inr, so we identified these elements in the putative V3 promoter (Figure 1). To identify response elements in the putative promoter, we used the software *PATCH Public 1.0* and identified several response elements, including binding sites for AP-1, AP-2, CREB, c-jun, c-Myb, CTCF, ER, GATA-1, NFAT, PAX, E2F, VDR, RAR-α1, RXR-α, and VDR (Figure 1).

We have cloned the complete promoter of 1735 bp, to determine if this region presents activity. The

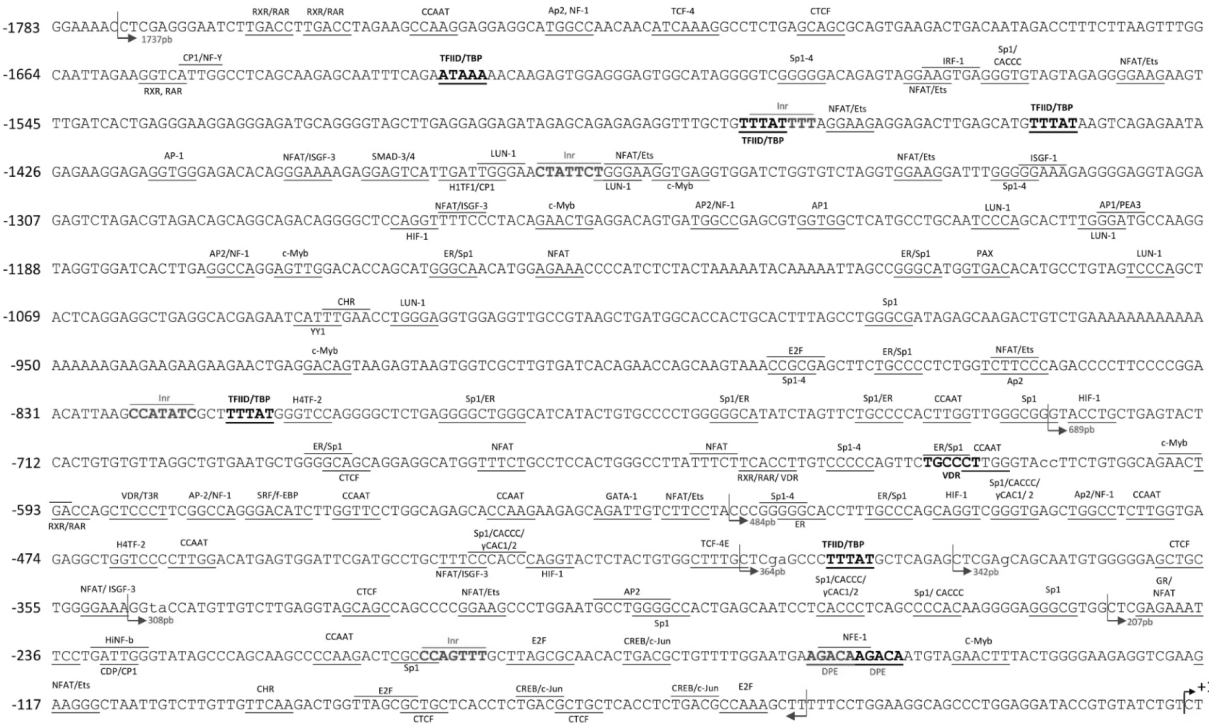

Figure 1. Schematic representation of V3 promoter of *ST3GAL4* gene. It is shown the nucleotide sequence. The reverse arrow represents the 3' extreme of all constructions, and the forwards arrows represent the extreme 5' of the different constructions, the nucleotide size of each promoter fragment is shown. The core promoter elements and the potential regulatory elements are described. Initiator sequences are shown in red. Transcriptional start site is marked with a red arrow. Nucleotides are numbered considering the transcription initiation site as +1.

experimental analysis showed that the region identified and characterized by *in silico* analysis has promoter activity (Figure 2).

To identify the minimal promoter region and the required motifs for basal promoter activity, we generated deleted versions of the complete promoter from the upstream region. Thus, six constructs were generated with the following base pair lengths: 689 bp, 484 bp, 364 bp, 342 bp, 308 bp, and 207 bp (Figure 2). In the first deleted version of 689 bp, four of the five TFIID/TBP sites, three Inr sites and several CCAAT boxes were eliminated, but the same activity of the complete promoter was maintained. The results indicated that the four TATA boxes, the 3 Inr sites, and the several CCAAT boxes eliminated in this construct did not play a role in basal promoter activity. The TATA box is a sequence recognized by the RNA pol II. This element has a position that usually ranges from approximately 40 to 100 nt, but the motifs identified in this region are located far from the transcription start site, which could explain why they do not affect the basal promoter activity (*19*). This could be applied to the Inr sites and the CCAAT boxes deleted in the construct as they are also distant from the transcription start site. In the 484 bp construct, different response elements such as RXR, RAR, cMyb, VDR, NFAT, Ets and two CCAAT boxes were eliminated; nevertheless, the activity was similar with respect to the complete promoter. In the 364 bp construct, a fragment containing GC and CCAAT boxes was eliminated, along with other response elements such as ER, CACCC, HIF1, Ap2, NF-1 and NFAT. The activity of this construct

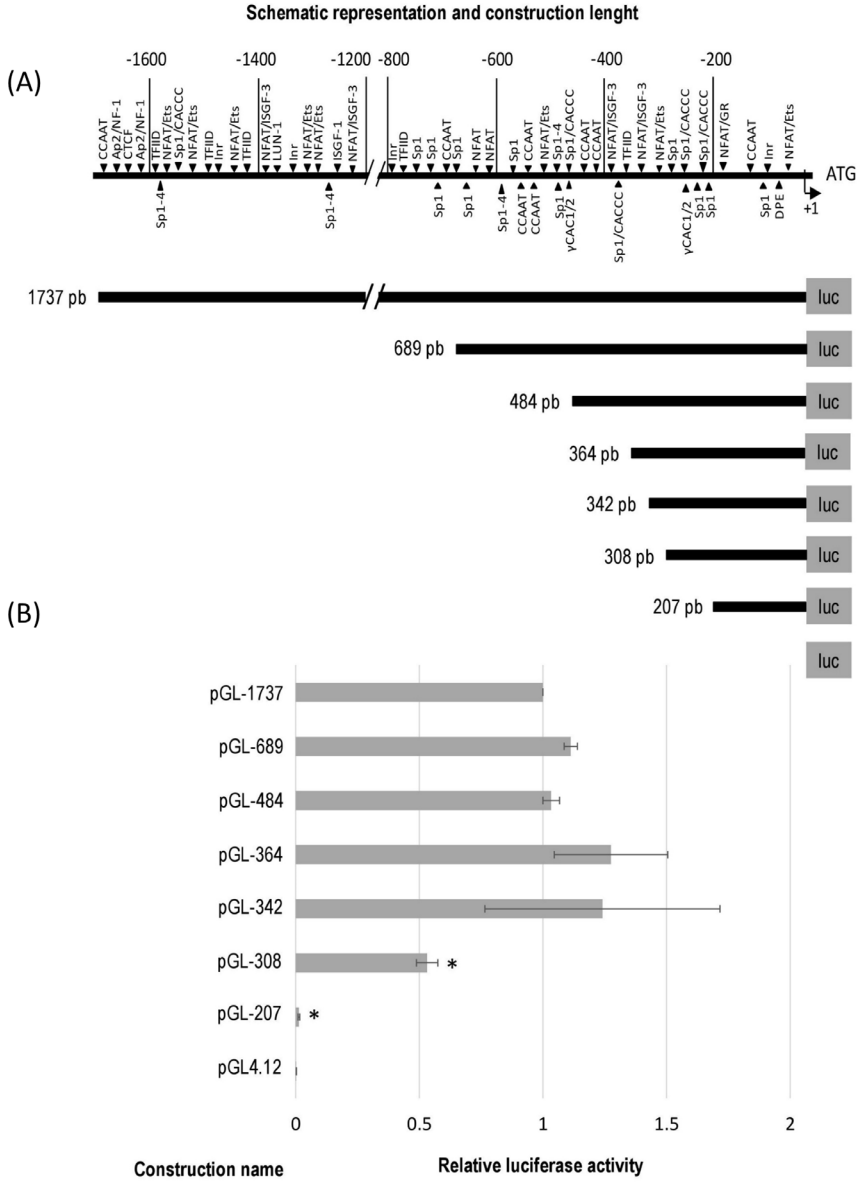

Figure 2. (**A**) Schematic representation of V3 promoter showing different response elements, including the core promoter elements. It is shown the size of the different constructs. (**B**) Relative luciferase activity of the different constructs is shown. All assay transfections were performed by triplicate in three different experiments. Data are expressed as mean ± SD (n = 3). Student's t-test was used and a $p < 0.05$ was considered statistically significant. *Statistical differences between the complete promoter activity and the different constructs.

was similar to that of the complete promoter. Therefore, these elements did not influence basal promoter activity. Next, in the 342 bp construct, the proximal TATA box was deleted, but this deletion did not modify the promoter activity. The constructs of 484 bp, 364 bp, 342 bp maintained the same activity as the complete promoter, none of the sequences eliminated participate in basal promoter activity.

Remarkably, the 308 bp construct had a decreased activity of 47% in comparison with that of the complete promoter. In this fragment, CTCF, NFAT and ISGF3 binding sites were deleted (Figures 1 and 2) ($p < 0.05$). The NFAT and ISGF3 sequences could participate in inducible activity, but not in basal activity. The CTCF binding site is a Zn-finger protein that can regulate gene transcription by activating or repressing promoters. At the promoter level, some evidence indicates that CTCF can activate the promoters of *c-Myc* and *GATA4* genes (*20,21*). In the former case, mutation assays indicate that a binding site for CTCF, alone, is required for the promoter activity of the *c-Myc* gene (*20*). Further molecular analysis, through ChIP assays, indicates that CTCF can bind and recruit RNA pol II at the CTCF binding site (*20*). In the latter case, immunoprecipitation assays show that CTCF can directly bind and recruit TAF3, a TBP-associated core promoter factor, to promoter distal sites of the *GATA4* gene (*21*). Site mutations could confirm the CTCF binding site as an activator of V3 promoter of the *ST3GAL4* gene.

Finally, the 207 bp fragment did not present promoter activity; for this construct, four GC boxes and other response elements, such as CTF, NFAT, Ets, AP2, and CACCC, were eliminated. The 207 bp fragment does not show any activity despite containing three elements: an Inr, a DPE and a CAAT box emphasizing the importance of the Sp1 boxes.

These results indicate that the minimal V3 promoter size of the *ST3GAL4* gene is approximately 308 bp. The region contains GC boxes, a CCAAT box, an Inr and DPE sites that together could maintain promoter activity (Figure 1 and 2). It is important to mention that the minimal construct that maintains the activity does not contain a TATA box, indicating that the V3 promoter is a TATA-less promoter and that other elements must participate in the activity of the promoter. Eukaryotic core promoters can include elements (a TATA box, the TFIIB-recognition element (BRE), an Inr, an MTE, a DPE and a DCE) that are necessary for the transcription preinitiation complex assembly, which includes general transcription factors such as TFIID and the RNA pol II, among others (*22*). Recently, bioinformatic analysis showed that approximately 80% of mammalian protein-coding genes are directed by TATA- less promoters (*23*).

Here, we showed that the version that maintains the promoter activity pGL4-12-308 contains several GC boxes (Sp1 binding sites) and CACCC, Inr and DPE sites. In TATA-less promoters, the presence of Sp1 is necessary for the binding of TFIID to the Inr site (*24*). It has been reported that Sp1 is a transcription factor that recognizes GC boxes and activates transcription through domains rich in glutamine residues (*25*). Therefore, in this core promoter, the binding sites for Sp1 must be essential for the activity. In TATA-less promoters, TFIID can bind to the Inr, primarily if Sp1 is bound to upstream sites (*24,26*). Molecular studies have shown that the DNA-binding domain of Sp1 is in contact with TAF7, and it has been proposed as a co-activator (*27*).

It could be possible that the GC boxes in the 308 bp fragment of the V3 promoter are crucial for the binding of TFIID to the Inr. This was supported by the deletion of the GC boxes in the 207 bp construct, which result in the loss of promoter activity. Additionally, it has been reported that both the Inr and the DPE can participate in basal transcriptional activity when the two elements are separated by 25-32 nt (*19*); however, when the distance between the elements increases, the function disappears (*28*). In the V3 promoter, the distance between these elements is 33 nt, so it could be of interest to determine the role of this binding site in promoter activity. Molecular studies have demonstrated that the Inr, alone or in conjunction with other elements, is capable of directing transcription initiation (*29*). More specifically, the Inr is recognized and binds to TFIID through the proteins TAF1/TAF2 (*24,29*).

It is important to mention that the V3 promoter contains several NFAT sites, and the NFAT (nuclear factor of activated T cells) proteins bind to certain regulatory elements in cytokine genes (*30*). For the pV2 promoter, it has been reported that its expression is induced by TNF, a cytokine that participates in inflammation, showing that the expression of this gene is modulated during inflammation (*3,9*). NFAT is a family of transcription factors that modulate the expression of genes that participate in the immune response, highlighting the importance of this gene in cancer and inflammatory disease (*30*). Nevertheless, further analysis is required to elucidate whether any of these binding sites are necessary for V3 promoter activity.

Finally, we have completed the gene structure including the promoters V1, V2 and V4 (previously reported) and the promoter V3, we also included the genomic structure of the V3 mRNA variant, which contains an extra exon named exon Y. It was named Y, considering that exon X corresponds to the V2 variant. Furthermore, the different exons that constitute the non-coding 5' region of the mRNA variants (V1-V9) are shown. V10 variant was not included because it does not codify for a protein (Figure 3).

In summary, we identified the V3 promoter of the *ST3GAL4* gene, which has a size of 1735 bp, and the core promoter was approximately 300 nt. The basal activity of this promoter is not regulated by a TATA box, and the results suggest that the GC boxes could

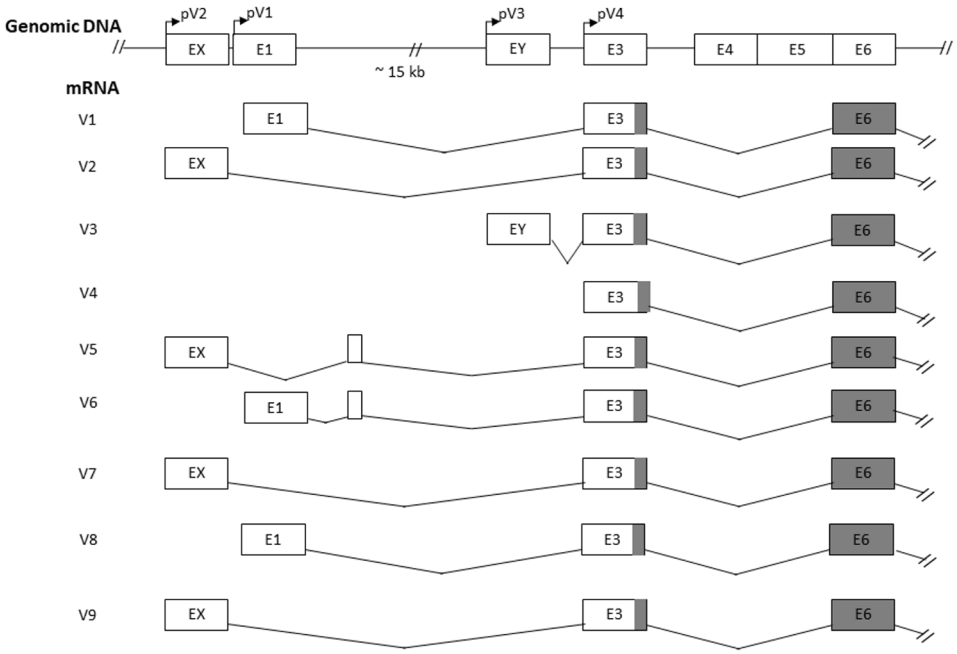

Figure 3. Schematic representation of the *ST3GAL4* gene structure including the promoters V1, V2 and V4 previously reported and the new promoter V3. It is shown in boxes the exons of the mRNA variants V1 to V9. It is also represented the structure of the mRNA variants at the non-coding 5' region, the grey boxes represent the coding region and the white boxes are the exons not translated.

regulate the basal activity in conjunction with the Inr and DPE elements. The promoter contains several NFAT sites that could participate in the transcription regulation of this gene during the immune response.

Acknowledgements

This study was supported by Programa Catedras CONACYT 2016 (no. 485), Fondo Redes Temáticas de Investigación CONACYT (253596) and Funds for Scientific Infrastructure from the IMSS (CTFIS/10RD/12/2011). We thank to Fundación IMSS for the fellowship awarded to JRL.

References

1. Harduin-Lepers A, Vallejo-Ruiz V, Krzewinski-Recchi MA, Samyn-Petit B, Julien S, Delannoy P. The human sialyltransferase family. Biochimie. 2001; 83:727-737.
2. Cohen EN, Fouad TM, Lee BN, *et al*. Elevated serum levels of sialyl Lewis X (sLe(X)) and inflammatory mediators in patients with breast cancer. Breast Cancer Res Treat. 2019; 176:545-556.
3. Colomb F, Krzewinski-Recchi MA, Steenackers A, Vincent A, Harduin-Lepers A, Delannoy P, Groux-Degroote S. TNF up-regulates *ST3GAL4* and sialyl-Lewisx expression in lung epithelial cells through an intronic ATF2-responsive element. Biochem J. 2017; 474:65-78.
4. Yamadera M, Shinto E, Tsuda H, Kajiwara Y, Naito Y, Hase K, Yamamoto J, Ueno H. Sialyl Lewis(x) expression at the invasive front as a predictive marker of liver recurrence in stage II colorectal cancer. Oncol Lett. 2018; 15:221-228.
5. Roa-de La Cruz L, Martinez-Morales P, Moran-Cruz I, *et al*. Expression analysis of *ST3GAL4* transcripts in cervical cancer cells. Mol Med Rep. 2018; 18:617-621.
6. Saito S, Yamashita S, Endoh M, Yamato T, Hoshi S, Ohyama C, Watanabe R, Ito A, Satoh M, Wada T, Paulson JC, Arai Y, Miyagi T. Clinical significance of ST3Gal IV expression in human renal cell carcinoma. Oncol Rep. 2002; 9:1251-1255.
7. Perez-Garay M, Arteta B, Llop E, Cobler L, Pages L, Ortiz R, Ferri MJ, de Bolos C, Figueras J, de Llorens R, Vidal-Vanaclocha F, Peracaula R. alpha2,3-Sialyltransferase ST3Gal IV promotes migration and metastasis in pancreatic adenocarcinoma cells and tends to be highly expressed in pancreatic adenocarcinoma tissues. Int J Biochem Cell Biol. 2013; 45:1748-1757.
8. Coordinators NR. Database resources of the National Center for Biotechnology Information. Nucleic Acids Res. 2018; 46:D8-D13.
9. Colomb F, Krzewinski-Recchi MA, El Machhour F, Mensier E, Jaillard S, Steenackers A, Harduin-Lepers A, Lafitte JJ, Delannoy P, Groux-Degroote S. TNF regulates sialyl-Lewisx and 6-sulfo-sialyl-Lewisx expression in human lung through up-regulation of *ST3GAL4* transcript isoform BX. Biochimie. 2012; 94:2045-2053.
10. Kitagawa H, Mattei MG, Paulson JC. Genomic organization and chromosomal mapping of the Gal beta 1,3GalNAc/Gal beta 1,4GlcNAc alpha 2,3-sialyltransferase. J Biol Chem. 1996; 271:931-938.
11. Kitagawa H, Paulson JC. Differential expression of five sialyltransferase genes in human tissues. J Biol Chem. 1994; 269:17872-17878.
12. Taniguchi A, Hasegawa Y, Higai K, Matsumoto K. Down-regulation of human Galbeta1,3GalNAc/Galbeta1,4GlcNAc alpha2,3-sialyltransferase (hST3Gal IV) gene during differentiation of the HL-60 cell line. Mol

Cell Biol Res Commun. 1999; 2:197-201.
13. Taniguchi A, Hioki M, Matsumoto K. Transcriptional regulation of human Galbeta1,3GalNAc/Galbeta1, 4GlcNAc alpha2,3-sialyltransferase (hST3Gal IV) gene in testis and ovary cell lines. Biochem Biophys Res Commun. 2003; 301:764-768.
14. Taniguchi A, Matsumoto K. Down-regulation of human sialyltransferase gene expression during *in vitro* human keratinocyte cell line differentiation. Biochem Biophys Res Commun. 1998; 243:177-183.
15. O'Leary NA, Wright MW, Brister JR, *et al*. Reference sequence (RefSeq) database at NCBI: current status, taxonomic expansion, and functional annotation. Nucleic Acids Res. 2016; 44:D733-745.
16. Taniguchi A, Matsumoto K. Epithelial-cell-specific transcriptional regulation of human Galbeta1,3GalNAc/ Galbeta1,4GlcNAc alpha2,3-sialyltransferase (hST3Gal IV) gene. Biochem Biophys Res Commun. 1999; 257:516-522.
17. Taniguchi A, Morishima T, Tsujita Y, Matsumoto Y, Matsumoto K. Genomic structure, expression, and transcriptional regulation of human Gal beta 1,3 GalNAc alpha 2,3-sialyltransferase gene. Biochem Biophys Res Commun. 2003; 300:570-576.
18. Taniguchi A. Promoter structure and transcriptional regulation of human beta-galactoside alpha2, 3-sialyltransferase genes. Curr Drug Targets. 2008; 9:310-316.
19. Butler JE, Kadonaga JT. The RNA polymerase II core promoter: a key component in the regulation of gene expression. Genes Dev. 2002; 16:2583-2592.
20. Chernukhin I, Shamsuddin S, Kang SY, *et al*. CTCF interacts with and recruits the largest subunit of RNA polymerase II to CTCF target sites genome-wide. Mol Cell Biol. 2007; 27:1631-1648.
21. Liu Z, Scannell DR, Eisen MB, Tjian R. Control of embryonic stem cell lineage commitment by core promoter factor, TAF3. Cell. 2011; 146:720-731.
22. Thomas MC, Chiang CM. The general transcription machinery and general cofactors. Crit Rev Biochem Mol Biol. 2006; 41:105-178.
23. FitzGerald PC, Shlyakhtenko A, Mir AA, Vinson C. Clustering of DNA sequences in human promoters. Genome Res. 2004; 14:1562-1574.
24. Kaufmann J, Smale ST. Direct recognition of initiator elements by a component of the transcription factor IID complex. Genes Dev. 1994; 8:821-829.
25. Pugh BF, Tjian R. Mechanism of transcriptional activation by Sp1: evidence for coactivators. Cell. 1990; 61:1187-1197.
26. Emami KH, Burke TW, Smale ST. Sp1 activation of a TATA-less promoter requires a species-specific interaction involving transcription factor IID. Nucleic Acids Res. 1998; 26:839-846.
27. Chiang CM, Roeder RG. Cloning of an intrinsic human TFIID subunit that interacts with multiple transcriptional activators. Science. 1995; 267:531-536.
28. Burke TW, Kadonaga JT. The downstream core promoter element, DPE, is conserved from Drosophila to humans and is recognized by TAFII60 of Drosophila. Genes Dev. 1997; 11:3020-3031.
29. Chalkley GE, Verrijzer CP. DNA binding site selection by RNA polymerase II TAFs: a TAF(II)250-TAF(II)150 complex recognizes the initiator. EMBO J. 1999; 18:4835-4845.
30. Pan MG, Xiong Y, Chen F. NFAT gene family in inflammation and cancer. Curr Mol Med. 2013; 13:543-554.

Received December 9, 2019; Revised March 26, 2020; Accepted March 27, 2020

**Address correspondence to:*
Verónica Vallejo-Ruiz, Instituto Mexicano del Seguro Social, Centro de Investigación Biomédica de Oriente, Laboratorio de Biología Molecular, Km 4.5 Carretera Federal, Atlixco-Metepec, C.P. Metepec, Puebla 74360, México.
E-mail: veronica_vallejo@yahoo.com

Lorena Milflores Flores, Facultad de Ciencias Biológicas, Benemérita Universidad Autónoma de Puebla, Puebla, Puebla 72570, México.
E-mail: lorenamilflo@yahoo.com.mx

Released online in J-STAGE as advance publication April 15, 2020.

Communication

DOI: 10.5582/bst.2020.01015

Health care reform in China from the perspective of physicians

Jing Lin[1,2,3,§], Jing Zhou[1,2,3,§], Ling Wang[1,2,3,*]

[1] Laboratory for Reproductive Immunology, Hospital & Institute of Obstetrics and Gynecology, Shanghai Medical College, Fudan University, Shanghai, China;
[2] Academy of Integrative Medicine, Fudan University, Shanghai, China;
[3] Shanghai Key Laboratory of Female Reproductive Endocrine-related Diseases, Shanghai, China.

SUMMARY Health care reform is a worldwide problem. To address the problems of costs, access, quality, efficiency, and equity, China initiated healthcare reform in 2009. The progress of China's healthcare reform has been internationally recognized as the reform has expanded insurance coverage and improved access to and reduced the costs of care over the ten-year period from 2008 to 2018. To achieve sustainable goals, attention must be focused on whether and how the reform encourages physicians. This paper highlights the role of physicians, the challenges that need to be addressed, and the direction in which to advance health reform in China from the perspective of physicians. The slow-growing and aging physician population cannot meet the ever-increasing medical demand. Physicians have a heavy workload, work long hours, have unsatisfactory income, and have a fraught relationship with patients. The situation calls for rethinking the value of physicians and rebuilding trust between physicians and patients. Further healthcare reform is needed to equitably allocate physicians with adequate training, time, and resources to deliver evidence-based practices and patient-centered care.

Keywords China, healthcare, reform, physicians

1. Introduction

Healthcare reform is a worldwide problem. For China, a developing country with a large population, it is even more difficult and challenging. In response to the problems of cost, access, quality, efficiency, and equity, China initiated the long-awaited and much-needed healthcare reform in 2009. From 2009 to 2012, the five priority areas were: *i*) expanding basic health insurance programs; *ii*) establishing an essential drug list; *iii*) upgrading primary care delivery; *iv*) greater parity between rural and urban public healthcare; and *v*) initiation of pilot reforms in public hospitals (*1,2*). From 2012 to 2015, the healthcare reform was aimed at deepening public hospital reforms in terms of their operation, governance, compensation, and other aspects. From 2015 to 2020, the strategic goals were: *i*) universal coverage of basic healthcare for all citizens by unifying three public insurance schemes; *ii*) providing an integrated health system by enhancing primary care and reforming public hospitals; and *iii*) a "Healthy China 2030" blueprint focusing on improvements in medical care and health determinants such as environment health, lifestyle, and health education (*3*).

The progress of China's healthcare reform has been internationally recognized (*4*). Over the ten-year period from 2008 to 2018, the percentage of the national gross domestic product (GDP) devoted to healthcare has been steadily increasing (Figure 1). Total healthcare expenditures increased from 1.453 trillion RMB in 2008 (*5*) to 5.800 trillion RMB in 2018 (*6*), an increase of 299% (Figure 1). With three major health insurance programs: the Urban Employee Basic Medical Insurance, the New Rural Cooperative Medical Scheme, and Urban Resident Basic Medical Insurance, insurance coverage improved markedly since 2003, thereby covering over 95% of citizens in 2018 (*7*). As a result of the improved benefits package under these insurance systems, the direct out-of-pocket spending as a share of total healthcare expenditures declined from 40.4% to 28.7% (Figure 1) (*5,6*). Markups in drug prices have been eliminated and drug prices have been reduced; consequently, China has seen a proportional decline in drug expenses over the ten-year period of the medical reform from 2008 to 2018 (*5,6*) (Table 1). According to Lancet's ranking of medical quality and accessibility in 195 countries and regions of the world, China rose from 60th place to 48th in 2015 and was one of the countries with the fastest progress (*8*).

However, medical reform initiatives focused on improving patient care may neglect the welfare of healthcare providers. To achieve sustainable goals,

attention must be focused on whether and how the reform encourages physicians. This paper highlights the role of physicians, the challenges that need to be addressed, and the direction in which to advance health reform in China from the perspective of physicians.

2. Supply of physicians

With an aging population and expanded medical insurance coverage, China is seeing an increasing demand for medical care and medical personnel. Data from the National Health Commission of the People's Republic of China showed that, from 2008 to 2018, the number of outpatient visits increased by 100.9% and the number of inpatient admissions increased by 170.8% (*5,6*). However, the growth rate of supply of physicians has not kept pace with growing healthcare demands. In 2018, China had 3.0 million licensed physicians, with 2.2 physicians per 1,000 population. The annual number of licensed physicians increased by only 1.2 million (68.0%) from 2008 to 2018 (Figure 2A). As the population ages and the demand outpaces supply, the physician shortage will intensify.

With the Gini coefficient as an indicator of distribution inequity, China has a severe geographical disparity in physicians (a Gini coefficient higher than 0.6), and this trend is worsening (*9,10*). The distribution of licensed physicians by age warrants attention as well (Figure 2B). The proportion of young physicians under the age of 35 was 26.4% in 2009 (*11*); in 2017, it fell to 21.1% (*12*). Moreover, the proportion of physicians over the age of 60 rose from 7.2% to 13.2%. The percentage of physicians with over 20 years of experience exceeded 47.7%, while the proportion of physicians with 10-20 years of experience steadily declined (*11,12*). There are many reasons for the slow-growing and aging physician population, such as extensive medical education and training (including undergraduate, postgraduate, and continuing education), mounting pressures at work, and a substantial decline in income. According to surveys in 2019, 46.6% of Chinese neurology postgraduates regretted their career choice (*13*) and the dropout rate

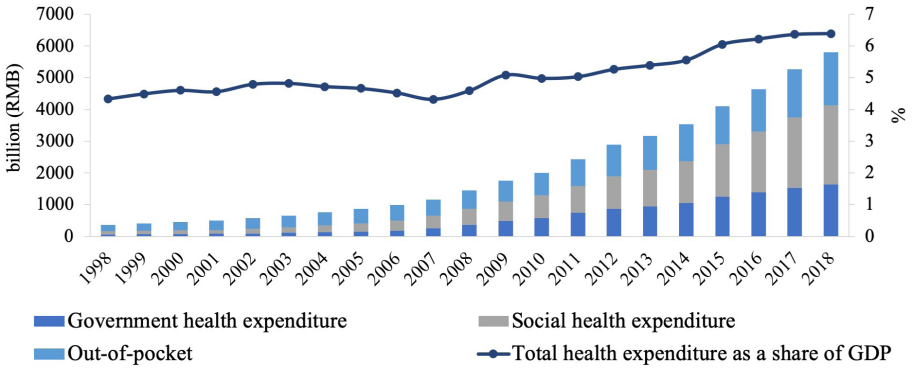

Figure 1. Nationwide healthcare expenditures. Changes in healthcare expenditures in China, 1998-2018. *Data are from the National Health Commission of the People's Republic of China.

Table 1. Hospital outpatient and inpatient costs

Year	Outpatient cost per visit (RMB)	Outpatient cost growth rate (%)	Outpatient drug expenses (%)	Inpatient cost per discharge (RMB)	Inpatient cost growth rate (%)	Inpatient drug expenses (%)
1995	39.9	-	64.2	1667.8	-	52.8
2000	85.8	-	58.6	3083.7	-	46.1
2005	126.9	7.5	52.1	4661.5	8.8	43.9
2006	128.7	1.4	50.5	4668.9	0.2	42.7
2007	135.8	5.5	50.0	4964.4	6.3	43.2
2008	146.5	7.6	51.3	5463.8	9.9	43.5
2009	152.0	9.9	51.5	5684.0	8.6	43.6
2010	166.8	9.7	51.3	6193.9	9	43.1
2011	179.8	7.8	50.6	6632.2	7.1	41.8
2012	192.5	7.1	50.3	6980.4	5.3	41.1
2013	206.4	7.2	49.3	7442.3	6.6	39.5
2014	220.0	6.6	48.3	7832.3	5.2	38.3
2015	233.9	6.3	47.3	8268.1	5.6	36.8
2016	245.5	5	45.5	8604.7	4.1	34.6
2017	257.0	4.7	42.7	8890.7	3.3	31.1
2018	274.1	6.7	40.9	9291.9	4.5	28.8

*Data are from the National Health Commission of the People's Republic of China. Note: growth rates are calculated at current prices.

of pediatricians was 12.6% (*14*). According to another survey, 71.0% of physicians in China would not encourage their children to pursue a medical specialty (*15*). An inadequate supply, uneven distribution, and low job satisfaction among physicians are the major obstacles facing China's healthcare system.

3. Work stress

A hierarchical medical system is at the core of the sustainable development of public healthcare in China. Since 2009, various approaches have been explored to establish an efficient, stable, and standardized mechanism for cooperation between public hospitals and primary healthcare providers, including prioritizing the development of primary care, building primary care facilities, a tiered reimbursement to encourage patients to receive primary care, dual referral systems, a standardized residency training program to equalize the delivery of quality care at all levels, and improving standard operating procedures for clinical practice (*16,17*). However, the uneven distribution of quality healthcare resources has not been properly addressed. Patients are still more willing to visit hospitals, and especially tertiary hospitals. Therefore, hospitals account for only a small proportion of total medical facilities (2-3%) in China, but they provided 43% of the outpatient care and 79% of the inpatient care in 2018 (*6*). Tertiary hospitals account for 6-8% of all hospitals, but tertiary hospitals account for 46% of inpatient admissions and 52% of outpatient visits.

The patient preference for large hospitals places a substantial burden on physicians in those hospitals. Physicians worked an average of 10 hours a day and slept 6 hours on average. Only 35.78% thought that they were in good health (*15*) and 64.8% were dissatisfied with their jobs (*18*). The prevalence of burnout among Chinese physicians ranged from 66.5 to 87.8%, according to a systematic review of 9,302 participants in 11 studies (*19*). In the United States, the burnout rate was 45.2% among resident physicians (*20*). Long working hours and severe burnout symptoms were independently associated with an increased risk of medical errors. According to a cross-sectional survey of 1,537 physicians in 46 hospitals across China, 39.6% of physicians in primary hospitals, 50.0% in secondary hospitals, and 59.5% in tertiary hospitals had recently made a medical error (*21*).

4. Financial stress

Controlling rising medical costs is one of the top priorities for healthcare reform. China's efforts to control the growth of costs are focused on eliminating markups in drug prices, reducing the price of drugs, and controlling the behavior of public hospitals. Public

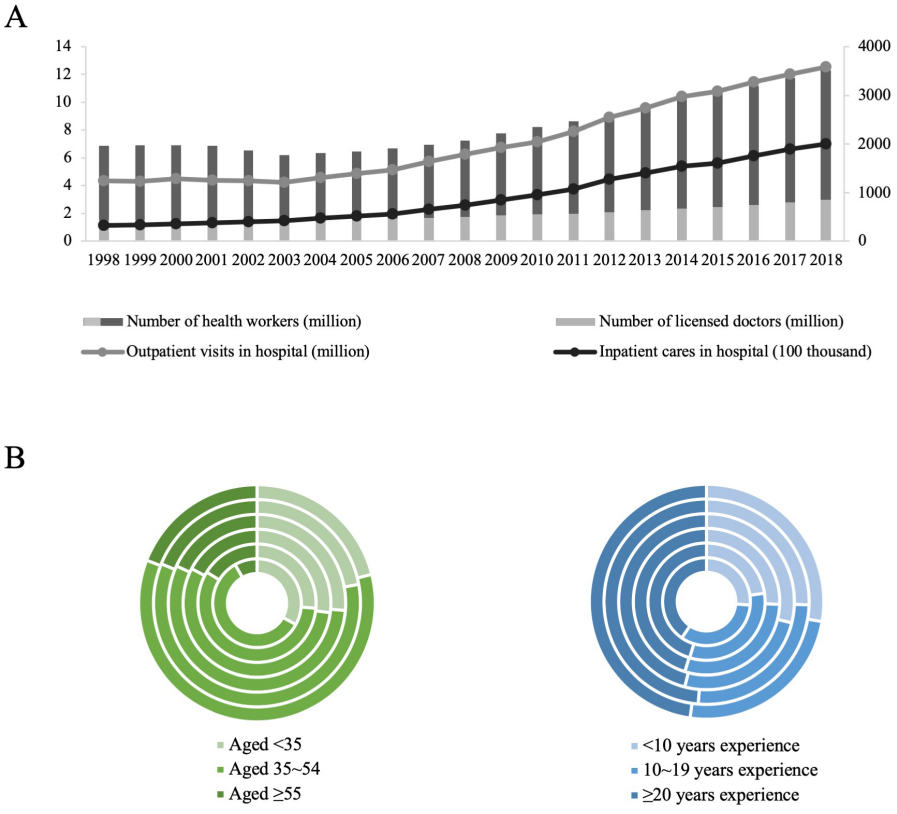

Figure 2. The trends in and features of the healthcare workforce supply in China. (**A**) Changes in the healthcare workforce supply and workload in China, 1998-2018. (**B**) Characteristics of licensed physicians, 2005-2017. Starting from the inside, each ring represents the years 2005, 2009, 2011, 2013, 2015, and 2017. *Data are from the National Health Commission of the People's Republic of China.

hospitals used to recoup medical costs through income from mark-ups on drugs because healthcare providers are underfunded and medical care is undervalued. Now, the brutal separation of medical care from drug sales prior to the establishment of a corresponding mechanism of compensation will place a great financial burden on hospitals and affect the income of medical staff. It will also reduce the motivation of medical personnel to implement healthcare reforms and raise doubts about the sustainability of those reforms.

According to a national survey of 17,945 physicians across China in 2016, 60.31% of physicians felt that the current medical pricing system did not reflect their value (*15*). The income distribution policy was one of the leading factors that influenced job satisfaction, according to 45.92% of physicians. Among 762 young physicians aged 15-45, 76.1% have a monthly income of 2,000 to 7,000 RMB (*22*). How to value physicians is one of the most discussed and highlighted problems for healthcare reform to address. Efforts are underway to more closely involve physicians in healthcare reform. Ways to encourage physicians include: prompting private actors to help supply medical care, encouraging physicians' mobility, and allowing multisite practice (*23*). Ultimately, how the society pays for care strongly influences how care is delivered.

5. Physician-patient relationship

Trust between physicians and patients is essential for the free flow of information necessary for medical care. However, there has been an unprecedented deterioration in the physician-patient relationship over recent years. Violence against physicians in China is particularly prevalent and severe. According to a survey of 2,617 physicians, respondents were often subjected to verbal abuse (76.2%), unreasonable demands (58.3%), baseless complaints (40.8%), disruptions (40.2%), threatening behavior (27.6%), physical violence (24.1%), and sexual harassment (7.8%) (*24*). From 2013 to 2016, there were 459 criminal cases of patient-initiated violence against medical staff in China (*25*). On December 24, 2019, Wen Yang, an emergency physician at the Beijing Civil Aviation General Hospital, was brutally killed by a patient's son who was dissatisfied with what he thought was the inadequate treatment of his 95-year-old mother (*26*). Workplace violence has strongly influenced physicians' regret of their career choice, professional turnover, and word-of-mouth communication (*27*).

Patient disappointment and resentment reflect a flawed medical system that victimizes both patients and physicians. In an effort to control medical fees, physicians need to be more productive and increase their competitiveness in order to make a profit, which means seeing patients faster. The average physician was seeing 40 patients per day, and 67.2% of physicians spent no more than 10 minutes with each outpatient (*28*). Moreover, there are many restrictions imposed on physicians that affect aspects of their work such as drugs they can prescribe and hospitalization. Paperwork, meetings, and scientific research have distracted physicians from actual patient care. Patients feel that physicians ignore their needs and are rushing them through simply to make a profit. The large proportion of negative news (74.9%) regarding the physician-patient relationship on Chinese social media has negatively affected the perceptions of both patients and physicians (*29,30*). Fixing this damaged relationship is central to healthcare reform.

6. Directions for the future

Physicians play a major decisive role in patient assessment, examination, diagnosis, and treatment planning, determining the total costs for medical care. Through direct communication with patients, physicians are key actors in the formation and development of the physician-patient relationship. Physicians' roles extend beyond an individual patient's health. They can shape and implement government public healthcare policy. They are of critical importance to medical research, basic health education, combating misinformation, and fighting epidemics. Following the outbreak of SARS, Ebola virus, H7N9 virus, and SARS-CoV-2, physicians are on the front line of the fight against disease regardless of the risks (*31,32*). While physicians are widely considered to be the most important human resources in the field of healthcare, the welfare of physicians is overlooked. The slow-growing and aging physician population cannot meet the ever-increasing medical demand. Physicians have a heavy workload, work long hours, have unsatisfactory income, and have a fraught relationship with patients. Rethinking the value of physicians and rebuilding trust between physicians and patients should be prioritized. The solution lies in further healthcare reform that equitably allocates physicians with adequate training, time, and resources to deliver evidence-based practices and patient-centered care throughout the country.

Acknowledgements

This work was supported by the National Natural Science Foundation of China (grant no. 31571196 to L Wang) and the Program to Guide Medicine ("Yixueyindao") of the Shanghai Municipal Science and Technology Commission (grant no.18401902200 to L Wang).

References

1. Li L, Fu H. China's health care system reform: Progress and prospects. Int J Health Plann Manage. 2017; 32:240-253.

2. Younger DS. Health care in China. Neurol Clin. 2016; 34:1115-1125.
3. Song P, Jin C, Tang W. New medical education reform in China: Towards Healthy China 2030. Biosci Trends. 2017; 11:366-369.
4. Yan F, Tang S, Zhang J. Global implications of China's healthcare reform. Int J Health Plann Manage. 2016; 31:25-35.
5. National Health Commission. 2008 Statistical Bulletin on the Development of the Healthcare Industry in China. *http://www.nhc.gov.cn/mohwsbwstjxxzx/s7967/200904/40250.shtml* (accessd on January 13, 2020) (in Chinese)
6. National Health Commission. 2018 Statistical Bulletin on the Development of the Healthcare Industry in China. *http://www.nhc.gov.cn/guihuaxxs/s10748/201905/9b8d52727cf346049de8acce25ffcbd0.shtml* (accessd on January 13, 2020) (in Chinese)
7. National Healthcare Security Administration. 2018 Statistical Bulletin on the Development of National Basic Medical Insurance. *http://www.nhsa.gov.cn/art/2019/6/30/art_7_1477.html* (accessd on January 13, 2020) (in Chinese)
8. GBD 2015 Healthcare Access and Quality Collaborators. Healthcare Access and Quality Index based on mortality from causes amenable to personal health care in 195 countries and territories, 1990-2015: A novel analysis from the Global Burden of Disease Study 2015. Lancet. 2017; 390:231-266.
9. Wu J. Measuring inequalities in the demographical and geographical distribution of physicians in China: Generalist versus specialist. Int J Health Plann Manage. 2018; 33:860-879.
10. Wu J, Yang Y. Inequality trends in the demographic and geographic distribution of health care professionals in China: Data from 2002 to 2016. Int J Health Plann Manage. 2019; 34:e487-e508.
11. National Health Commission (ed.). Medical personnel. In: China's Health Statistics Yearbook 2010. Publishing House of Beijing Medical College, Beijing, China, 2010; pp. 38-39.
12. National Health Commission (ed.). Medical personnel. In: China's Health Statistics Yearbook 2018. Publishing House of Beijing Medical College, Beijing, China, 2018; pp. 38-39.
13. Tian L, Pu J, Liu Y, Zhong X, Gui S, Song X, Xu S, Zhou X, Wang H, Zhou W, Chen J, Xie P. Relationship between burnout and career choice regret among Chinese neurology postgraduates. BMC Med Educ. 2019; 19:162.
14. Zhang Y, Huang L, Zhou X, *et al.* Characteristics and workload of pediatricians in China. Pediatrics. 2019; 144:e20183532.
15. Sun J, Ma J, Hu G, Zhao Q, Yuan C, Si W, Zhang X, Liu Y. Welfare, wellness, and job satisfaction of Chinese physicians: A national survey of public tertiary hospitals in China. Int J Health Plann Manage. 2017; 32:270–284.
16. Li X, Lu J, Hu S, Cheng KK, Maeseneer JD, Meng Q, Mossialos E, Xu DR, Yip W, Zhang H, Krumholz HM, Jiang L, Hu S. The primary health-care system in China. Lancet. 2017; 390:2584-2594.
17. Zhu J, Li W, Chen L. Doctors in China: Improving quality through modernisation of residency education. Lancet. 2016; 388:1922–1929.
18. Liu J, Yu W, Ding T, Li M, Zhang L. Cross-sectional survey on job satisfaction and its associated factors among doctors in tertiary public hospitals in Shanghai, China. BMJ Open. 2019; 9:e023823.
19. Lo D, Wu F, Chan M, Chu R, Li D. A systematic review of burnout among doctors in China: A cultural perspective. Asia Pac Fam Med. 2018; 17:3.
20. Dyrbye LN, Burke SE, Hardeman RR, Herrin J, Wittlin NM, Yeazel M. Association of clinical specialty with symptoms of burnout and career choice regret among US resident physicians. JAMA. 2018; 320:1114-1130.
21. Wen J, Cheng Y, Hu X, Yuan P, Hao T, Shi Y. Workload, burnout, and medical mistakes among physicians in China: A cross-sectional study. Biosci Trends. 2016; 10:27-33.
22. Liang Y, Wang H, Tao X. Quality of life of young clinical doctors in public hospitals in China's developed cities as measured by the Nottingham Health Profile (NHP). Int J Equity Health. 2015; 14:85.
23. Liu GG, Vortherms SA, Hong X. China's health reform update. Annu Rev Public Health. 2017; 38:431-448.
24. Sun T, Gao L, Li F, Shi Y, Xie F, Wang J, Wang S, Zhang S, Liu W, Duan X, Liu X, Zhang Z, Li L, Fan L. Workplace violence, psychological stress, sleep quality and subjective health in Chinese doctors: A large cross-sectional study. BMJ Open. 2017; 7:e017182.
25. Cai R, Tang J, Deng C, Lv G, Xu X, Sylvia S, Pan J. Violence against health care workers in China, 2013-2016: Evidence from the national judgment documents. Hum Resour Health. 2019; 17:103.
26. Chinese Medical Doctor's Association. Say no to violence against doctors. *http://www.cmda.net/jrtt/13432.jhtml* (accessd on January 13, 2020) (in Chinese)
27. Zhan Y, Kim SK, Zhou L, Xie B, Li Y, Wen B, Nie L. Patient violence and health professionals' occupational outcomes in China: A time-lagged survey study. Int J Nurs Stud. 2019; 94:120-130.
28. Zhang C, Liu Y. The salary of physicians in Chinese public tertiary hospitals: A national cross-sectional and follow-up study. BMC Health Serv Res. 2018; 18:661.
29. Hu G, Han X, Zhou H, Liu Y. Public perception on healthcare services: Evidence from social media platforms in China. Int J Environ Res Public Health. 2019; 16:1273.
30. Sun J, Liu S, Liu Q, Wang Z, Wang J, Hu C, Stuntz M, Ma J, Liu Y. Impact of adverse media reporting on public perceptions of the doctor-patient relationship in China: An analysis with propensity score matching method. BMJ Open. 2018; 8:e022455.
31. Sun M, Xu N, Li C, *et al*. The public health emergency management system in China: Trends from 2002 to 2012. BMC Public Health. 2018; 18:474.
32. Shepherd A. Congolese fight against Ebola. BMJ. 2018; 363:k4814.

Received January 19, 2020; Revised February 17, 2020; Accepted March 19, 2020.

[§]These authors contributed equally to this work.
**Address correspondence to:*
Ling Wang, Laboratory for Reproductive Immunology, Hospital & Institute of Obstetrics and Gynecology, Fudan University, 419 Fangxie Road, Shanghai 200011, China.
E-mail: Dr.wangling@fudan.edu.cn

Released online in J-STAGE as advance publication March 27, 2020.

Communication

DOI: 10.5582/bst.2020.03072

Update on use of chloroquine/hydroxychloroquine to treat coronavirus disease 2019 (COVID-19)

Jianjun Gao[1,*], Shasha Hu[2]

[1] Department of Pharmacology, School of Pharmacy, Qingdao University, Qingdao, China;
[2] Department of Pathology, the Affiliated Hospital of Qingdao University, Qingdao, China.

SUMMARY Drugs that are specifically efficacious against SARS-CoV-2 have yet to be established. Chloroquine and hydroxychloroquine have garnered considerable attention for their potential to treat coronavirus disease 2019 (COVID-19). Increasing evidence obtained from completed clinical studies indicates the prospects for chloroquine/hydroxychloroquine to treat COVID-19. More randomized control clinical studies are warranted to determine the feasibility of these two drugs in treating COVID-19.

Keywords SARS-CoV-2, COVID-19, chloroquine, hydroxychloroquine

Coronavirus disease 2019 (COVID-19) has caused more than 1 million confirmed cases and approximately 70,000 deaths worldwide as of April 6, 2020 (*1*). Drugs that are specifically efficacious against SARS-CoV-2 have yet to be established. Chloroquine and hydroxychloroquine have garnered considerable attention for their potential to treat COVID-19. In China, chloroquine was added to the "Guidance for Corona Virus Disease 2019: Prevention, Control, Diagnosis, and Management" issued by the National Health Commission on February 18, 2020 (*2*). The U.S. Food and Drug Administration (FDA) issued an emergency use authorization for chloroquine/hydroxychloroquine to treat COVID-19 on March 28, 2020 (*3*). The European Medicines Agency contended that the two drugs should be used in clinical trials or national emergency use programs for the treatment of COVID-19 on April 1, 2020 (*4*). The low cost and easy availability of chloroquine/hydroxychloroquine may help to curb this global public health emergency if their efficacy and safety are ultimately verified in clinical studies.

Chloroquine phosphate is the first drug reported to display efficacy against COVID-19 in early clinical studies in China (*5,6*). Based on this encouraging finding, chloroquine phosphate was added to the Sixth Edition of the Guidance for tentative treatment of COVID-19 (*2*). The Sixth Edition recommended that adult patients in whom chloroquine is not contraindicated should take chloroquine phosphate tablets, 500 mg (300 mg for chloroquine) twice a day for no more than 10 days (*7*). To reduce the risk of adverse effects of chloroquine, the Seventh Edition of the Guidance, issued on March 3, 2020, recommends a reduced dosage and shortened duration of treatment (*8*). Specifically, the dosage of chloroquine phosphate for adult patients (ages 18-65) with a body weight greater than 50 kg is 500 mg twice a day for 7 days and that for adult patients (ages 18-65) with a body weight less than 50 kg is 500 mg twice a day for the first 2 days and 500 mg once a day for the following 3-7 days (*8*). Regarding the treatment strategy, chloroquine and another antiviral favipiravir that also displayed efficacy in clinical trials are highlighted for their use in mild and moderate COVID-19 cases to prevent disease progression (*9*).

In a pilot study (*10*) aiming to evaluate the efficacy and safety of chloroquine in inpatients with COVID-19, 10 patients (3 with severe disease and 7 with moderate disease) received chloroquine phosphate 500 mg orally twice a day for 10 days, and 12 patients (5 with severe disease and 7 with moderate disease) received lopinavir/ritonavir 400/100 mg orally twice a day for 10 days. Chloroquine was slightly superior to lopinavir/ritonavir in terms of virus-negative conversion since the chloroquine group tested negative for SARS-CoV-2 at a slightly higher rate than the control group on day 7, day 10, and day 14 post-treatment (*10*). However, chloroquine was superior to lopinavir/ritonavir in improving the radiological appearance of the lungs and decreasing the duration of hospitalization. Adverse events including vomiting, abdominal pain, nausea, diarrhea, a rash or itch, a cough, and shortness of breath were observed in the chloroquine group, but chloroquine was not discontinued in any of the patients during the treatment period. The efficacy and safety of chloroquine

phosphate was also tested in an open-label, multicenter, non-randomized trial in China and the results were disclosed in an international meeting to share experiences to prevent and control COVID-19 (*11*). Chloroquine demonstrated significant efficacy in reducing the time until virus-negative conversion and returning body temperature to normal (*11*).

Hydroxychloroquine, a more tolerable derivative of chloroquine, also displayed potent activity against SARS-CoV-2 *in vitro* (*12*). A study in France by Raoult *et al*. (*13*) evaluated the efficacy of hydroxychloroquine in 26 patients with COVID-19 and found that administration of hydroxychloroquine 200 mg, three times a day led to a significant reduction in viral carriage on day 6 post-treatment compared to that in the control group, which did not receive hydroxychloroquine. That study also revealed that adding azithromycin to hydroxychloroquine appears to more efficiently clear the virus. A subsequent study by Raoult *et al*. (*14*) involving 80 patients with COVID-19 found that treatment with hydroxychloroquine and azithromycin resulted in a rapid decline in the nasopharyngeal viral load, with a virus-negative rate of 83% on day 7 and a rate of 93% on day 8. Although a control group was not included in that study, its results suggest the potential of hydroxychloroquine to treat COVID-19 given that the recorded median duration of viral shedding is 20 days in survivors (*15*). In addition to the studies cited above, a Chinese team recently released the results of a clinical study on hydroxychloroquine to treat COVID-19 (*16*). That study divided 62 patients into a hydroxychloroquine group and a control group at a ratio of 1:1. Patients in the control group received standard treatment including oxygen therapy, antivirals, antibacterials, and immunoglobulin with or without corticosteroids. Patients in the hydroxychloroquine group received hydroxychloroquine sulfate 200 mg, twice a day for 5 days in addition to the standard treatment. Results indicated that hydroxychloroquine helped reduce the time until body temperature returned to normal, it decreased the duration of cough, and it improved lung imaging findings (*16*). The above studies together favors the usefulness of hydroxychloroquine in treating COVID-19.

A point worth noting is that a pilot study (*17*) in China found that hydroxychloroquine might not help promote virus-negative conversion, reduce the time until body temperature returned to normal, or prevent disease progression. The pilot study involved 30 patients who were randomly divided into a hydroxychloroquine group and a control group at a ratio of 1:1. Patients in the control group received antivirals recommended in the Guidance including IFN-α (100% of patients), arbidol (66.7% of patients), and lopinavir/ritonavir (13.3% of patients). Patients in the hydroxychloroquine group received hydroxychloroquine 400 mg once a day for 5 days (100% of patients), IFN-α (100% of patients), and arbidol (80% of patients). Results indicated that on day 7 post-inclusion the virus-negative rate was 86.7% in the hydroxychloroquine group and 93.3% in the control group (*17*). The median time until virus-negative conversion, the time until body temperature returned to normal, and the rate of disease progression were comparable in both groups (*17*). As patients in both groups received multiple antivirals except for hydroxychloroquine and prognosis was good for all patients, distinguishing the effects of hydroxychloroquine from those of the other antivirals used is difficult. Another possibility is that the combination of antivirals had a ceiling effect since both groups had a high rate of virus-negative conversion.

In general, completed clinical studies have yielded relatively promising results regarding the efficacy and safety of chloroquine/hydroxychloroquine in the treatment of COVID-19. More randomized control clinical studies are warranted to verify the value of these two drugs. To obtain clear and strong evidence, the World Health Organization is launching multi-country clinical trials to test the feasibility of chloroquine/hydroxychloroquine in treating COVID-19, and those results are keenly awaited.

References

1. COVID-19 Map. *https://coronavirus.jhu.edu/map.html* (accessed April 6, 2020).
2. National Health Commission. Interpretation of the Sixth Edition of the Guidance for COVID-19: Prevention, Control, Diagnosis, and Management. *http://www.nhc.gov.cn/xcs/fkdt/202002/54e1ad5c2aac45c19eb541799bf637e9.shtml* (accessed April 2, 2020). (in Chinese)
3. Lenzer J. Covid-19: US gives emergency approval to hydroxychloroquine despite lack of evidence. BMJ. 2020; 369:m1335.
4. COVID-19: chloroquine and hydroxychloroquine only to be used in clinical trials or emergency use programmes. European Medicines Agency. *https://www.ema.europa.eu/en/documents/press-release/covid-19-chloroquine-hydroxychloroquine-only-be-used-clinical-trials-emergency-use-programmes_en.pdf* (accessed April 6, 2020).
5. The Multicenter Collaboration Group of Department of Science and Technology of Guangdong Province and Health Commission of Guangdong Province for Chloroquine in the Treatment of Novel Coronavirus Pneumonia. Expert consensus on chloroquine phosphate for the treatment of novel coronavirus pneumonia. Zhonghua Jie He He Hu Xi Za Zhi. 2020; 43:E019. (in Chinese)
6. Gao J, Tian Z, Yang X. Breakthrough: Chloroquine phosphate has shown apparent efficacy in treatment of COVID-19 associated pneumonia in clinical studies. Biosci Trends. 2020; 14:72-73.
7. Notice on Issuance of the Sixth Edition of the Guidance for COVID-19: Prevention, Control, Diagnosis, and Management. National Health Commission. *http://www.nhc.gov.cn/yzygj/s7653p/202002/8334a8326dd94d329df351d7da8aefc2.shtml* (accessed April 2, 2020). (in Chinese)

8. Notice on Issuance of the Seventh Edition of the Guidance for COVID-19: Prevention, Control, Diagnosis, and Management. National Health Commission. *http://www.nhc.gov.cn/yzygj/s7653p/202003/46c9294a7dfe4cef80dc7f5912eb1989.shtml* (Accessed April 2, 2020). (in Chinese)
9. National Health Commission. Audio transcript of a news briefing held by the State Council of China on March 17, 2020. *http://www.nhc.gov.cn/xcs/fkdt/202003/01426fc0590249ecac89a2874214e523.shtml* (accessed April 6, 2020). (in Chinese)
10. Huang M, Tang T, Pang P, *et al*. Treating COVID-19 with Chloroquine. J Mol Cell Biol. 2020.
11. International meeting to share experiences to prevent and control COVID-19. *https://e.dxy.cn/broadcast/live/id/13818?source=pagesidebar* (Accessed April 8, 2020).
12. Liu J, Cao R, Xu M, Wang X, Zhang H, Hu H, Li Y, Hu Z, Zhong W, Wang M. Hydroxychloroquine, a less toxic derivative of chloroquine, is effective in inhibiting SARS-CoV-2 infection *in vitro*. Cell Discov. 2020; 6:16.
13. Gautret P, Lagier JC, Parola P, *et al*. Hydroxychloroquine and azithromycin as a treatment of COVID-19: results of an open-label non-randomized clinical trial. Int J Antimicrob Agents. 2020;105949. DOI: 10.1016/j.ijantimicag.2020.105949.
14. Gautret P, Lagier JC, Parola P, *et al*. Clinical and microbiological effect of a combination of hydroxychloroquine and azithromycin in 80 COVID-19 patients with at least a six-day follow up: An observational study. Méditerranée Infection. 2020. *https://www.mediterranee-infection.com/wp-content/uploads/2020/03/COVID-IHU-2-1.pdf* (accessed April 6, 2020).
15. Zhou F, Yu T, Du R, *et al*. Clinical course and risk factors for mortality of adult inpatients with COVID-19 in Wuhan, China: A retrospective cohort study. Lancet. 2020; 395:1054-1062.
16. Chen ZW, Hu JJ, Zhang ZW, Jiang S, Han SM, Yan DD, Zhuang RH, Hu B, Zhang Z. Efficacy of hydroxychloroquine in patients with COVID-19: Results of a randomized clinical trial. medRxiv. 2020; doi: https://doi.org/10.1101/2020.03.22.20040758.
17. Chen J, Liu DP, Liu L, Xu QN, Xia L, Ling Y, Huang D, Song SL, Zhang DD, Qian ZP, Li T, Shen YZ, Lu HZ. A pilot study of hydroxychloroquine in treatment of patients with common coronavirus disease-19 (COVID-19). Zhe Jiang Da Xue Xue Bao. 2020. (in Chinese).

Received April 6, 2020; Revised April 10, 2020; Accepted April 11, 2020.

**Address correspondence to:*
Jianjun Gao, Department of Pharmacology, School of Pharmacy, Qingdao University, Qingdao, China.
E-mail: gaojj@qdu.edu.cn

Released online in J-STAGE as advance publication April 13, 2020.

Letter

DOI: 10.5582/bst.2020.03058

Macrolide treatment for COVID-19: Will this be the way forward?

Masashi Ohe[1,*], Haruki Shida[1], Satoshi Jodo[1], Yoshihiro Kusunoki[1], Masahide Seki[1], Ken Furuya[1], Houman Goudarzi[2]

[1] Department of Internal Medicine, JCHO Hokkaido Hospital, Sapporo, Japan;
[2] Department of Respiratory Medicine, Faculty of Medicine and Graduate School of Medicine, Hokkaido University, Sapporo, Japan.

SUMMARY The severe acute respiratory syndrome coronavirus 2 (SARS-CoV-2) pandemic that has developed in late 2019 and 2020 is a serious threat to human health. With no vaccines or drugs approved for prevention and treatment until now, all efforts at drug design and/or clinical trials of already approved drugs are worthy and creditable. Using structure-based drug selection for identification of SARS-CoV-2 protease inhibitors, old drugs such as macrolides (MAC) were predicted to be effective for COVID-19. Lately, the anti-viral effects of macrolides have attracted considerable attention. Very recently, hydroxychloroquine in combination with azithromycin treatment was reported to be effective for COVID-19. We believe that treatments with macrolides alone or in combination with other drugs are promising and open the possibility of an international strategy to fight this emerging viral infection.

Keywords COVID-19, SARS-CoV-2, macrolide

The severe acute respiratory syndrome coronavirus 2 (SARS-CoV-2) outbreak in late 2019 and 2020 is taking a severe toll on human health, and has been acknowledged as a pandemic. Since no vaccines or drugs to combat the disease (COVID-19) have been approved for use until now, all efforts at developing drugs and/or carrying out clinical trials of already approved drugs based on their mechanism of action are worthy and creditable. Anti-viral drugs include inhibitors against protease, integrase, and polymerase enzymes. Among these, the protease inhibitors appear to be effective in terms of blocking virus replication and may prove to be a promising treatment for COVID-19 (*1*). Dayer found several candidates for COVID-19 treatment using structure-based drug selection for the identification of SARS-CoV-2 protease inhibitors. The candidates with binding capacity and inhibitory potency are as follows: tipranavir > indinavir> atazanavir > darunavir > ritonavir > amprenavir used as human immunodeficiency virus-1 protease inhibitors, and cefditoren > cefixime > erythromycin (EM) > clarithromycin (CAM) used as anti-bronchitis medicines (*1*). Macrolides (MAC) such as erythromycin, clarithromycin, and azithromycin (AZM) not only have anti-bacterial activity but also have immunomodulatory effects, including anti-inflammatory effects. Lately, the anti-viral effects of macrolides have attracted considerable attention. Erythromycin is the first macrolide proved to have efficacy in the treatment of rhinovirus (RV) and influenza virus (INFV) (*2*). Thereafter, clarithromycin and azithromycin were also proved to be effective for rhinovirus, respiratory syncytial virus, and influenza virus (*2,3*). Apart from the above-mentioned respiratory viruses, Zika and Ebola viruses have been reported to be inhibited by azithromycin (*4,5*). Tran *et al*. indicated that influenza progeny virus replication was remarkably inhibited by treating influenza virus with azithromycin before infection. During the early phase of influenza virus infection, azithromycin blocked influenza virus internalization into host cells. Furthermore, azithromycin targeted newly budded progeny virus from the host cells and inactivated their endocytic activity. These findings indicate the potential of azithromycin treatment before and after influenza virus infection (*3*).

Regarding macrolides treatment for COVID-19, Gautret *et al*. enrolled patients with COVID-19 and divided them into three groups: six patients with COVID-19 treated with hydroxychloroquine (HC) (200 mg, 3 times per day, for 10 days) in combination with azithromycin (500 mg on day 1, followed by 250 mg per day for the next 4 days), 14 patients with COVID-19 treated with hydroxychloroquine as a single drug, and 16 control patients with COVID-19. In these three groups, patient viral load was assessed daily by real-

time reverse transcription polymerase chain reaction (PCR)-based analysis of nasopharyngeal swabs. As a result, on day 6, 100% of patients treated with hydroxychloroquine in combination with azithromycin exhibited virological cure. In comparison, only 57.1% of the patients treated with hydroxychloroquine as a single drug and 12.5% in the control group exhibited virological cure ($P < 0.001$). Furthermore, one patient, who was treated with hydroxychloroquine as a single drug and still PCR-positive at day 6, received azithromycin, resulting in virological cure. The authors propose that hydroxychloroquine in combination with azithromycin treatment might be an efficient anti-viral therapy for COVID-19 (*6*). Based on the findings for the above-mentioned candidates for COVID-19 treatment, macrolides, especially erythromycin, may generally be effective for COVID-19. Although the mechanism of azithromycin against SARS-CoV-2 is unclear at present unlike the clearly established mechanism of macrolides against influenza virus, we may be able to prescribe the low-priced erythromycin not only as a drug for treatment but also as a preventive drug. We believe that treatments with macrolides alone or in combination with other drugs are promising and open the possibility of an international strategy to fight this emerging viral infection.

References

1. Dayer MR. Old drugs for newly emerging viral disease, COVID-19: Bioinformatic Prospective. arXiv: 2003.04524, 2020-arxiv.org. *https://arxiv.org/ftp/arxiv/papers/2003/2003.04524.pdf* (accessed April 1, 2020).
2. Min JY, Jang YJ. Macrolide therapy in respiratory viral infections. Mediators Inflamm. 2012;2012:649570.
3. Tran DH, Sugamata R, Hirose T, Suzuki S, Noguchi Y, Sugawara A, Ito F, Yamamoto T, Kawachi S, Akagawa KS, Omura S, Sunazuka T, Ito N, Mimaki M, Suzuki K. Azithromycin, a 15-membered macrolide antibiotics, inhibits influenza A(H1N1) pdm09 virus infection by interfering with virus internalization process. J Antibiot. (Tokyo). 2019; 72:759-768.
4. Bosseboeuf E, Aubry M, Nhan T, Pina JJ, Rolain JM, Raoult D, Musso D. Azithromycin inhibits the replication Zika virus. J Antivir Antietrovir. 2018; 10:6-11.
5. Madrid PB, Panchal RG, Warren TK, Shurtleff AC, Endsley AN, Green CE, Kolokoltsov A, Davey R, Manger ID, Gilfillan L, Bavari S, Tanga MJ. Evaluation of Ebola virus inhibitors for drug repurposing. ACS Infect Dis. 2015; 1:317-326.
6. Gautret P, Lagier JC, Parola P, *et al*. Hydroxychloroquine and azithromycin as a treatment of COVID-19: results of an open-label non-randomized clinical trial. Int J Antimicrob Agents. 2020; 20:105949.

Received April 2, 2020; Revised April 4, 2020; Accepted April 4, 2020.

**Address correspondence to:*
Masashi Ohe, Department of Internal Medicine, JCHO Hokkaido Hospital, 1-8-3-18 Nakanoshima, Toyohira-ku, Sapporo 062-8618, Japan.
E-mail: oektsp1218@sweet.ocn.ne.jp

Released online in J-STAGE as advance publication April 5, 2020.

BST
BioScience Trends

Guide for Authors

1. Scope of Articles

BioScience Trends (Print ISSN 1881-7815, Online ISSN 1881-7823) is an international peer-reviewed journal. BioScience Trends devotes to publishing the latest and most exciting advances in scientific research. Articles cover fields of life science such as biochemistry, molecular biology, clinical research, public health, medical care system, and social science in order to encourage cooperation and exchange among scientists and clinical researchers.

2. Submission Types

Original Articles should be well-documented, novel, and significant to the field as a whole. An Original Article should be arranged into the following sections: Title page, Abstract, Introduction, Materials and Methods, Results, Discussion, Acknowledgments, and References. Original articles should not exceed 5,000 words in length (excluding references) and should be limited to a maximum of 50 references. Articles may contain a maximum of 10 figures and/or tables. Supplementary Data are permitted but should be limited to information that is not essential to the general understanding of the research presented in the main text, such as unaltered blots and source data as well as other file types.

Brief Reports definitively documenting either experimental results or informative clinical observations will be considered for publication in this category. Brief Reports are not intended for publication of incomplete or preliminary findings. Brief Reports should not exceed 3,000 words in length (excluding references) and should be limited to a maximum of 4 figures and/or tables and 30 references. A Brief Report contains the same sections as an Original Article, but the Results and Discussion sections should be combined.

Reviews should present a full and up-to-date account of recent developments within an area of research. Normally, reviews should not exceed 8,000 words in length (excluding references) and should be limited to a maximum of 10 figures and/or tables and 100 references. Mini reviews are also accepted, which should not exceed 4,000 words in length (excluding references) and should be limited to a maximum of 5 figures and/or tables and 50 references.

Policy Forum articles discuss research and policy issues in areas related to life science such as public health, the medical care system, and social science and may address governmental issues at district, national, and international levels of discourse. Policy Forum articles should not exceed 3,000 words in length (excluding references) and should be limited to a maximum of 5 figures and/or tables and 30 references.

Communications are short, timely pieces that spotlight new research findings or policy issues of interest to the field of global health and medical practice that are of immediate importance. Depending on their content, Communications will be published as “Comments” or “Correspondence”. Communications should not exceed 1,500 words in length (excluding references) and should be limited to a maximum of 2 figures and/or tables and 20 references.

Editorials are short, invited opinion pieces that discuss an issue of immediate importance to the fields of global health, medical practice, and basic science oriented for clinical application. Editorials should not exceed 1,000 words in length (excluding references) and should be limited to a maximum of 10 references. Editorials may contain one figure or table.

News articles should report the latest events in health sciences and medical research from around the world. News should not exceed 500 words in length.

Letters should present considered opinions in response to articles published in BioScience Trends in the last 6 months or issues of general interest. Letters should not exceed 800 words in length and may contain a maximum of 10 references. Letters may contain one figure or table.

3. Editorial Policies

Ethics: BioScience Trends requires that authors of reports of investigations in humans or animals indicate that those studies were formally approved by a relevant ethics committee or review board.

Conflict of Interest: All authors are required to disclose any actual or potential conflict of interest including financial interests or relationships with other people or organizations that might raise questions of bias in the work reported. If no conflict of interest exists for each author, please state "There is no conflict of interest to disclose".

Submission Declaration: When a manuscript is considered for submission to BioScience Trends, the authors should confirm that 1) no part of this manuscript is currently under consideration for publication elsewhere; 2) this manuscript does not contain the same information in whole or in part as manuscripts that have been published, accepted, or are under review elsewhere, except in the form of an abstract, a letter to the editor, or part of a published lecture or academic thesis; 3) authorization for publication has been obtained from the authors' employer or institution; and 4) all contributing authors have agreed to submit this manuscript.

Cover Letter: The manuscript must be accompanied by a cover letter prepared by the corresponding author on behalf of all authors. The letter should indicate the basic findings of the work and their significance. The letter should also include a statement affirming that all authors concur with the submission and that the material submitted for publication has not been published previously or is not under consideration for publication elsewhere. The cover letter should be submitted in PDF format. For example of Cover Letter, please visit: (Download Centre)

Copyright: Before a manuscript is accepted for publication in BioScience Trends, the transfer of copyright is necessary. A JOURNAL PUBLISHING AGREEMENT (JPA) form will be e-mailed to the authors by the Editorial Office and must be returned by the authors as a scan. Only forms with a hand-written signature are accepted. This copyright will ensure the widest possible dissemination of information. Please note that your manuscript will not proceed to the next step in publication until the JPA Form is received. In addition, if excerpts from other copyrighted works are included, the author(s) must obtain written permission from the copyright owners and credit the source(s) in the article.

Suggested Reviewers: A list of up to 3 reviewers who are qualified to assess the scientific merit of the study is welcomed. Reviewer information including names, affiliations, addresses, and e-mail should be provided at the same time the manuscript is submitted online. Please do not suggest reviewers with known conflicts of interest, including participants or anyone with a stake in the proposed research; anyone from the same institution; former students, advisors, or research collaborators (within the last three years); or close personal contacts. Please note that the Editor-in-Chief may accept one or more of the proposed reviewers or may request a review by other qualified persons.

Language Editing: Manuscripts prepared by authors whose native language is not English should have their work proofread by a native English speaker before submission. If not, this might delay the publication of your manuscript in BioScience Trends.

The Editing Support Organization can provide English proofreading, Japanese-English translation, and Chinese-English translation services to authors who want to publish in BioScience Trends and need assistance before submitting a manuscript. Authors can visit this organization directly *at http://www.iacmhr.com/iac-eso/support.php?lang=en*. IAC-ESO was established to facilitate manuscript preparation by researchers whose native language is not English and to help edit works intended for international academic journals.

4. Manuscript Preparation

Manuscripts are suggested to be prepared in accordance with the "Recommendations for the Conduct, Reporting, Editing, and Publication of Scholarly Work in Medical Journals", as presented at *http://www.ICMJE.org*.

Manuscripts should be written in clear, grammatically correct English and submitted as a Microsoft Word file in a single-column format. Manuscripts must be paginated and typed in 12-point Times New Roman font with 24-point line spacing. Please do not embed figures in the text. Abbreviations should be used as little as possible and should be explained at first mention unless the term is a well-known abbreviation (*e.g.* DNA). Single words should not be abbreviated.

Title page: The title page must include 1) the title of the paper (Please note the title should be short, informative, and contain the major key words); 2) full name(s) and affiliation(s) of the author(s), 3) abbreviated names of the author(s), 4) full name, mailing address, telephone/fax numbers, and e-mail address of the corresponding author; and 5) conflicts of interest (if you have an actual or potential conflict of interest to disclose, it must be included as a footnote on the title page of the manuscript; if no conflict of interest exists for each author, please state "There is no conflict of interest to disclose"). Please visit Download Centre and refer to the title page of the manuscript sample.

Abstract: The abstract should briefly state the purpose of the study, methods, main findings, and conclusions. For articles that are Original Articles, Brief Reports, Reviews, or Policy Forum articles, a one-paragraph abstract consisting of no more than 250 words must be included in the manuscript. For Communications, Editorials, News, or Letters, a brief summary of main content in 150 words or fewer should be included in the manuscript. Abbreviations must be kept to a minimum and non-standard abbreviations explained in brackets at first mention. References should be avoided in the abstract. Three to six key words or phrases that do not occur in the title should be included in the Abstract page.

Introduction: The introduction should be a concise statement of the basis for the study and its scientific context.

Materials and Methods: The description should be brief but with sufficient detail to enable others to reproduce the experiments. Procedures that have been published previously should not be described in detail but appropriate references should simply be cited. Only new and significant modifications of previously published procedures require complete description. Names of products and manufacturers with their locations (city and state/country) should be given and sources of animals and cell lines should always be indicated. All clinical investigations must have been conducted in accordance with Declaration of Helsinki principles. All human and animal studies must have been approved by the appropriate institutional review board(s) and a specific declaration of approval must be made within this section.

Results: The description of the experimental results should be succinct but in sufficient detail to allow the experiments to be analyzed and interpreted by an independent reader. If necessary, subheadings may be used for an orderly presentation. All figures and tables must be referred to in the text.

Discussion: The data should be interpreted concisely without repeating material already presented in the Results section. Speculation is permissible, but it must be well-founded, and discussion of the wider implications of the findings is encouraged. Conclusions derived from the study should be included in this section.

Acknowledgments: All funding sources should be credited in the Acknowledgments section. In addition, people who contributed to the work but who do not meet the criteria for authors should be listed along with their contributions.

References: References should be numbered in the order in which they appear in the text. Citing of unpublished results, personal communications, conference abstracts, and theses in the reference list is not recommended but these sources may be mentioned in the text. In the reference list, cite the names of all authors when there are fifteen or fewer authors; if there are sixteen or more authors, list the first three followed by et al. Names of journals should be abbreviated in the style used in PubMed. Authors are responsible for the accuracy of the references. The EndNote Style of BioScience Trends could be downloaded at EndNote

Examples are given below:

Example 1 (Sample journal reference):

Inagaki Y, Tang W, Zhang L, Du GH, Xu WF, Kokudo N. Novel aminopeptidase N (APN/CD13) inhibitor 24F can suppress invasion of hepatocellular carcinoma cells as well as angiogenesis. Biosci Trends. 2010; 4:56-60.

Example 2 (Sample journal reference with more than 15 authors):

Darby S, Hill D, Auvinen A, *et al.* Radon in homes and risk of lung cancer: Collaborative analysis of individual data from 13 European case-control studies. BMJ. 2005; 330:223.

Example 3 (Sample book reference):

Shalev AY. Post-traumatic stress disorder: Diagnosis, history and life course. In: Post-traumatic Stress Disorder, Diagnosis, Management and Treatment (Nutt DJ, Davidson JR, Zohar J, eds.). Martin Dunitz, London, UK, 2000; pp. 1-15.

Example 4 (Sample web page reference):

World Health Organization. The World Health Report 2008 – primary health care: Now more than ever. http://www.who.int/whr/2008/whr08_en.pdf (accessed September 23, 2010).

Tables: All tables should be prepared in Microsoft Word or Excel and should be arranged at the end of the manuscript after the References section. Please note that tables should not in image format. All tables should have a concise title and should be numbered consecutively with Arabic numerals. If necessary, additional information should be given below the table.

Figure Legend: The figure legend should be typed on a separate page of the main manuscript and should include a short title and explanation. The legend should be concise but comprehensive and should be understood without referring to the text. Symbols used in figures must be explained. Any individually labeled figure parts or panels (A, B, *etc.*) should be specifically described by part name within the legend.

Figure Preparation: All figures should be clear and cited in numerical order in the text. Figures must fit a one- or two-column format on the journal page: 8.3 cm (3.3 in.) wide for a single column, 17.3 cm (6.8 in.) wide for a double column; maximum height: 24.0 cm (9.5 in.). Please make sure that the symbols and numbers appeared in the figures should be clear. Please make sure that artwork files are in an acceptable format (TIFF or JPEG) at minimum resolution (600 dpi for illustrations, graphs, and annotated artwork, and 300 dpi for micrographs and photographs). Please provide all figures as separate files. Please note that low-resolution images are one of the leading causes of article resubmission and schedule delays.

Units and Symbols: Units and symbols conforming to the International System of Units (SI) should be used for physicochemical quantities. Solidus notation (*e.g.* mg/kg, mg/mL, mol/mm^2/min) should be used. Please refer to the SI Guide www.bipm.org/en/si/ for standard units.

Supplemental data: Supplemental data might be useful for supporting and enhancing your scientific research and BioScience Trends accepts the submission of these materials which will be only published online alongside the electronic version of your article. Supplemental files (figures, tables, and other text materials) should be prepared according to the above guidelines, numbered in Arabic numerals (*e.g.*, Figure S1, Figure S2, and Table S1, Table S2) and referred to in the text. All figures and tables should have titles and legends. All figure legends, tables and supplemental text materials should be placed at the end of the paper. Please note all of these supplemental data should be provided at the time of initial submission and note that the editors reserve the right to limit the size and length of Supplemental Data.

5. Submission Checklist

The Submission Checklist will be useful during the final checking of a manuscript prior to sending it to BioScience Trends for review. Please visit Download Centre and download the Submission Checklist file.

6. Online Submission

Manuscripts should be submitted to BioScience Trends online at http://www.biosciencetrends.com. The manuscript file should be smaller than 5 MB in size. If for any reason you are unable to submit a file online, please contact the Editorial Office by e-mail at office@biosciencetrends.com

7. Accepted Manuscripts

Proofs: Galley proofs in PDF format will be sent to the corresponding author *via* e-mail. Corrections must be returned to the editor (proof-editing@biosciencetrends.com) within 3 working days.

Offprints: Authors will be provided with electronic offprints of their article. Paper offprints can be ordered at prices quoted on the order form that accompanies the proofs.

Page Charge: Page charges will be levied on all manuscripts accepted for publication in BioScience Trends ($140 per page for black white pages; $340 per page for color pages). Under exceptional circumstances, the author(s) may apply to the editorial office for a waiver of the publication charges at the time of submission.

(*As of February 2020*)

BioScience Trends

Editorial and Head Office
Pearl City Koishikawa 603
2-4-5 Kasuga, Bunkyo-ku
Tokyo 112-0003
Japan
E-mail: office@biosciencetrends.com